Università degli Studi di Padova

Department of Chemical Sciences

PHD COURSE IN: MOLECULAR SCIENCES
CURRICULUM: CHEMICAL SCIENCES
SERIES: XXXVIII

ADVANCED MATERIALS FOR BUILDING-INTEGRATED PHOTOVOLTAICS: IMPLEMENTATION OF LANTHANIDE COMPLEXES AND ORGANIC CHROMOPHORES IN LUMINESCENT SOLAR CONCENTRATORS

Coordinator: Ch.mo Prof. Stefano Corni

Supervisor: Ch.ma Prof.ssa Lidia Armelao

Co-supervisor: Egr. Dott. Gregorio Bottaro

Ph.D. candidate: Irene Motta

Abstract

The solar energy landscape is experiencing an unprecedented growth, not only in terms of global installed capacity, but also in the design of innovative solar devices for distributed and customized installations. Building-Integrated Photovoltaics (BIPVs) is a promising approach to boost the energy efficiency of heavily urbanized areas by designing photovoltaic devices as proper building elements. In this context, Luminescent Solar Concentrators (LSCs) emerge as an innovative BIPV technology to achieve photovoltaic windows, ensuring energy production and transparency at the same time. LSCs typically consist of slates of transparent material, doped or coated with luminescent chemical species. The emission of such luminophores is stimulated by a certain wavelength range of the solar spectrum. The photons generated inside the slate are waveguided to its edges, where they can be collected by conventional PV cells. This thesis work reports the design, development and characterization of new luminescent materials for LSCs, with BIPV as the main target application.

A first LSC case study focused on the development of highly transparent and colourless photovoltaic windows that selectively absorb UV photons. Super bright Lanthanide Organic Cages (LOCs) based on Eu^{3+}, with the general formula $[Eu_2L_4]^{2-}$, were embedded into poly(methyl methacrylate) (PMMA) through bulk-polymerization to realize $50 \times 50 \times 3$ mm^3 planar luminescent tiles. The red emission of the LOCs is stimulated by UV light through the antenna effect, leading to a favourable large pseudo-Stokes shift (≈ 200 nm). The obtained materials showed excellent aesthetic quality, with transparency and colour rendering comparable to standard window glass (AVT: Average Visible Transmittance ≈ 92%, CRI: Colour Rendering Index > 98). Electrical performances were evaluated by coupling the waveguides to silicon solar cells and collecting standard figures of merit for photovoltaic devices (J-V: Current density-Voltage curves, EQE: External Quantum

Efficiency spectra). The Power Conversion Efficiency (PCE, *i.e.*, the electrical efficiency) assessed for the best performing devices was 0.1%, a value typical of highly transparent photovoltaics. Remarkably, the LSCs herein developed yielded such performances at a greatly reduced use of Eu^{3+}, down to a hundred-fold when compared to analogous literature case studies. Furthermore, the LSCs absorbed quantitatively the incident UV photons within the 300 – 400 nm range, providing a desirable UV-blocking feature. This aspect was further exploited to investigate the multifunctionality of the LSCs as visible-blind UV photodetectors. The LSC-based photodetectors demonstrated complete selectivity towards UV radiation and sensor performances comparable to conventional heterojunction-based systems, while maintaining the simple “waveguide + PV cell” architecture inherent of LSCs.

A second LSC case study involved a series of visible-absorbing, strongly fluorescent oligothiophenes. The luminophores were specifically designed to have an enhanced Stokes shift (100 – 150 nm), so to mitigate reabsorption losses usually occurring in LSCs based on organic dyes. A series of LSCs was prepared using the oligothiophenes and a state-of-the-art dye as reference. The slot die coating technique was used to fabricate 35 μm thick luminescent films deposited onto 3 mm thick glass with 50 × 50 mm^2 active area. Several films were realized, containing the luminophores at increasing concentration. Highest luminophore loadings produced at the same time the lowest AVTs and the highest PCEs, evidencing the intrinsic trade-off between aesthetic rendering and energy production in transparent photovoltaics. Hence, the different devices were evaluated based on their Light Utilization Efficiency ($LUE = PCE \times AVT$), a metric indicating how a photovoltaic device can simultaneously optimize both transparency and electrical output. Best-performing devices based on oligothiophenes showed LUE and photostability competitive with the state-of-the-art and the relevant literature, while offering a range of alternative waveguide colorations (yellow to orange) with respect to frequently proposed red-coloured LSCs.

Lastly, the thesis work comprised also a study on a predictive model for the electrical output of coloured PV modules. The model was developed based on a simplified Device Under Test (DUT), consisting in a silicon solar cell and a single coloured layer. The model aimed to provide accurate predictions of the electrical spectral output of the coloured PV stack by exploiting simple input parameters relative to its discrete components, as the spectral response of the PV cell, the transmittance of the coloured

layer, and the spectral power distribution of the incident light. The simulations of the spectral short-circuit current were then compared to experimental data recorded on a coloured PV prototype to verify the accuracy of the model's predictions. Three different colouring technologies were investigated: non-diffusive glass filters, ground-glass diffusers, and fluorescent PMMA films originally developed for the LSC application. For the glass filters and diffusers, the model showed excellent accuracy of the simulated outputs, with a percentage square error ($SE\%$) below 2% with respect to experimental data. For the fluorescent films, the beneficial effect of the fluorescence photons on the cell's electrical output was observed. However, the accuracy of the predictions slightly decreased, especially within the luminophore's absorption region, evidencing how a rigorous modelling of the fluorescence photons is necessary to efficiently simulate a PV module laminated with this kind of coloured layer.

Index

CHAPTER 3

CHAPTER 4

CHAPTER 5

CHAPTER 6

CHAPTER 7

CHAPTER 8

CHAPTER 9

APPENDIX A

APPENDIX B

APPENDIX C

Symbols and acronyms

A	Absorbance
AMW	Average Molecular Weight
a-Si	Amorphous silicon
ACQ	Aggregation Caused Quenching
AIBN	Azobisisobutyronitrile
AM	Air mass
AVT	Average Visible Transmittance
B	Molar brightness
BEnT	Back energy transfer
BIPVs	Building-Integrated Photovoltaics
BPO	Benzoyl peroxide
btfa	Benzoyltrifluoroacetone
CCD	Charge Coupled Device
CCDC	Cambridge Crystallographic Data Centre
CIE	Commission Internationale de l’Éclairge
CH_2Cl_2	Dichloromethane
$CHCl_3$	Chloroform
CIGS	Copper indium gallium selenide
c-Si	Monocrystalline silicon
CRI	Colour Rendering Index
D*	Specific detectivity
DSSC	Dye-Sensitized Solar Cell

DMSO	Dimethyl sulfoxide
DOSY	Diffusion-Ordered NMR Spectroscopy
DUT	Device Under Test
EQE	External Quantum Efficiency
ESI-MS	Electrospray Ionization Mass Spectrometry
EVA	Ethylene-vinyl acetate
FF	Fill factor
FRET	Forster Resonance Energy Transfer
FWHM	Full Width at Half Maximum
g	Geometric correction factor
G	Geometric gain
I	Electrical current
ISC	Inter-System Crossing
ITO	Indium tin oxide
IUPAC	International Union of Pure and Applied Chemistry
J	Electrical current density
LDR	Linear Dynamic Range
LED	Light Emitting Diode
Ln	Lanthanide
LOCs	Lanthanide Organic Cages
LOD	Limit Of Detection
LR305	Lumogen® F Red 305
LSC	Luminescent Solar Concentrator
LSC-PV	Luminescent Solar Concentrator (coupled to photovoltaic cell)
LUE	Light Utilization Efficiency
MMA	Methyl methacrylate
n	Refractive index
NEP	Noise Equivalent Power
NIR	Near Infrared
NMR	Nuclear Magnetic Resonance

OC	Optical coupling
OPVs	Organic Photovoltaics
P	Power (optical, electrical)
PC	Polycarbonate
PCE	Power Conversion Efficiency
phen	1,10-phenathroline
PL	Photoluminescence
PLQY	Photoluminescence Quantum Yield
PMMA	Poly(methyl methacrylate)
PSC	Perovskite Solar Cell
PTFE	Polytetrafluoroethylene
PV	Photovoltaic
PVB	Polyvinyl butyral
PVC	Polyvinyl chloride
QDs	Quantum Dots
R	Responsivity
RF	Radiofrequency
S_0	Ground singlet state
S_1	First excited singlet state
SE%	Percentage relative square error
SMU	Source Meter Unit
sccm	Standard cubic centimetre per minute
SR	Spectral Response
T_1	First excited triplet state
T_{bp}	Boiling point temperature
TEAOH	Tetraethylammonium hydroxide
Tg	Glass transition temperature
THF	Tetrahydrofuran
TIR	Total Internal Reflection
tta	Thenoyltrifluoroacetone

UV	Ultraviolet
V	Electrical voltage
VIS	Visible
V_{OC}	Open-circuit voltage
XRD	X-Ray Diffraction
α, A%	Absorptance
χ_{bi}	Bifaciality coefficient
ε	Molar extinction coefficient, or absorptivity
λ	Wavelength
η_{int}	Internal photon efficiency
$\eta_{s,abs}$	Total solar absorptance
θ_c	Critical angle
ρ	Density
ρ, R%	Reflectance
σ	Standard deviation
τ, T%	Transmittance

Chapter 1

Introduction: molecule-driven innovation in photovoltaics

1.1 The solar energy picture

As decarbonisation has become ever more urgent, ever greater investments in renewable energy technologies are needed. Among renewables, hydropower and wind provide the largest contributions in terms of actual produced electricity, followed by solar.[1,2] Nonetheless, the global solar energy landscape is currently characterized by unprecedented growth and significant technological advancements, positioning photovoltaics (PV) as a cornerstone in the ongoing energy transition and indicating a future shift in the renewable energy production ranking.

In 2024, global installed solar capacity surpassed the 2 terawatts milestone (**Fig. 1.1**), with nearly 600 gigawatts installed in 2024 alone, marking a 33% increase over the previous year.[1,3] Utility-scale solar plants lead solar installations, but distributed PV still provides a significant contribution with commercial, industrial, and residential rooftop arrays. In the future, such distributed installations will become increasingly prominent, as electrification policies are pushing for a higher grid flexibility and a smarter, more diffuse power generation ensuring ubiquitous access to solar energy.

The remarkable progress in solar energy is largely attributed to the continuous improvements in silicon solar cells. Monocrystalline silicon (c-Si) remains indeed the dominant material in the PV module market, as research in cell design keeps breaking new commercial efficiency records (27.8% most recent).[4]

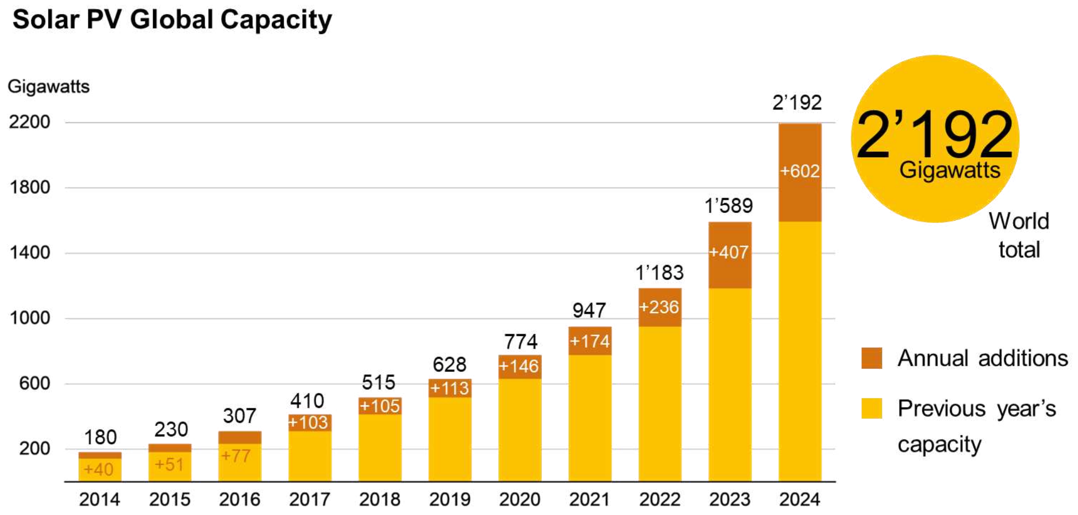

Figure 1.1. Global installed solar capacity chart highlighting annual additions, 2014 – 2024. Elaborated with data from the “Renewables 2025 Global Status Report” provided by REN21.[3]

While silicon modules are the pillar of the solar energy capacity increase, significant research and development is focused on next-generation photovoltaics. Third generation PVs, in particular, rely on new materials and device architectures to maximize spectral utilization and enhance light management, often introducing additional functionalities such as flexibility, transparency and thermalization losses reduction.[5–7] Devices in this family offer great product customization, which is essential in applications such as Building Integrated Photovoltaics (BIPVs) or indoor installations.

Perovskite Solar Cells (PSCs), Dye-Sensitized Solar Cells (DSSCs) and Organic Photovoltaics (OPVs) are the third-generation technologies most intensively researched at present as alternatives for solar cells, aiming to be competitive with silicon.[6–8] On a different note, Luminescent Solar Concentrators (LSCs) are another emerging PV technology that exploits luminescent chemical species to convert and redirect incident radiation on a target PV material. They are compatible with conventional Si solar cells, but also with the third-generation technologies listed above, unlocking new possibilities for a smart, application-targeted production of solar energy. The innovative designs characterizing PSCs, DSSCs, OPVs and LSCs endow them with high versatility, optical properties tunability and generally low-cost production. However, as emerging technologies, a common issue they share is the reduced device lifetime due to poor thermal and/or photo stability of their components. A brief overview on each of these devices is presented, highlighting for each of them their working mechanism, their potential applications and the limitations to overcome to reach commercialization.

Perovskite Solar Cells have emerged as the most rapidly advancing third-generation photovoltaic in recent years, demonstrating laboratory electrical efficiencies up to 25% that rival those of traditional silicon solar.[9,10] This is especially true for tandem configurations, where multiple perovskite materials with different absorption properties are interfaced to extend the solar spectral coverage.[11,12] Their defining characteristic is the photoactive layer composed of a perovskite, the core material absorbing incident photons and converting them into charge carriers (**Fig. 1.2**).

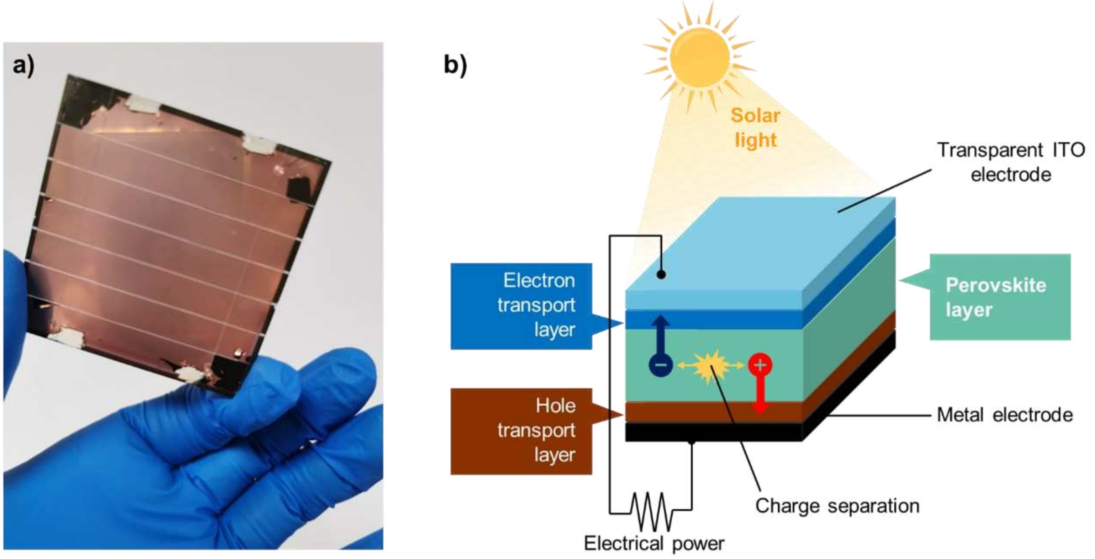

Figure 1.2. a) Mixed Pb-Sn perovskite-based PSC. Credit: Lin *et al.*[11] **b)** Schematics of a PSC's structure and working mechanism.

The perovskite is sandwiched between two charge transport layers which are injected with photogenerated holes and electrons, respectively. The whole stack is comprised between two outer electrodes, one metallic and one transparent to allow light penetration. Transparent electrodes typically consist of glass coated with a conductive metal oxide layer. The most employed one is indium tin oxide (ITO), which electrodes are already widely commercialized. The term "perovskite", originally indicating the calcium titanium oxide mineral $CaTiO_3$, refers to a whole class of compounds having similar structure and the general formula ABX_3, where A and B are cations and X is the anion (often O^{2-} or a halide like I^-, Br^-). Halide perovskites based on organic cations (A cation) and Pb^{2+}/Sn^{2+} (B cation) have sparked interest as light absorbers for thin film solar cells. In fact, by tuning the chemical composition of the perovskite, its optical bandgap can be modified to reach optimized light absorption across different regions of the solar spectrum,[13,14] which is crucial for high efficiency tandem applications. Perovskites offer some further advantages, such as solution processability compatible with large area manufacturing, and high absorption coefficients (10^4 M^{-1} cm^{-1}) enabling the use of very thin active layers (10^1 – 10^2 nm) for reduced material consumption.[15] A primary concern hindering PSCs' market deployment is the intrinsic instability of perovskite materials when exposed to oxygen, moisture and continuous UV irradiation.[16,17] Secondly, many of the most efficient reported PSCs contain lead,[18–20] which is of environmental concern due to the possibility of leakage in damaged modules.

Dye-Sensitized Solar Cells, often referred to as Grätzel cells from the name of their inventor,[21] are photoelectrochemical systems that offer great aesthetic versatility at relatively low manufacturing costs. The core of a DSSC consists of a sensitizer organic or organometallic dye adsorbed on TiO_2 nanoparticles, which are deposited on the cell's photoanode (**Fig. 1.3**). The dye is responsible for absorbing sunlight and injecting photoexcited electrons into the conduction band of TiO_2 and then in the cell's external circuit. The oxidised dye is regenerated thanks to a redox-active electrolyte in contact with the counter electrode. Both electrodes are transparent, and bifacial functionality can be implemented.[23] The choice of the sensitizer dye allows for a wide range of colours and transparency degrees.[24,25]

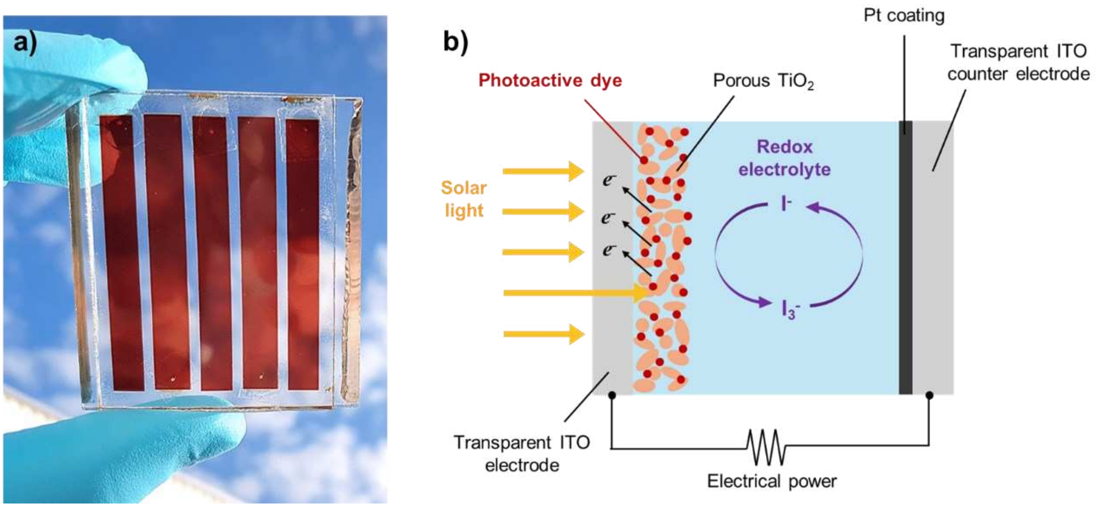

Figure 1.3. a) Benzothiadiazole based DSSC. Credit: Godfroy *et al.*[22] **b)** Schematics of a DSSC's structure and working mechanism.

DSSCs perform well under diffuse light conditions, such as indoor illumination, and can be fabricated using solution-based printing techniques at low temperatures. Average electrical efficiencies are established around 10%,[22,26] with records of 15% for best devices. However, they still lack a robust manufacturing process ensuring the sealing of the liquid electrolyte and are generally affected by electrolyte and dye stability issues.[27,28]

Organic Photovoltaics utilize organic semiconducting polymers or small molecules as the active light-absorbing and charge-transport materials. These cells leverage the unique properties of organic semiconductors, offering the potential for low-cost, flexible, lightweight and transparent solar modules.[29–31] The active layer in an OPV is a "bulk heterojunction", consisting of a blend of electron-donating and electron-accepting organic materials. Other configurations are accessible, as bilayer heterojunctions, where the two organic materials are put together in a stack rather than being blended together (**Fig. 1.4**).

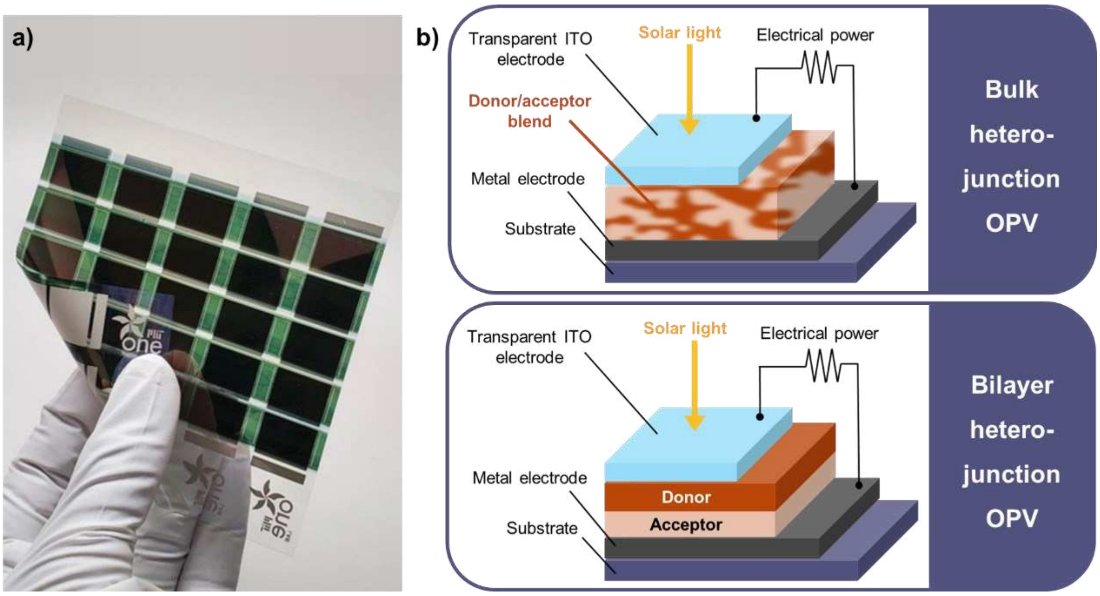

Figure 1.4. a) Printed OPV module. Credit: Saravanapavanantham *et al.*[32] **b)** Schematics of bulk (top) and bilayer (bottom) heterojunction structures used in OPVs.

When light is absorbed by either donor or acceptor, an exciton is generated. At the interface between the two materials, excitons generated in the donor split by transferring the electron to the acceptor and retaining the hole in the donor. Excitons generated in the acceptor undergo the opposite split. The separated charges then diffuse in the bulk of the respective materials to the corresponding electrodes. Similarly to PSCs, charge transport layers can be introduced between the photoactive material and the electrodes. OPVs can be produced using high-throughput, roll-to-roll printing techniques from solution-processed inks, significantly reducing manufacturing costs.[32] The use of organic materials allows for fabrication on flexible plastic substrates, enabling lightweight applications in portable electronics, wearable devices and curved surfaces.[33,34] The absorption of organic semiconductors can be tuned, offering also for OPVs different colourations and degrees of transparency.[35] While significant progress has been made in terms of electrical efficiency, with best devices reaching 20%,[36,37] OPVs still suffer from exciton dissociation and charge transport issues due to the intrinsic structural disorder of organic materials. Unequal mobilities of electrons and holes in the two materials of the bulk heterojunction further limit efficiency by leading to excessive charge recombination.[38]

Finally, Luminescent Solar Concentrators offer a different approach to solar energy harvesting, by spatially separating the functions of light collection and power generation. First proposed in 1977 by Goetzberger and Greube,[39] LSCs typically consist of large, transparent panels doped or coated with luminescent species (called luminophores, or emitters), which emission is stimulated by sunlight (**Fig. 1.5**). Emitted photons travel, waveguided, inside the panel by total internal reflection (TIR) and concentrate on its edges. Such concentrated light is ultimately converted into electricity by thin PV cells placed at the edges.

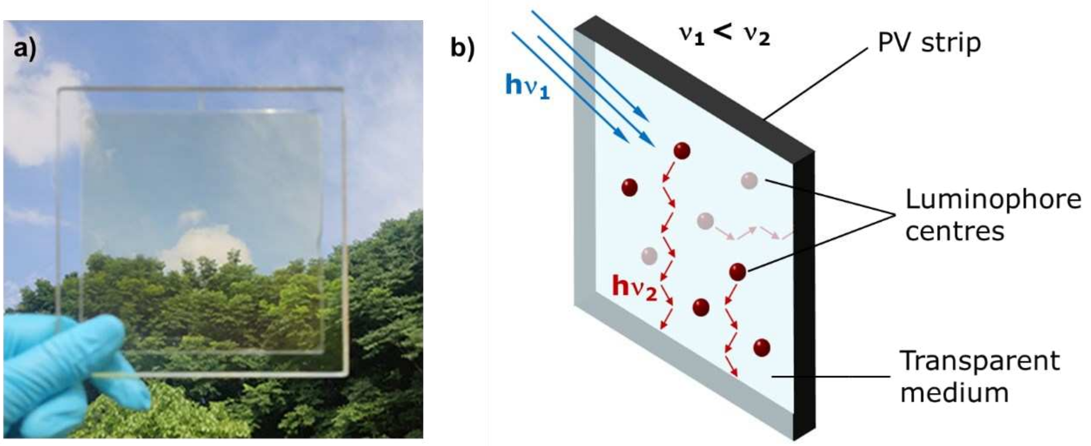

Figure 1.5. a) Si quantum dots based LSC. Credit: Huang *et al.*[40] **b)** Schematics of an LSC's structure and working mechanism.

LSCs display the simplest architecture among the examined technologies, and they can be fabricated with easily affordable methods either when bulk-doped with the luminophore or when coated with a luminescent active layer. LSCs are less affected by electrical efficiency drops due to diffuse or scattered light conditions (*i.e.*, cloudy days, vertical surfaces), thus not needing complex sun-tracking mechanisms.[41,42] Furthermore, they are less sensitive to shading with respect to solar cells, because the edge-coupled PV cells never get directly shadowed. Rather, they receive continuous irradiation from the light emitted inside the waveguide, avoiding the overheating and parasitic resistance effects occurring in typical shading phenomena. This technology is particularly appealing for its aesthetic versatility and potential for large-scale integration into transparent or semi-transparent architectural elements (BIPVs), without compromising natural light penetration as traditional opaque PV panels would.[43,44] Additionally, the coupling between a large collecting area and a relatively small PV area reduces the overall amount of semiconductor material required and mitigates thermal effects on the cells' efficiency. However, LSCs present inherent optical losses occurring in the waveguide,[45,46] as incomplete absorption by luminophores, re-absorption of emitted light, non-unity quantum yield and escape cone losses (light not undergoing TIR). Luminophore stability is once again a crucial aspect still to be addressed. An in-depth analysis on LSCs' state of the art is provided later (see *Section 1.3*).

1.2 Building-integrated photovoltaics

Building Integrated Photovoltaics hold a pivotal position in the transition towards energetically sustainable architecture and urban development. When considering climate change, buildings are a major energy consuming sector, accounting for one third of global energy consumption and one quarter of global CO_2 emissions.[47] By generating solar energy directly at the point of consumption, BIPV systems reduce buildings' reliance on fossil fuels and boost grid coverage, contributing to net-zero or even energy-positive targets.[48,49] Demonstrating the importance of BIPV, its market share is increasing year by year, with Europe in a leading position thanks to solid regulatory frameworks promoting the utilization of renewable energy sources.[51]

Essentially, BIPVs are PV modules specifically designed to be integrated into the structural envelope of a building, directly as architectural components (**Fig. 1.6**).

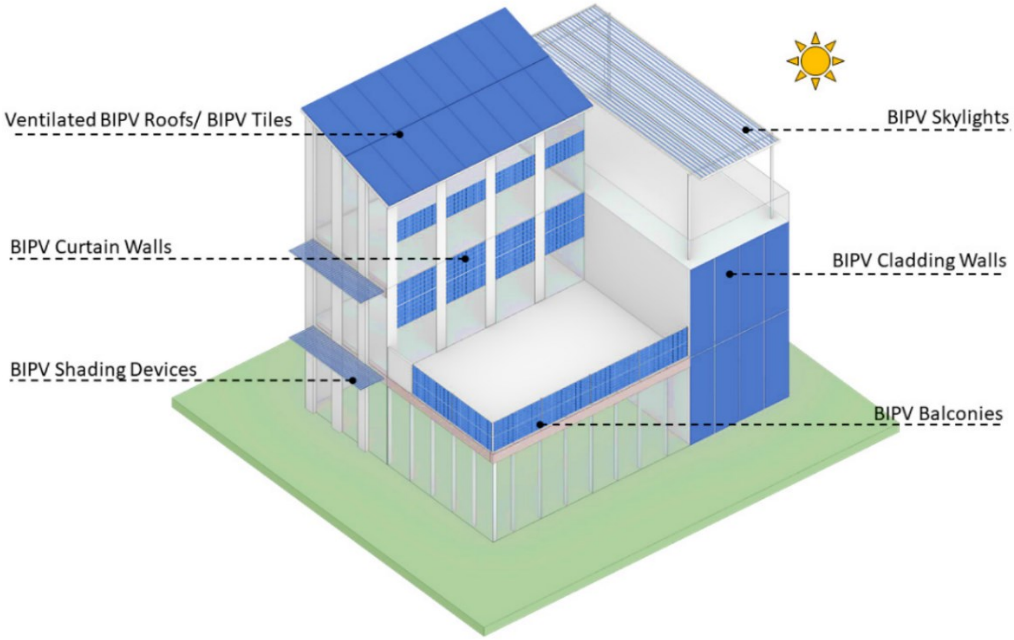

Figure 1.6. Potential integration of PV systems into different building elements. Credit: Chen *et al.*[50]

This includes roofs (shingles, skylights), façades (curtain walls) and glazing elements (windows, balcony railings, canopies).[50] By converting a building itself in an energy generating unit, BIPVs eliminate the requirements for additional space allocation or separate module installation. This is of particular importance in densely populated areas, where the urban landscape is mainly comprised of tall, multi-floor buildings.

Beyond the quantifiable energy benefits, BIPVs offer seamless solutions to mitigate the visual impact of photovoltaic devices. This aesthetic integration is achieved through transparent and semi-transparent PV windows, coloured solar façades and customizable module shapes and sizes. It follows that, to reach widespread adoption, BIPVs must appeal not only to performance metrics but also to aesthetic requirements of designers and occupants, the latter often prevailing. This is the case of BIPV windows, where implementing an energy generating device cannot compromise their primary functionality of letting visible light to pass through. A common aspect of transparent PVs is that electrical efficiency and transparency face an intrinsic trade-off between one another.[52–54] The more visible light the device allows through, the higher the fraction of photons lost to transmission, consequently not available for absorption and charge carrier generation. With recent architectural designs progressively increasing the window-to-wall ratio, especially in high-rise buildings, developing efficient and aesthetically compliant photovoltaic glass is paramount.

Just in 2022, BIPV glass accounted for 37% of global BIPV installations,[55] underscoring the need to exploit each and every building element available for solar energy production. Currently deployed technologies for achieving BIPV glass comprise spatially segmented photovoltaics and thin-film photovoltaics[56,57] (**Fig. 1.7**).

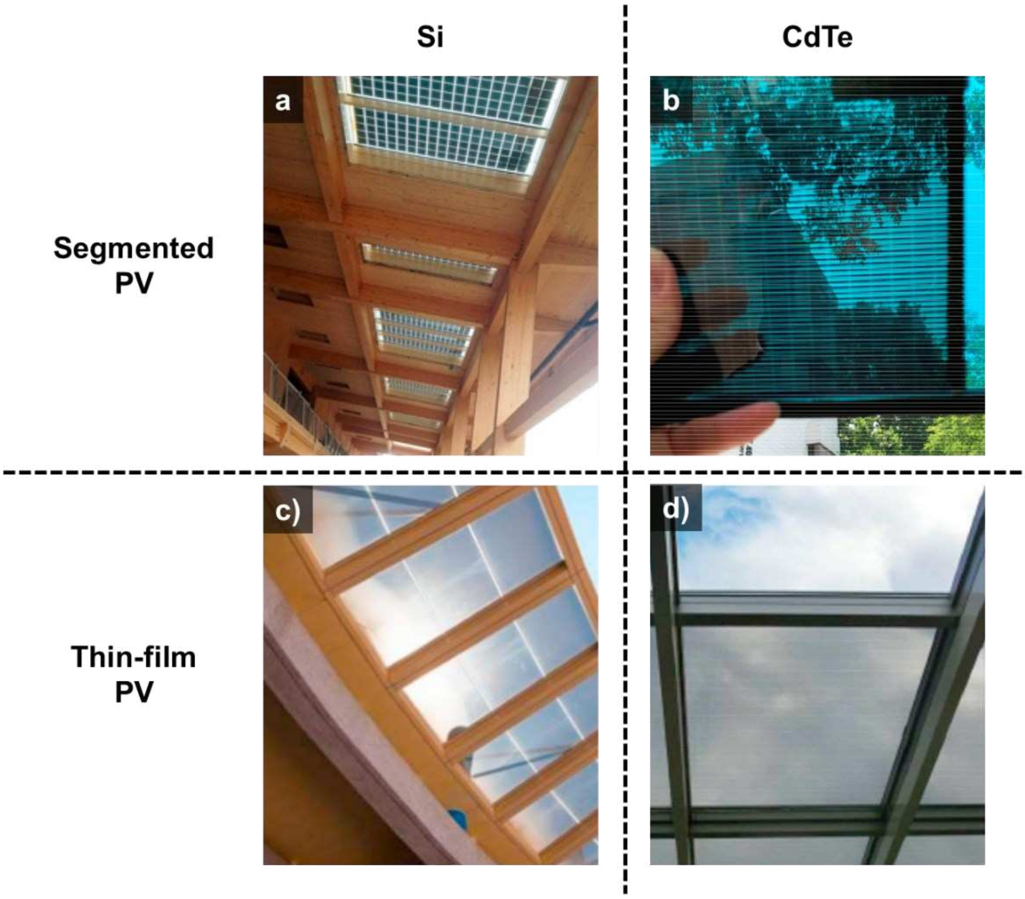

Figure 1.7. Examples of segmented and thin-film BIPV windows employing different semiconductors. Credits: **a)**, **c)**, **d)** Sun *et al.*[57] ; **b)** Shi and Zhu.[56]

The first approach achieves transparency by physically segmenting opaque solar cells into micro-stripes or small, discrete cells. These tiny, opaque PV cells are then spaced out on a transparent glass substrate. The gaps between the segments allow visible light to pass through, creating a semi-transparent effect. If the cells are small enough, they become individually indistinguishable by the human eye at practical viewing distances. This technique is a "non-wavelength-selective" approach, meaning it doesn't rely on absorbing specific wavelengths of the solar spectrum. The level of transparency is directly related to the spacing and size of the opaque segments, as wider gaps transmit more light, but reduce the active area for energy generation. In any case, this method offers a straightforward way to integrate conventional PV materials into transparent applications. Thin-film technologies instead rely on extremely thin layers of semiconductor material deposited onto transparent substrates like glass or polymers. These films are typically only a few nanometres to tens of micrometres thick. By controlling the thickness, material composition and deposition method, manufacturers can achieve varying degrees of transparency. Currently commercialized materials to realize thin film PVs include amorphous silicon (a-Si),[58] cadmium telluride (CdTe)[59] and copper indium gallium selenide (CIGS).[60] Semi-transparent panels of this kind often have a subtle tint due to the materials not being wavelength-selective. Organic photovoltaics and perovskite solar cells could provide wavelength selectivity and tunability, although they are still undergoing development to solve the issues mentioned before (see *Section 1.1*).

Luminescent solar concentrators are another promising technology under research for the implementation of fully transparent BIPV windows. The luminophores can be designed to selectively absorb light outside the visible spectrum (UV or NIR), to produce electricity without compromising on aesthetic requirements for building integration (**Fig. 1.8a**).

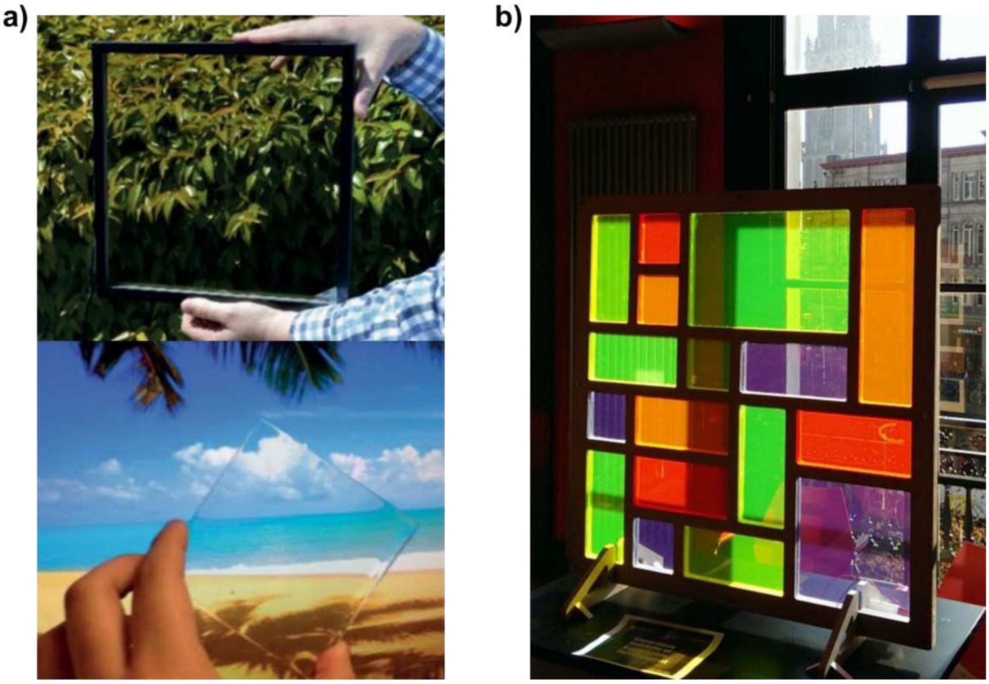

Figure 1.8. Examples of **a)** transparent and colourless LSCs with high aesthetic rendering (Credit: Traverse *et al.*[54]) and **b)** a composition of colourful LSCs with varying transparency. (Credit: van Sark *et al.*[65]).

Due to selective absorption, efficiencies of colourless LSCs are intrinsically lower with respect to other non-wavelength-selective technologies, but they provide the highest flexibility of installation, having transmission and colour rendering properties closest to commercial glass. The calculated practical efficiency limit for visibly transparent LSCs has been stated as 9 – 11%,[61,62] given full absorption of the accessible photons in both the UV and the NIR spectral regions (300 – 1000 nm). However, reported efficiencies for visibly transparent LSCs do not surpass the 2% record established by Bergren *et al.* in 2018.[63,64] Research aims to improve this by designing dual systems coupling both UV and NIR absorbers, and by fundamentally improving the photophysical characteristics of the luminophores to achieve ideal absorption and emission properties.

On the other hand, when employing coloured luminophores, LSCs could provide a further BIPV solution for artistic or customized installations (**Fig. 1.8b**).[65] By absorbing photons in the visible region of the solar spectrum, coloured LSCs produce generally higher electrical outputs. A maximum electrical efficiency of 7.1% for a coloured LSC was reported and certified in 2008 by Slooff *et al.*,[66] although they used a back reflector to enhance performance. More aesthetically compliant tinted LSCs display average efficiencies values around 2 – 3%.[67–69]

1.3 LSCs: state of the art

The core of a luminescent solar concentrator is its luminophore, which enables the operation of the whole device by absorbing solar light and re-emitting it with a certain red shift. Given a highly transparent matrix, tailoring the absorption region of the emitter determines the overall appearance of the final product, as in light transmission properties and coloration. An ideal luminophore should quantitatively absorb incident photons and then re-emit them with unity quantum yield. Overlap between the absorption and emission bands should be null to prevent reabsorption of the emitted photons by other luminophore centres. The optical quality of the embedding medium also plays a crucial role in transporting efficiently the emitted photons to the edge-coupled cells. Finally, tailored matching between the luminophore's emission wavelengths and the PV cell's conversion efficiency maximum is desirable. Based on all these considerations, selecting the right materials to achieve the best possible performance for a given application scenario is fundamental to design highly efficient LSCs.

Optimizing an LSC often means mitigating efficiency losses.[45,46] Self-absorption is one of the major loss mechanisms in LSCs, and is exacerbated either by high luminophore concentrations or by small Stokes shifts. Optimizing luminophore concentration is crucial to balance light absorption with reabsorption probability. A strategy often used for low Stokes shifts is to deposit a highly concentrated luminescent film on an undoped transparent substrate with similar refractive index. In this way, absorption is confined in a small layer at high luminophore concentration, but then emitted photons travel for the most part in the underlying substrate, which is free from other reabsorbing centres. Nonetheless, the best strategy to reduce reabsorption losses is to design luminophores with enhanced Stokes shifts, also in view of LSC scale up.[70–72] Reabsorption is indeed the main efficiency loss pathway occurring in larger devices, as the photons generated farthest from the edges have the lowest probability to reach the PV cells.

The second most important optical loss comes from non-unity TIR. Total internal reflection is the fundamental principle for light guiding in LSCs and relies on consecutive reflections of the emitted photons between the two LSC front faces. TIR occurs if the emitted photons generated inside the waveguide have an incidence angle with the waveguide-air interface greater than a certain value, defined as the "critical angle (θ_c)". This is determined by the refraction index (n) difference between the waveguide and the surrounding air.[73] Conversely, if a photon reaches the waveguide's boundaries with an incidence angle smaller than the critical angle, it escapes the LSC through its front faces rather than being waveguided to the edges (**Fig. 1.9**). The fraction of photons exiting the waveguide is calculated as the ratio between the solid angle defined by $2\theta_c$ and the total solid angle of a sphere, assuming that emission is isotropic. For most transparent materials, n_{guide} = 1.5 and the derived critical angle is 42°, meaning that 12.5% of the emitted photons falls inside the escape cone solid angle of one waveguide-air interface. This value doubles to 25% considering that TIR losses occur from both top and bottom surfaces of the LSC. The remaining 75% of the emitted photons is successfully waveguided to the edges.

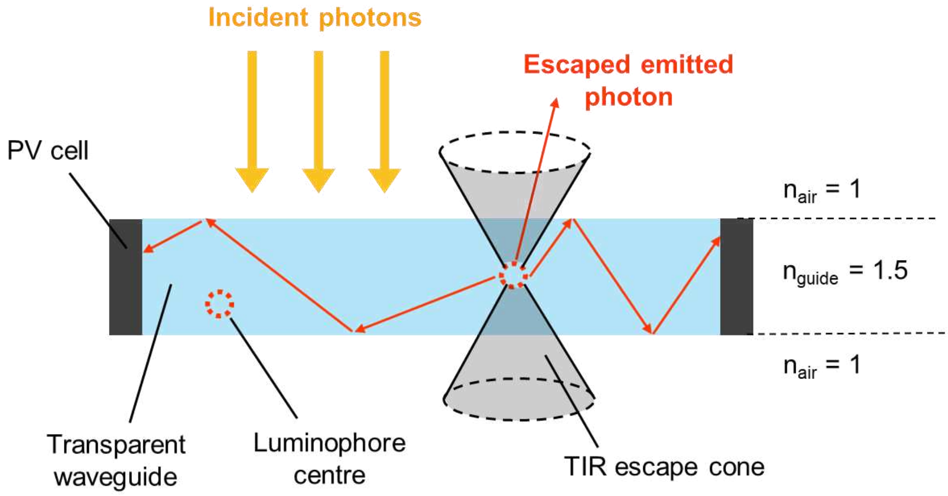

Figure 1.9. Schematics of the photon transport mechanism occurring through total internal reflection inside a transparent, non-scattering LSC and related escape cone losses.

One mitigation strategy for escape cone losses is using waveguide materials with a high refractive index to reduce the critical angle and increase TIR efficiency. However, high refractive index materials generally reflect a higher fraction of the incident light, preventing it to enter the LSC and being absorbed at all by the luminophore. Adding back reflective layers can redirect light that would otherwise exit the LSC through the escape cone, but this would significantly alter the appearance of the device and limit its scope of application. Since transparency is a key characteristic of LSCs, the amount of escaped emitted photons (25% for n_{guide} = 1.5) is commonly accounted for as an inherent optical efficiency loss of the system. Nonetheless, alternative solutions to back reflectors, like nano-structuring of the LSC's collection surface,[74] have recently been proposed as an efficient way to enhance the waveguide's trapping efficiency, while retaining its original aesthetic quality.

Imperfections within the waveguide material, such as impurities or microscopic bubbles, non-uniform dispersion of the luminophore or surface roughness, can cause light to scatter. This scattering redirects photons out of their intended path, leading to premature exit from the waveguide and a reduction in the overall efficiency.[75] High-quality, optically clear waveguide materials with minimal defects are necessary, as well as complete and homogeneous luminophore dispersion. Maintaining smooth surface finishes on the LSC's edges minimizes scattering at the interfaces.

Lastly, non-unity photoluminescence quantum yield ($PLQY$), caused by non-radiative decay pathways, is an intrinsic limitation of the luminophore that directly translates to device reduced efficiency. Developing luminophores both highly absorbing and highly emitting is a fundamental challenge in LSC research, and the key for breaking current efficiency records. This analysis of optical losses underscores how designing an LSC is a multi-parameter problem, where all components and their reciprocal interactions must be considered collectively to achieve the best possible solution within end-destination requirements. The current LSC picture presents a plethora of different materials, luminophores and device designs, highlighting the versatility of this technology. The following discussion offers an overview of the present state of the art. The choice of the waveguide material dictates the overall transparency and light propagation efficiency of the LSC. Polymeric materials, such as poly(methyl methacrylate) (PMMA) and polycarbonate (PC) are widely employed as LSC substrates.[76,77] They offer excellent transparency from 300 nm up to 1500 nm, displaying transmission and optical clarity akin to glass. The wide transmission window makes them suitable for embedding also UV selective absorbers, thanks to the low parasitic light absorption of the matrix (**Fig. 1.10**).

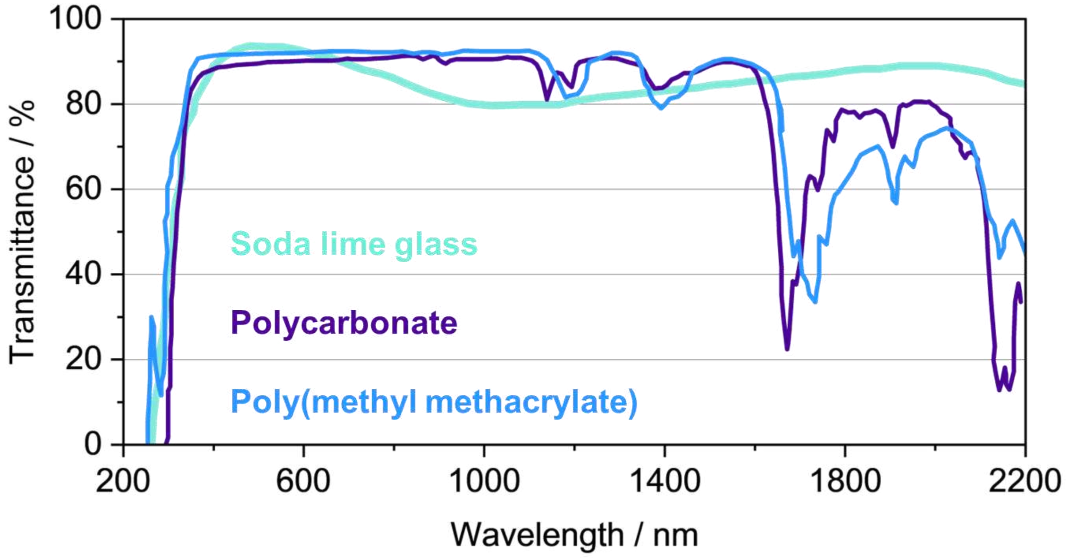

Figure 1.10. Transmittance spectra of polycarbonate, poly(methyl methacrylate) and soda-lime glass, evidencing their excellent transparency to UV and visible photons.

These polymers are also lightweight and possess high scratch and shattering resistance.[77] PMMA is a common waveguide material due to its low cost and ease of fabrication, allowing for various processing techniques like casting and extrusion. Having become a commodity polymer, PMMA is already amply commercialized

(Lucite®, Plexiglass®, Perspex®) and has an established industrial supply chain. As LSC waveguide materials, polymers could present some downsides related to their long-term stability, like yellowing caused by prolonged UV exposure, with a consequent reduction in transparency.[78] Specific plastic additives and stabilizers can be added to curb this problem. On the other hand, glass-based substrates, including float glass, offer superior thermal stability and UV resistance for LSC applications, retaining excellent optical transparency throughout their shelf life. Even so, glass is not typically used for bulk embedment of luminophores due to the intrinsic synthetic difficulties and harsh processing conditions required. Despite some notable examples of bulk-doped glass LSCs,[79,80] it is preferable to use it as a transparent substrate for luminescent coatings. Polymeric films deposited on glass provide an LSC configuration easily affordable by many research laboratories. In the end, glass is also more expensive, heavier and more brittle than its polymeric alternatives, which can complicate deployment in large-area BIPV installations. Research efforts are exploring alternative and hybrid substrate materials to overcome the limitations of conventional polymers and glass. This includes investigations into silicone-based waveguides,[81–83] which offer a balance of flexibility and improved environmental stability, as well as hybrid structures that aim to combine the cost and fabrication benefits of polymers with the durability and superior optical quality offered by glass.[84,85]

Moving to the choice of luminophore, three main classes of compounds can be distinguished:

- *Organic dyes*, such as perylenes, rhodamines, cyanines and coumarins;
- *Quantum dots*, either of semiconducting material or perovskites;
- *Rare earth ions*, often coordinated by organic ligands to form antenna complexes.

Organic dyes have historically been the first class of luminophores to be studied for LSC development[39,86] and served as a model system for theorizing LSC principles of operation.[87,88] They offer broadband absorption with high molar extinction coefficients and their emission spectra can be tuned through molecular functionalization. They exhibit generally high $PLQY$s and display large solubility in many organic solvents, allowing for easy manipulation and increased luminophore loading. Additionally, a lot of organic dyes are already commercially available at a relatively low cost. They typically absorb in the visible region, consequently providing coloured LSCs (**Fig. 1.11**).

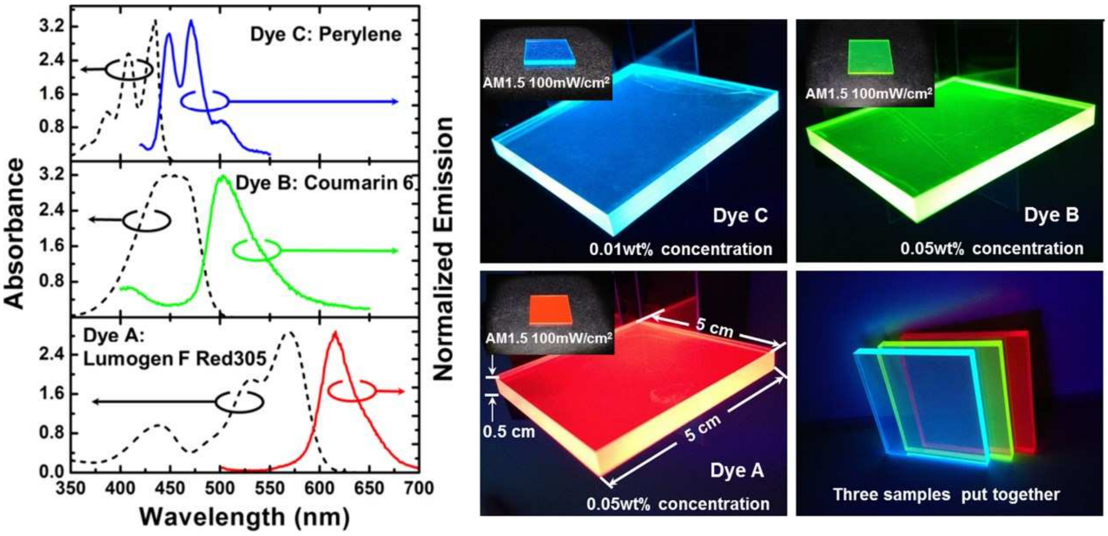

Figure 1.11. Absorption and emission spectra of three strongly coloured organic dyes, with photographs of the corresponding PMMA-based LSCs. Credit: Liu and Li.[89]

However, organic dyes suffer from significant drawbacks, the first being the poor photostability, especially when exposed to UV radiation.[90] An UV-blocking coating would then be necessary to reduce photoinduced degradation of the luminophore. Organic dyes often exhibit low Stokes shifts with large absorption-emission overlap, increasing the likelihood of reabsorption losses. Despite reaching high loadings, at high concentrations they can experience aggregation caused quenching (ACQ) due to intermolecular interactions.[82,91] To limit reabsorption, when implementing organic dyes in LSCs it is preferable opting for a supported film configuration, or tailoring the dyes by molecular functionalization for augmented Stokes shift.[92–94] Additionally, multi-dye systems can be employed to match the emission of one species to the absorption of another and build Forster energy resonance transfer (FRET) networks.[67,95,96] LSC plates containing up to three FRET interconnected dyes have been reported, declaring up to a 2.7-fold electrical output enhancement with respect to the corresponding single-dye plates.[95] Maximising the $PLQY$ and minimizing the Stokes shift of the last dye in the chain is essential to achieve optimal performance.

Quantum dots (QDs) represent a significant advancement in luminophore technology. LSCs realized with such luminophores have been extensively reviewed[97–99] and count some of the most efficient large-area devices realized to date.[64,69] QDs are colloidal semiconductor nanocrystals which exhibit size-tuneable absorption and emission, with increasing bandgap as the dimensions of the nanocrystals decrease. The bandgap can be modified also by altering the QDs' chemical composition with sensitizers and dopants. This allows for precise spectral matching to the PV cell's response and for increased Stokes shift. They have broad absorption spectra and high $PLQY$s, while displaying greatly reduced reabsorption with respect to organic dyes, thanks to narrower emission bands (**Fig. 1.12**).

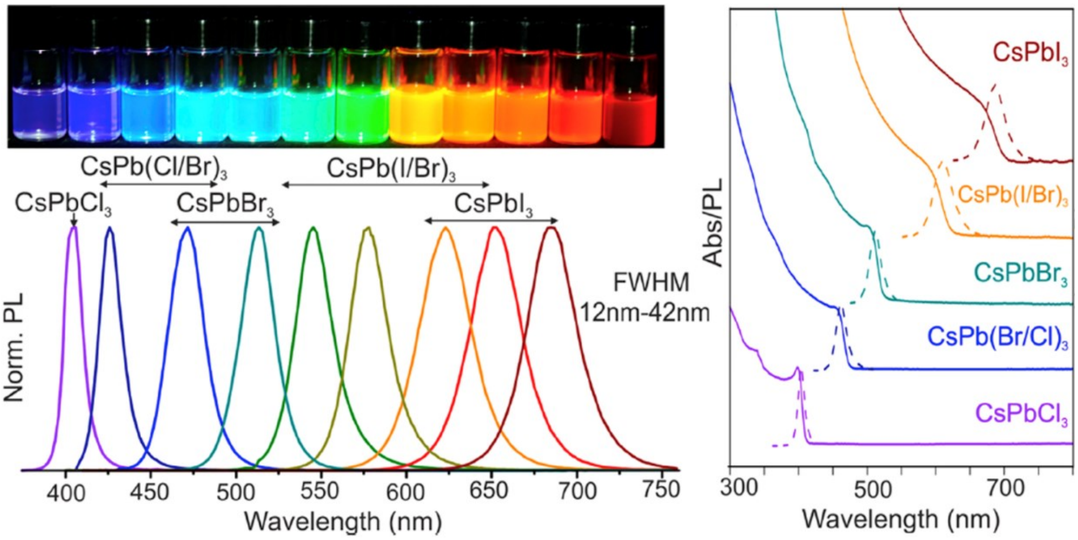

Figure 1.12. Typical emission colours of quantum dot Cs-Pb halides with increasing size (left to right) and representative Abs/PL spectra. FWHM = Full Width at Half Maximum. Credit: Zaho and Rosei.[99]

Due to the colloidal nature of QDs, they need to be stabilized by passivating the surface dangling bonds with organic ligands, which binding function is usually heteroatom-based (S: thiols, siloxanes and acids; P: phosphines, phosphine oxides and phosphates, N: amides and amines, O: long-chain fatty acids and aromatic carboxylic acids).[100] Surface ligands offer further fine-tuning of the emission properties of the QD, and determine solubility in the target medium. Another strategy to passivate the surface of the colloidal particles is to employ a core-shell architecture, in which the QD core is capped with a robust inorganic shell that prevents surface chemistry. Depending on whether the bandgap of the core is smaller or larger than the one of the shell, different types of core-shell architectures can be obtained, differing for the localization of the charge carriers inside the QD.[99] Core-shell architectures have also been known to enhance $PLQY$ and improve thermal and photophysical stability.[101]

Despite the excellent photophysical properties of QDs and the breakthrough LSC efficiencies reported, they are generally less compatible with polymeric matrices like PMMA, with low solubility and potential long-term leakage issues. This is particularly concerning for certain QD compositions containing lead or cadmium, due to environmental and health safety reasons. Ternary alloys of I-III-VI semiconductors ($CuInS_2$, $CuInSe_2$)[46,64,71] and indirect bandgap semiconductors (Si, Ge)[68,98] have been proposed as more ecologic alternatives. QDs are also more susceptible to moisture and atmospheric oxygen, so they need controlled handling and processing, which could increase manufacturing costs.

Finally, rare earth ions, such as Eu^{3+}, Tb^{3+} and Yb^{3+}, have garnered attention for LSC development thanks to their peculiar photophysical behaviour.[102,103] They are characterized by discrete energy levels leading to sharp, spectrally selective emission bands resembling atomic emission lines (**Fig. 1.13**).

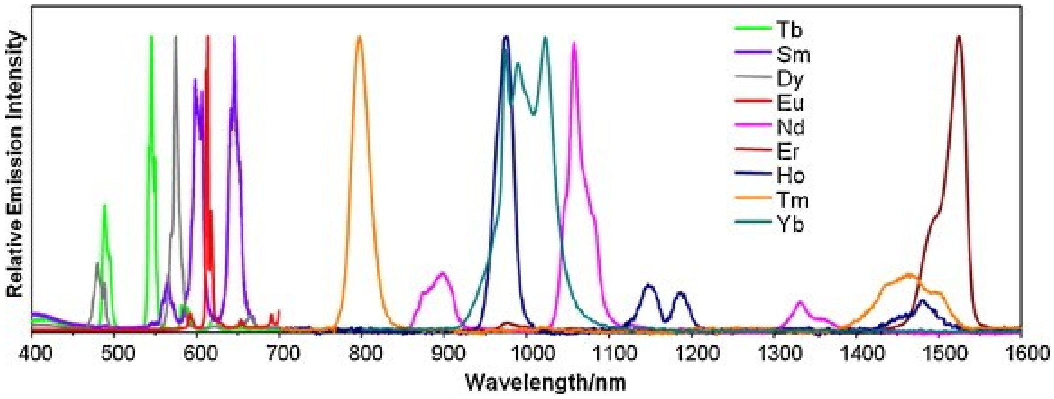

Figure 1.13. Normalized emission spectra of lanthanide ions' complexes. Credit: Uh and Petoud.[104]

Such emission spectra arise from intra-configurational $f \rightarrow f$ electronic transitions, which are parity-forbidden due to Laporte rule. This translates to enhanced emission intensities and prolonged luminescence lifetimes, but at the same time greatly limits light absorption probability. Absorption cross sections for bare lanthanide ions rarely exceed 10^{-1} M^{-1} cm^{-1} as order of magnitude, meaning that they are significantly less efficient than organic dyes and QDs in harvesting solar light. The solution to this problem has been found in designing antenna complexes, namely by coordinating the ions with organic ligands that act as sensitizers.[104–106] The organic antenna harvests solar radiation and stimulates emission from the coordinated ion through intramolecular energy processes. Absorption and emission occur in very distinct spectral regions, giving rise to pseudo-Stokes shifts of over 200 nm and eliminating the probability of reabsorption losses. Absorption usually takes place in the UV region, while emission falls in the visible or NIR depending on the specific rare earth ion. The photophysical events take place as follows (**Fig. 1.14**). The organic ligand absorbs incident radiation and transitions from the ground singlet state (S_0) to the first excited singlet state (S_1). The ligand undergoes inter-system crossing (ISC) from S_1 to the corresponding excited triplet state (T_1), which energy is tailored to the emissive excited state of the lanthanide ion. Thanks to this matching between energy levels, an energy transfer occurs from T_1 to the coordinated ion, populating the target excited state which ultimately decays radiatively, giving intense photoluminescence.

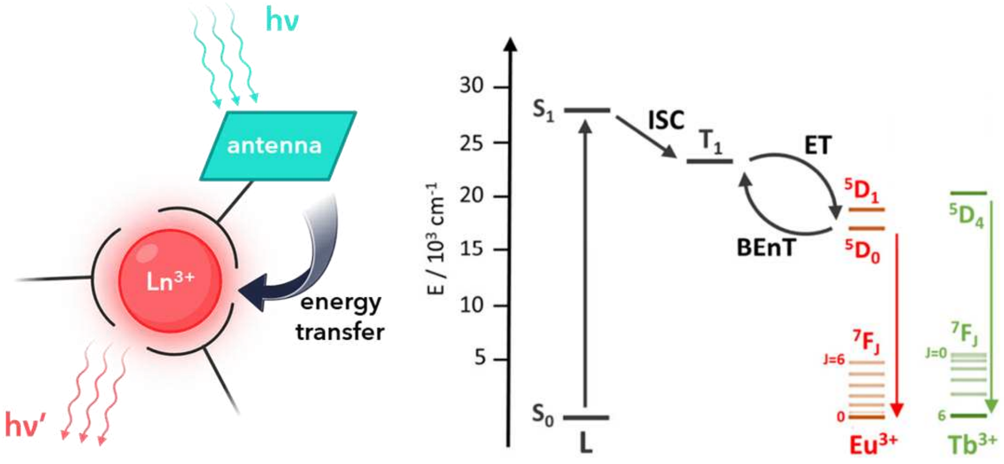

Figure 1.14. Schematics of the sensitization mechanism in lanthanide antenna complexes, with energy levels diagram for red emitter Eu^{3+} and green emitter Tb^{3+}.

The total sensitization efficiency of the process can be tuned via chromophore design.[107–109] In the ideal antenna complex, non-radiative decay pathways and back energy transfer (BEnT) probabilities should be completely suppressed. BEnT occurs when the triplet energy level of the ligand and the target energy level of the lanthanide ion are too close. To prevent this, T_1 should be higher in energy than the lanthanide's emissive level by at least 1850 cm^{-1}.[110] Deactivation can occur also by vibrational relaxation towards high energy oscillators like O-H and N-H stretching modes, especially when they are directly coordinating the lanthanide ion.[105] A method to reduce vibrational quenching is to design a rigid molecular scaffold around the ion that saturates its coordination sites and efficiently shields it from solvent interactions. Frequently employed ligands for lanthanide sensitization are polyaminocarboxylates, β-diketonates, acyclic Schiff base derivatives and aromatic chromophores such as phenanthroline and bipyridine.[111] Lanthanide antenna complexes display greatly enhanced absorption with respect to the bare ions and bright emission intensities. Since absorption occurs in the UV region, the resulting LSCs usually display high transparency and low to no tinting (**Fig. 1.15**).[85,112,113]

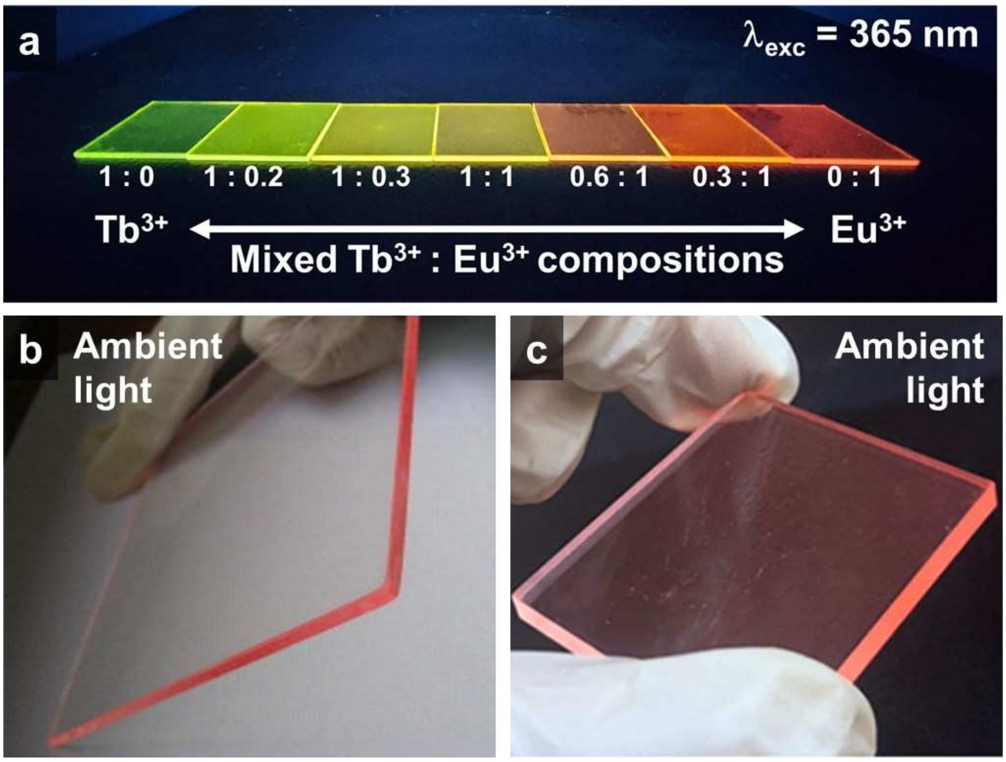

Figure 1.15. a) Photographs of LSCs doped with pure Tb^{3+} (left, green edge emission), pure Eu^{3+} (right, red edge emission) and mixed Eu^{3+}/Tb^{3+} antenna complexes under UV illumination. **b)**, **c)** Photographs of LSCs doped with pure Eu^{3+} antenna complexes in ambient lighting conditions. Credits: **b)** Wang, X. *et al.*[112]; **c)** Wang, Y. *et al.*[85]

Due to the unique electronic structure of lanthanide ions, coordination with the antenna does not alter the $f \rightarrow f$ transitions responsible for emission, which fall at the same wavelengths both for the free ion and the complex. Lower $PLQY$s with respect to organic dyes and QDs and reduced solubility are the two most significant drawbacks. By introducing an organic component, antenna complexes become more susceptible to photodegradation with respect to classic inorganic phosphors like Eu^{3+}:Y_2O_3. Nonetheless, the greatly enhanced brightness (the product of the absorption coefficient and the $PLQY$) of lanthanide organic antenna complexes makes them viable for the LSC application.

Although less frequently employed, also complexes of *d* metals with organic ligands have been proposed as LSC luminophores, as standalone[114] or in tandem configurations with QDs.[115]

Table 1.1 provides a closing summary of the available LSC luminophore technologies, highlighting their advantages and limitations.

Table 1.1. Defining characteristics of the three examined classes of LSC luminophores: organic dyes, quantum dots and rare earth ions.

	Organic dyes	**Quantum dots**	**Rare earth ions**
UV/NIR selective absorption	No	Bandgap can be tuned	Yes
Average absorption cross sections / M^{-1} cm^{-1}	10^4	$10^5 - 10^6$	10^{-1} for bare ions, increased to $10^4 - 10^5$ in antenna complexes
Average $PLQY$	0.5 – 1	0.5, increased by designing heterostructures	Ion-dependent, 0.3 – 0.8 for Eu^{3+} and Tb^{3+} complexes
Emission FWHM / nm	50 – 100	10 – 50	2 – 10
Reabsorption probability	High	Moderate, can be lowered by designing heterostructures	Null
Photostability	Low	High	High for ions in inorganic matrices, decreases for complexes
Compatibility with PMMA	High	Low, surface functionalization is needed	Low for bare ions, increased solubility by complexing with organic ligands

1.4 Other applications of LSCs

Beyond their primary application in BIPVs, LSCs are devices that exhibit a remarkable versatility, lending themselves to a diverse array of scientific fields.

One significant area of application lies in microreactors and photocatalysis.[116,117] LSCs can be integrated into microfluidic devices to deliver concentrated and spectrally tailored light directly to the photocatalytic reaction sites. This precise light delivery enhances reaction rates, improves selectivity and reduces energy consumption in various chemical processes, including water purification, hydrogen production and organic synthesis. The emission band of the LSC can be tuned to match the absorption spectrum of the photocatalyst, maximizing the utilization of incident solar energy and overcoming limitations associated with diffuse light or inefficient light penetration in traditional batch reactors. For instance, LSC-integrated microreactors have been used to develop a solar-powered mini plant for the production of chemicals, retaining high performance also with cloudy weather (**Fig. 1.16**).[118] Research has shown significant improvements in reaction yields and kinetics when LSCs are employed, paving the way for more compact and efficient photoreactors.

Figure 1.16. Example of an LSC-based microreactor for outdoor, sun-powered operation. The reactor keeps working even with cloudy weather. Credit: Masson *et al.*[118]

Agrivoltaics offer further opportunities for LSC integration, where greenhouse roofs and walls can be designed to selectively transmit photosynthetically active radiation to crops, while exploiting non-utilized parts of the solar spectrum like UV and NIR for electricity generation.[116,119] Additionally, fibre-shaped LSCs could be deployed in algae cultivations or in vertically developing crops for a more efficient light penetration underwater or inside thick foliage, respectively.[120]

In the field of optical communications, LSCs are being explored for their potential to act as light collectors with ample field of view for free-space optical communication systems or in environments with limited direct line of sight.[121,122] They can efficiently gather modulated light signals, even if weak or diffuse, and produce a modulated electrical response in return. This capability is particularly appealing for enabling energy-efficient, wireless data transmission[123,124] or even for smart BIPV windows, where a modulated visible light signal can trigger specific functions such as electrochromic colouring. While still an emerging field, LSCs could potentially enhance the signal-to-noise ratio in low-light communication scenarios by concentrating weak optical signals.

Photodetectors represent another alternative use of LSCs, which could offer again enhanced signal-to-noise ratio for weak optical signals. Thanks to the large collection area, low intensity input optical signals could be efficiently converted to concentrated light output signals and redirected onto small, edge-coupled conventional photodetectors. This could provide a useful and low cost solution to increase the detector sensitivity in critical spectral regions, such as UV.[125]

1.5 Thesis outline

The field of solar energy is fast adapting to the needs of modern society, one example being the emergence of distributed PV applications such as Building-Integrated Photovoltaics. In this prospect, Luminescent Solar Concentrators are a promising technology aimed to integrate the production of solar energy in highly transparent architectural elements. The thesis work reports the design, preparation and characterization of LSCs based on different materials and device configurations. The multifunctionality of the proposed systems is also investigated.

In *Chapter 2*, the employed LSC preparation methods are reported, focusing on their optimization on laboratory scale and equipment. The fabrication of PMMA bulk-doped

LSCs by bulk polymerization of methyl methacrylate (MMA) is described. PMMA is cast into planar tiles of approximately 3 mm thickness and variable collecting area from 25 × 25 mm^2 to 50 × 50 mm^2. The challenges in obtaining products of high optical quality and the measures taken to overcome them are extensively discussed. Supported film LSCs with active areas of 25 × 25 mm^2 or 50 × 50 mm^2 have also been realized with slot die coating. The optimization of luminescent PMMA films depositions onto glass substrates using a compact slot die coater, as in finding the optimal feedstock chemical composition, tailoring the coating parameters and pre-treating the substrates is described. The quality of the products has been monitored by measuring the thickness of the film and its spatial homogeneity.

Chapter 3 offers an analysis of the terminology and the good-practice guidelines used in LSC measuring and reporting. Following literature consensus statements from field experts, the development of compliant experimental setups for LSC characterization is described. Adjustment to reporting guidelines includes: i) accounting for luminescence photons in transmittance spectra measurement, ii) designing a versatile benchtop station for electrical data acquisition (Current density – Voltage curves, External Quantum Efficiency) and iii) correct elaboration of experimental data for the calculation of relevant figures of merit.

A first LSC case study is presented in *Chapter 4*. Highly transparent and colourless PMMA bulk-doped LSCs have been developed, based on a family of Eu^{3+} Lanthanide Organic Cages (LOCs) as luminophores. The employed antenna complexes are super-bright binuclear Eu^{3+} cages, where the two lanthanide ions are coordinated by four bis-β-diketonate ligands. The ligands efficiently sensitize the two Eu^{3+} ions through two benzoyltrifluoroacetone (btfa) moieties, connected by a central spacer with different molecular structure depending on the ligand. The photophysical properties of the luminophores have been characterized in MMA, before bulk polymerization, and later in the obtained PMMA LSCs. Aesthetic quality of the materials has been evaluated based on Average Visible Transmission (AVT), Colour Rendering Index (CRI) and $CIELAB$ ($a*$, $b*$) colour coordinates. Electrical characterizations have been performed with the testbench described in the previous chapter, edge-coupling the waveguides to small silicon PV cells. A comparison of the obtained devices' performance with the literature on highly transparent LSCs is offered.

In *Chapter 5*, the multifunctionality of the Eu^{3+}-based LSCs is explored, studying their behaviour as visible-blind UV photodetectors. The aim of the study is to evaluate the

UV light detection properties offered by a basic device architecture like that of LSCs, opposed to conventional heterojunction-based detector technologies. The relevant figures of merit for photodetectors are described and translated to the LSC system. Measurements have been conducted on the same testbench developed for proper LSC characterizations, by using discrete UV LEDs as light source. Both power and time response were recorded, providing with preliminary data for LSC-based UV photodetector development.

A second LSC case study is presented in *Chapter 6*. Here, a set of oligothiophenes was investigated as fluorophores for developing visible absorbing, coloured LSCs with reduced reabsorption thanks to enhanced Stokes shift. The project has been conducted in collaboration with researchers form CNR-ISOF (Bologna, Italy), who provided the as-synthetized oligothiophenes. The most suitable LSC fluorophores have been selected by performing a pre-screening of their photophysical properties in solution. Then, the selected molecules have been embedded in PMMA films deposited onto glass slides using slot die coating. The standard optical and electrical reporting of LSC materials and devices has been conducted, and performances have been compared with other literature systems based on similar fluorophores.

Chapter 7 focuses on a project on coloured PV modules for BIPV applications, carried out in collaboration with researchers from Eurac Research (Bolzano, Italy) and CNR-ICCOM (Firenze, Italy). A predictive model for the electrical output of coloured PV stacks has been proposed and experimentally validated for a range of different colouring technologies, including coloured glass, white diffusing glass and film LSCs based on organic dyes. The testbench developed for LSC electrical characterizations has been adjusted to collect the coloured PV prototype's current response using monochromatic illumination. A colorimetric analysis on the prototypes has also been performed to evaluate the colour altering properties of the specific technology considered and link them to the observed electrical output of the PV module.

Finally, *Chapter 8* shows a summary of the obtained results and future perspectives for the LSC systems described in this thesis, while *Chapter 9* reports all the experimental details of the scientific activity.

1.6 Bibliography

1 Renewable capacity statistics 2025, https://www.irena.org/Publications/2025/Mar/Renewable-capacity-statistics-2025, (accessed 16 July 2025).

2 A. Elkhatat and S. A. Al-Muhtaseb, *Energies*, 2023, **16**, 4471.

3 GSR 2025 | RENEWABLES 2025 GLOBAL STATUS REPORT, https://www.ren21.net/gsr-2025//gsr-2025/, (accessed 24 July 2025).

4 Best Research-Cell Efficiency Chart | Photovoltaic Research | NREL, https://www.nrel.gov/pv/cell-efficiency, (accessed 16 July 2025).

5 N. Shah, A. A. Shah, P. K. Leung, S. Khan, K. Sun, X. Zhu and Q. Liao, *Processes*, 2023, **11**, 1852.

6 M. A. Green, *Phys. E Low-Dimens. Syst. Nanostructures*, 2002, **14**, 65–70.

7 G. Conibeer, *Mater. Today*, 2007, **10**, 42–50.

8 V. Fthenakis, *Third Generation Photovoltaics*, 2012.

9 B. Jiao, L. Tan, Y. Ye, N. Ren, M. Li, H. Li, X. Li and C. Yi, *Energy Environ. Sci.*, 2025, **18**, 5437–5447.

10 M. Afroz, R. K. Ratnesh, S. Srivastava and J. Singh, *Sol. Energy*, 2025, **287**, 113205.

11 R. Lin, K. Xiao, Z. Qin, Q. Han, C. Zhang, M. Wei, M. I. Saidaminov, Y. Gao, J. Xu, M. Xiao, A. Li, J. Zhu, E. H. Sargent and H. Tan, *Nat. Energy*, 2019, **4**, 864–873.

12 A. S. R. Bati, Y. L. Zhong, P. L. Burn, M. K. Nazeeruddin, P. E. Shaw and M. Batmunkh, *Commun. Mater.*, 2023, **4**, 2.

13 Z. Hu, Z. Lin, J. Su, J. Zhang, J. Chang and Y. Hao, *Sol. RRL*, 2019, **3**, 1900304.

14 M. H. Miah, M. U. Khandaker, M. B. Rahman, M. Nur-E-Alam and M. A. Islam, *RSC Adv.*, 2024, **14**, 15876–15906.

15 W. Fu, C. Pan, A. Zhou, P. Shi, Z. Yi and Q. Zeng, *Materials*, 2024, **17**, 6284.

16 D. Zhang, D. Li, Y. Hu, A. Mei and H. Han, *Commun. Mater.*, 2022, **3**, 58.

17 C. C. Boyd, R. Cheacharoen, T. Leijtens and M. D. McGehee, *Chem. Rev.*, 2019, **119**, 3418–3451.

18 M. Shao, T. Bie, L. Yang, Y. Gao, X. Jin, F. He, N. Zheng, Y. Yu and X. Zhang, *Adv. Mater.*, 2022, **34**, 2107211.

19 S. Zhang, F. Ye, X. Wang, R. Chen, H. Zhang, L. Zhan, X. Jiang, Y. Li, X. Ji, S. Liu, M. Yu, F. Yu, Y. Zhang, R. Wu, Z. Liu, Z. Ning, D. Neher, L. Han, Y. Lin, H. Tian, W. Chen, M. Stolterfoht, L. Zhang, W.-H. Zhu and Y. Wu, *Science*, 2023, **380**, 404–409.

20 Y. Y. Kim, T.-Y. Yang, R. Suhonen, A. Kemppainen, K. Hwang, N. J. Jeon and J. Seo, *Nat. Commun.*, 2020, **11**, 5146.

21 B. O’Regan and M. Grätzel, *Nature*, 1991, **353**, 737–740.

22 M. Godfroy, J. Liotier, V. M. Mwalukuku, D. Joly, Q. Huaulmé, L. Cabau, C. Aumaitre, Y. Kervella, S. Narbey, F. Oswald, E. Palomares, C. A. G. Flores, G. Oskam and R. Demadrille, *Sustain. Energy Fuels*, 2021, **5**, 144–153.

23 J. Barichello, P. Mariani, L. Vesce, D. Spadaro, I. Citro, F. Matteocci, A. Bartolotta, A. D. Carlo and G. Calogero, *J. Mater. Chem. C*, 2024, **12**, 2317–2349.

24 S. Shalini, R. Balasundaraprabhu, T. S. Kumar, N. Prabavathy, S. Senthilarasu and S. Prasanna, *Int. J. Energy Res.*, 2016, **40**, 1303–1320.

25 S. Kaliramna, S. S. Dhayal, R. Chaudhary, S. Khaturia, K. L. Ameta and N. Kumar, *Braz. J. Phys.*, 2022, **52**, 136.

26 F. Gao, Y. Wang, J. Zhang, D. Shi, M. Wang, R. Humphry-Baker, P. Wang, S. M. Zakeeruddin and M. Grätzel, *Chem. Commun.*, 2008, 2635–2637.

27 A. Ebenezer Anitha and M. Dotter, *Energies*, 2023, **16**, 5129.

28 J. B. Baxter, *J. Vac. Sci. Technol. A*, 2012, **30**, 020801.

29 C. M. Nkinyam, C. O. Ujah, K. C. Nnakwo and D. V. V. Kallon, *Unconv. Resour.*, 2025, **5**, 100121.

30 M. E. Ramoroka, S. T. Yussuf, K. C. Nwambaekwe, K. D. Modibane, V. S. John-Denk, S. F. Douman and E. I. Iwuoha, *Sol. RRL*, 2024, **8**, 2300982.

31 E. K. Solak and E. Irmak, *RSC Adv.*, 2023, **13**, 12244–12269.

32 M. Saravanapavanantham, J. Mwaura and V. Bulović, *Small Methods*, 2023, **7**, 2200940.

33 J. Zhu, J. Xia, Y. Li and Y. Li, *ACS Appl. Mater. Interfaces*, 2025, **17**, 5595–5608.

34 J. Wan, R. Zhang, Y. Li and Y. Li, *Wearable Electron.*, 2024, **1**, 26–40.

35 R. Meng, Q. Jiang and D. Liu, *Npj Flex. Electron.*, 2022, **6**, 39.

36 X. Xiao, M. Chalh, Z. R. Loh, E. Mbina, T. Xu, R. C. Hiorns, Y. Li, M. Das, K. N'konou and L. W. T. Ng, *Cell Rep. Phys. Sci.*, 2025, **6**, 102390.

37 F. Furlan and N. Gasparini, *Nat. Mater.*, 2025, **24**, 336–337.

38 M. Ghorab, A. Fattah and M. Joodaki, *Optik*, 2022, **267**, 169730.

39 A. Goetzberger and W. Greube, *Appl. Phys.*, 1977, **14**, 123–139.

40 J. Huang, J. Zhou, E. Jungstedt, A. Samanta, J. Linnros, L. A. Berglund and I. Sychugov, *ACS Photonics*, 2022, **9**, 2499–2509.

41 M. Barragán Sánchez-Lanuza, I. Lillo-Bravo, A. Menéndez-Velázquez and J.-M. Delgado-Sanchez, *Sol. Energy Mater. Sol. Cells*, 2024, **276**, 113073.

42 T. K. Baikie, B. Daiber, E. Kensington, J. Xiao, N. C. Greenham, B. Ehrler and A. Rao, *Joule*, 2024, **8**, 799–816.

43 B. S. Richards and I. A. Howard, *Energy Environ. Sci.*, 2023, **16**, 3214–3239.

44 S. Castelletto and A. Boretti, *Nano Energy*, 2023, **109**, 108269.

45 C. Tummeltshammer, A. Taylor, A. J. Kenyon and I. Papakonstantinou, *Sol. Energy Mater. Sol. Cells*, 2016, **144**, 40–47.

46 R. Sumner, S. Eiselt, T. B. Kilburn, C. Erickson, B. Carlson, D. R. Gamelin, S. McDowall and D. L. Patrick, *J. Phys. Chem. C*, 2017, **121**, 3252–3260.

47 Greenhouse Gas Emissions from Energy - Data product, https://www.iea.org/data-and-statistics/data-product/greenhouse-gas-emissions-from-energy, (accessed 17 July 2025).

48 *Directive (EU) 2024/1275 of the European Parliament and of the Council of 24 April 2024 on the energy performance of buildings (recast) (Text with EEA relevance)*, 2024.

49 Net Zero by 2050 – Analysis, https://www.iea.org/reports/net-zero-by-2050, (accessed 21 July 2025).

50 T. Chen, Y. An and C. K. Heng, *Sustainability*, 2022, **14**, 10160.

51 *Directive (EU) 2018/2001 of the European Parliament and of the Council of 11 December 2018 on the promotion of the use of energy from renewable sources (recast) (Text with EEA relevance.)*, 2018, vol. 328.

52 K. Lee, H.-D. Um, D. Choi, J. Park, N. Kim, H. Kim and K. Seo, *Cell Rep. Phys. Sci.*, 2020, **1**, 100143.

53 R. R. Lunt, *Appl. Phys. Lett.*, 2012, **101**, 043902.

54 C. J. Traverse, R. Pandey, M. C. Barr and R. R. Lunt, *Nat. Energy*, 2017, **2**, 849–860.

55 Building Integrated Photovoltaics Market Size, Report, 2034, https://www.cervicornconsulting.com/building-integrated-photovoltaics-market, (accessed 21 July 2025).

56 S. Shi and N. Zhu, *Sustainability*, 2023, **15**, 15876.

57 Y. Sun, K. Shanks, H. Baig, W. Zhang, X. Hao, Y. Li, B. He, R. Wilson, H. Liu, S. Sundaram, J. Zhang, L. Xie, T. Mallick and Y. Wu, *Appl. Energy*, 2018, **231**, 972–984.

58 H. Maurus, M. Schmid, B. Blersch, P. Lechner and H. Schade, *Refocus*, 2004, **5**, 22–27.

59 M. J. Sorgato, K. Schneider and R. Rüther, *Renew. Energy*, 2018, **118**, 84–98.

60 T. Feurer, P. Reinhard, E. Avancini, B. Bissig, J. Löckinger, P. Fuchs, R. Carron, T. P. Weiss, J. Perrenoud, S. Stutterheim, S. Buecheler and A. N. Tiwari, *Prog. Photovolt. Res. Appl.*, 2017, **25**, 645–667.

61 C. Yang and R. R. Lunt, *Adv. Opt. Mater.*, 2017, **5**, 1600851.

62 T. A. de Bruin and W. G. J. H. M. van Sark, *Front. Phys.*, 2022, **10**, 856799.

63 T. A. de Bruin and W. G. J. H. M. van Sark, *Adv. Photonics Res.*, 2025, **6**, 2400068.

64 M. R. Bergren, N. S. Makarov, K. Ramasamy, A. Jackson, R. Guglielmetti and H. McDaniel, *ACS Energy Lett.*, 2018, **3**, 520–525.

65 W. van Sark, P. Moraitis, C. Aalberts, M. Drent, T. Grasso, Y. L'Ortije, M. Visschers, M. Westra, R. Plas and W. Planje, *Sol. RRL*, 2017, **1**, 1600015.

66 L. H. Slooff, E. E. Bende, A. R. Burgers, T. Budel, M. Pravettoni, R. P. Kenny, E. D. Dunlop and A. Büchtemann, *Phys. Status Solidi RRL – Rapid Res. Lett.*, 2008, **2**, 257–259.

67 B. Zhang, P. Zhao, L. J. Wilson, J. Subbiah, H. Yang, P. Mulvaney, D. J. Jones, K. P. Ghiggino and W. W. H. Wong, *ACS Energy Lett.*, 2019, **4**, 1839–1844.

68 F. Meinardi, S. Ehrenberg, L. Dhamo, F. Carulli, M. Mauri, F. Bruni, R. Simonutti, U. Kortshagen and S. Brovelli, *Nat. Photonics*, 2017, **11**, 177–185.

69 L. Wang, X. Wang and H. Zhao, *Adv. Funct. Mater.*, 2025, **35**, 2423422.

70 H. Li, K. Wu, J. Lim, H.-J. Song and V. I. Klimov, *Nat. Energy*, 2016, **1**, 16157.

71 F. Meinardi, H. McDaniel, F. Carulli, A. Colombo, K. A. Velizhanin, N. S. Makarov, R. Simonutti, V. I. Klimov and S. Brovelli, *Nat. Nanotechnol.*, 2015, **10**, 878–885.

72 F. Meinardi, A. Colombo, K. A. Velizhanin, R. Simonutti, M. Lorenzon, L. Beverina, R. Viswanatha, V. I. Klimov and S. Brovelli, *Nat. Photonics*, 2014, **8**, 392–399.

73 K. C. Kao, in *Dielectric Phenomena in Solids*, ed. K. C. Kao, Academic Press, San Diego, 2004, pp. 115–212.

74 J. G. Guerrero-Felix, S. F. H. Correia, M. Alexandre, C. D. Gonzalez-Gomez, V. Sencadas, L. Fu, E. Ruiz-Reina, P. S. André, C. L. Moraila-Martinez, M. J. Mendes, R. A. S. Ferreira and M. A. Fernandez-Rodriguez, *Mater. Des.*, 2025, **252**, 113817.

75 R. D. Breukers, G. J. Smith, H. L. Stirrat, A. J. Swanson, T. A. Smith, K. P. Ghiggino, S. G. Raymond, N. M. Winch, D. J. Clarke and A. J. Kay, *Appl. Opt.*, 2017, **56**, 2630–2635.

76 G. Griffini, *Front. Mater.*, 2019, **6**, 29.

77 Y. Li, X. Zhang, Y. Zhang, R. Dong and C. K. Luscombe, *J. Polym. Sci. Part Polym. Chem.*, 2019, **57**, 201–215.

78 N. S. Allen, M. Edge and S. Hussain, *Polym. Degrad. Stab.*, 2022, **201**, 109977.

79 Z. Wang, S. Wei, F. Huang, G. Bai, X. Zhang and S. Xu, *Sol. Energy*, 2024, **269**, 112334.

80 E. İlter, U. Ekim, E. Asadi, K. Tsoi, S. Yerci, M. Çelikbilek Ersundu and A. E. Ersundu, *Adv. Funct. Mater.*, 2025, 2506829.

81 X. Li, J. Qi, J. Zhu, Y. Jia, Y. Liu, Y. Li, H. Liu, G. Li and K. Wu, *J. Phys. Chem. Lett.*, 2022, **13**, 9177–9185.

82 W. Lee, S. Lee, B. S. Joo, J. Kang, H. S. Jang, H. Ko and G. Kang, *Appl. Surf. Sci.*, 2024, **669**, 160444.

83 I. A. Carbone, K. R. Frawley and M. K. McCann, *Int. J. Photoenergy*, 2019, **2019**, 8680931.

84 A. Kaniyoor, B. McKenna, S. Comby and R. C. Evans, *Adv. Opt. Mater.*, 2016, **4**, 444–456.

85 Y. Wang, Y. Liu, G. Xie, J. Chen, P. Li, Y. Zhang and H. Li, *ACS Appl. Mater. Interfaces*, 2022, **14**, 5951–5958.

86 J. A. Levitt and W. H. Weber, *Appl. Opt. Vol 16 Issue 10 Pp 2684-2689*, 1977, **16**, 2684–2689.

87 A. Goetzberger, *Appl. Phys.*, 1978, **16**, 399–404.

88 A. M. Hermann, *Sol. Energy*, 1982, **29**, 323–329.

89 C. Liu and B. Li, *J. Opt.*, 2015, **17**, 025901.

90 A. P. Demchenko, *Methods Appl. Fluoresc.*, 2020, **8**, 022001.

91 H. Fan, L. Nurtay, N. E. Safronov, P. A. Slepukhin, N. P. Belskaya and E. Benassi, *J. Mol. Liq.*, 2025, **433**, 127901.

92 F. Corsini, A. Nitti, E. Tatsi, G. Mattioli, C. Botta, D. Pasini and G. Griffini, *Adv. Opt. Mater.*, 2021, **9**, 2100182.

93 P. Meti, F. Mateen, D. Y. Hwang, Y.-E. Lee, S.-K. Hong and Y.-D. Gong, *Dyes Pigments*, 2022, **202**, 110221.

94 M. Bartolini, C. Micheletti, A. Picchi, C. Coppola, A. Sinicropi, M. Di Donato, P. Foggi, A. Mordini, G. Reginato, A. Pucci, L. Zani and M. Calamante, *ACS Appl. Energy Mater.*, 2023, **6**, 4862–4880.

95 S. T. Bailey, G. E. Lokey, M. S. Hanes, J. D. M. Shearer, J. B. McLafferty, G. T. Beaumont, T. T. Baseler, J. M. Layhue, D. R. Broussard, Y.-Z. Zhang and B. P. Wittmershaus, *Sol. Energy Mater. Sol. Cells*, 2007, **91**, 67–75.

96 B. A. Swartz, T. Cole and A. H. Zewail, *Opt. Lett.*, 1977, **1**, 73–75.

97 J. Song, C. Kim, S. Lee, H. Lee, J. Seo and H.-J. Song, *Korean J. Chem. Eng.*, 2024, **41**, 3573–3592.

98 T. Mandal, S. R. Mishra, M. Kumar and V. Singh, *Sustain. Energy Fuels*, 2024, **8**, 5638–5671.

99 H. Zhao and F. Rosei, *Chem*, 2017, **3**, 229–258.

100 F. Purcell-Milton and Y. K. Gun'ko, *J. Mater. Chem.*, 2012, **22**, 16687–16697.

101 B. O. Dabbousi, J. Rodriguez-Viejo, F. V. Mikulec, J. R. Heine, H. Mattoussi, R. Ober, K. F. Jensen and M. G. Bawendi, *J. Phys. Chem. B*, 1997, **101**, 9463–9475.

102 R. Hull, J. Parisi, R. M. Osgood, H. Warlimont, G. Liu and B. Jacquier, Eds, *Spectroscopic Properties of Rare Earths in Optical Materials*, Springer, Berlin, Heidelberg, 2005.

103 J.-C. G. Bünzli and S. V. Eliseeva, in *Lanthanide Luminescence*, eds P. Hänninen and H. Härmä, Springer Berlin Heidelberg, Berlin, Heidelberg, 2010, vol. 7, pp. 1–45.

104 H. Uh and S. Petoud, *Comptes Rendus Chim.*, 2010, **13**, 668–680.

105 L. Armelao, S. Quici, F. Barigelletti, G. Accorsi, G. Bottaro, M. Cavazzini and E. Tondello, *Coord. Chem. Rev.*, 2010, **254**, 487–505.

106 S. I. Weissman, *J. Chem. Phys.*, 1942, **10**, 214–217.

107 G. A. Crosby, R. E. Whan and R. M. Alire, *J. Chem. Phys.*, 1961, **34**, 743–748.

108 C. De Mello DonegÁ, S. J. L. Ribeiro, R. R. Gon çalves and G. Blasse, *J. Phys. Chem. Solids*, 1996, **57**, 1727–1734.

109 G. F. de Sá, O. L. Malta, C. de Mello Donegá, A. M. Simas, R. L. Longo, P. A. Santa-Cruz and E. F. da Silva, *Coord. Chem. Rev.*, 2000, **196**, 165–195.

110 M. Latva, H. Takalob, V. M. Mukkala, C. Matachescu, J. C. Rodríguez-Ubis and J. Kankare, *J. Lumin.*, 1997, **75**, 149–169.

111 J.-C. G. Bünzli and C. Piguet, *Chem. Soc. Rev.*, 2005, **34**, 1048–1077.

112 X. Wang, T. Wang, X. Tian, L. Wang, W. Wu, Y. Luo and Q. Zhang, *Sol. Energy*, 2011, **85**, 2179–2184.

113 A. R. Frias, M. A. Cardoso, A. R. N. Bastos, S. F. H. Correia, P. S. André, L. D. Carlos, V. de Zea Bermudez and R. A. S. Ferreira, *Energies*, 2019, **12**, 451.

114 V. Fiorini, N. Monti, G. Vigarani, G. Santi, F. Fasulo, M. Massi, L. Giorgini, A. B. Muñoz-García, M. Pavone, A. Pucci and S. Stagni, *Dyes Pigments*, 2021, **193**, 109532.

115 J. Choi, K. Kim and S.-J. Kim, *Sci. Rep.*, 2021, **11**, 13833.

116 D. Benetti and F. Rosei, *Nanoenergy Adv.*, 2022, **2**, 222–240.

117 S. D. A. Zondag, T. M. Masson, M. G. Debije and T. Noël, *Photochem. Photobiol. Sci.*, 2022, **21**, 705–717.

118 T. M. Masson, S. D. A. Zondag, K. P. L. Kuijpers, D. Cambié, M. G. Debije and T. Noël, *ChemSusChem*, 2021, **14**, 5417–5423.

119 K. Loh, K. Harbick, N. Eylands, U. Kortshagen and V. Ferry, *AgriVoltaics Conf. Proc.*, 2024, **3**, doi 10.52825/agripv.v3i.1376.

120 N. S. Makarov, K. Ramasamy, A. Jackson, A. Velarde, C. Castaneda, N. Archuleta, D. Hebert, M. R. Bergren and H. McDaniel, *ACS Nano*, 2019, **13**, 9112–9121.

121 F. Meinardi, F. Bruni, C. Castellan, M. Meucci, A. M. Umair, M. La Rosa, J. Catani and S. Brovelli, *Adv. Energy Mater.*, 2024, **14**, 2304006.

122 M. Portnoi, P. A. Haigh, T. J. Macdonald, F. Ambroz, I. P. Parkin, I. Darwazeh and I. Papakonstantinou, *Light Sci. Appl.*, 2021, **10**, 3.

123 M. Meucci, M. Aresti, G. Cossu, L. Gilli, L. Oliviero, M. Bartolini, A. Pucci, E. Ciaramella and J. Catani, *Adv. Opt. Mater.*, 2025, **13**, 2402367.

124 G. Cossu, L. Gilli, L. Oliviero, M. Meucci, M. Aresti, M. Calamante, A. Pucci, J. Catani and E. Ciaramella, *Sci. Rep.*, 2025, **15**, 16509.

125 W. Wang and J. C. Ho, *Light Sci. Appl.*, 2022, **11**, 125.

Chapter 2

LSC preparation methods

This *Chapter* describes the procedures used for the preparation of the LSCs, either in bulk tile or supported film configuration. In both cases, the experimental protocols have been optimized for the processing of PMMA as host material, and for the realization of LSCs having a 25 × 25 mm^2 or 50 × 50 mm^2 active area. Target thicknesses were of 3 mm for bulk-doped tiles and of 35 μm for supported films. Improvements in the procedures have been evaluated based on the homogeneity, optical quality and overall macroscopic appearance of the final products.

To realize PMMA bulk-doped tiles, the industrial batch cell procedure for producing acrylic sheets has been adapted to laboratory scale. Subsequent modifications of the experimental setup and protocol are described, along with the corresponding effects observed on the obtained samples.

As for the supported film LSCs, a slot die coater has been implemented for their preparation. After a brief introduction on slot die coating theory, the optimization of the film deposition procedure is described, as in researching ideal feedstock composition, substrate pre-treatment and coating parameters. Other than the samples' overall appearance, quality evaluations were also based on the PMMA films' thickness homogeneity. To this purpose, a non-invasive method to collect spatially resolved thickness maps has been introduced.

2.1 PMMA bulk polymerization

As already mentioned, PMMA provides an ideal host material for LSCs thanks to its high transparency, although the ease of processing is also key in its widespread use. PMMA can be synthesized from its monomer, methyl methacrylate, through thermally activated, free radical polymerization (**Fig. 2.1**).

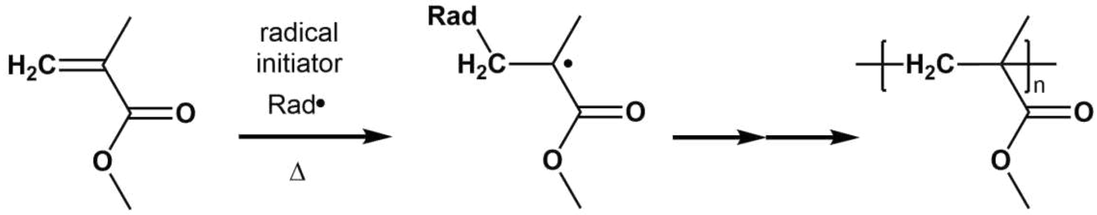

Figure 2.1. Reaction scheme for the free radical polymerization of methyl methacrylate.

The first reported casting of PMMA into sheets from its monomer is attributed to Rhom and Bauer in 1932, who patented the "batch cell" technique (or "water bath" technique) for the bulk polymerization of MMA.[1,2] The term "bulk" indicates the absence of any solvent or dispersant. The starting pure monomer is in the liquid state and, as the reaction proceeds, it becomes increasingly viscous until a solid polymer is obtained. Due to quantitative mass conversion, bulk polymerization is an extremely low waste process. Modern industrial protocols adopt a very similar procedure to Rhom's,[3,4] where acrylic sheets are obtained by conducting the free radical polymerization inside flat glass-walled moulds, which confer to the final product mirror-smooth, parallel surfaces with excellent optical quality. To initiate polymerization, the moulds are immersed in a heated water bath at a controlled temperature. This process usually exploits a thermally labile radical initiator that decomposes above a given temperature, generating free radicals. The most frequently employed initiators for the fabrication of acrylics are azobisisobutyronitrile (AIBN) and benzoyl peroxide (BPO) (**Fig. 2.2**). Generally, AIBN is the preferred choice because it generates smaller, highly mobile radicals and has shorter half-life with respect to BPO.[5] The polymerization reaction mixture is then comprised of undiluted monomer, radical initiator, a variable amount of the target polymer and the necessary plastic additives. In the case of LSCs, the luminophore is also present. It follows that all these chemicals must be soluble in the monomer at the desired concentration.

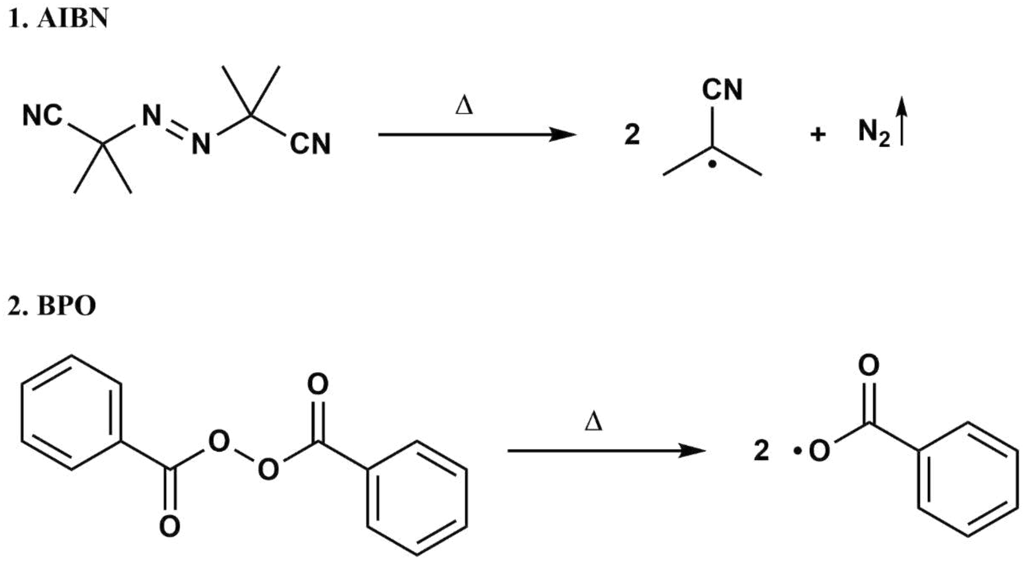

Figure 2.2. Molecular structure and decomposition products of radical initiators AIBN and BPO.

The bulk-doped LSCs presented in *Chapter 4* have been prepared as described in the following paragraphs.

2.1.1 Water bath casting

Preparing PMMA sheets with water bath casting is nowadays a consolidated procedure at the industrial level, but there are some key aspects to account for when replicating it on a lab scale. The first crucial factor is the volume shrinkage occurring during bulk polymerization. MMA is a liquid at room temperature: as chain growth proceeds, its density increases from ρ_{MMA} = 0.94 g cm^{-3} to ρ_{PMMA} = 1.19 g cm^{-3} in going from the liquid to the solid state. This causes a volume decrease in the final sheet of around 26% with respect to the starting mixture.[6] The shrinkage can be reduced if, instead of starting from the pure monomer, a monomer/polymer syrup is used. By dissolving 15% – 20% by weight of PMMA in MMA prior to polymerization, the viscosity can be effectively increased. Another strategy is to perform a pre-polymerization step of the pure monomer in the presence of the initiator to thicken the mixture. Nonetheless, the curing mould should not be entirely rigid but still allow some volume accommodation. Similarly to reported protocols,[7–10] a first curing mould was designed to cast LSC tiles with 25 × 25 mm^2 active area. This was comprised by two 3 mm thick, 50 × 50 mm^2 large glass slides held parallel to one another and separated by a 3 mm thick plastic spacer, called "gasket". Flexible polyvinyl chloride (PVC) was chosen as gasket material thanks to it being easily bendable and compressible enough for the mould to tolerate the volume shrinkage. Furthermore, PVC is chemically inert to the materials involved in the polymerization. After curing, the gasket stays attached to the PMMA sheet, but it can be easily removed by cutting it out at a later stage. Taking this aspect into account, tiles were cast in size bigger than the target one by 10 – 20 mm per active area dimension.

Glass slides and gasket were held in place by simple foldback paper clips (**Fig 2.3a**). The mould was assembled and filled as follows:

- the gasket is placed between the glass slides, running around three sides, and the components are clipped together;
- the casting mixture is poured into the mould from the top, open edge by means of a funnel (the mixture should be poured in a continuous stream to avoid incorporating air bubbles);
- after filling, the mould is closed by sliding the free end of the gasket between the glass slides, clamping also the fourth edge to ensure sealing.

The same design was adopted also for the 50 × 50 mm^2 tiles, with some modifications to the mould: 8 mm thick, 100 × 100 mm^2 glass plates and sturdier, screw-closed metal clamps were employed to sustain the greater shrinkage strains happening over the larger casted area (**Fig. 2.3b**).

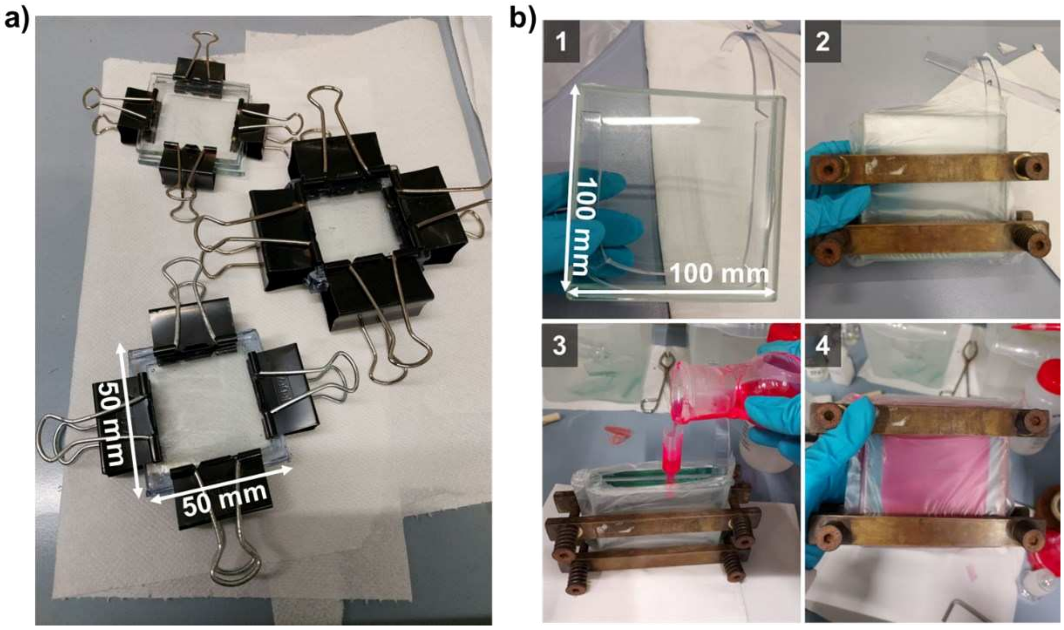

Figure 2.3. Glass moulds used for batch cell casting of **a)** 25 × 25 mm^2 and **b)** 50 × 50 mm^2 PMMA tiles. In both cases the PVC gasket is 3 mm thick.

The thickness of the final PMMA tile can be modulated by varying the thickness of the plastic gasket, even if the volume shrinkage causes it to slightly decrease during polymerization. Here, using a 3 mm thick gasket yielded 2.7 mm thick LSCs.

The second critical aspect to consider is the temperature control over the reaction system. Due to the gel effect (also called "Trommsdorf" or "Norrish-Smith" effect),[5] MMA radical polymerization is a highly exothermic process and the monomer can start to boil if adequate heat management is not provided. This exothermic behaviour is typical of bulk polymerizations and is caused by a large increase in the reaction rate with increasing mixture viscosity, called "auto-acceleration". If the monomer reaches boiling point, unwanted gas evolution with formation of bubbles inside the final PMMA tile is observed. The water bath has the double function of activating the initiator and at the same time thermalizing the mould by dissipating the heat generated by the reaction. The suggested range of temperatures for the water bath is 50 – 80 °C, as AIBN activation occurs above 45 °C but MMA boils at 101 °C. Such range offers a good compromise between maximising radicals formation rate and preventing the monomer from boiling.

Initially, a 5 L crystallizing dish was used as water bath container, in which the moulds could be placed horizontally. Polymerizations were conducted overnight, leaving the bath on a hotplate at 60 °C for 15 consecutive hours. This setup provided sufficient heat dissipation for smaller, 25 × 25 mm^2 tiles. These were indeed obtained with good repeatability between attempts: 4 successes out of 5 syntheses. When moving to the bigger, 50 × 50 mm^2 tiles, success rate dropped to 1 out of 5 syntheses.

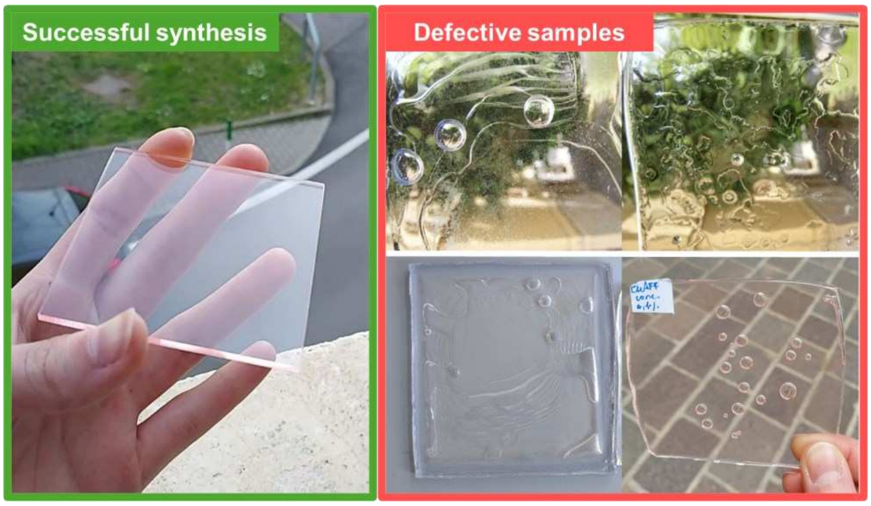

Figure 2.4. Photographs of PMMA tiles obtained from successful (green highlight) and unsuccessful (red highlight) batch cell syntheses.

For clarity, a synthesis has been considered “successful” if the casted tile showed no sign of visible discontinuities, as surface defects or trapped gas bubbles (**Fig. 2.4**). Still, target LSC dimensions were attainable also from some “unsuccessful” syntheses, due to bubbles often forming near mould edges and so being easily removed when cutting the tiles to size. Surface irregularities occurred randomly in the first LSC batches, but tiles with this problem would often present one smooth surface and one botched, which was usually the bottom one. To decrease the occurrence of surface defects, the mould's glass plates were pre-treated by keeping them in a HCl 6 M solution for ≈ 15 hours before use. Additionally, spacers were placed below the mould to raise it and allow more water to flow under it, providing a greater thermalizing mass for that region. These two precautions effectively eliminated the occurrence of surface defects. Instead, formation of gas bubbles inside PMMA was not influenced by any of these expedients. Since the only way in which gas could be generated inside the sealed mould was by monomer boiling, bubble formation was attributed to an insufficient heat dissipation when synthesizing the bigger tiles. The experimental setup was then scaled up to a 20 L plastic tank as water bath, connected to a circulator to keep the water in motion and achieve a more efficient heat exchange (**Fig. 2.5a**). Furthermore, the mould clamps were modified based on the ones used for industrial PMMA batch cell casting, achieving a more reliable mould sealing (**Fig. 2.5b**).

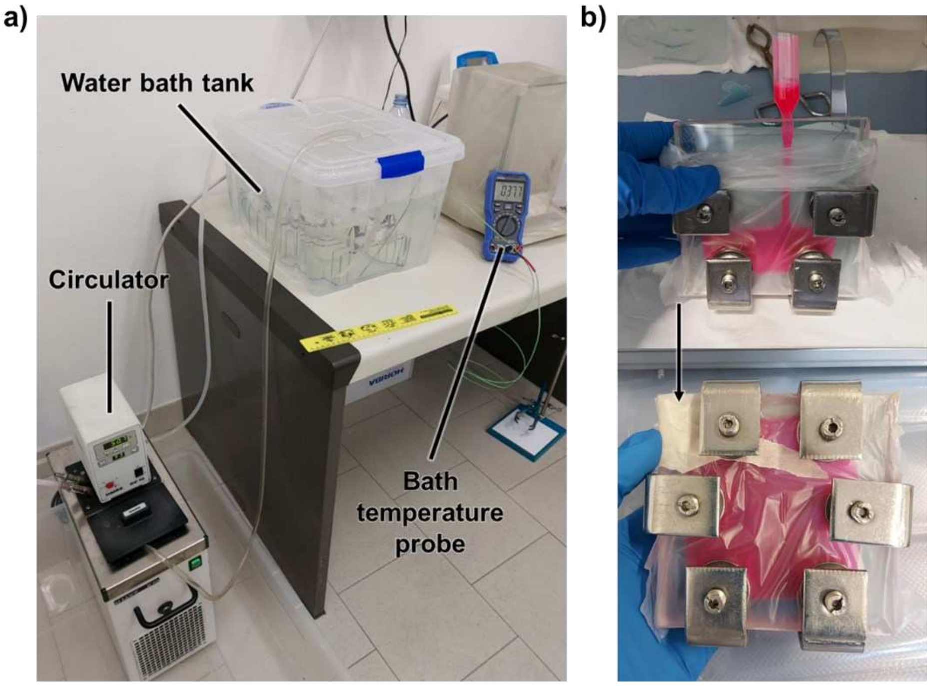

Figure 2.5. a) Scaled-up batch cell reactor. **b)** New metal clamps introduced for 50 × 50 mm^2 castings.

With this setup, polymerization times were shortened to 8 hours, still a sufficient timespan to achieve high conversion and mixture solidification. Unfortunately, changing the polymerization equipment did not significantly improve the repeatability of the process, even if too few syntheses have been conducted yet to provide a statistic. Further investigation into the temperature reached by the mixture inside the mould at different reaction times is needed. This could help in determining the gel effect temperature onset and in designing a specific temperature program for the studied polymerization.[11,12] In addition, the heat exchange efficiency of the water bath could be increased by using higher water flow rates.

2.1.2 Post-processing

Due to the great viscosity increase at high polymerization conversion rates, the mobility of radicals decreases. The polymerization slows down and eventually stops when the radicals cannot move fast enough inside the reaction mixture to reach the unreacted monomer units. Initiator diffusion is heavily hindered and becomes the bottleneck step of the process above 80% conversion rate.[6] For PMMA obtained with bulk polymerization, it is estimated that, after curing in the water bath, up to 15% by weight of unreacted monomer is still present in the material.[9] To maximise conversion, a post-curing step is necessary. This means heating the polymer above its glass transition temperature (Tg_{PMMA} = 105 – 110 °C) to soften it and allow the remaining radicals to reach the residual monomer. Post-curing is usually carried out in a hot air oven with the mould still sealed to maintain casting shape. The employed heating treatment is summarized in **Table 2.1**.

Table 2.1. Curing temperature and time of each step of the employed post-curing process.

	Step 1	**Step 2**	**Step 3**	**Step 4**
Temperature / °C	80	100	110	120
Time / h	2	1	1	1

The residual monomer fraction before and after post-curing has not been quantified in this work, but the difference between untreated and treated samples was detectable even with a simple visual inspection. If exposed to sunlight, untreated samples would develop visible defects just a few weeks after synthesis (**Fig. 2.6**).

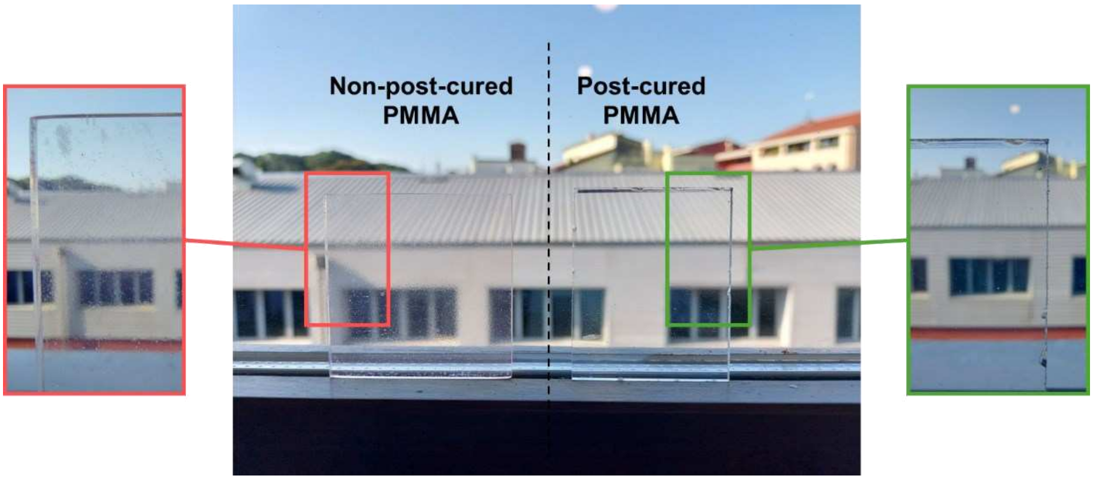

Figure 2.6. Comparison between PMMA tiles with and without post-curing.

Such defects acted as light scattering centres, decreasing the optical quality of the LSC. If untreated samples were left in the dark, the same phenomenon would occur but on a longer timescale (4 to 6 months). Conversely, post-cured samples were not affected in any capacity, retaining homogeneity over even longer periods (currently 2 years for the older post-cured batches). The formation of defects inside untreated PMMA has been attributed to a delayed polymerization of the residual monomer trapped in the solidified mixture. At temperatures lower than the polymer's Tg, AIBN radicals diffuse much slower than during post-curing, but they are still reactive and could still trigger polymerization over time. Additionally, it is known that AIBN, like many other radical polymerization initiators, can also be activated via UV irradiation.[13] It is possible that exposure to sunlight, which contains an UV component, accelerates the delayed polymerization in non-post-cured PMMA. Hence, analogous samples kept in the dark or exposed to indoor illumination would show defects much later because of much less intense or fully absent UV exposure. In any case, post-curing is an essential step to ensure the homogeneity and durability of the final material.

After curing in oven, the mould is slowly cooled at room temperature and opened to retrieve the casted PMMA tile. At this stage, the PVC gasket has become attached to the polymer and must be removed by cutting it out. Tiles were hand cut to size with a Japanese saw. Such tool is ideal for cutting brittle materials like plastics, as the blade is specifically designed to reduce burrs and cracks.

Finally, the LSC edges need to be sanded and polished to reach acceptable optical quality. This step was performed manually as well, by using progressively finer grit sandpaper for smoothing the edges, followed by cerium oxide on a wet cloth for the final polishing. An example of edge processing with results is shown in **Fig. 2.7**.

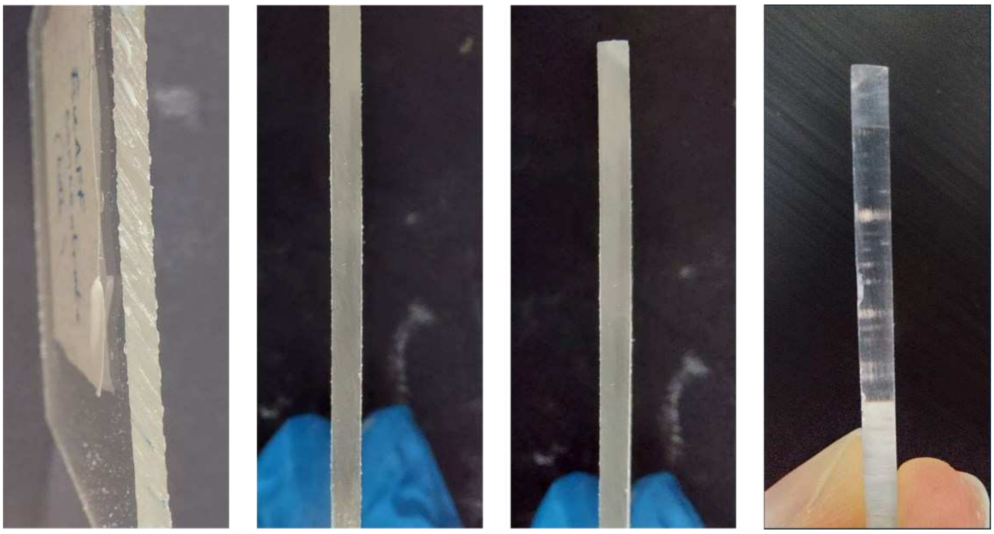

Figure 2.7. Subsequent (left to right) sanding and polishing steps of a PMMA tile's edge.

2.1.3 Procedure outline

The following workflow summarizes the water bath casting procedure used for the bulk-doped LSCs:

1. Dissolve the target amount of luminophore into the monomer.
2. Prepare the monomer/polymer syrup by dissolving 25% by weight of PMMA in MMA. Moderate heating and stirring is suggested to speed up solubilization.
3. Let the syrup cool to room temperature and add 0.08% by weight of AIBN.
4. Assemble the mould (HCl 6 M pre-treated glass plates, gasket, clamps) leaving extra space with respect to final target size and fill it with the reaction mixture.
5. Seal the mould and place it in a 60 °C water bath for 8 hours to cure.
6. Post-cure the mould in a hot-air oven to complete polymerization.
7. Let the mould cool to room temperature, open it and retrieve the casted PMMA.
8. Refine tile edges by cutting away the gasket and mechanically polishing them.

2.2 Slot die coating

Polymeric materials can be readily processed in the form of supported films by a variety of coating techniques, usually solvent mediated. Among these, slot die coating has become increasingly popular thanks to the excellent uniformity of the deposited films and the high sample reproducibility.[14,15] First invented by Beguin in 1956 for producing photographic paper,[16] slot die coating has been further developed as an improved version of doctor blading, allowing for large throughput and easy scalability.[17]

In the slot die coating process, a stock solution with a target composition is loaded onto the system in a syringe pump. The feedstock then reaches a coating element (the head) with a certain flow rate, filling an internal reservoir. Then the solution is dispensed from the head through a narrow, fixed slot, to form a liquid meniscus with the substrate. The height of this meniscus is determined by the gap between head and substrate. The substrate is placed onto a moving element (the stage) which slides away from the head, resulting in the deposition of a thin wet film as the meniscus runs over the substrate (**Fig. 2.8**). The final dry film is obtained after full evaporation of the solvent, usually aided by heating the stage.

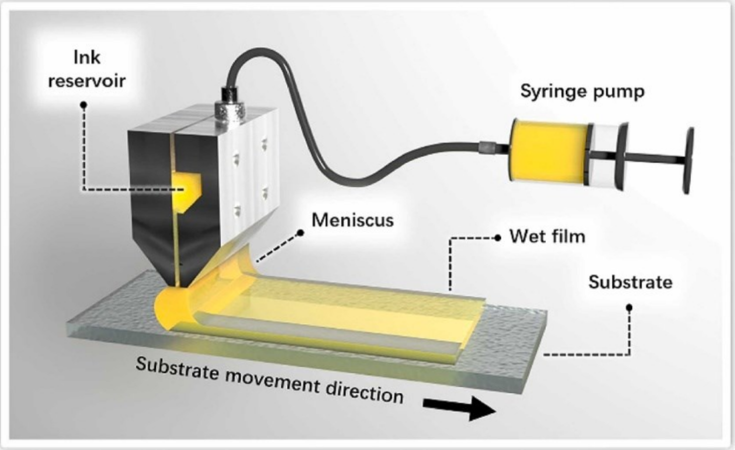

Figure 2.8. Schematics of the slot die coating process. Credit: Tu *et al.*[17]

Slot die coating figures among "pre-metered" techniques, meaning that the only factor influencing the film thickness is the flow rate of the stock solution through the system. This can be controlled by regulating some key coating parameters, like the stage speed and the syringe dispense rate. Solution composition is also crucial in designing a reliable coating protocol, as it influences viscosity and film drying.

The following paragraphs report how a highly efficient and reproducible coating method has been developed on a slot die coater by Ossila Ltd. to realize 35 μm thick PMMA films deposited onto a glass surface. The optimized method has then been used to prepare the supported film LSCs presented in *Chapter 6*.

2.2.1 Feedstock formulation

A first screening of feedstock solution compositions was conducted to find the most suitable medium to carry out PMMA slot die coating. **Table 2.2** reports investigated solutions, prepared with a PMMA weight content of 10%. Previous studies on drop casting of polymeric solutions revealed this to be a good starting polymer concentration to achieve manageable solution viscosities.

Table 2.2. Screened feedstock compositions, with details about solvents boiling points (T_{bp}) and densities. Occurrence of a coffee ring is specified.

Solution	Solvent	Solvent T_{bp} / °C	Solvent density / g cm^{-3}	Coffee ring y/n
1	$CHCl_3$	61	1.48	no
2	Toluene	111	0.87	yes
3	THF	66	0.89	yes
4	DMSO	189	1.10	no

To ascertain suitability, each solution was drop-casted onto soda-lime glass to form a small circular droplet and visually inspected for the "coffee ring" effect upon drying. The coffee ring effect refers to a specific patterning observed at liquid-gas interfaces, caused by different evaporation rates in different regions of the liquid.[18,19] Taking a fluid droplet as an example, the evaporation rate of the liquid in the bulk of the droplet will be slower with respect to the edge regions, which are most in contact with air. This gradient in evaporation rates generates surface tension driven flows that affect the liquid's spatial distribution. In circular liquid droplets, the surface tension flows push the material towards the droplet's edges, causing depletion of the central region and producing a coffee ring pattern (**Fig. 2.9**).

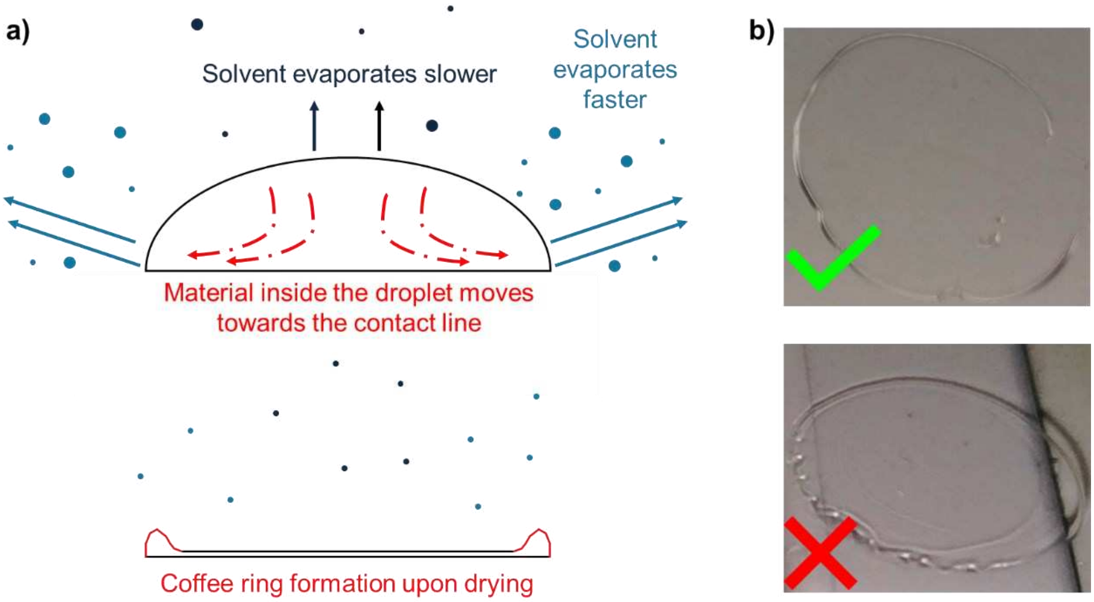

Figure 2.9. a) Schematics of the coffee ring effect on a circular liquid droplet (vertical section view) and **b)** example of dried droplets of a polymer solution differently affected by surface tension flows.

If a solid is dispersed inside the fluid and the coffee ring effect takes place, the solid will accumulate as well around the edges, building up a circular solid deposit. Such phenomenon is unfavourable in many processes, including film coating because it affects the homogeneity and overall appearance of the film. Slowing down solvent evaporation generally helps in mitigating the coffee ring effect thanks to a more controlled film drying. This can be achieved by choosing high boiling solvents or switching to multi-solvent systems.[20]

After the first screening, preliminary tests were carried out on the coater with solutions **1** ($CHCl_3$) and **4** (DMSO). The $CHCl_3$ formulation was discarded due to the fast solvent evaporation which caused the head to frequently become clogged with dry polymer, even when performing the depositions at room temperature. Conversely, the DMSO solution presented the opposite issue: solvent evaporation was too slow and often incomplete, with the films being still wet even after 2 – 3 hours of heating at 90 °C. This was the upper temperature operational limit, as it was important to not reach PMMA's Tg (105 °C). Two-solvent formulations between DMSO and low boiling solvents $CHCl_3$ and THF were then investigated. Both co-solvents shortened film drying times, but THF was chosen in the end as DMSO / $CHCl_3$ solutions were too viscous to handle on the coater. Despite THF-only PMMA solutions giving the coffee ring effect, the optimized DMSO / THF 3:2 vol/vol formulation showed no sign of it, so it was deemed ideal for slot die coater use.

2.2.2 Coating parameters optimization

Regulation of the gap between the head and the substrate is important to form a stable meniscus and consequently a defect-free film. The ideal gap height can be derived from the solution composition and the desired final dry film thickness. Wet (t_{wet}) and dry (t_{dry}) film thicknesses are related by the following equation:[21]

$$t_{wet} = \frac{t_{dry}}{V\%_{solids}} \quad ; \quad V\%_{solids} = \frac{\frac{m_{solids}}{\rho_{solids}}}{\frac{m_{liquids}}{\rho_{liquids}} + \frac{m_{solids}}{\rho_{solids}}} \qquad \textbf{Eq. 2.1}$$

where $V\%_{solids}$ is the volume fraction of solid components dispersed in the solution, calculated from mass (m) and density (ρ) of its components. Once t_{wet} is known, an initial value for the gap height (h_{gap}) can be calculated using the viscous model approximation:[22]

$$h_{gap} < 2t_{wet} \qquad \textbf{Eq. 2.2}$$

Considering a target t_{dry} of 35 μm and the optimized feedstock formulation, a h_{gap} value of 800 μm was set as coating gap height.

Another important parameter is the temperature of the substrate during and after coating, because it heavily influences solvent evaporation rates. The employed slot die coater features a stage that can be heated up to 120 °C, useful to set substrate temperature. The temperature program was designed as follows:

- film depositions are carried out at 60 °C;
- after coating, the stage is heated at 90 °C for 1 hour to evaporate a first consistent part of the solvent;
- full drying is completed later in a hot-air oven at 90 °C for ≈ 15 hours (overnight).

With system parameters set, a coating program for 50 × 50 mm^2 wide, 3 mm thick substrates was designed. On the employed slot die coater, user editable parameters are: *i*) the coating length (in mm, the distance covered by the moving stage); *ii*) the coating speed (in mm s^{-1}, the moving stage velocity); *iii*) the dispense rate (μL s^{-1}, the volume of solution dispensed by the syringe pump). Finding the right relationship between such parameters is essential to achieve a stable meniscus and a continuous film.

In a deposition experiment, the target glass slide was pre-treated with a HCl 6 M bath, similarly to the glass used in the PMMA casting moulds described in *Section 2.1.1*. To avoid edge defects at the start and at the end of the coating, two sacrificial substrates of the same size of the target one were placed before and after it on the stage (**Fig. 2.10**). As a general rule, fluid apport was interrupted during the last 10 mm of the coating length, (*i.e.*, over the second sacrificial substrate), to prevent the build-up of solution at the end of the film once the stage stopped moving. This excess dispensed solution would then spread along the substrates reaching the target one and consequently affecting the quality of the deposited film.

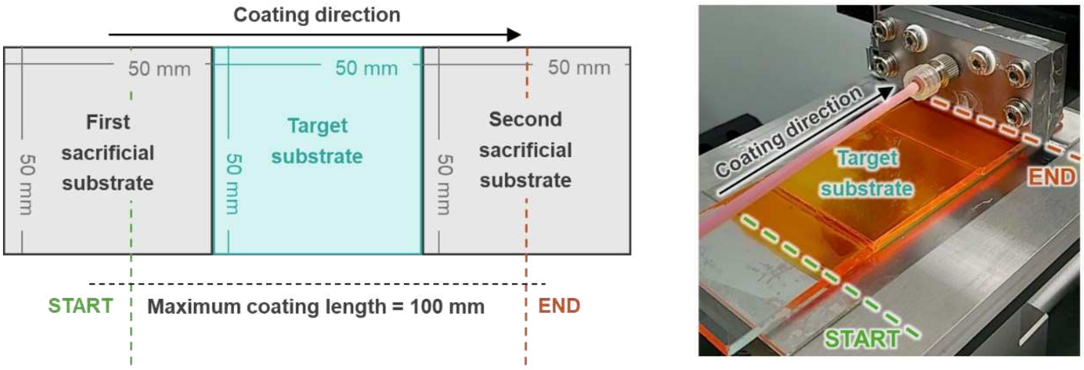

Figure 2.10. Disposition of the different substrates over the slot die coater's stage.

Table 2.3. Summary of the progressive versions of the slot die coating program optimized for depositing 50 × 50 mm^2, 35 μm thick PMMA films.

Program version	**Step**	**Coating length / mm**	**Coating speed / mm s^{-1}**	**Dispense rate / μL s^{-1}**
1	a	90	1.5	40
	b	10	5	0
2	a	50	1.5	40
	b	40	0.7	20
	c	10	5	0
3	a	50	2.5	50
	b	40	5	100
	c	10	5	0

Table 2.3 lists the modifications made to the coating parameters during optimization. Besides evaluating the film's aesthetic characteristics, progress in film optimization was assessed by monitoring the thickness of the final dry films over different positions, collecting 40 × 40 mm^2 maps. Thickness values were acquired indirectly through reflectance measurements, using the Swanepoel method (see *Appendix A*). Thickness maps shown below have all been normalized on the median value of the distribution.

In program version **1**, fixed coating speed and dispense rate were used for the whole target substrate's length. The obtained films systematically displayed a decrease in thickness from half-length onwards (**Fig. 2.11a**).

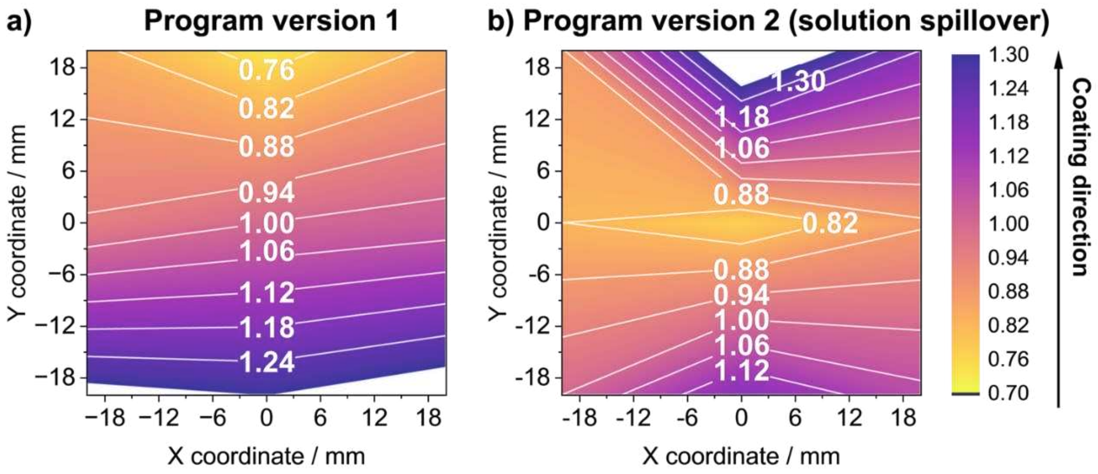

Figure 2.11. 40 × 40 mm^2 thickness maps collected on films made with program version **a) 1** and **b) 2**.

The **1a** step (*i.e.*, the step in which the solution is dispensed) was then split into two sub-steps for program version **2**, before (**2a**) and after (**2b**) half-length of the target substrate. In step **2b** the coating speed was slowed down and the dispense rate modified accordingly to keep the same parameter ratio as step **2a**. This had a slightly beneficial effect on the thickness homogeneity but caused more frequent spillovers of the solution from the target substrate's edges (*i.e.*, destabilization of the coating bead), which resulted in total loss of control over the film thickness (**Fig. 2.11b**). In program version **3**, based on a previous slot die coating parameters analysis,[20] step **3b** (solution dispensed after half-length of the target substrate) was further modified so to have both double coating speed and dispense rate with respect to step **3a** (solution dispensed before half-length of the target substrate). This caused a significant improvement in the overall thickness homogeneity and it was considered a reasonable convergence point in program optimization (**Fig. 2.12a**).

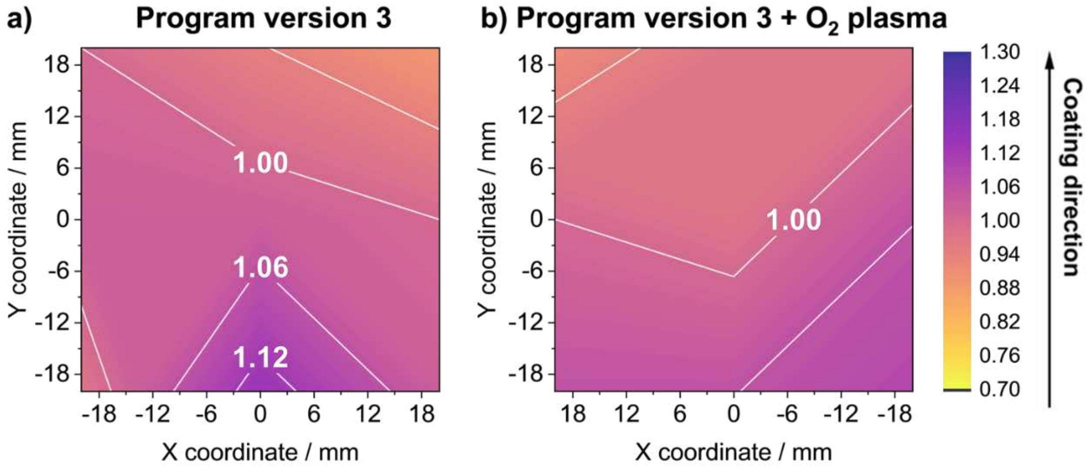

Figure 2.12. 40 × 40 mm^2 thickness map collected on a film made with program version **3**, **a)** before and **b)** after introducing an O_2 plasma pre-treatment.

Table 2.4. List of the samples considered for a statistical analysis of film thickness homogeneity. Single sample standard deviation (σ) is calculated on the absolute thickness values acquired for each single film. Batch sample σ is calculated on the median thickness values across multiple films.

Sample	Median thickness	Single sample σ	Batch sample σ
HCl 6M glass pre-treatment			
A	41	± 3.3	± 2.8
B	38	± 4.1	
C	37	± 3.4	
D	35	± 3.4	
E	35	± 2.5	
F	33	± 4.1	
HCl 6M + O_2 plasma glass pre-treatment			
G	34	± 2.0	± 0.5
H	33	± 2.3	
I	36	± 1.7	
J	35	± 2.9	
K	35	± 2.9	
L	33	± 1.9	

With the optimized program, the best value of thickness homogeneity reached was 35 ± 2.5 μm. Furthermore, repeatability of the process was extensively tested, assessing a standard deviation (σ) of ± 2.8 μm between median thickness values of different films (**Table 2.4**). Nonetheless, a plasma pre-treatment step of the target glass substrate was introduced to facilitate a more even spreading of the meniscus over its whole surface, and to reduce side edge defects such as corrugation and creasing. An O_2 cold plasma (see *Appendix B*) was used to activate the glass surface, just before carrying out the coating process. Such pre-treatment resulted in a higher optical quality of the films (**Fig. 2.12b**), with reduced edge defects and improved homogeneity of the deposit: 35 ± 1.7 μm on single film (best value); ± 0.5 μm between median values of different films (**Table 2.4**).

Slot die coating was used to coat also smaller substrates, with 25 × 25 mm^2 active area and 1 mm thickness. Reduced size was necessary to perform emission spectroscopy characterizations due to the dimensions of the instrument sample chamber. For these substrates, program version **3** was adapted to version **3s** (**s** = small). Updated parameters are reported in **Table 2.5**. Average film thickness was 25 μm.

Table 2.5. Coating parameters used for coating 25 × 25 mm^2 glass slides.

Program version	**Step**	**Coating length / mm**	**Coating speed / $mm\ s^{-1}$**	**Dispense rate / $\mu L\ s^{-1}$**
3s	a	25	2.5	25
	b	20	5	50
	c	10	5	0

2.2.3 Procedure outline

The following workflow summarizes the slot die coating procedure used for the supported film LSCs:

1. Set the coating gap height at 800 μm and the stage temperature at 60 °C.
2. Pre-treat the target substrate with HCl 6 M and O_2 cold plasma.
3. Place the target substrate onto the stage between two sacrificial slides.

4. Load the feedstock solution into the system and run the syringe pump until a meniscus is formed between head and substrate.
5. Run the coating program.
6. Bring stage temperature to 90 °C and leave the film to dry for 1 hour.
7. Remove the coated substrate and treat overnight in a hot-air oven at 90 °C.

2.3 Bibliography

1 United States, US2091615A, 1937.

2 United States, US2154639A, 1939.

3 K. Albrecht, M. Stickler and T. Rhein, in *Ullmann's Encyclopedia of Industrial Chemistry*, John Wiley & Sons, Ltd, 1st edn., 2013.

4 R. V. Slone, in *Encyclopedia of Polymer Science and Technology*, John Wiley & Sons, Ltd, 1st edn., 2001.

5 Odian, George G., in *Principles of Polymerization*, John Wiley & Sons, Ltd, 4th edn., 2004, pp. 198–349.

6 K. Albrecht, M. Stickler and T. Rhein, in *Ullmann's Encyclopedia of Industrial Chemistry*, Wiley, 1st edn., 2013.

7 X. Gong, W. Ma, Y. Li, L. Zhong, W. Li and X. Zhao, *Org. Electron.*, 2018, **63**, 237–243.

8 E. Bagherzadeh-Khajehmarjan, A. Nikniazi, B. Olyaeefar, S. Ahmadi-Kandjani and J.-M. Nunzi, *Sol. Energy Mater. Sol. Cells*, 2019, **192**, 44–51.

9 L. R. Wilson, Thesis, Heriot-Watt University, 2010.

10 K. Kowalczyk, T. Spychaj, A. Ubowska and B. Schmidt, *Appl. Clay Sci.*, 2014, **97–98**, 96–103.

11 Y. Suzuki, D. Cousins, J. Wassgren, B. B. Kappes, J. Dorgan and A. P. Stebner, *Compos. Part Appl. Sci. Manuf.*, 2018, **104**, 60–67.

12 X. Cui, X. Gui, J. Hu, Z. Gong, R. Zhou, D. He, S. Lin, Y. Dong and Y. Tu, *J. Loss Prev. Process Ind.*, 2023, **83**, 105074.

13 M. Yamashina, Y. Sei, M. Akita and M. Yoshizawa, *Nat. Commun.*, 2014, **5**, 4662.

14 H. Peng, H. Hu, J. Ding, G. Cheng and J. Ding, *J. Coat. Technol. Res.*, 2024, **21**, 1649–1661.

15 T. Guo, D. Zhou, M. Gao, S. Deng, M. Jafarpour, J. Avaro, A. Neels, E. Hack, J. Wang, J. Heier and C. (John) Zhang, *Adv. Funct. Mater.*, 2023, **33**, 2213183.

16 United States, US2681294A, 1954.

17 Y. Tu, J. Ye, G. Yang, Y. Zang, L. Zhang, Y. Wang, G. Li, L. Chu and W. Yan, *J. Alloys Compd.*, 2023, **942**, 169104.

18 M. J. Hertaeg, C. Rees-Zimmerman, R. F. Tabor, A. F. Routh and G. Garnier, *J. Colloid Interface Sci.*, 2021, **591**, 52–57.

19 S. Das, A. Dey, G. Reddy and D. D. Sarma, *J. Phys. Chem. Lett.*, 2017, **8**, 4708–4709.

20 A.-M. STOBO, Masters, Durham University, 2017.

21 P. M. Schweizer, in *Premetered Coating Methods: Attractiveness and Limitations*, ed. P. M. Schweizer, Springer International Publishing, Cham, 2022, pp. 387–452.

22 X. Ding, J. Liu and T. A. L. Harris, *AIChE J.*, 2016, **62**, 2508–2524.

Chapter 3

LSC terminology and reporting

Up until recently, literature on LSCs lacked established guidelines for unified terminology and characterization protocols, making it difficult to compare results between independent laboratories. The need for standardized reporting methods prompted field experts to reach a consensus and publish good-practice recommendations for LSC practical characterization and data elaboration.

The present *Chapter* offers an overview of the terminology and the experimental procedures used from here on to address LSC studies, in compliance with the most recently published guidelines. This includes defining mandatory figures of merit, applying correct measurement procedures and developing custom testbenches for enabling reliable LSC characterization. For simplicity, the following discussion concerns a square planar LSC model.

3.1 Luminophore and waveguide

The first and most basic information to provide for an LSC is its size, as in length, width and thickness. This is particularly important because the dimensions of the waveguide define the geometric gain (G) as follows:

$$G = \frac{A_{in}}{A_{out}} \qquad \textbf{Eq. 3.1}$$

where A_{in} (cm^2) is the active area, or aperture area, receiving solar irradiation, and A_{out} (cm^2) is the emitted light collection area, generally the edge area which will eventually be coupled to the PV cells. The geometric factor is a fundamental concept in LSCs because it defines the theoretical light concentration limit of the waveguide.[1] A higher G value means also a higher aperture-to-edge area ratio, and so less PV material needed per LSC area unit. In the following LSC case studies, an active area equal to 25 cm^2 has been chosen because it has been proposed as a reasonable standard size for easily comparing results between independent LSC studies on a laboratory scale.[2,3] The fraction of incident photons absorbed by the active area of the LSC for a given wavelength (λ) is known as the absorptance (α):

$$\alpha = \frac{n_{abs}}{n_{in}} \qquad at\ any\ \lambda \qquad \textbf{Eq. 3.2}$$

where n_{abs} is the number of absorbed photons and n_{in} is the number of incident photons. Care must be taken not to mix the different terms related to the absorption phenomenon in an LSC: “absorptance”, “absorbance” (A) and “absorptivity” (ε) all bear a different meaning. Absorptance contributes to the total photon balance of the waveguide interacting with light (**Eq. 3.3**) and can be determined from it by subtracting the fractions of transmitted and reflected photons, referred to as transmittance (τ) and reflectance (ρ), respectively.

$$\frac{n_{abs}}{n_{in}} + \frac{n_{tr}}{n_{in}} + \frac{n_r}{n_{in}} = \alpha + \tau + \rho = 1 \qquad at\ any\ \lambda \qquad \textbf{Eq. 3.3}$$

where n_{tr} is the number of transmitted photons and n_r is the number of reflected photons. Due to transmittance and reflectance being commonly measured using a spectrophotometer on a scale from 0 to 100, the photon balance can be expressed in a more practical way using percentage terms, with α, τ and ρ indicated as $A\%$, $T\%$ and

$R\%$, respectively. Absorbance is instead defined by IUPAC as the “logarithm of the ratio of incident to transmitted radiant power through a sample (excluding the effects on cell walls)”.[4] This implies that reflections at sample interfaces are not present, or they can be subtracted by using a “blank” sample. Absorbance is closely related to transmittance by the Beer-Lambert law:[5]

$$A = log_{10}(\tau) = \varepsilon\, L\, C \qquad\qquad at\ any\ \lambda \qquad \textbf{Eq. 3.4}$$

where ε (M^{-1} cm^{-1}) is the absorptivity, also known as the molar extinction coefficient, L (cm) is the optical path length and C is the solution molar concentration (M). Absorbance and absorptivity are useful parameters to characterize the luminophore's absorption properties before and after embedment in the solid matrix, provided that in both cases the system is non-scattering. The comparison between the photophysical properties in the solution and in the embedding medium can offer qualitative insights into whether materials processing alter the luminophore. In any case, since using blank samples to subtract reflections is less reliable for LSCs with respect to solutions, the material’s absorption is better expressed by absorptance, which is the recommended reporting metric. By integrating the absorptance over the whole solar spectrum, it is possible to estimate the fraction of the total incident photons effectively absorbed by the LSC, defined as the total solar absorptance ($\eta_{s,abs}$):

$$\eta_{s,abs} = n_s^{-1} \int_s \alpha(\lambda)\, \Phi_{ph}^{AM1.5G}(\lambda)\, d\lambda \quad ; \quad n_s = \int_s \Phi_{ph}^{AM1.5G}(\lambda)\, d\lambda \qquad \textbf{Eq. 3.5}$$

where $\Phi_{ph}^{AM1.5G}$ is the standard AM1.5G photon flux (m^{-2} s^{-1})[a]. It is important that a luminophore maximizes $\eta_{s,abs}$ within its absorption wavelengths, especially for UV and NIR absorbers (**Fig. 3.1**). In the first case, the UV photon population of the AM1.5G spectrum is inherently low, so a good UV absorber should completely absorb

---

[a] The AM1.5G solar spectrum is the standardized solar irradiation profile recommended for PV tests under simulated illumination. Its total integrated irradiance is 1000 W m^{-2}, corresponding to an illumination of “1 sun”. The spectrum was derived as a representative average of the illumination received by the U.S.A. over a period of one year. The receiving surface is defined as an inclined plane at 37° tilt toward the equator, and an air mass (AM) coefficient of 1.5 is specified. This coefficient is associated with the distance travelled by light through the atmosphere before reaching the terrestrial surface, and consequently with the reduction of incident radiant power due to absorption by air and atmospheric particulate. AM = 1 identifies the sun at the zenith, and so the shortest possible distance travelled by light, while AM = 1.5 corresponds to a solar zenith angle of 48° (https://www.nrel.gov/grid/solar-resource/spectra-am1.5.html, last accessed on July 27th, 2025).

incoming radiation to maximise its utilization efficiency. For the NIR region, the coupling with Si solar cells (*i.e.*, the most frequently employed with LSCs) is the limiting factor.

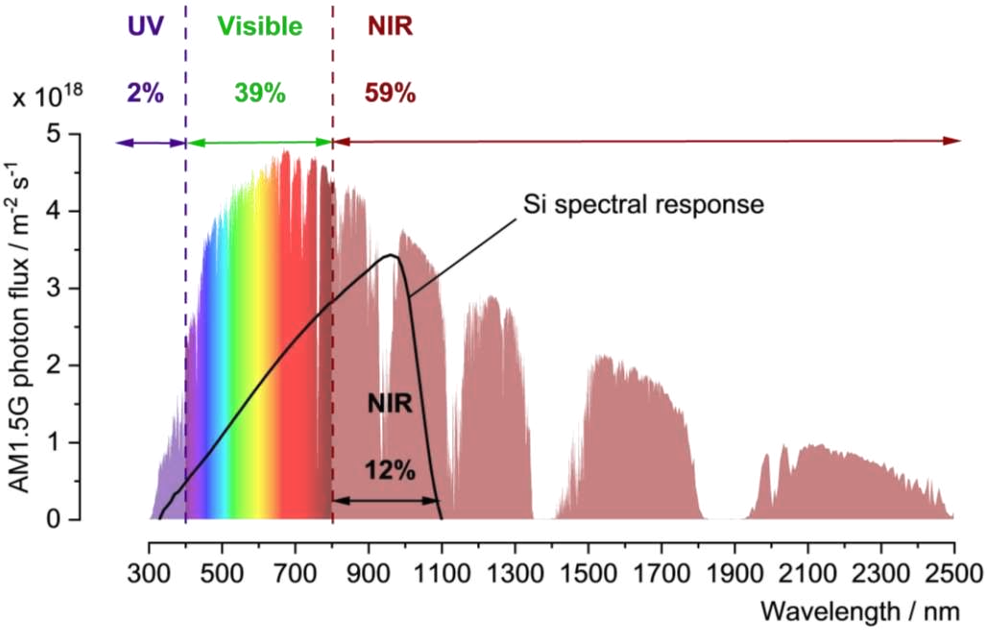

Figure 3.1. AM1.5G photon flux spectral distribution, with UV, Visible and NIR regions highlighted. In the most common case of an LSC coupled to Si solar cells, the NIR photon fraction available for absorption is greatly reduced with respect to the total.

Transmittance and reflectance spectra for absorptance determination are usually collected on a spectrophotometer using an integrating sphere. Due to the conventional experimental setup geometry, the sphere collects also the photoluminescence (PL) photons exiting the LSC via the escape cone (see *Section 1.3*). Without a proper filtering of these photons, highly luminescent samples can exhibit artifacts in their spectra, typically resulting in higher T% and R% values within the luminophore absorption region. At the wavelengths stimulating luminophore emission, the detector reads both the transmitted/reflected photons at the given excitation wavelength, plus the emitted photons not waveguided to the edges, which enter the sphere (**Fig. 3.2**). This problem can be solved either by introducing a second monochromator between the sphere and the detector (*i.e.*, by using a spectrofluorometer setup), or by applying external optical filters between the sample and the sphere. Due to equipment configuration, the second method was deemed the best to acquire correct T% and R% spectra for LSC samples. Two short pass filters were chosen, with consecutive transmission windows to characterize both UV and visible absorbing LSCs (**Fig. 3.3**).

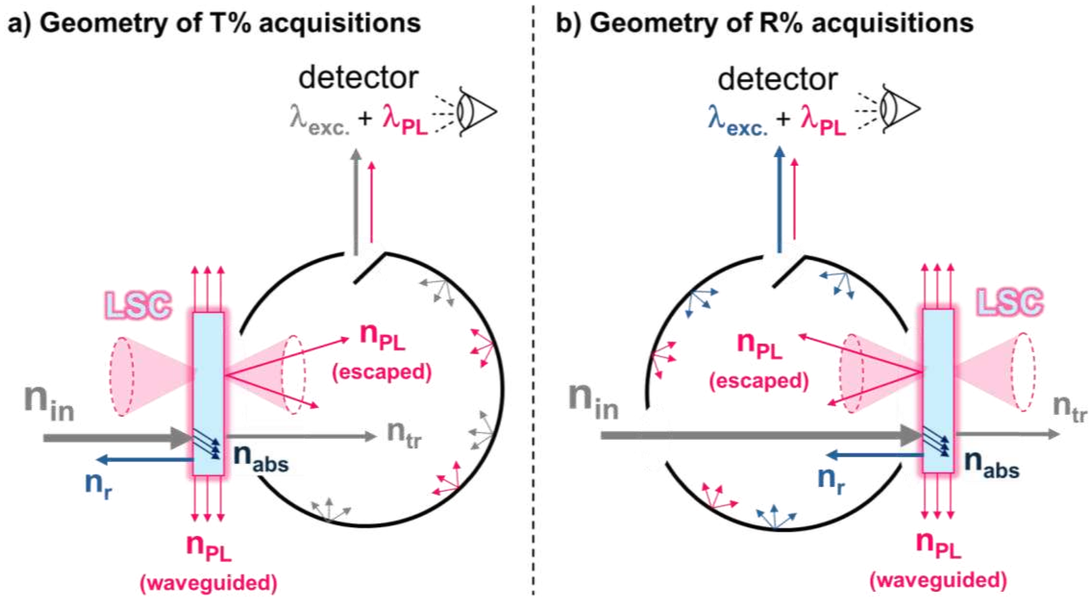

Figure 3.2. Schematics of the sample/sphere geometry used for the LSCs **a)** $T\%$ and **b)** $R\%$ spectra acquisitions. The PL photons lost via escape cone enter the sphere and reach the detector. Labels: n_{in} = total incident photons, n_{abs} = absorbed photons, n_r = reflected photons, n_{tr} = transmitted photons, n_{PL} = emitted photons, λ_{exc} = excitation wavelength, λ_{PL} = emission wavelength.

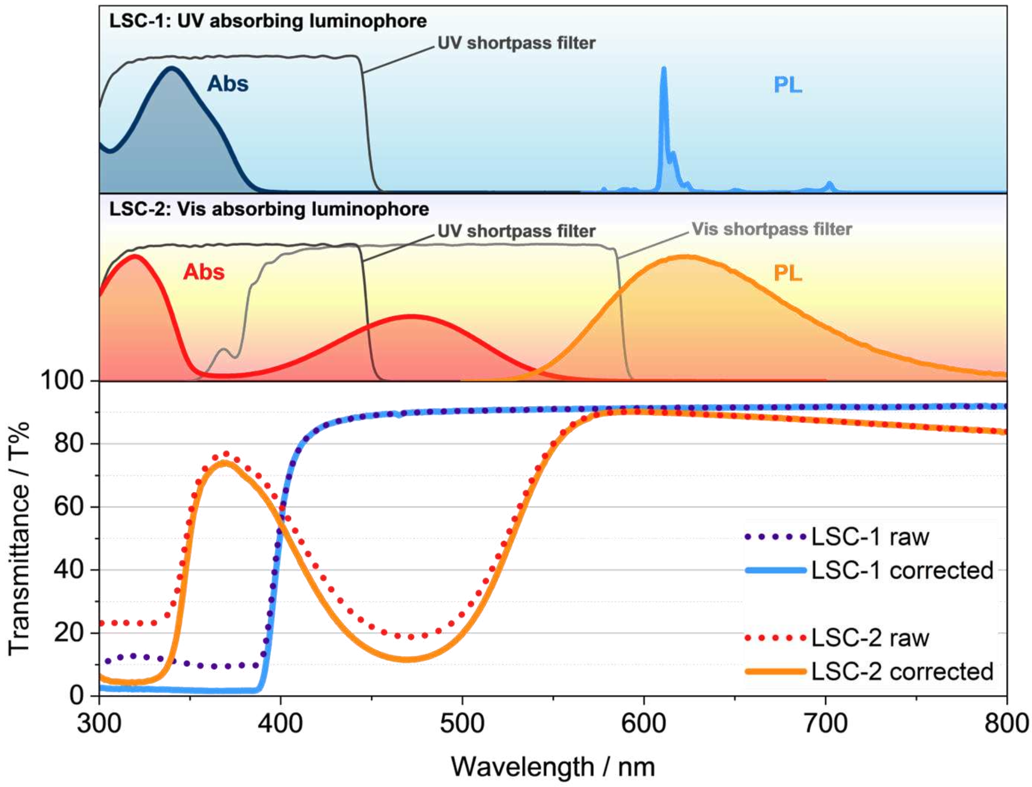

Figure 3.3. Effects of using optical short pass filters for acquiring the $T\%$ spectra of two LSCs, one UV absorbing and one visible absorbing. The absorption and emission spectra of the luminophores are highlighted, as well as the transmittance profiles of the filters.

Depending on the excitation bandwidth of the luminophores, just the UV or both the UV and Vis filters were used, and the spectral acquisitions were split into two or three wavelength segments, respectively. **Fig. 3.3** highlights the difference in using the filters with respect to acquiring the raw spectra. The overestimation of $T\%$ and $R\%$ leads to a significant underestimation of $A\%$, and consequently of $\eta_{s,abs}$, underrating the overall absorption capabilities of the LSC.

When designing a luminophore for LSCs, light emission should be maximised as well as absorption. The light emission behaviour of an LSC can be expressed through the photoluminescence quantum yield of the embedded luminophore. The $PLQY$ is defined as:[6]

$$PLQY = \frac{n_{PL}}{n_{abs}} \qquad \textbf{Eq. 3.6}$$

where n_{abs} is the number of photons absorbed by the sample and n_{PL} is the number of these photons effectively re-emitted. The $PLQY$ of an LSC is measured by using the absolute method, which requires a spectrofluorometer equipped with an integrating sphere. An equivalent, undoped sample is used as blank to account for reflection and transmission of the excitation beam. By comparing the LSC and blank output spectra, it is possible to determine both n_{abs} and n_{PL}, thus obtaining the $PLQY$. Due to reduced sample chamber dimensions in conventional integrating spheres, the $PLQY$ of large-area LSCs is usually measured on smaller, equivalent samples. Comparing the $PLQY$ of the luminophore in solution and after embedment in the solid medium is another useful check to determine if material processing influences the photophysical properties of the luminophore or, in the case of low Stokes shifts, if reabsorption is present.[7] Preliminary evaluation of the luminophore's $PLQY$ in solution can also help in choosing the best emitters for LSC development. However, considering only the $PLQY$ as a discriminant yields just a partial evaluation of the picture. It is important to always relate the fraction of emitted photons to the number of absorbed photons, so to maximise emission per unit area and per unit time. For molecules and complexes in solution, this parameter is well represented by the molar brightness B (M^{-1} cm^{-1}):[6]

$$B = \varepsilon \times PLQY \qquad \textbf{Eq. 3.7}$$

Brightness becomes particularly useful in the case of luminophores displaying similar absorption and emission spectra. In the LSC case studies presented later on, this parameter has been adopted as reference metric for assessing the photophysical performance of the available luminophores in solution and finding those most suitable for device development.

3.2 LSC visual impact and aesthetic quality

Considering BIPVs as the main application field for LSCs, evaluating how they are visually perceived is extremely important, especially if they are intended as replacements for residential or shop windows. To objectively quantify the aesthetic quality of an LSC, some key parameters have been recommended for reporting:[8,9] i) the Average Visible Transmittance (AVT), ii) the Colour Rendering Index (CRI) and iii) the $CIELAB$ colour coordinates ($a*$, $b*$). Such parameters are often considered as selection criteria for integration by many glass and greenhouse industries, regardless of the device's electrical efficiency.

The AVT is widely utilized for transparent photovoltaics to evaluate their overall visible transparency. It is calculated by weighting the transmittance profile of the device and the AM1.5G spectrum against the human eye photopic response, by applying the following integration:[10]

$$AVT\% = \frac{\int T\%(\lambda) \cdot V(\lambda) \cdot \Phi_{ph}^{AM1.5G}(\lambda) d\lambda}{\int V(\lambda) \cdot \Phi_{ph}^{AM1.5G}(\lambda) d\lambda} \qquad \textbf{Eq. 3.8}$$

where $T\%(\lambda)$ is the transmittance spectrum, $\Phi_{ph}^{AM1.5G}(\lambda)$ is the AM1.5G photon flux and $V(\lambda)$ is the photopic response function[11] (**Fig. 3.4**). Given the shape of $V(\lambda)$, it is evident that the integration ends are defined solely by the function, independent of any $T\%(\lambda)$ wavelength range. Attenuation of the photon flux where the photopic response is larger will impact the most the final AVT value. This is the case for green light absorbers, which generally determine lower AVTs with respect to blue and red light absorbers.

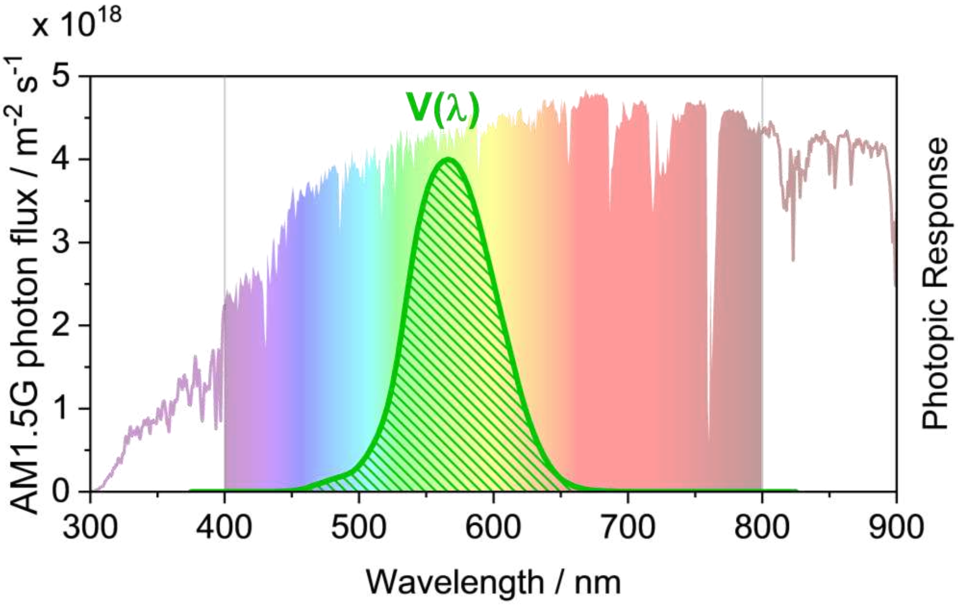

Figure 3.4. Human eye's photopic response function $V(\lambda)$ superimposed to AM1.5G photon flux in the visible region. $V(\lambda)$ indicates the spectral sensitivity of the human vision to light of different wavelengths in bright illumination conditions.

The CRI was originally introduced as a standardized method to assess the quality of a light source in reproducing the colour of objects it illuminates.[12] The evaluation is based on the comparison between a "test light source" and a "reference light source", the latter usually corresponding to the Planckian blackbody radiator with colour temperature closest to the test source. In transparent photovoltaics, rather than using an arbitrary blackbody radiator as reference source, the AM1.5G energy flux is the preferred choice, while the test source is the energy flux transmitted by the device, defined as AM1.5G $\cdot$ $T\%(\lambda)$. The calculation of the CRI is based on both chromaticity ($u*$, $v*$ colour coordinates) and luminous intensity ($L*$) differences between reference and test, expressed as follows:

$$CRI = \frac{1}{8}\sum_{n=1}^{8}\left[100 - 4.6 \cdot \sqrt{(\Delta u_i^*)^2 + (\Delta v_i^*)^2 + (\Delta L_i^*)^2}\right] \qquad \textbf{Eq. 3.9}$$

The chromaticity and luminous intensity differences are calculated for eight test-colour samples and then averaged to provide the global CRI. Note that the chromaticity used for CRI determination is expressed in terms of $CIELUV$ colour coordinates, instead of the previously mentioned $CIELAB$ ($a*$, $b*$) coordinates. The two colour spaces were developed jointly by the Commission Internationale de l'Éclairage (CIE) in 1976 to provide more perceptually uniform colour spaces with respect to the earlier established $CIEXYZ$ colour system (dated 1931).[13] The two spaces are used alternatively to describe colour rendering in different contexts: $CIELUV$ is more suitable for additive colour applications such as displays and monitors, while $CIELAB$ is suggested for subtractive colour applications such as printed and dyed surfaces.[14] In practical terms, the recommended CRI definition for LSC reporting is the one expressed by **Eq. 3.9,** based on the ($u*$, $v*$) coordinates, while the inherent LSC tint is to be provided according to the ($a*$, $b*$) coordinates, which are the standard adopted by the window industry.[15]

The $CIELAB$ system provides a tri-dimensional colour space, where the chromaticity is defined along the $a*$ axis (red to green) and the $b*$ axis (yellow to blue). The lightness $L*$ is reported as the third dimension, on a scale from 0 to 100 (**Fig. 3.5**).

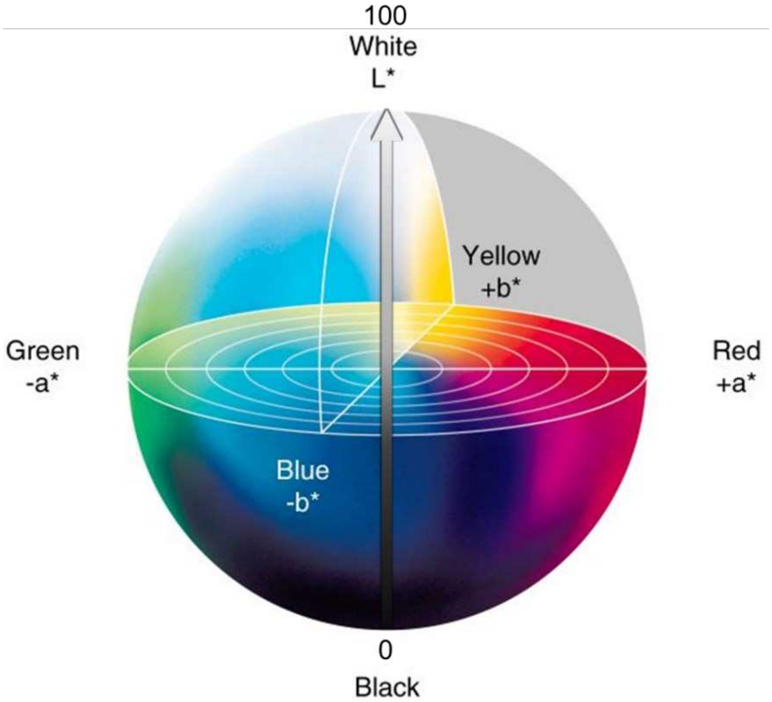

Figure 3.5. $CIELAB$ colour system.

In this system, $a*$ and $b*$ at the origin is (0, 0), corresponding to the absence of colour. In the glass industry, tinted panels with coordinates near the origin (neutral/grey) or negative $a*$ (greenish) and negative $b*$ (bluish) are considered less visually impacting with respect to positive $a*$ (reddish) and positive $b*$ (yellowish).[10] CRI and colour coordinates are interdependent parameters, as a single transmittance profile is used to calculate both. Hence, both values should be reported for an LSC, to fully identify its perceived colour and the colour rendering of the transmitted light. The same considerations apply also for the reflected light, as CRI and ($a*$, $b*$) coordinates can be calculated in the same way based on the LSC's reflectance profile. Considering building integration, both transmitted and reflected light colour rendering are important to assess the visual impact of the window from both indoors and outdoors perspectives.[15]

In their guide on how to report transparent solar cells,[10] Lunt *et al.* also provided a comprehensive spreadsheet for the calculation of AVT, CRI and $CIELAB$ coordinates from $T\%$ or $R\%$ spectra. This useful tool has been employed in the present work to calculate LSC aesthetic quality parameters.

3.3 LSC-PV device characterization

Although fundamental, the quantification of the electrical performance of LSC devices has been the most controversial point of the concerning literature, only recently addressed. Heterogeneity in both the characterization protocols and the reported figures of merit has made it difficult to interpret and compare results between independent studies. The reference works from Warner *et al.*[9] (2022) and Lunt *et al.*[8,10] (2019), plus a consensus statement signed by all prominent researchers in the field[3] (2022), translated and adapted the definitions and concepts used in classic photovoltaics to the LSC technology, providing a set of good-practice recommendations to follow for publishing any LSC study. The following discussion highlights the requirements for an accurate device reporting and how, in this work, the necessary experimental setups were built in compliance with the guidelines.

An LSC electrical device is obtained when the waveguide is coupled to PV cells along its collection area (the edges), to harvest the emitted and concentrated light. From here on, the term "LSC" will refer to the bare luminescent waveguide, while "LSC-PV" will be used to address the same when coupled with the photovoltaic components.

Primary electrical parameters to report for an LSC-PV are its Power Conversion Efficiency (PCE) and External Quantum Efficiency (EQE). Both definitions are borrowed from the field of photovoltaics, to provide consistency of terminology and physical meaning. PCE is the electrical efficiency of the device, as the ratio of the output electrical power (P_{out}) to the received incident optical power (P_{in}), both expressed in Watt units.

$$PCE = \frac{P_{out}}{P_{in}} = \frac{I_{SC}\, V_{OC}\, FF}{A_{in}\, P_0} \qquad \textbf{Eq. 3.10}$$

For a generic photovoltaic device, the PCE is derived experimentally by measuring its current-voltage (I-V) characteristic. This is performed by applying a linear voltage sweep to the PV, while registering its output current, by means of a Source Meter Unit (SMU). From the I-V curve, the power-voltage (P-V) curve can be derived by applying Ohm's law: $P = I \times V$. The typical I-V and P-V shapes of an illuminated PV device are shown in **Fig. 3.6**. The notable points used for PCE calculation are the short-circuit current I_{SC} (Amperes, A), the open-circuit voltage V_{OC} (Volts, V) and the fill factor FF, defined as the ratio of the maximum output power to the product of I_{SC} and V_{OC}.

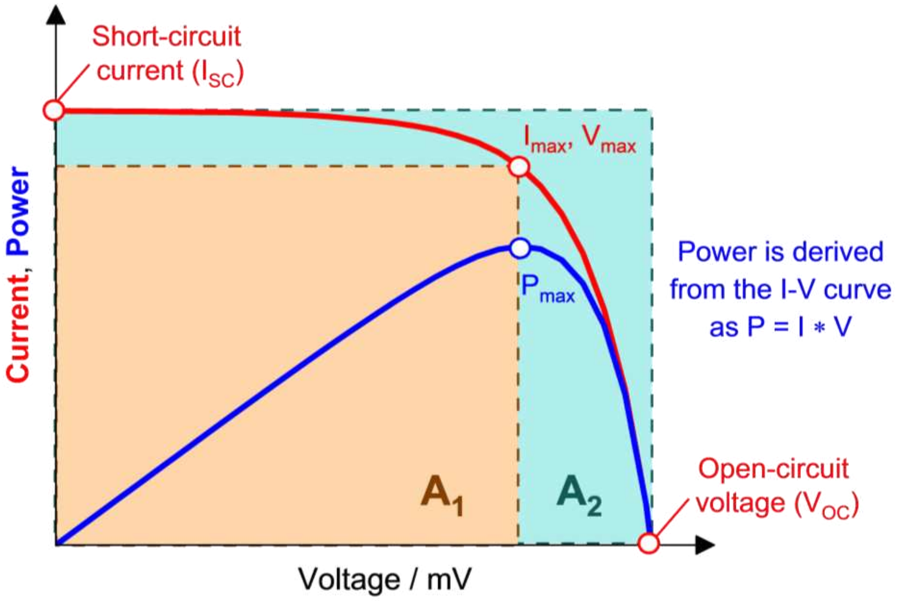

Figure 3.6. Typical current-voltage and power-voltage curves of a generic PV device under illumination. Relevant parameters for PCE calculation are highlighted.

By normalizing the I-V curve to the device illuminated area, the same plot is obtained, expressed in current-density versus voltage (J-V). The term I_{SC}/A_{in} in **Eq. 3.10** can be then rewritten as the short-circuit current density J_{SC} (A cm^{-2}). In LSC early literature, one widely discussed issue was the choice of the area to use for the current density calculation. It has been established that the aperture area of the LSC A_{in} (**Eq. 3.1**) should be used to normalize the I_{SC}, as it is the region of the LSC-PV receiving direct solar irradiation. If the smaller edge area A_{out} (**Eq. 3.1**) is chosen, both J_{SC} and PCE values will be overestimated, even exceeding the device's thermodynamic limits.[9] J-V measurements should be performed by exposing the LSC-PV to standard solar irradiation. This means using the AM1.5G illumination profile and optical power density (P_0 = 1 sun = 1000 W m^{-2} = 100 mW cm^{-2}). In laboratory settings, the AM1.5G spectrum can be efficiently reproduced by using a solar simulator. Solar simulators usually equip Xe or halogen lamps, which provide emission spectra very similar to the sun's. An AM1.5G filter is incorporated to better match the lamp's emission profile to the standard one. LED-based solar simulators have also been proposed as a reliable alternative, thanks to their low cost, compactness, lower power consumption and fast switch on/off.[16] In this work, a custom solar simulator has been built by assembling a Xe arc lamp with an AM1.5G filter and regulating the lamp intensity to achieve an average 1 sun irradiation over a 25 cm^2 area. The mapping of the illuminated area has been performed both with a calibrated power meter and with a c-Si solar cell analogous to the ones used for LSC-PV edge-coupling, observing good agreement between the two sensors.

Another issue of early LSC works was the heterogeneity in the materials used to cover the uncoupled LSC edges and the backdrop. A frequently used configuration for J-V collection is to couple just one edge of the waveguide to PV cells, to simplify electrical wiring. In the case of a square planar LSC-PV, the overall PCE can be obtained by multiplying to a factor of four the single-edge PCE.[8] This has been extensively verified and is valid only if certain precautions are respected. First, the backdrop of the LSC-PV should be lined with a matte black material, to prevent stray light from environmental reflections from entering the waveguide. Second, the uncoupled edges should be blackened as well, to suppress internal waveguide reflections. Finally, excess PV material, exceeding the edge area due to occasional size mismatch, should be completely shielded to avoid direct illumination from the simulator and consequently LSC-PV output overestimation. Correct electrical measurements should allow only the emitted light to reach the edge-coupled PV cells. When all these conditions apply, the four-edge output corresponds to four times the single-edge output, and the global performance of the device is reliably estimated. The use of back and edge reflectors,[17,18] although boosting the device's performance, is not recommended for a first-time LSC-PV reporting. The J-V setup herein developed for LSC-PV characterization is shown in **Fig. 3.7** and complies to said guidelines. Since the used

PV cells (7 mm high) were larger than the LSCs edges (3 mm high), a tailored cell holder was designed to leave a 3 mm aperture to lodge the LSC and efficiently shield the rest of the PV area from the simulator and ambient light. All J-V curves later reported are relative to 50 × 50 mm^2 samples, coupled with two monocrystalline Si cells along one edge (PV cell dimensions: 22 × 7 × 2 mm^3).

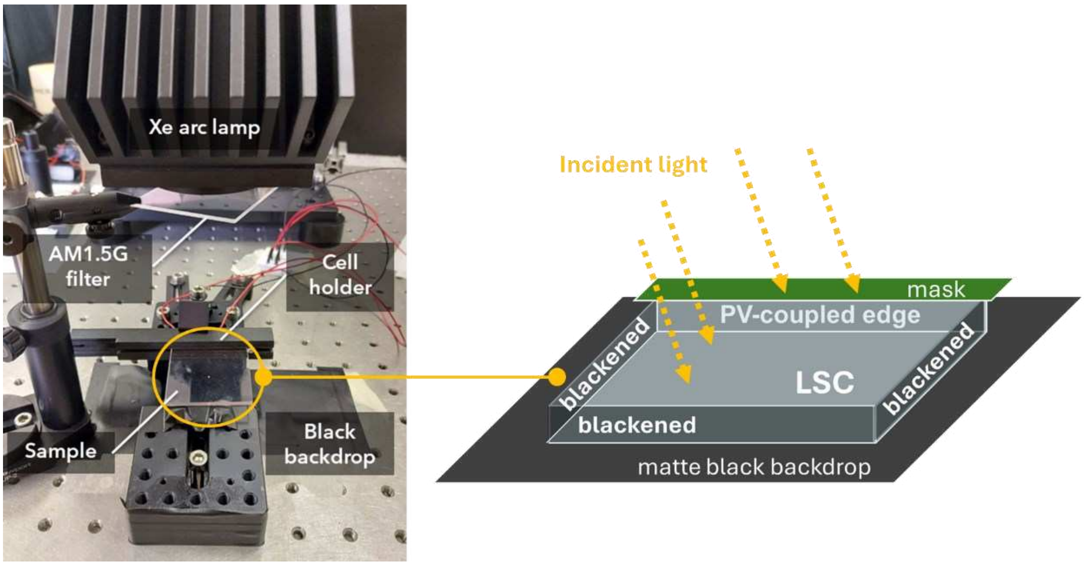

Figure 3.7. Experimental setup developed for the J-V characterization of LSCs. The cell holder prevents any stray or incident light from reaching the PV cells.

Moving to the EQE, this quantity evaluates the ability of a photovoltaic device to convert incident photons into charge carriers, and is proportional to the ratio between the produced electrical current (I_{SC}) and the incident electrical power (P_{in}), also known as the responsivity (R), at each given wavelength:

$$EQE = \frac{1240}{\lambda}\frac{I_{SC}}{P_{in}} = \frac{1240}{\lambda}R \qquad \text{at any } \lambda \qquad \textbf{Eq. 3.11}$$

The EQE is typically measured by shining monochromatic light over the whole PV device and collecting the current output at each wavelength to yield a spectral response curve (*i.e.*, the responsivity spectrum). A white light bias is also applied to simulate the device's real working conditions.[19] For LSC-PVs, the beam size is reduced to a focused spot, that is scanned over the waveguide's active area. The standard procedure would need all four edges to be PV coupled, and to perform multiple scans placing the illumination spot in several symmetrical positions over the LSC.[8] Due to complicated electrical wiring, LSC-PV electrical characterizations are often performed with only one edge coupled to the cells. To acquire the EQE in such configuration, the illumination spot is positioned at different distances from the PV-coupled edge along the centerline (**Fig. 3.8**). The other three uncoupled edges should be blackened and a matte black backdrop should be used also in this case. Exceeding PV area should be adequately masked as well.

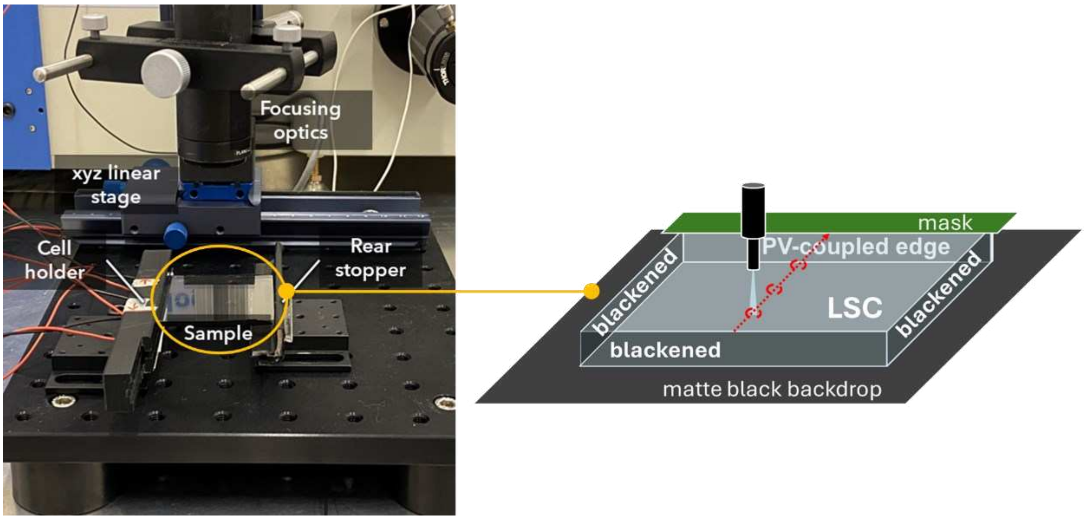

Figure 3.8. Experimental setup developed for EQE characterization of LSCs. The cell holder prevents any stray or incident light from reaching the PV cells.

The raw EQE spectra are then corrected for a geometrical factor (g) to simulate the four-edge configuration. The position-dependent, corrected spectra are ultimately averaged to yield the global LSC-PV EQE. The g factor accounts for geometrical correction only along the centerline and is calculated as:

$$g = \frac{\pi}{tan^{-1}\left(\frac{L}{2d}\right)} \qquad \textbf{Eq. 3.12}$$

where L is the length of the PV-coupled edge, and d is the distance between the edge and the illumination spot. For LSC-PVs, **Eq. 3.11** becomes:

$$EQE_{LSC-PV} = g \cdot \frac{1240}{\lambda} R \qquad at\ any\ \lambda \qquad \textbf{Eq. 3.13}$$

Fig. 3.8 shows the experimental setup herein developed for EQE acquisitions. Similarly to the J-V setup, measurements were performed in one-edge configuration, using the same PV cell holder design. Monochromatic illumination was achieved by using the Xe arc lamp and excitation monochromator of a research-grade spectrofluorometer, coupled with an optical fibre and focusing optics to direct the excitation beam onto the LSC's active area.

The whole illuminator element was mounted on a XYZ stage, allowing precise movement of the excitation beam over the LSC and highly reproducible alignment, especially important along the Z axis. Minimum steps along the directions of the stage were 1 mm for X and Y, and 0.25 mm for Z. The incident optical power and the output short-circuit current spectra were acquired connecting the power meter and the PV cells, respectively, to a SMU synchronized with the excitation monochromator.

The EQE spectrum provides with two important consistency checks for LSC-PV devices. The first is borrowed as well from the field of photovoltaics and consists in comparing the integrated J_{SC} to the experimental one derived from the J-V curve. The integrated J_{SC} is the short-circuit current density that is obtained by integrating the EQE spectrum over the AM.1.5G spectrum as follows:

$$J_{SC,int} = e \cdot \int_S EQE(\lambda)\ \Phi_{ph}^{AM1.5G}(\lambda)\, d\lambda \qquad \textbf{Eq. 3.14}$$

where e is the elementary charge (Coulomb, C) and $\Phi_{ph}^{AM1.5G}(\lambda)$ is the AM1.5G photon flux. This is the most important consistency check for any photovoltaic device and should be provided in any LSC study. For LSC-PVs specifically, discrepancies between the experimental and integrated short-circuit current densities are symptomatic of direct PV cell illumination and/or inaccurate calibration of the simulated solar irradiation intensity. The stated tolerance for this check is a 20% mismatch between the experimental and integrated values.[3] The second consistency check is derived from the photon balance (**Eq. 3.3**). Since the EQE quantifies how many of the photons incident on the LSC-PV generate a charge carrier pair, its value can at best match that of absorptance, at any wavelength. Given $EQE \leq \alpha$ at any wavelength, independent measurements of EQE, transmittance and reflectance should always satisfy the condition $EQE + \tau + \rho \leq 1$.

Finally, the internal photon efficiency (η_{int}) of an LSC-PV, defined as the ratio of the edge-emitted photons (n_{out}) to the absorbed photons (n_{abs}), should be provided to assess waveguide internal losses such as reabsorption, $PLQY$ and scattering. Although the number of absorbed and emitted photons can be quantified through optical methods, this usually implies a complicated measurement procedure and a dedicated experimental setup. Alternatively, η_{int} can be derived from already discussed electrical and optical parameters through a verified method:[20]

$$\eta_{int} = \frac{n_{out}}{n_{abs}} = \frac{1}{G\,\eta_{s,abs}} \frac{I_{LSC-PV}}{I_{PV}} \frac{\langle Q_s \rangle}{\langle Q_{PL} \rangle} \qquad \textbf{Eq. 3.15}$$

where I_{LSC-PV} and I_{PV} are the short-circuit currents of the LSC-PV and of the bare PV cell, respectively. G (**Eq. 3.1**) and $\eta_{s,abs}$ (**Eq. 3.5**) are the geometric gain and the total solar absorptance, respectively, both previously defined in *Section 3.1*. The terms $\langle Q_s \rangle$ and $\langle Q_{PL} \rangle$ are obtained by averaging the EQE of the bare PV cell over the AM1.5G spectrum and over the luminophore emission spectrum, respectively.

3.4 Summary of key LSC metrics

Table 3.1 offers an overview of all the figures of merit recommended for LSC reporting, as stated in the referenced guidelines.

Table 3.1 List of LSC figures of merit recommended for reporting and related quantities.

Property	Related parameters
Device structure	Length, width, thickness, geometric gain (G), PV cell type, edges (PV-coupled, reflectors, blackened)
Luminophore / lightguide	Molar brightness (explicating ε and $PLQY$), emission spectra, absorptance (α)
Visual impact	AVT, CRI and $CIELAB$ coordinates
Power Conversion Efficiency (PCE)	Including J-V characteristic and device active area (A_{in})
External Quantum Efficiency (EQE)	Including consistency checks
Internal photon efficiency (η_{int})	Can be derived from electrical parameters

Furthermore, during this work, all relevant calculations for extracting LSC and LSC-PV performance metrics (excluding aesthetic quality parameters) have been collected in a comprehensive Matlab Live Script (available at: https://it.mathworks.com/matlabcentral/fileexchange/166426-luminescent-solar-concentrators-pv-characterization). Experimental input data can be directly uploaded into the script to perform necessary elaboration and obtain the output parameters.

3.5 Bibliography

1 V. I. Klimov, T. A. Baker, J. Lim, K. A. Velizhanin and H. McDaniel, *ACS Photonics*, 2016, **3**, 1138–1148.

2 M. G. Debije, R. C. Evans and G. Griffini, *Energy Environ. Sci.*, 2021, **14**, 293–301.

3 C. Yang, H. A. Atwater, M. A. Baldo, D. Baran, C. J. Barile, M. C. Barr, M. Bates, M. G. Bawendi, M. R. Bergren, B. Borhan, C. J. Brabec, S. Brovelli, V. Bulović, P. Ceroni, M. G. Debije, J.-M. Delgado-Sanchez, W.-J. Dong, P. M. Duxbury, R. C. Evans, S. R. Forrest, D. R. Gamelin, N. C. Giebink, X. Gong, G. Griffini, F. Guo, C. K. Herrera, A. W. Y. Ho-Baillie, R. J. Holmes, S.-K. Hong, T. Kirchartz, B. G. Levine, H. Li, Y. Li, D. Liu, M. A. Loi, C. K. Luscombe, N. S. Makarov, F. Mateen, R. Mazzaro, H. McDaniel, M. D. McGehee, F. Meinardi, A. Menéndez-Velázquez, J. Min, D. B. Mitzi, M. Moemeni, J. H. Moon, A. Nattestad, M. K. Nazeeruddin, A. F. Nogueira, U. W. Paetzold, D. L. Patrick, A. Pucci, B. P. Rand, E. Reichmanis, B. S. Richards, J. Roncali, F. Rosei, T. W. Schmidt, F. So, C.-C. Tu, A. Vahdani, W. G. J. H. M. van Sark, R. Verduzco, A. Vomiero, W. W. H. Wong, K. Wu, H.-L. Yip, X. Zhang, H. Zhao and R. R. Lunt, *Joule*, 2022, **6**, 8–15.

4 T. I. U. of P. and A. Chemistry (IUPAC), IUPAC - absorbance (A00028), https://goldbook.iupac.org/terms/view/A00028, (accessed 31 July 2025).

5 T. I. U. of P. and A. Chemistry (IUPAC), IUPAC - Beer–Lambert law (B00626), https://goldbook.iupac.org/terms/view/B00626, (accessed 31 July 2025).

6 K.-L. Wong, J.-C. G. Bünzli and P. A. Tanner, *J. Lumin.*, 2020, **224**, 117256.

7 L. R. Wilson and B. S. Richards, *Appl. Opt.*, 2009, **48**, 212–220.

8 C. Yang, D. Liu and R. R. Lunt, *Joule*, 2019, **3**, 2871–2876.

9 T. Warner, K. P. Ghiggino and G. Rosengarten, *Sol. Energy*, 2022, **246**, 119–140.

10 C. Yang, D. Liu, M. Bates, M. C. Barr and R. R. Lunt, *Joule*, 2019, **3**, 1803–1809.

11 CIE TC 2-93, ISO/CIE 23539, https://cie.co.at/publications/photometry-cie-system-physical-photometry-3, (accessed 26 September 2025).

12 Method of measuring and specifying colour rendering properties of light sources | CIE, https://cie.co.at/publications/method-measuring-and-specifying-colour-rendering-properties-light-sources, (accessed 1 August 2025).

13 Cambridge University Press, 1931.

14 V. Cheung, in *Handbook of Visual Display Technology*, Springer, Cham, 2016, pp. 187–196.

15 C. Yang, M. C. Barr and R. R. Lunt, *Phys. Rev. Appl.*, 2022, **17**, 034054.

16 V. Esen, Ş. Sağlam and B. Oral, *Renew. Sustain. Energy Rev.*, 2017, **77**, 1240–1250.

17 G. Iasilli, R. Francischello, P. Lova, S. Silvano, A. Surace, G. Pesce, M. Alloisio, M. Patrini, M. Shimizu, D. Comoretto and A. Pucci, *Mater. Chem. Front.*, 2019, **3**, 429–436.

18 Y. Liu, N. Li, R. Sun, W. Zheng, T. Liu, H. Li, Y. Chen, G. Liu, H. Zhao, H. Liu and Y. Zhang, *Nano Energy*, 2021, **85**, 105960.

19 W. Ananda, in *2017 15th International Conference on Quality in Research (QiR) : International Symposium on Electrical and Computer Engineering*, 2017, pp. 450–456.

20 H. Li, K. Wu, J. Lim, H.-J. Song and V. I. Klimov, *Nat. Energy*, 2016, **1**, 16157.

Chapter 4

Towards aesthetically compliant Eu^{3+} photovoltaic windows

In this *Chapter*, a study on Eu^{3+}-based bulk-doped LSCs is reported. The discussion opens with the synthesis of UV absorbing, super-bright $[Eu_2L_4]^{2-}$ cages bearing bis-β-diketonate ligands and their subsequent embedding in PMMA by casting of 50 × 50 × 2.7 cm^3 planar LSCs. A close-related mononuclear Eu^{3+} complex has been taken as reference compound during the experimental investigation. Spectroscopic characterisations of the luminophores have been conducted before and after embedment in the polymeric matrix, to evaluate weather materials processing affected the integrity of the emitters. Aesthetic quality parameters (AVT, CRI, $CIELAB$ coordinates) have been analysed in respect to the window glass industry requirements. Finally, the electrical performance of the LSC-PV devices obtained by edge-coupling the waveguides with monocrystalline Si solar cells has been characterized. A perspective on the literature regarding Eu^{3+}-based concentrators is also offered, with the aim to compare the results of the present study with the relevant state of the art.
The contents of this *Chapter* are based on a recently published research[1] by authors Motta I., Bottaro G., Rando M., Rancan M., Seraglia R. and Armelao L., in Journal of Materials Chemistry A (2024, 12, 22516–22527), reproduced with permission.

4.1 Luminophores

The LSCs herein described have been developed based on a series of supramolecular, binuclear europium bis-β-diketonates with general formula $[\mathrm{Eu_2L_4}]^{2-}$ ($L = L^A, L^B, L^M, L^F$) and structure depicted in **Fig. 4.1a**. For comparative analysis, the mononuclear complex Eu(tta)$_3$phen (tta = thenoyltrifluoroacetone, phen = 1,10-phenanthroline, **Fig. 4.1b**) was also included as a reference luminophore, given its established use for lanthanide-based LSCs.[2,3] The ligands L^A, L^B and L^M differ for the molecular scaffold spacing the two benzoyltrifluoroacetone (btfa) groups, which are the moieties responsible for sensitizing the Eu^{3+} emission. L^F is a modified version of L^A, incorporating an additional $-CF_2-$ unit within its fluorinated terminal chains to ultimately enhance cage solubility. The synthesis of L^B and L^M involved a Friedel-Crafts acylation followed by a Claisen condensation, while L^A and L^F were prepared via a Cu(I) catalysed N-C coupling reaction, also followed by a Claisen condensation. The self-assembly of these quadruple-stranded cages occurs upon deprotonation of the ligands with tetraethylammonium hydroxide (TEAOH) and subsequent addition of an Eu^{3+} inorganic salt (detailed procedures are provided in *Chapter 9: Experimental*).

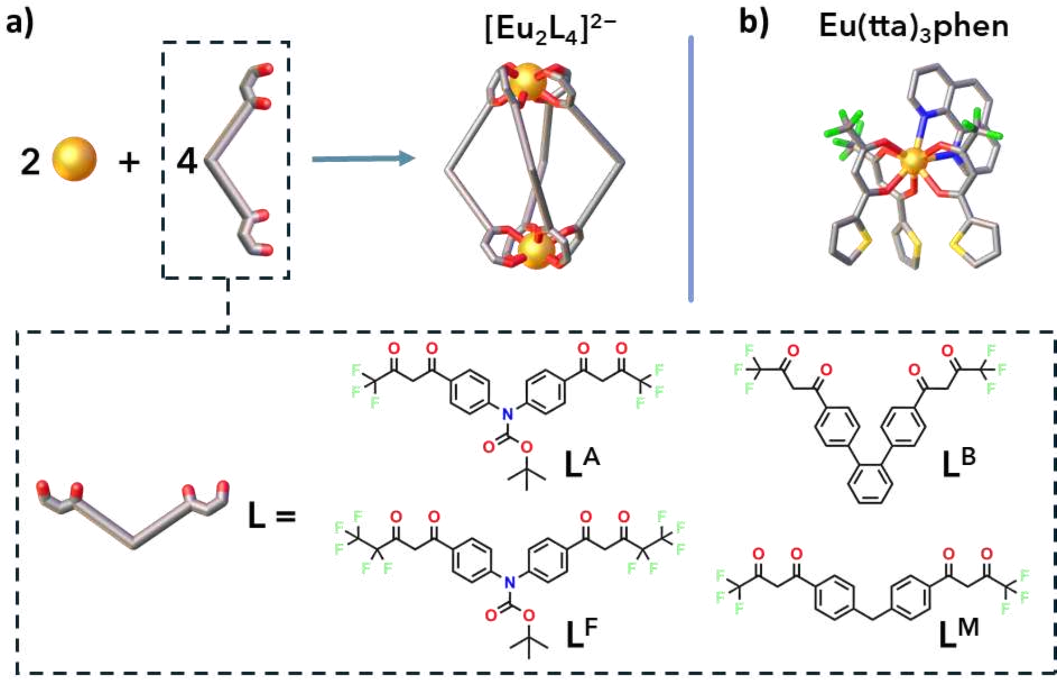

Figure 4.1. a) Self-assembly of the $[\mathrm{Eu_2L_4}]^{2-}$ cages and molecular structures of the employed ligands. **b)** Structure of the Eu(tta)$_3$phen complex.

The comprehensive characterization of L^A, L^B and L^M and their corresponding Ln cages, along with the self-assembly pathway of the metallo-supramolecular structures, has been reported elsewhere.[4–6] The following discussion will primarily focus on the newly synthesized ligand L^F and its Eu^{3+} complex. Successful ligand synthesis and correct structural formation were confirmed by ^{1}H-NMR spectroscopy (**Fig. 4.2a**), single-crystal XRD analysis (*Appendix C1.1*) and ESI-MS spectrometry (*Appendix C1.2*).

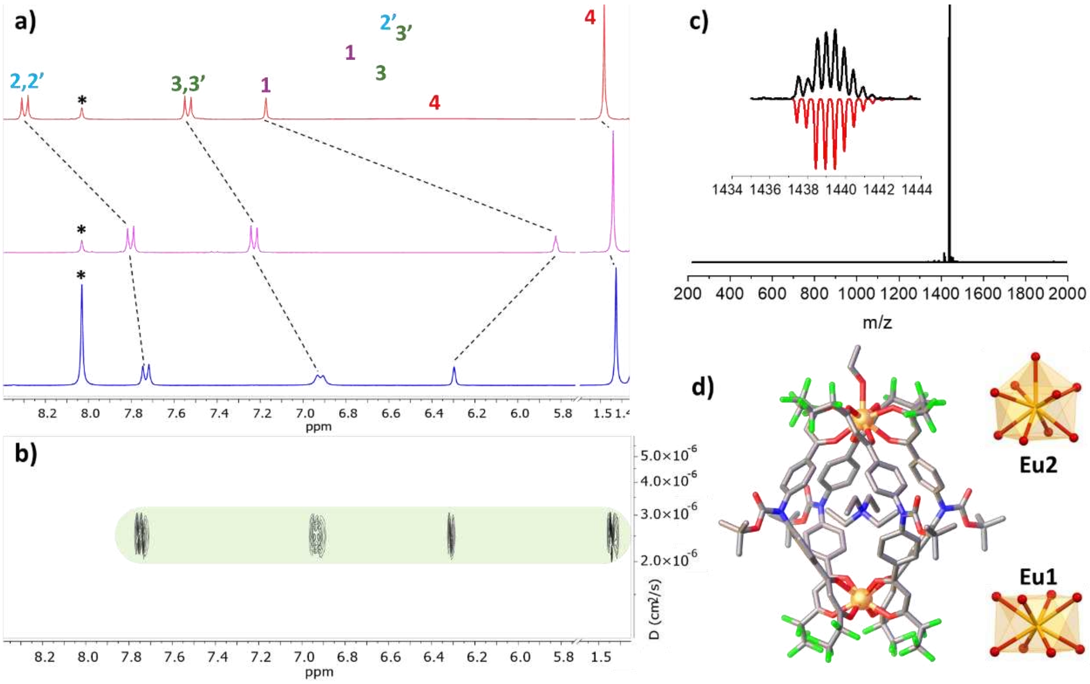

Figure 4.2. a) ^{1}H-NMR spectra (25 °C, 300 MHz, DMF-d_7) of ligand H_2L^F, deprotonated ligand $L^{F\,2-}$ and the cage $[La_2L^F_4]^{2-}$ (* = DMF). **b)** DOSY of $[La_2L^F_4]^{2-}$. **c)** ESI-MS spectrum of the $\{[Eu_2L^F_4])(NEt_4)_2\}$ cage. Inset: experimental (black) and simulated (red) isotopic patterns. **d)** Crystal structure of the $\{[Eu_2L^F_4])(NEt_4)_2\}$ cage (helicate M, ΛΛ form) and coordination polyhedra for Eu1 and Eu2. H atoms and the external NEt_4^+ cation were omitted for clarity. Colour code: C, grey; O, red; N, blue; F, green; Eu, orange; La, yellow.

The formation of the cage was monitored and confirmed through ^{1}H-NMR spectroscopy. As shown in **Fig. 4.2a**, the spectra of the ligand (H_2L^F, $L^{F\,2-}$) and of the cage analogue $[La_2L^F_4]^{2-}$ reveal significant upfield shifts for all ligand signals upon deprotonation. The most notable effect is observed for proton H1, located in the α position of the β-diketonate moiety. Following La^{3+} ion coordination, the cage exhibits a single set of signals, consistent with the ligand's C_2 symmetry and the average C_4 symmetry of the quadruple-stranded $[La_2L^F_4]^{2-}$ architecture. To obtain dimensional information and confirm the cage integrity in solution, Diffusion-Ordered NMR Spectroscopy (DOSY) was conducted (**Fig. 4.2b**), yielding a calculated hydrodynamic diameter of 22.2 Å for $[La_2L^F{}_4]^{2-}$. The Eu^{3+} cage displayed a remarkably clean ESI-MS spectrum, with a single signal corresponding to the $[Eu_2L^F{}_4]^{2-}$ double-negative charged species (**Fig. 4.2c**). The crystal structure of the newly synthesized $\{[Eu_2L^F{}_4](NEt_4)_2\}$ was determined by single-crystal X-ray diffraction (**Fig. 4.2d**). The H···H distances between the tert-butyl groups of opposing ligands ranged from 21.3 to 22.8 Å. This measurement well aligns with the hydrodynamic diameter of 22.2 Å calculated from the DOSY experiment for the La^{3+} cage. Consistent with previous observations for the $[Eu_2L^M{}_4]^{2-}$, $[Eu_2L^B{}_4]^{2-}$[4] and $[Eu_2L^A{}_4]^{2-}$[5] cages, one of the two tetraethylammonium cations is hosted within the quadruple-stranded cage. In this kind of quadruple-stranded Ln^{3+} cages, the ligand scaffold and guest molecule can influence the formation of either helicates or mesocates.[7] The $[Eu_2L^F{}_4]^{2-}$ cage forms a helicate, with both right-handed (*P*, ΔΔ) and left-handed (*M*, ΛΛ) isomers present in a 1:1 ratio within the unit cell.

Finally, the crystal structure revealed that the two Eu centres possess different coordination numbers. Both ions are tetrakis-chelated by four beta-diketonate groups, but Eu2 has the ninth coordination site further occupied by an ethanol molecule. Previous studies[5] have shown that solvent molecules like water and ethanol are loosely bound to the Ln^{3+} ion and can be present or absent depending on experimental conditions. Stereochemical analysis using continuous shape measures (*Appendix C1.1*)[8] assessed that the eight-coordinated centre exhibits a square antiprismatic coordination geometry, while the nine-coordinated ion displays a capped square antiprismatic coordination geometry.

The synthesis of $Eu(tta)_3phen$ involved a first deprotonation of tta using NaOH, followed by Eu^{3+} salt addition to the mixture of phen and deprotonated tta. The target product was achieved by employing a metal:tta:NaOH:phen molar ratio of 1:3:3:1. ESI-MS (*Appendix C1.2*) confirmed the nature of the synthesised product.

Once obtained all the luminophores, their photophysical behaviour was analysed in methyl methacrylate solution, since this is the only reaction solvent involved in the bulk-polymerization to cast PMMA tiles. UV/Vis absorption and photoluminescence spectra (**Fig. 4.3a**) confirmed that the antenna effect effectively sensitizes the europium emission. The β-diketonate ligands absorb light exclusively in the 300 – 380 nm range, leading to ligand-centered excitation. The only PL profile observed is that originating from the Eu^{3+} ion. The Eu^{3+} PL spectrum shows five distinct peaks, corresponding to transitions from the $^5D_0$ excited state to the ^7F_J ground state (where J = 0, 1, 2, 3, and 4). The prominent $^5D_0 \rightarrow {}^7F_2$ hypersensitive transition at 612 nm dominates the emission spectrum of Eu^{3+} β-diketone complexes and is responsible for their characteristic red luminescence.[9,10] There is no overlap between the absorption and emission spectra, resulting in a pseudo-Stokes shift of approximately 200 nm.

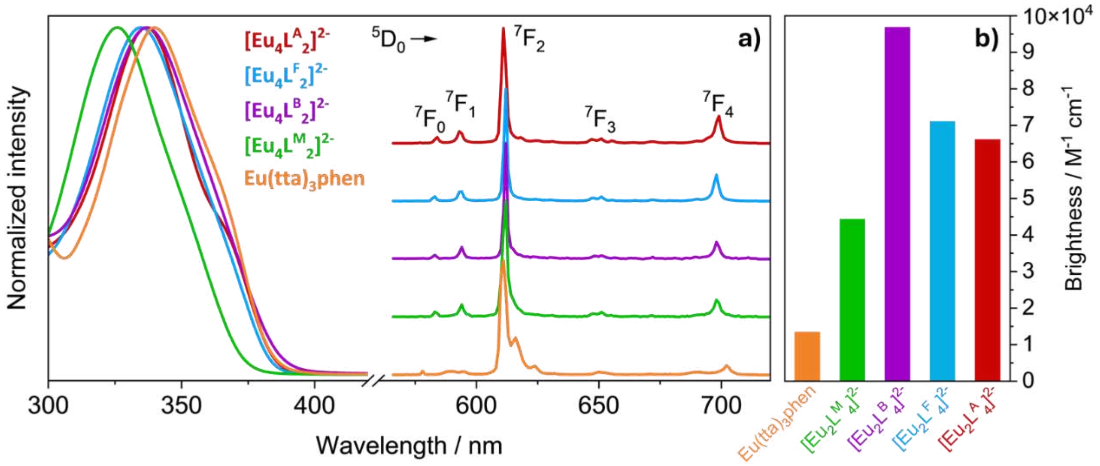

Figure 4.3. a) Normalized absorption and emission spectra of $1 \cdot 10^{-5}$ M solutions of the luminophores in MMA. **b)** Histogram displaying the brightness at λ_{max} of the investigated luminophores in MMA solutions. Color code: orange, $Eu(tta)_3phen$; green, $[Eu_2L^M{}_4]^{2-}$; purple, $[Eu_2L^B{}_4]^{2-}$; light blue, $[Eu_2L^F{}_4]^{2-}$; red, $[Eu_2L^A{}_4]^{2-}$.

As evidenced in *Chapter 3*, the molar brightness is a useful parameter to assess the viability of different luminophores for LSC development. Since the luminophores here discussed display similar absorption and emission spectra, comparing the brightness values relative to the absorption maximum is sufficient (**Fig. 4.3b** and **Table 4.1**).

In MMA solutions, $[Eu_2L^B{}_4]^{2-}$ emerged as the brightest complex in the family, with a B value of 96880 M^{-1} cm^{-1}. Cages $[Eu_2L^A{}_4]^{2-}$ and $[Eu_2L^F{}_4]^{2-}$ follow, both with B values around 70000 M^{-1} cm^{-1}, and then $[Eu_2L^M{}_4]^{2-}$ with B close to 45000 M^{-1} cm^{-1}. Notably, the binuclear lanthanide bis-β-diketonates $[Eu_2L_4]^{2-}$ (where L = L^A, L^B, L^M) showed a brightness approximately an order of magnitude higher than $Eu(tta)_3phen$ (13500 M^{-1} cm^{-1}). Based on these brightness values in MMA solutions, $[Eu_2L^B{}_4]^{2-}$ appeared to be the most promising candidate for LSC development. However, photophysical performance in solution is not sufficient to discriminate among luminophores.

Table 4.1. Molar extinction coefficient (ε_{max}), photoluminescence quantum yield ($PLQY$) and molar brightness (B) values collected for $1{\cdot}10^{-5}$ M solutions of the luminophores in MMA. Maximum solubility achieved for the luminophores in MMA. The values of $PLQY$ and absorption coefficients relative to the luminophores embedded in PMMA are reported in parentheses.

Luminophore	$\varepsilon_{max} \times 10^5$ / M^{-1} cm^{-1}	$PLQY$	B / M^{-1} cm^{-1}	**Solubility in MMA / mM**
$[Eu_2L^{A}{}_4]^{2-}$	1.61 (1.65)	0.41 (0.39)	66 010	0.0184
$[Eu_2L^{F}{}_4]^{2-}$	1.42 (1.43)	0.50 (0.53)	71 000	0.321
$[Eu_2L^{B}{}_4]^{2-}$	1.73 (–[a])	0.56 (–[a])	96 880	0.0195
$[Eu_2L^{M}{}_4]^{2-}$	1.01 (–[a])	0.48 (–[a])	48 480	0.0216
Eu(tta)$_3$phen	0.50 (0.53)	0.27 (0.25)	13 500	5.02

Material processing, and in particular solubility of the emitters in the solvents relevant to experimental procedures, is equally important to evaluate the suitability of a luminophore for the LSC application. The solubility of Eu(tta)$_3$phen in MMA was approximately two orders of magnitude greater than that of $[Eu_2L^{A}{}_4]^{2-}$, $[Eu_2L^{B}{}_4]^{2-}$, and $[Eu_2L^{M}{}_4]^{2-}$ (**Table 4.1**). To address this, the L^F ligand was appositely synthetized by slightly modifying L^A to increase the corresponding cage's solubility in MMA, ultimately achieving a twenty-fold improvement. Additionally, before synthesizing and characterizing the materials, the compatibility of the luminophores with the PVC gasket used as lateral walls in the PMMA casting mould was investigated. Gasket strips (approximately 10 × 30 × 3 mm^3) were immersed in MMA solutions of the luminophores at the same concentrations used for LSC castings. After approximately 20 hours (the longest polymerization time used), the PVC pieces were removed, dried, and observed under a 365 nm UV lamp to detect any residual cage presence. The PVC strip immersed in the $[Eu_2L^{B}{}_4]^{2-}$ solution exhibited noticeably brighter luminescence compared to the others, suggesting a strong affinity between $[Eu_2L^{B}{}_4]^{2-}$ and PVC. This indicated a potential issue during material synthesis. Noticeably, $[Eu_2L^{F}{}_4]^{2-}$ showed no detectable interaction with the PVC gasket.

---

[a] $PLQY$ and ε_{max} were not measured for these samples in the polymeric matrices because $[Eu_2L^{B}{}_4]^{2-}$ and $[Eu_2L^{M}{}_4]^{2-}$ give rise to issues during material synthesis and were not employed to develop LSC devices (for details see *Section 4.2*).

4.2 Materials

All luminophores have been incorporated into PMMA through the batch-cell casting procedure described in *Chapter 2*, to prepare square planar LSC tiles with active area of 50 × 50 mm^2 and thickness of 2.7 mm (geometric gain G = 4.63). The amount of luminophores available for casting was directly tied to their solubility in MMA, which varied significantly among the studied complexes (**Table 4.1**). Eu(tta)$_3$phen and [Eu$_2$L$^F{}_4$]$^{2-}$, displaying the highest solubilities in the reaction solvent, achieved luminophore loadings in PMMA of 0.5% and 0.1% by weight, respectively. In contrast, the other cages ([Eu$_2$L$^A{}_4$]$^{2-}$, [Eu$_2$L$^B{}_4$]$^{2-}$, and [Eu$_2$L$^M{}_4$]$^{2-}$) had solubilities and maximum luminophore loadings that were two orders of magnitude lower. To obtain a series of samples doped at the same concentration, five LSCs were prepared using each luminophore at the 0.005% by weight. Additionally, an LSC for both Eu(tta)$_3$phen and [Eu$_2$L$^F{}_4$]$^{2-}$ at their respective upper loading limit was prepared. An undoped PMMA tile was also included as a reference blank sample. The specific labelling for each prepared LSC, and the derived LSC-PV devices, is listed in **Table 4.2**.

Table 4.2. Labelling of the prepared LSCs and of the corresponding devices obtained by edge-coupling monocrystalline Si solar cell to the LSCs.

LSC	LSC-PV	Luminophore	Loading / wt %
LSC-Fc	**LSC-Fc^{PV}**	[Eu$_2$L$^F{}_4$]$^{2-}$	0.1
LSC-Tc	**LSC-Tc^{PV}**	Eu(tta)$_3$phen	0.5
LSC-A	**LSC-A^{PV}**	[Eu$_2$L$^A{}_4$]$^{2-}$	0.005
LSC-B	**-**	[Eu$_2$L$^B{}_4$]$^{2-}$	
LSC-M	**-**	[Eu$_2$L$^M{}_4$]$^{2-}$	
LSC-F	**LSC-F^{PV}**	[Eu$_2$L$^F{}_4$]$^{2-}$	
LSC-T	**LSC-T^{PV}**	Eu(tta)$_3$phen	
PM	**PM^{PV}**	none	/

The absorption spectra of the luminophores within the PMMA matrix (**Fig. 4.4a**) closely matched the absorbance profiles previously obtained for the respective MMA solutions. When excited with UV light at λ = 365 nm, all LSCs exhibited bright red luminescence effectively concentrated on the edges (**Fig.s 4.4b** to **d**). The same light-guiding properties were already visible to the naked eye for all doped LSCs when exposed just to natural daylight (**Fig.s 4.4e** and **f**).

The Eu^{3+} emission spectrum is highly sensitive to the ion's coordination environment, and morphological changes in its coordination geometry can result in changes in the emission spectrum of the corresponding Eu^{3+} complex.[10] This characteristic served as a valuable qualitative tool to assess whether embedding the luminophores into the PMMA matrix caused any structural alterations. The PL profiles recorded for the LSCs (**Fig. 4.4a**) closely matched those obtained from the solutions for all Eu^{3+} complexes. This agreement indicates that neither the PMMA matrix nor the batch-cell casting procedure negatively impacted the structural integrity of the luminophores. Accordingly, absorption coefficients and $PLQY$s were fully consistent between solutions and PMMA tiles.

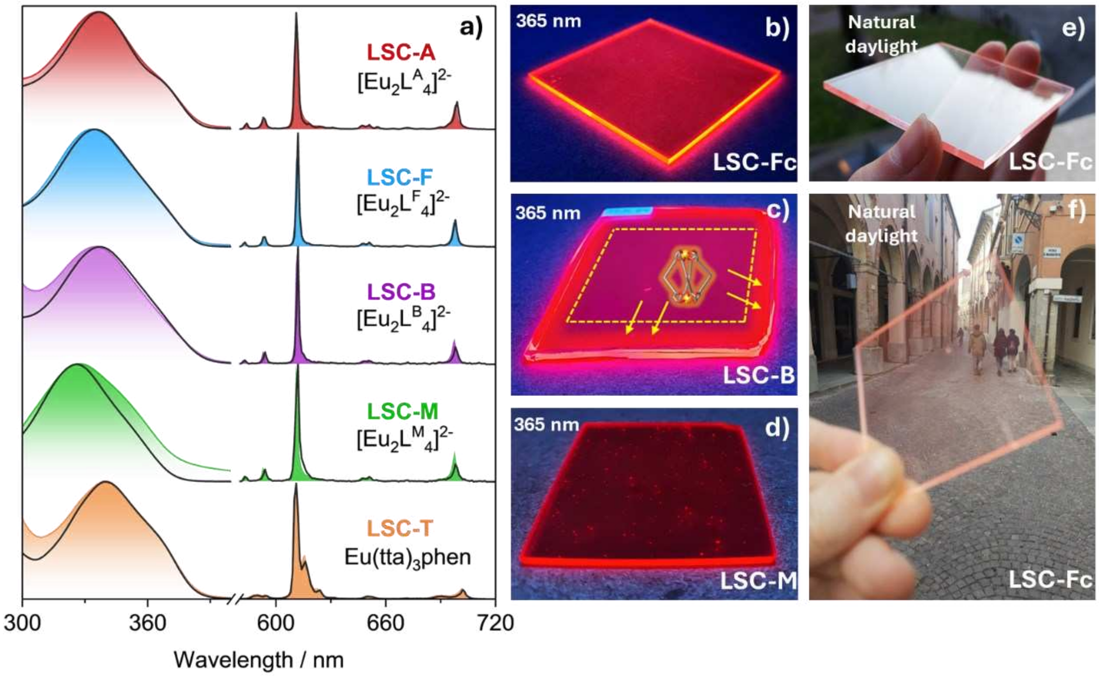

Figure 4.4. a) Normalized absorption and emission spectra of LSCs containing the different luminophores at 0.005% wt. (filled colours), superimposed to normalized absorption and emission spectra of the corresponding $1\cdot10^{-5}$ MMA solutions (black solid lines). **b) LSC-Fc**, **c) LSC-B** and **d) LSC-M** under 365 nm UV illumination. **e)**, **f) LSC-Fc** directly exposed to natural daylight.

While **LSC-A**, **LSC-F/Fc**, and **LSC-T/Tc** resulted homogeneous and defect-free, **LSC-B** exhibited luminophore segregation towards the tile's edges when observed under 365 nm excitation (**Fig. 4.4c**). This spatial redistribution was attributed to the luminophore's preferential absorption into the PVC gasket used to seal the casting mould. This led to a loss of control over the precise loading of $[Eu_2L^B{}_4]^{2-}$ into PMMA, a behaviour that was anticipated from the preliminary PVC tests. Furthermore, when illuminated with UV light, **LSC-M** displayed numerous bright spots randomly dispersed throughout the polymeric matrix (**Fig. 4.4d**). These spots were identified as precipitated $[Eu_2L^M{}_4]^{2-}$ aggregates, likely occurring during the polymerization process within the matrix. Due to such drawbacks, $[Eu_2L^B{}_4]^{2-}$ and $[Eu_2L^M{}_4]^{2-}$ were deemed unsuitable for the development of LSC tiles through MMA bulk-polymerization and were excluded from the initial pool of luminophores for the rest of the study. This is to emphasize that material processing can affect individual luminophores differently, even when their molecular structures differ only for minor variations. A significant finding was the substantial solubility increase achieved by introducing a $-CF_2-$ moiety into the terminal chain of the L^A ligand (**Fig. 4.1a**). Therefore, the suitability of an emitter for LSC applications should always be evaluated based both on its nominal photophysical properties and on its behaviour after embedment in the solid medium.

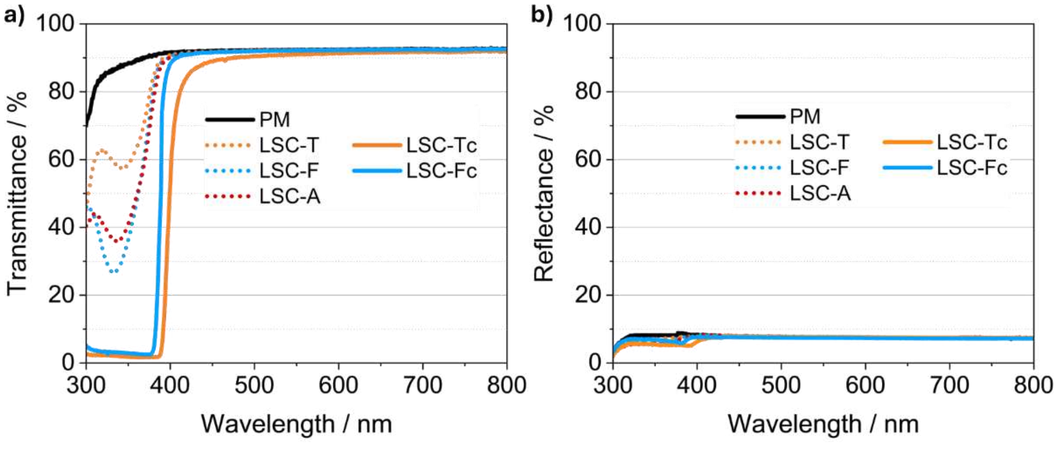

Figure 4.5. a) Transmittance and **b)** reflectance spectra recorded for the selected LSCs using an integrating sphere equipped with short pass filters (see *Section 3.1*).

Considering the selective absorption of UV photons, the prepared LSCs showed potential for the development of photovoltaic windows for seamless building integration. Their aesthetic quality was evaluated based on the key parameters described in *Chapter 3*: AVT, CRI and $CIELAB$ colour coordinates. For the determination of these metrics, AM1.5G, AM1.5G · $T\%$ and AM1.5G · $R\%$ were used as source spectra. **Fig. 4.5** reports the UV/Vis transmittance and reflectance spectra for LSCs doped with $[\mathrm{Eu_2L^A{}_4}]^{2-}$, $[\mathrm{Eu_2L^F{}_4}]^{2-}$, and $\mathrm{Eu(tta)_3phen}$, alongside those of undoped PMMA. The fabricated LSCs demonstrate the highest visible transparency, with AVT values approximately of 92% for all samples (**Table 4.3**). They also exhibit minimal visual impact on the transmitted and reflected light, with CRI values close to 100.

A recent survey on a wide inventory of commercially available and mass-market glass products has provided reference key levels for the aesthetic quality of transparent window products in the glazing industry.[11] Acceptable standards for window glass destined to colour neutral applications have been established as $CRI \geq 85$ and $CIELAB$ coordinates of $-7 < a^* < 0$ and $-3 < b^* < 7$. Not only the aesthetic characteristics of the $\mathrm{Eu^{3+}}$-based LSCs fall amply within the specified intervals, but also CRI values comprised between 95 and 100 denote a material with excellent colour and imaging fidelity. Notably, the entire series of doped LSCs shows CRI and $CIELAB$ coordinates comparable to plain PMMA, indicating that the presence of the luminophores does not alter the visible appearance or light-transmitting properties of the pristine material.

Table 4.3. Total solar absorptance ($\eta_{s,abs}$), average visible transmittance (AVT), color rendering index (CRI) and (a^*, b^*) $CIELAB$ coordinates calculated for the selected LSCs. Colour parameters are given both for transmittance and reflectance characterizations.

Sample	$\eta_{s,abs}$ %	AVT %	$T\%$			$R\%$		
			CRI	a^*	b^*	CRI	a^*	b^*
LSC-Fc	1.66	92.17	99.52	- 0.05	0.43	98.14	- 0.10	- 0.62
LSC-Tc	2.56	91.82	98.40	- 0.38	1.42	98.42	- 0.31	- 0.47
LSC-A	0.62	92.24	99.51	- 0.05	0.43	96.94	-0.11	- 1.08
LSC-F	0.57	92.27	99.53	- 0.05	0.41	97.22	-0.11	- 0.96
LSC-T	0.40	92.35	99.64	- 0.02	0.32	97.27	- 0.09	- 0.95
PM	/	92.41	99.73	0.01	0.23	96.91	-0.08	-1.15

The optimal aesthetic quality of the LSCs containing $[Eu_2L^F_4]^{2-}$ and Eu(tta)$_3$phen is maintained even at higher luminophore loadings. Both **LSC-Fc** and **LSC-Tc** retain high transparency and absence of visually detectable tinting. Their higher luminophore loading (0.1% wt. and 0.5% wt., respectively) enables them to harvest more light across a broader portion of the UV region, leading to a greater total solar absorptance ($\eta_{s,abs}$) compared to the less concentrated samples (**Table 4.3**). Specifically, their absorption onsets shift from 380 nm up to 395 nm and 410 nm, respectively (**Fig. 4.6a**).

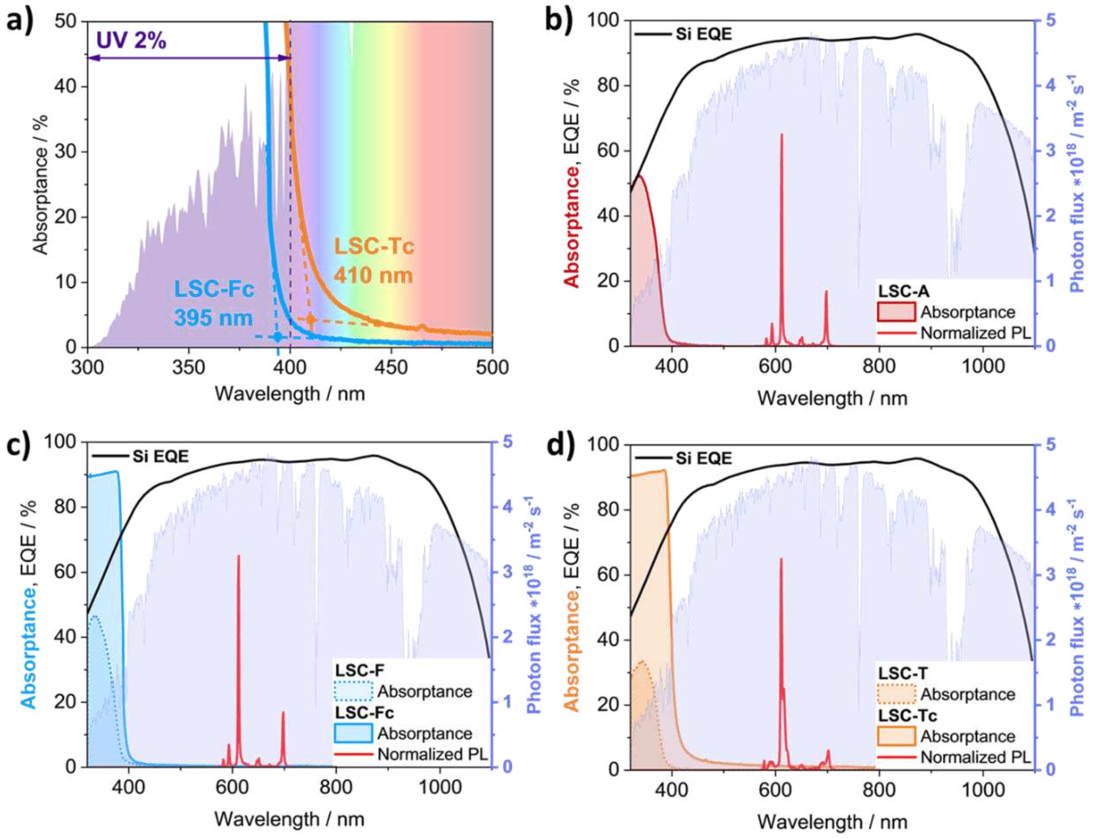

Figure 4.6. a) Enlarged absorption onsets of **LSC-Fc** and **LSC-Tc** due to increased luminophore loading. **b)**, **c)**, **d)** Absorptance and normalized PL spectra of the selected LSCs superimposed to the employed Si cells' EQE curve and to the AM1.5G solar photon flux.

To better illustrate the light absorption capability of these materials, it is useful to refer to the total solar absorptance, which clearly shows that achieving a high luminophore concentration is crucial for more efficient light absorption (**Fig.s 4.6b** to **d**). When expressed as photon flux, approximately 2% of the AM1.5G spectrum falls between 280 and 400 nm. With $A\%$ values close to 92% within their absorption regions, **LSC-Fc** and **LSC-Tc** quantitatively absorb incident UV photons, displaying optimal UV-blocking properties. The remaining 8% is the fraction of light reflected by the

PMMA matrix, in agreement to the Fresnel equations for reflection at normal incidence,[12] meaning that within the LSCs absorption region no UV photons are effectively transmitted. The difference in their $\eta_{s,abs}$ values (1.66% for **LSC-Fc** and 2.56% for **LSC-Tc**) is attributed to their absorption onsets, with **LSC-Tc** having a broader absorption band bordering with the visible region. Given the substantial gap between the absorbing and emitting regions displayed by $[Eu_2L^F{}_4]^{2-}$ and $Eu(tta)_3phen$, the possibility of self-absorption losses can be safely excluded, even with the increased luminophore loading in **LSC-Fc** and **LSC-Tc**. Consequently, these two samples are expected to produce significantly higher electrical outputs when coupled with Si cells in an LSC-PV configuration, compared to their less concentrated counterparts.

Beyond energy generation, UV-blocking capabilities are highly desirable for residential and shop windows to prevent the fading of furniture, artwork and flooring. Traditionally, this is achieved through passive window treatments that simply absorb UV light. However, luminescent solar concentrators based on europium antenna complexes offer an innovative approach, transforming these passive elements into active ones by converting blocked UV radiation into useful visible light while simultaneously generating electricity. Furthermore, the proposed LSCs could be employed in tandem architectures to shield a second underlying LSC panel from UV radiation, to prolong the shelf life of its luminophore. UV shielding layers could be useful also in combination with third generation solar cells (PSCs, DSSCs, OPVs) which are generally susceptible to degradation from high energy radiation like UV.

4.3 Devices

The selected LSCs were coupled with monocrystalline Si solar cells to obtain the corresponding LSC-PV devices. The one-edge configuration was used for both J-V and EQE acquisitions, by employing two PV cells with active area of 22×7 mm^2, connected in parallel. Optical coupling between the LSC and the PV cells was introduced. The electrical characterizations of the LSC-PVs were performed using the testbench previously described in *Chapter 3*. The labelling of the devices has already been reported in **Table 4.2**. **Fig. 4.7** displays the J-V and the P-V characteristics collected under AM1.5G simulated solar irradiation. The relevant electrical parameters and the PCEs extracted from the curves are listed in **Table 4.3**.

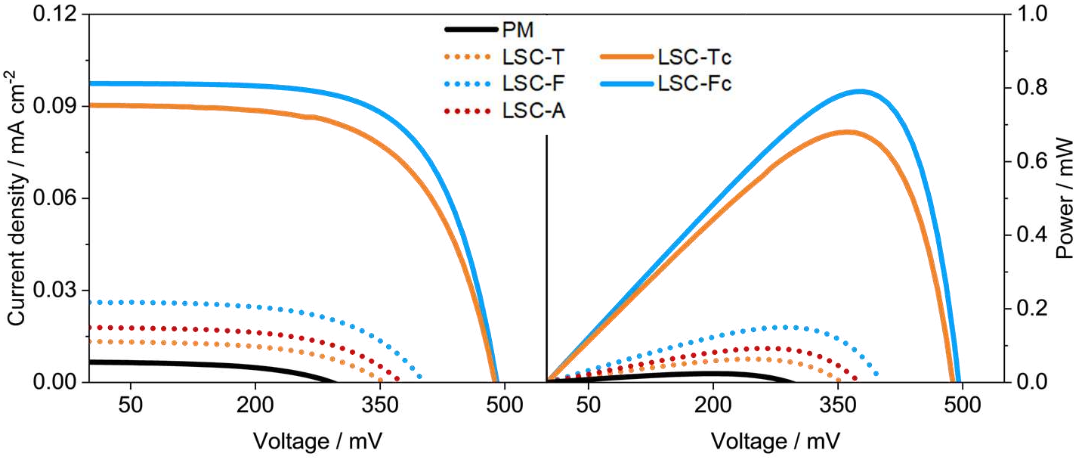

Figure 4.7. J-V (left) and P-V (right) curves recorded for the selected LSC-PVs with one PV-coupled edge. LSC-PV data of the undoped PMMA sample are reported for reference.

Table 4.3. Short-circuit current density (J_{SC}), open-circuit voltage (V_{OC}), fill factor (FF), maximum power (P_{max}) and power conversion efficiency (PCE) values of tested LSC-PVs. The "Exp." and "Int." labels indicate the experimental J_{SC} extracted from the J-V curves and the J_{SC} integrated from the EQE spectra, respectively.

Sample	**J_{SC} / mA cm^{-2}**		**V_{OC} / mV**	**FF**	**P_{max} / mW**	**PCE / % 1 edge (4 edges)**
	Exp.	**Int.**				
LSC-Fc^{PV}	0.097	0.097	490	0.65	0.780	0.031 (0.124)
LSC-Tc^{PV}	0.090	0.091	488	0.62	0.680	0.027 (0.108)
LSC-A^{PV}	0.018	/	375	0.55	0.093	0.0037 (0.015)
LSC-F^{PV}	0.026	/	403	0.57	0.150	0.0060 (0.024)
LSC-T^{PV}	0.013	/	355	0.54	0.063	0.0025 (0.010)
PM^{PV}	0.007	/	292	0.50	0.024	0.001 (0.004)

LSC-Fc^{PV} and **LSC-Tc^{PV}** exhibited the highest J_{SC}, V_{OC} and maximum output power P_{max}, indicating a positive correlation between luminophore loading and electrical performance. Specifically, **LSC-Fc^{PV}** achieved a maximum output power of 0.780 mW. Power conversion efficiencies for these samples at higher luminophore loadings were an order of magnitude higher than those of the less concentrated samples. The following discussion is focused on the best performing devices **LSC-Fc^{PV}** and **LSC-Tc^{PV}**. Both LSC-PVs demonstrated comparable electrical outputs, with **LSC-Fc^{PV}** exhibiting slightly better performance. Approximately 4% of the calculated PCEs was attributed to simple waveguiding of edge-reflected photons by the sole PMMA matrix, as determined from the undoped LSC study. Correction of the one-edge measurements for all four sides yielded global PCE values of 0.124% for **LSC-Fc^{PV}** and 0.108% for **LSC-Tc^{PV}**.

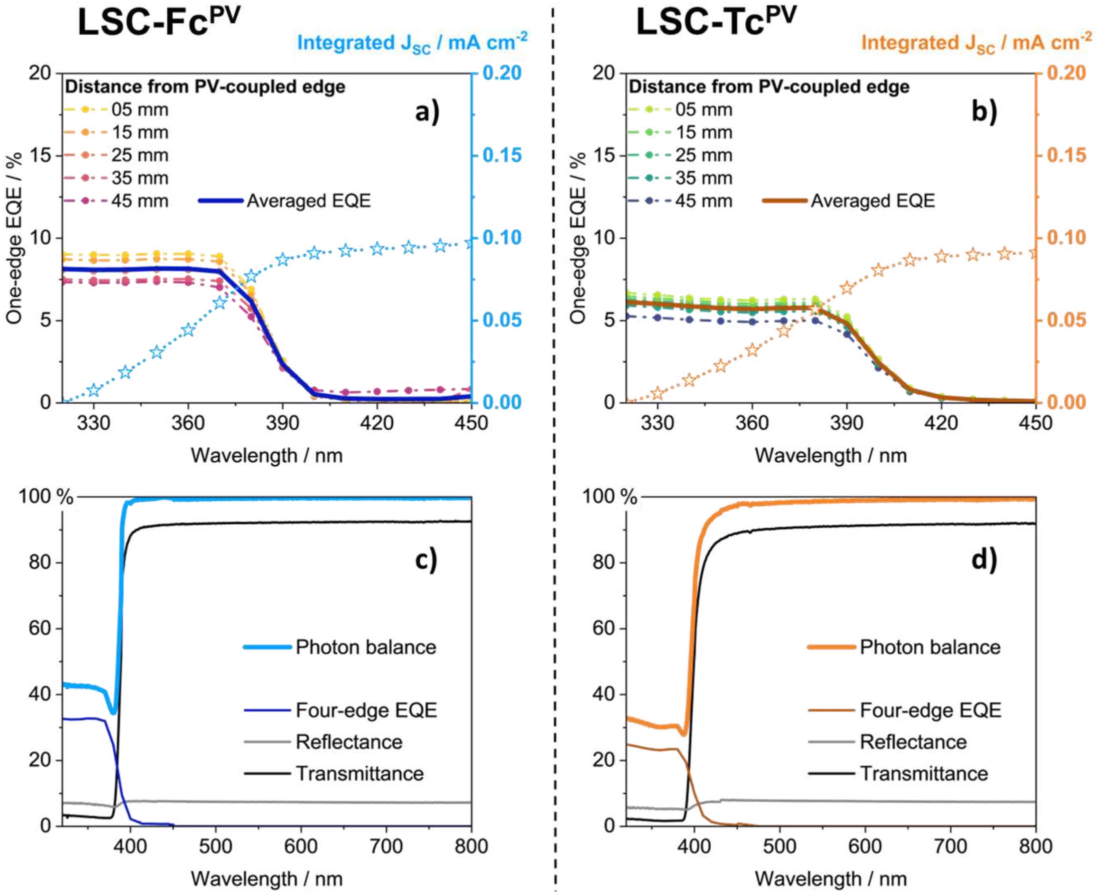

Figure 4.8. Position-dependent EQE spectra collected from one-edge measurements on **a) LSC-Fc^{PV}** and **b) LSC-Tc^{PV}**, with averaged EQE spectrum highlighted (solid line). Corresponding J_{SC} integrals are displayed on the right Y axis. Consistency checks on the photon balance for **c) LSC-Fc^{PV}** and **d) LSC-Tc^{PV}**. Displayed EQE spectra have been derived by correcting one-edge measurements for the geometric factor and averaging the corrected spectra.

Notably, **LSC-Fc^{PV}** produced comparable, if not higher, electrical outputs despite containing one-fifth of the luminophore loading by weight with respect to the reference device **LSC-Tc^{PV}**. Position-dependent, one-edge EQE spectra were collected within the luminophore absorption range and are reported in **Fig.s 4.8a** and **b**, with the average EQE spectrum highlighted for each set. The averaged EQEs were used to calculate the integrated short-circuit current densities ($J_{SC,int}$), to compare with the experimental values extracted from the J-V curves ($J_{SC,exp}$). The integrated J_{SC} is reported as well in **Table 4.3**, showing excellent agreement with the experimental one for both LSC-PVs. This consistency check validates both the experimental data and the entire measurement setup. Furthermore, the accurate correlation between measured and calculated J_{SC} values confirms the absence of scattering centres or particulate matter within the waveguides, already assessed qualitatively at a visual inspection and quantitatively through AVT determination.

The EQE spectra closely mirror the absorptance spectra, exhibiting identical absorption onsets. The photon balance consistency check was verified through the inequality $EQE_{4\,edges}\% + T\% + R\% \leq 100$, which was fulfilled by both devices (**Fig.s 4.8c** and **d**). After correcting for four edges, maximum EQE values reached approximately 32% at 360 nm for **LSC-Fc^{PV}** and approximately 23% at 320 nm for **LSC-Tc^{PV}**. **LSC-Fc^{PV}** exhibited a higher EQE than **LSC-Tc^{PV}**, also yielding a larger integrated J_{SC} and consequently higher electrical outputs. Conversely, **LSC-Tc^{PV}**, despite having a lower EQE, displayed a wider absorption range enabling it to harvest an additional portion of the AM1.5G spectrum where the photon population increases rapidly. This resulted in J-V curves and PCE values similar to those of **LSC-Fc^{PV}**, despite the considerable difference in EQEs. The broadening of absorption bands due to increased luminophore loadings is thus a favourable factor for enhancing electrical power production, provided that the LSC aesthetic quality is unaltered. Further functionalization of the $[Eu_2L_4]^{2-}$ cages to increase their solubility in MMA could facilitate full utilization of the UV region by the proposed LSC-PVs.

The collected electrical parameters were further used to derive the internal photon efficiency (η_{int}) of the two LSC-PVs. The calculated η_{int} values are 55% for **LSC-Fc^{PV}** and 34% for **LSC-Tc^{PV}**. As the internal photon efficiency accounts solely for the optical losses within the LSC (excluding coupling to the photovoltaic component), scattering, $PLQY$ and reabsorption are the primary contributing factors to this metric. Given the absence of scattering and reabsorption losses in our LSC-PVs, the larger η_{int} of $\mathbf{LSC\text{-}Fc^{PV}}$ is attributed to the higher $PLQY$ of $[Eu_2L^F{}_4]^{2-}$ compared to $Eu(tta)_3phen$.

Lastly, a comparative analysis of the performance of our devices with other published Eu^{3+}-based concentrators is presented in **Table 4.4**. PCE was chosen as the primary metric for comparison, as recommended for LSC-PV characterization. For studies predating the publication of the reference reporting guidelines, PCE values were calculated based on the provided experimental data.

Table 4.4. Survey of literature regarding Eu^{3+}-based LSCs, including for each publication the luminophore formula, the employed matrix, the geometric gain (G), the device structure, the power conversion efficiency (PCE) and the weight concentration of europium with respect to the matrix.

Device	**Luminophore**	**Matrix**	$\boldsymbol{G}$	**Device structure**	$\boldsymbol{PCE}$ **/ %**	$\mathbf{Eu^{3+}}$ **/ wt.%**
This work	$[Eu_2L^F{}_4](NEt_4)_2$	PMMA	4.63	50 × 50 × 2.7 mm^3 bulk tile	0.031	0.01
This work	$Eu(tta)_3phen$	PMMA	4.63	50 × 50 × 2.7 mm^3 bulk tile	0.027	0.08
A[2]	$Eu(tta)_3phen$	Polyvinyl butyral (PVB)	6.50	film (thickness not specified) deposited onto 78 × 78 × 3 mm^3 glass	0.044	0.24
	$Eu(tta)_3Dpbt$				0.050	0.20
B[13]	[B(TMSP)Im] $[Eu(tta)_4]$	PMMA	7.85	5.1 µm thick film deposited onto 75 × 20 × 1 mm^3 glass	0.002	2.28
C[14]	$Eu(2mCND)_3$	Siloxane-polyether (di-ureasil)	2.89	320 µm thick film deposited onto 50 × 50 × 4 mm^3 acrylic sheet	0.138[b]	1.05

---

[b] Value not reported in the publication, calculated based on provided experimental data.

As stated before, accurate PCE comparison necessitates a careful consideration of the device structure, including: i) clear specification of the number of PV-coupled edges; ii) efficient shielding from direct illumination of the edge-coupled PV cells; iii) blackening of the uncoupled edges and of the backdrop to minimize stray light contribution. Literature examples in **Table 4.4** all relate to one-edge measurements, but device structures vary significantly.

For instance, **Device A** had blackened edges with an unspecified backdrop,[2] while **Device B** featured reflective edges and background.[13] **Device C** edges were untaped, and a white paper foil served as a reflective backdrop, leading to a reported 92% enhancement in output power.[14] While finding literature data on devices with analogous structures remains challenging, the presented study demonstrates how **LSC-Fc$^{\mathbf{PV}}$** and **LSC-Tc$^{\mathbf{PV}}$** produce electrical outputs comparable in magnitude to most published Eu^{3+}-based LSC-PVs. This is a significant finding, considering that the weight content of the Eu^{3+} ion in our devices (0.01 wt% for **LSC-Fc$^{\mathbf{PV}}$** and 0.08 wt% for **LSC-Tc$^{\mathbf{PV}}$**) is largely inferior with respect to the explored literature, down to a hundred-fold factor in the case of **LSC-Fc$^{\mathbf{PV}}$**. Such literature survey specifically compared the developed LSC-PVs to other analogous Eu^{3+}-based systems possessing comparable aesthetic properties (high transparency and lack of colour). Notably, Jin *et al.*[15] recently reported LSCs with very similar aesthetic quality, based on a different emitter: Ag,Mn:ZIS/ZnS quantum dots. The study also adhered to the suggested reporting guidelines, enabling direct comparison of device metrics. The QD-based LSCs exhibited an AVT of 90%, a CRI of 95.8 and a PCE (4 edges) of 0.09%. These values closely resemble the results herein reported, indicating that **LSC-Fc$^{\mathbf{PV}}$** and **LSC-Tc$^{\mathbf{PV}}$** are competitive devices among the best UV-selective LSC technologies.

4.4 Bibliography

1 I. Motta, G. Bottaro, M. Rando, M. Rancan, R. Seraglia and L. Armelao, *J. Mater. Chem. A*, 2024, **12**, 22516–22527.

2 X. Wang, T. Wang, X. Tian, L. Wang, W. Wu, Y. Luo and Q. Zhang, *Sol. Energy*, 2011, **85**, 2179–2184.

3 M. Tonezzer, G. Maggioni, A. Campagnaro, S. Carturan, A. Quaranta, M. della Pirriera and D. Gutierrez Tauste, *Prog. Photovolt. Res. Appl.*, 2015, **23**, 1037–1044.

4 M. Rancan, J. Tessarolo, A. Carlotto, S. Carlotto, M. Rando, L. Barchi, E. Bolognesi, R. Seraglia, G. Bottaro, M. Casarin, G. H. Clever and L. Armelao, *Cell Rep. Phys. Sci.*, 2022, **3**, 100692.

5 M. Rancan, M. Rando, L. Bosi, A. Carlotto, R. Seraglia, J. Tessarolo, S. Carlotto, G. H. Clever and L. Armelao, *Inorg. Chem. Front.*, 2022, **9**, 4495–4505.

6 M. Rando, A. Carlotto, S. Carlotto, R. Seraglia, M. Rancan and L. Armelao, *Inorg. Chem. Front.*, 2025, **12**, 1890–1899.

7 S. Carlotto, L. Armelao and M. Rancan, *Int. J. Mol. Sci.*, 2022, **23**, 10619.

8 M. Pinsky and D. Avnir, *Inorg. Chem.*, 1998, **37**, 5575–5582.

9 K. Binnemans, in *Handbook on the Physics and Chemistry of Rare Earths*, Elsevier, 2005, vol. 35, pp. 107–272.

10 K. Binnemans, *Coord. Chem. Rev.*, 2015, **295**, 1–45.

11 C. Yang, M. C. Barr and R. R. Lunt, *Phys. Rev. Appl.*, 2022, **17**, 034054.

12 Hecht, Eugene, *Optics*, Boston: Pearson Education, Inc, 5 edition. Global edition., 2017.

13 A. R. Frias, M. A. Cardoso, A. R. N. Bastos, S. F. H. Correia, P. S. André, L. D. Carlos, V. de Zea Bermudez and R. A. S. Ferreira, *Energies*, 2019, **12**, 451.

14 Y. Liu, N. Li, R. Sun, W. Zheng, T. Liu, H. Li, Y. Chen, G. Liu, H. Zhao, H. Liu and Y. Zhang, *Nano Energy*, 2021, **85**, 105960.

15 L. Jin, E. Hamzehpoor, G. S. Selopal, J. Liu, P. Kumar, D. Benetti, X. Tong, D. F. Perepichka, Z. M. Wang and F. Rosei, *Small Methods*, **n/a**, 2301695.

Chapter 5

Exploring multifunctionality in LSCs: visible-blind UV sensors

The LSCs presented in *Chapter 4* exploited Eu^{3+} antenna complexes to convert incident UV photons into red, almost monochromatic light, which is then redirected onto edge-coupled PV cells to produce electricity. The same emitting properties and device architecture are herein investigated as visible-blind UV photodetectors, *i.e.*, a system designed to respond exclusively to ultraviolet radiation while remaining insensitive to visible light.

The experimental testbench previously developed for LSC-PV electrical characterizations was also employed for sensor characterizations. After a brief introduction on photodetectors' established technologies and figures of merit, the characterization of the LSC-PV systems for UV sensing is provided. The sensors' electrical response to incident optical power variations has been investigated, spanning the 270 – 395 nm range. The temporal response has been characterized as well, and the selectivity towards UV photons has been verified. The performance of the LSC-based sensors is evaluated and compared with conventional semiconductor-based photodetectors. A perspective on future system refinement closes the discussion.

5.1 Introduction to photodetectors

A photodetector is a device that converts an optical input into an electrical output, allowing to quantify the intensity of the incident radiation. Among the different types of photodetectors, semiconductor-based devices are employed in many application fields, ranging from spectroscopy to imaging and optical communications. The core element of modern photodetectors design involves a semiconductor p-n junction.[1,2] When a photon with sufficient energy strikes the junction, it generates an electron-hole pair. The minimum energy needed to trigger charge carrier generation corresponds to the bandgap of the semiconductor (E_g, eV), which determines also the cutoff wavelength of the detector (λ_0, nm):

$$\lambda_0 = \frac{hc}{E_g} \qquad \textbf{Eq. 5.1}$$

where h is Planck's constant (m^2 kg s^{-1}) and c is the speed of light (m s^{-1}). Opposite charge carriers separate between the p- and the n- doped materials, to reach in the end the external circuit and produce an electrical output signal proportional to the received radiation intensity. Depending on the type of junction and on the operation mode, a voltage or current output can be extracted. The following discussion focuses on the latter, but all equations can be analogously rewritten as a function of voltage. The responsivity of a photodetector (R) is defined as the ratio of this current (I) output to the incident optical power (P_{in}), after subtraction of the dark signal (I_{dark}, *i.e.*, the small electrical signal produced by the device when not illuminated):

$$R = \frac{I - I_{dark}}{P_{in}} \quad (A/W) \qquad \textbf{Eq. 5.2}$$

The responsivity is essentially the proportionality constant between output and input signals and quantifies how effective a detector is in converting the incident radiation into an electrical current. Higher R values indicate higher efficiency, because the detector produces a larger output signal for a given input power. The responsivity is expressed as a function of the wavelength, as the active material's absorption and reflection properties change with the energy of the incident radiation. The plot of the responsivity against the wavelength is called a spectral response (SR) curve, which is a fundamental characterization provided by any photodetector manufacturer.

Responsivity alone is not sufficient in evaluating the quality of a photodetector, as its detecting ability depends also on how well a signal can be distinguished from noise. The parameters accounting for this aspect are the noise equivalent power (NEP) and the detectivity (D). The NEP is defined as the incident optical power at which the photodetector generates a signal equal to noise. The reciprocal term of the NEP is the detectivity. However, both NEP and D are dependent on the area of the photodetector, making it difficult to compare the properties of different devices. A "specific" or "normalized" detectivity (D^*, in Jones: Hz$^{1/2}$ W^{-1}) can then be defined as:

$$D^* = \frac{\sqrt{A\,\Delta f}}{NEP} \qquad \textbf{Eq. 5.3}$$

where A is the area of the photodetector and Δf is the electrical bandwidth. Electrical bandwidth refers to the range of input frequencies over which a detector can effectively operate:[2] a large bandwidth means that the sensor can transduce more frequencies, including fast-paced events, but at the same time integrates more noise. When detecting weak signals, it is preferable to limit the bandwidth of the photodetector to reduce noise integration and enhance its sensitivity. If, as in most cases, the main contribution to noise arises mainly from the dark current of the photodetector, then the expression for the specific detectivity can be rewritten in more practical terms:[3,4]

$$D^* = \frac{R}{\sqrt{2e\,J_{dark}}} \qquad \textbf{Eq. 5.4}$$

where e is the elementary charge and J_{dark} is the dark current density, measured in the same conditions as responsivity. As it can be deduced, lower dark currents enhance the performance of the photodetector. The specific detectivity D^* is the preferred metric for comparing the intrinsic detecting properties of different devices. A good photodetector is also characterized by a photocurrent response that is linear with incident optical power over a wide range. This means that the device exhibits a constant responsivity when exposed to very different radiation intensities. The linearity of a photodetector can be quantified using the linear dynamic range (LDR, in dB), depending on the smallest (I_{min}) and the largest (I_{max}) current signals between which the current response is linear with the incident radiation:

$$LDR = 20 \log\left(\frac{I_{max}}{I_{min}}\right) \quad \textbf{Eq. 5.5}$$

The lower limit of the range usually corresponds with the smallest signal detectable by the sensor, its limit of detection (LOD), while the upper limit of the range is established by the maximum output signal that the detector can produce before reaching saturation. Typically, the LOD is defined as a threshold value above which any output signal is considered a true signal and not noise. The threshold (χ_{th}) is determined from the mean dark current value ($\overline{\chi_{dark}}$) and its standard deviation (σ_{dark}) as follows:

$$\chi_{th} = \overline{\chi_{dark}} + k\,\sigma_{dark} \quad \textbf{Eq. 5.6}$$

where k is an arbitrary numerical factor chosen according to the desired confidence level of the measurement. Such definition is conveyed by the analytical scientific field, where the LOD threshold is "the smallest measure that can be detected with reasonable certainty for a given analytical procedure" (from the IUPAC Gold Book[5]).

Lastly, the time response indicates how fast the photodetector reacts upon irradiation switch on and off. The speed of response is quantified through the rise time and fall time. Both can be measured by sending pulsed light signals with a certain frequency onto the detector and following its time-modulated output with an oscilloscope.

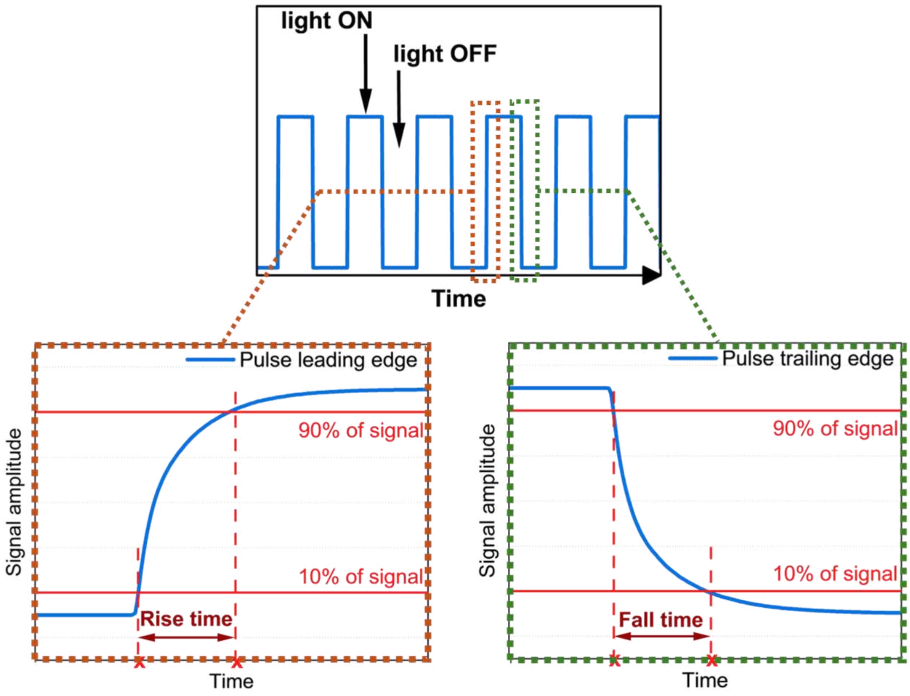

Figure 5.1. Typical leading and trailing edge shapes of a photodetector's output waveform upon exposure to pulsed light. The method for extrapolating the rise and fall time is depicted.

Considering an isolated single pulse, the rise time is defined as the time interval necessary for the output signal to go from 10% to 90% of its maximum amplitude, on the leading edge of the pulse (**Fig. 5.1**). Conversely, fall time is the time interval necessary for the signal to go from 90% to 10% of its maximum amplitude, on the trailing edge of the pulse.

A diverse range of materials is used to fabricate photodetectors, each chosen for its specific operational wavelength window and performance. Common materials for visible and infrared detection are silicon (Si),[6,7] indium gallium arsenide (InGaAs)[8–10] and cadmium sulphide (CdS).[11,12] UV photodetection instead necessitates of wide bandgap materials able to detect radiation below 400 nm (above 3.1 eV, **Fig. 5.2**).

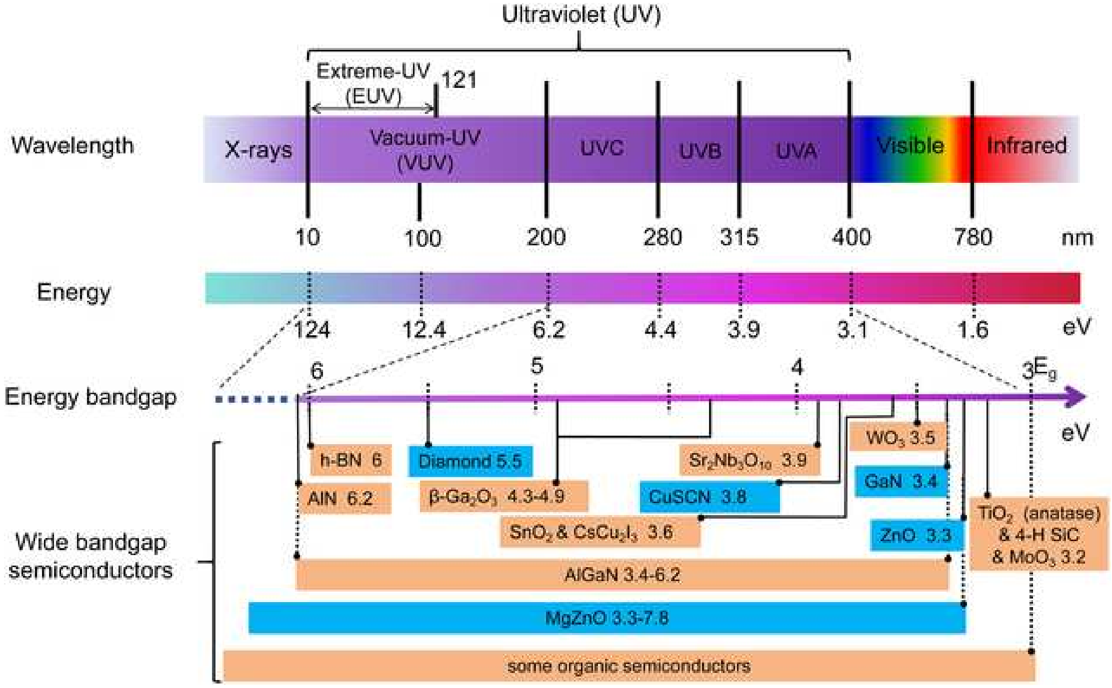

Figure 5.2. Wide bandgap semiconductors for UV photodetection. Credit: Cao *et al.*[4]

In many applications of UV photodetectors, selectivity towards a certain range of UV photons is crucial, leading to the development of visible-blind (λ_0 = 400 nm) or even solar-blind (λ_0 = 280 nm) sensors. Prominent materials for UV photodetectors are gallium nitride (GaN) and its alloy aluminium gallium nitride (AlGaN), which bandgap can be tuned by regulating the Al content.[13–15] Wide bandgap metal oxides like ZnO, TiO_2 and Ga_2O_3 are also an interesting option, thanks to the possibility of enhancing detector performance by modifying their surface morphology and crystalline structure.[16–18]

Despite considerable achievements in the development of wide bandgap materials for UV sensing, they still present some key drawbacks. Although some of them have already been commercialized, like GaN, many of the materials listed in **Fig. 5.2** have high production costs due to the epitaxial growth methods employed for their fabrication.[4,13] Additionally, integration into Si-based circuits is not always straightforward due to compatibility issues between different materials. Many photodetectors based on alternative materials (perovskites,[19,20] organic semiconductors,[21,22] hybrid materials[23]) necessitate multi-stack systems complete of charge extraction layers (**Fig. 5.3a**), adding up to overall fabrication costs.
Conversely, LSCs offer a basic device architecture and simple working principle (**Fig. 5.3b**).

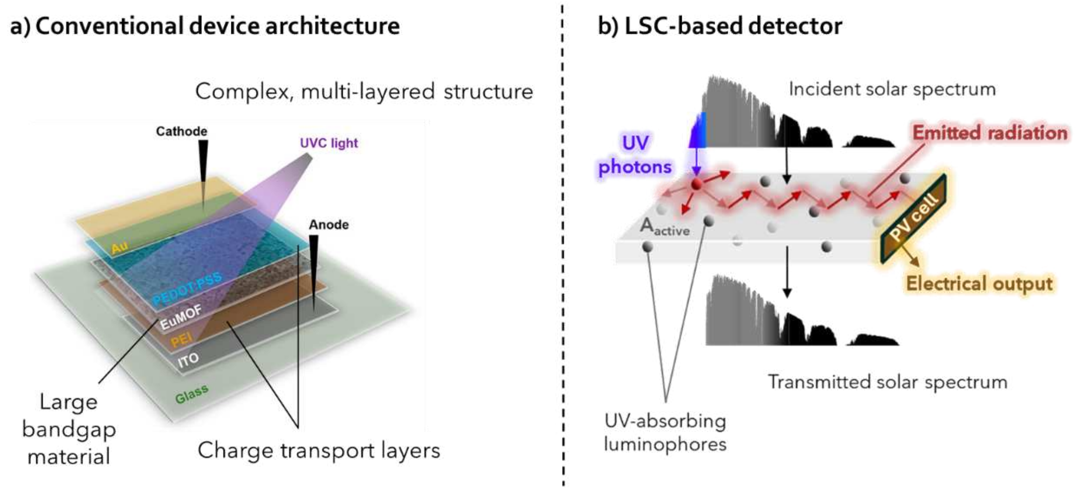

Figure 5.3. Comparison between the device configurations of **a)** a multi-stack UV photodetector (Credit: Nguyen and Bark[23]) and **b)** an LSC-PV based photodetector, containing UV absorbing luminophores.

By employing a suitable luminophore, UV photons can be converted into less energetic radiation within the operational wavelengths of Si or other well established semiconductors. The LSC geometry could enable easy and inexpensive scale up of the waveguide element for detection over larger areas, while redirecting the output light signal onto a small edge area to be interfaced with a classic semiconductor-based photodetector. Up until now, there have been a few studies on the use of luminescent layers deposited directly onto Si photodetectors to enhance detection in the UV region.[24–26] LSCs have been proposed as viable tools to fabricate broadband photodetectors.[27,28] In 2022, Ding *et al.* presented an extended range photodetector based on multiple bulk heterojunctions and an LSC, able to sense optical radiation from 200 to 1000 nm.[29] To the author’s knowledge, visible-blind or even solar-blind photodetectors based on the LSC configuration have not yet been investigated, underscoring the novelty of the case study herein presented.

5.2 Bare cell photodetector characterization

The LSC-PVs based on complexes $[\mathrm{Eu_2L^F}_4]^{2-}$ and $\mathrm{Eu(tta)_3phen}$ described in *Chapter 4* were investigated as UV sensors. The same Si PV cells were used as edge-photodetection element, adopting a basic experimental configuration. No bias was applied to the cells, collecting the short-circuit current generated upon illumination as the detector’s output signal.

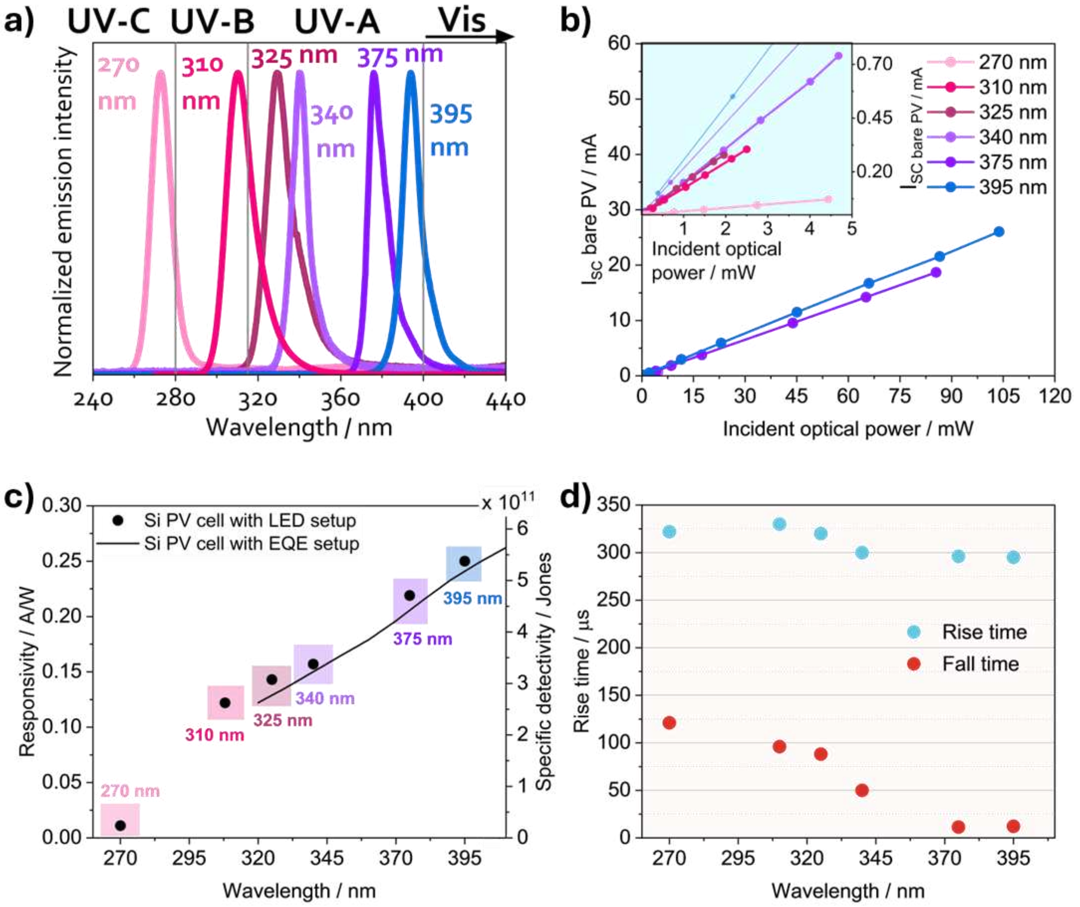

Figure 5.4. **a)** Emission spectra of the employed UV LEDs. **b)** Plots of the bare cell’s short-circuit current at increasing incident optical power for each LED (inset: enlargement of 270, 310, 325 and 340 nm plots). **c)** Spectral response of the bare cell measured with the LED setup, compared to the one measured with the setup developed for EQE acquisitions. **d)** Rise and fall times of the bare PV cell with varying wavelength.

Before studying the whole LSC-PV systems, the PV component was characterized separately under direct UV illumination. A series of UV LEDs was used as light source, adequately distributed to provide good spectral coverage of the UV region, with at least one representative wavelength for UV-A, UV-B and UV-C (**Fig. 5.4a**). Current trends at increasing incident optical power for each wavelength are reported in **Fig. 5.4b**, exhibiting the typical linear behaviour of Si. The measurements were performed in continuous illumination mode. **Fig. 5.4c** displays the plots of responsivity and specific detectivity against wavelength. Excellent agreement is observed between the spectral response measured with the LED illumination and the spectral response of the bare cell measured with the EQE setup based on the spectrofluorometer (see *Section 3.3*). Finally, the time response of the bare PV cell was assessed, registering decreasing rise times (from 120 to 10 μs) with increasing wavelength, while the fall time remained approximately constant with an average value of 310 μs (**Fig. 5.4d**).

5.3 LSC-PV photodetector characterization

Two series of samples, doped with $[Eu_2L^F{}_4]^{2-}$ (**F**) and Eu(tta)$_3$phen (**T**) respectively, were coupled to the previously characterized Si solar cells and investigated as UV photodetectors. Each series comprised three LSC slides with increasing active area (**Fig. 5.5a**): 15 × 15 mm^2 (**225**), 15 × 30 mm^2 (**450**) and 15 × 50 mm^2 (**750**). Analogous samples were prepared also with undoped PMMA (**PM**). Labelling is reported in **Table 5.1**. The LSCs were coupled with a single PV cell on the 15 mm side.

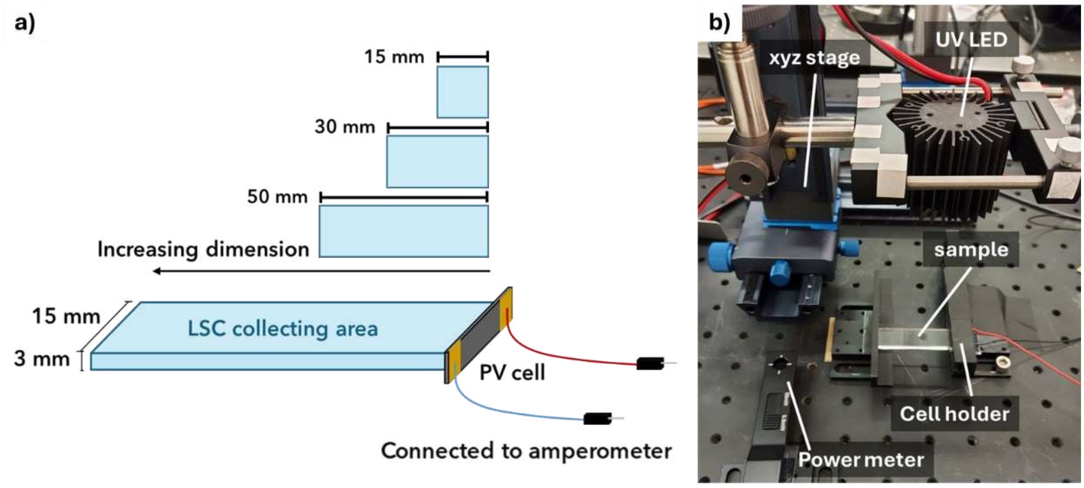

Figure 5.5. a) Dimensions of the LSC samples used in the photodetectors. **b)** Experimental setup employed for LSC-PV photodetector characterizations.

Table 5.1. Labelling of the photodetectors derived from the Eu^{3+}-based LSC-PV, according to the LSC size and the luminophore content.

Sample	Dimensions	Luminophore	Loading / wt%
F225	15 × 15 mm^2	$[Eu_2L^F{}_4]^{2-}$	0.1
F450	15 × 30 mm^2		
F750	15 × 50 mm^2		
T225	15 × 15 mm^2	Eu(tta)$_3$phen	0.5
T450	15 × 30 mm^2		
T750	15 × 50 mm^2		
PM225	15 × 15 mm^2	none	/
PM450	15 × 30 mm^2		
PM750	15 × 50 mm^2		

An LSC-PV configuration without optical coupling between the LSC and the cell was employed, and the short-circuit current generated upon illumination of the LSC was again monitored as output signal. The UV LEDs used as light source were mounted on a XYZ stage, allowing for easy alignment over the sample (**Fig. 5.5b**). The divergent emission profile of the LEDs proved advantageous, enabling homogeneous sample illumination through simple adjustment of the source-sample distance, thus eliminating the requirement for optical components. For the **750** samples, the maximum incident optical power variation was of 5% across the whole illuminated area. Responsivity and detectivity were acquired for each sample at each incident wavelength, deriving the corresponding spectral responses (**Fig. 5.6a**). Electrical current outputs were normalized on the active area of the LSC (A_{in}, **Eq. 3.1**), as it is the component receiving direct illumination.

The photodetectors based on undoped PMMA produce negligible signals with respect to the Eu^{3+}-based devices, confirming that the luminophores successfully enable the UV sensing functions of the LSC-PVs. Except for the 395 nm data, the **F** series shows generally higher responsivity with respect to the **T** series.

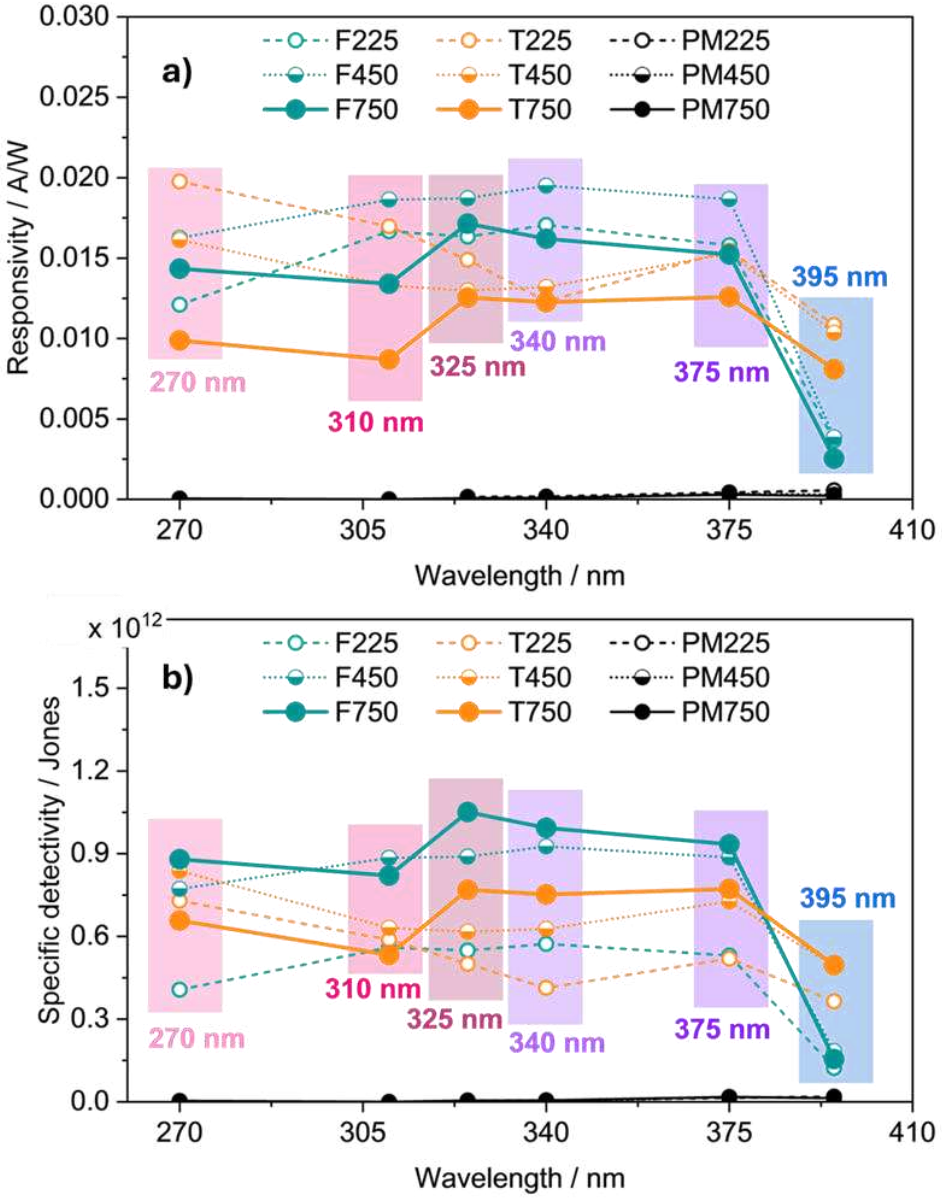

Figure 5.6. Plots of **a)** responsivity and **b)** specific detectivity versus wavelength for each sample. Thicker plots correspond to the **750** samples. The experimental points of the **F** and **T** series are grouped within coloured boxes according to the illumination wavelength.

Within each series, the devices with smaller active area (**225** and **450**) exhibit slightly higher responsivity than the **750** analogues. Conversely, when calculating the specific detectivity, the **750** samples show the highest values, meaning that they are better at distinguishing target light input signals from noise (**Fig. 5.6b**). Maximum D^* values are 1.05 × 10^{12} Jones at 325 nm for **F750** and 0.77 × 10^{12} Jones at 375 nm for **T750**. This evidences that responsivity alone is not sufficient to fully evaluate the quality of a photodetector.

At 395 nm, the performances of the **F** series systematically drop below the **T** series. The inversion in the trend can be explained by considering the different absorption onsets of the two luminophores embedded into PMMA. As already presented in *Chapter 4*, **LSC-Fc** showed absorption up to 395 nm, while **LSC-Tc** absorption spanned all the UV-B, the UV-A, and a small portion of the visible up to 410 nm (**Fig. 5.7a**). The photodetectors based on the corresponding LSCs follow such behaviours in that their electrical output depends on the absorption characteristics of the two Eu^{3+} complexes. LSC absorption onsets determine the cutoff wavelengths of the resulting photodetector.

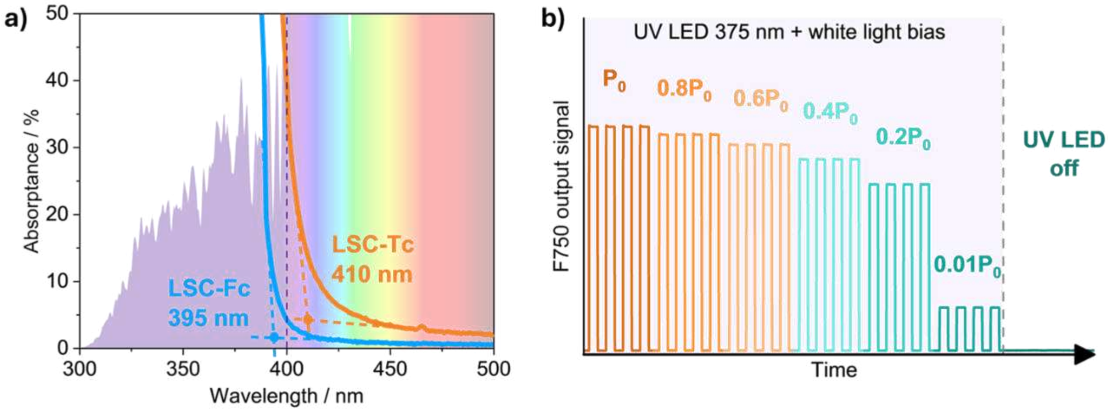

Figure 5.7. a) Absorption onsets of the LSC-PVs from which the photodetectors were derived. **b)** Plot of the modulated current output of **F750** exposed to pulsed UV light at varying incident optical power over time. The experiment was performed in the presence of a continuous white light bias.

In accordance with such observations and considering the desirable visible-blind properties, a simple test was carried out on **F750** (*i.e.*, the best performing sample) to assess its selectivity towards UV photons. The device was exposed to pulsed light at 375 nm, in the presence of a continuous white light bias. The intensity of the UV light was gradually reduced, observing good follow-up behaviour of **F750** (**Fig. 5.7b**), until the LED was completely switched off. In the presence of just the white light, no signal but the dark current was detected, underscoring the complete selectivity of the device towards UV radiation.

The linear dynamic range of **F750** was then investigated using two illumination wavelengths representative of very different UV spectral regions: 270 nm (UV-C) and 375 nm (UV-A). The plots of the output current versus incident optical power density are shown in **Fig. 5.8a**. The *LDR* is defined as the range of illumination intensities within which the output electric signal maintains linearity (**Eq. 5.5**). This theoretically coincides with constant responsivity across the whole range, observed also experimentally with good approximation. In both illumination conditions, **F750** displays LDR around 40 dB.

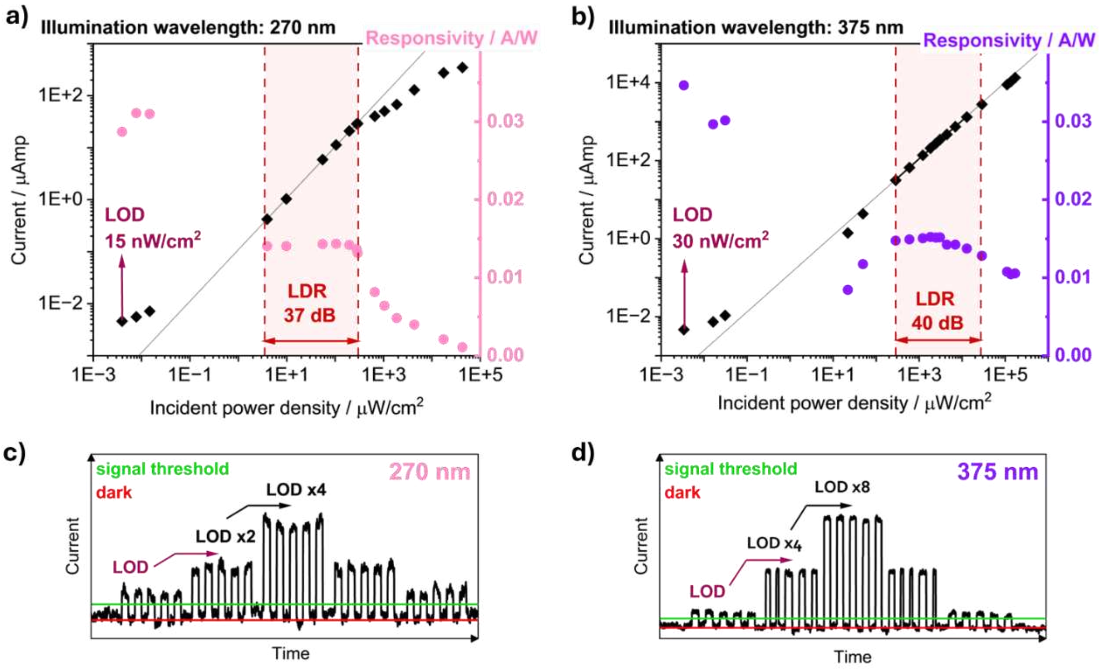

Figure 5.8. Plots of output current versus incident optical power density for **F750** exposed to **a)** 270 nm and **b)** 375 nm irradiation. The LDR regions, showing constant responsivity, are highlighted. Smallest detected signals report the corresponding LOD values. **c)**, **d)** Excellent follow-up behaviour to pulsed light signals is observed also in the LOD's optical power range.

Fig.s 5.8a and **b** display also the limit of detection (LOD) values for **F750** under 270 nm and 375 nm illumination. In both cases, the device can detect signals down to a few tenths of nW cm^{-2}. LODs were determined by greatly lowering the LEDs' incident optical power through neutral density filters until the output current reached the desired threshold value. This was calculated as the dark current (3.8 nA) plus ten times (k coefficient in **Eq. 5.6**) its standard deviation (170 pA). Typically, LODs are given with k = 2 – 3. In this specific case, due to the basic setup used, the confidence level was purposedly set with extremely limiting conditions (k = 10) to fully prevent false positives. The responsivity values calculated from the LOD investigation resulted systematically higher than those previously assessed for higher power intensities. This may be due to the simple experimental setup, which will need future improvements to perform accurate measurements in low light conditions. Nonetheless, it is worth noting that, with just the basic device architecture of the LSC-PVs, the devices were able to track pulsed light signal even at incident optical power values in the range of LODs (**Fig.s 5.8c** and **d**).

Finally, the photodetectors based on the **F** and **T** series were characterized in terms of their time response to UV light switch on and off. **Fig. 5.9a** shows the rise and fall time plots of the **750** samples at varying illumination wavelength. Smaller samples were characterized at the representative wavelengths of 270 and 375 nm.

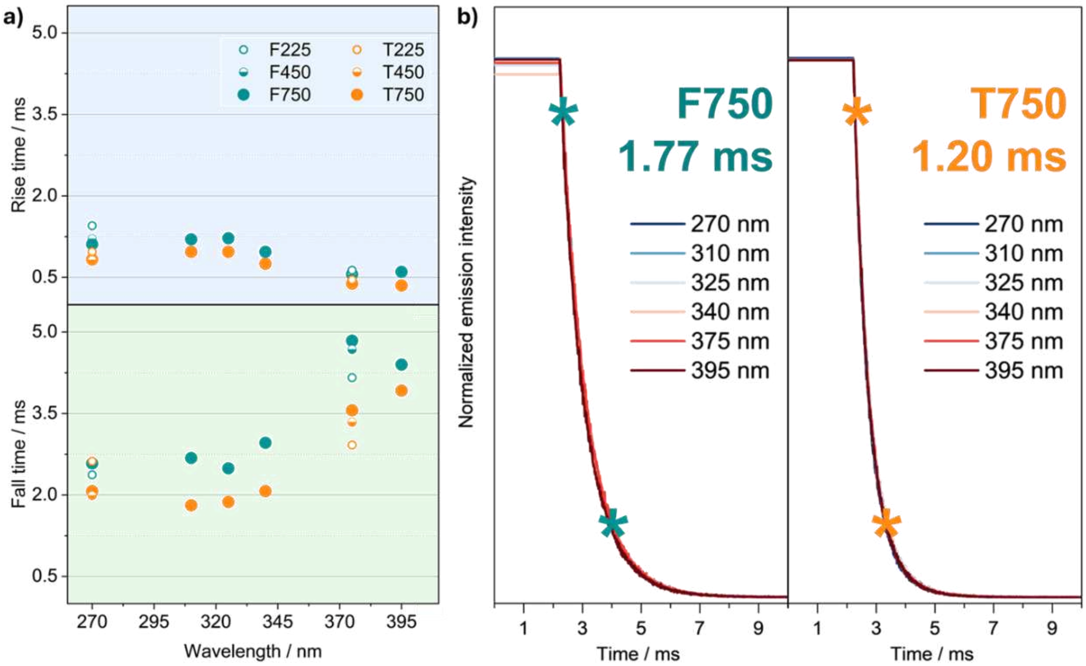

Figure 5.9. a) Rise (top) and fall (bottom) time plots versus wavelength for selected **F** and **T** samples. **b)** PL decay curves of **F750** (left) and **T750** (right) at different wavelengths, showing identical behaviour within each set.

The size factor does not influence significantly the speed of the photodetectors. Measured rise times are all below 1.5 ms, while fall times take longer (< 5 ms). Furthermore, an increase of the fall times in going towards higher wavelengths is observed in both sample series. At first approximation, the fall time of the LSC-PV photodetectors can be split in two contributions: the fall time of the Si PV cell and the fall time of the luminophores excited state. The former has been previously quantified, and it is approximately constant across the whole investigated spectral range (310 μs). As for the latter, the photoluminescence decay curves (see acquisition details in *Chapter 9: Experimental*) shown in **Fig. 5.9b** yield a fall time of 1.77 ms for **F750** and of 1.20 ms for **T750**, in both cases independent from the excitation wavelength. These values are shorter than those derived from device characterization, which suggests that the fall time of the device is not simply the sum of the contributions from the molecular emitter and the Si solar cell.

Table 5.2. Survey of the literature regarding semiconductor-based, visible-blind photodetectors, including for each publication the materials composition, the cutoff wavelength (λ_0), the operation bias, the maximum values of responsivity (R) and specific detectivity (D^*), the rise time, the fall time and the linear dynamic range (LDR).

Device	Materials	λ_0 / nm	Bias / V	R / A/W	D^* / Jones	Rise/fall time	LDR / dB
This work	PMMA/$[Eu_2L^F{}_4]^{2-}$	395	0	0.017	1.05×10^{12}	1.2/4.9 ms	40
***A*[31]**	PMMA/ZnO PS/ZnO P(VDF-TrFE)/ZnO	400	2	0.016 0.638 14.43	1.05×10^{11} 1.89×10^{12} 2.27×10^{13}	15/46 s 12/10 s 9/7 s	48 67 83
***B*[32]**	Al/ZnO	400	0	0.028	1.85×10^{12}	105/94 ms	14[a]
***C*[33]**	InGaN/GaN	395	-10	0.180	2.77×10^{11}	95/30 ms	-
***D*[34]**	CoPc/GaN	380	0	0.588	4.80×10^{12}	0.71/0.5 s	80
***E*[35]**	Cs_2SnCl_6:Bi/GaN	400	-2	0.208	1.20×10^{12}	75/91 µs	71
***F*[36]**	$MAPbCl_3$/GaN	400	0.5	0.430	4.11×10^{12}	70/72 µs	160
***G*[37]**	4H-SiC	380	-0.5	0.042	4.92×10^{11} [a]	1.7/1.8 ms	100
H[38]	TiO_2/Co_3O_4	400	0	3	2.70×10^{11}	0.2/1 ms	77

---

[a] Value not reported in the publication, calculated based on provided experimental data.

The developed LSC-PV devices show performances largely comparable to the state of the art for wide bandgap photodetectors.[4,18,30] **Table 5.2** offers a comparison between **F750** and representative examples for semiconductor-based, visible-blind photodetectors. Reported devices were chosen on the basis of their cutoff wavelength, close to the one of **F750**.

Responsivity values reported in the literature are generally higher than **F750**. Nonetheless, the specific detectivity, which properly quantifies the detecting capabilities of a photodetector, falls amply within the literature range. Considering the time response, **F750**, with rise and fall times of a few milliseconds, shows remarkable speed with respect to other devices (from ***A*** to ***D***, based on ZnO and GaN composites). Devices ***F*** and ***G*** (SiC and TiO_2, respectively) show comparable time responses to **F750**, while devices ***E*** and ***F*** (GaN/perovskite heterojunctions) reach the microseconds scale. Similarly to the responsivity, the semiconductor-based photodetectors possess generally larger linear dynamic ranges with respect to **F750**. However, when discussing these two parameters for the presented LSC-PV photodetectors, it is reasonable to assume that both are underestimated, a finding that can be attributed to the intentionally basic setup employed. Considering that the measurements were performed with just one PV-coupled edge and results were not corrected for any geometrical factor, the overall performance of the LSC sensors if all four edges were PV-coupled would increase by at least a factor of four. Based on previous experimental evidence, introducing optical coupling between the waveguide and the cell would further increase the electrical outputs by 30%. Additionally, using a proper photodetector rather than a PV cell as edge sensor, like an amplified photodiode, would significantly improve the sensitivity of the whole system to optical power variations (*i.e.*, the responsivity).

Future investigations will surely replace the PV cell with such a device and introduce a transimpedance amplifier for low light measurements. Even so, with the simple experimental setup herein presented, the potential functionality of Eu^{3+}-based LSC-PVs as UV visible-blind photodetectors has been demonstrated.

5.4 Bibliography

1 K. W. A. Chee, in *Advances in Photodetectors - Research and Applications*, IntechOpen, 2018.

2 M. Wadsworth, in *Encyclopedia of Imaging Science and Technology*, John Wiley & Sons, Ltd, 2002.

3 X. Gong, M. Tong, Y. Xia, W. Cai, J. S. Moon, Y. Cao, G. Yu, C.-L. Shieh, B. Nilsson and A. J. Heeger, *Science*, 2009, **325**, 1665–1667.

4 F. Cao, Y. Liu, M. Liu, Z. Han, X. Xu, Q. Fan and B. Sun, *Research*, 2024, **7**, 0385.

5 T. I. U. of P. and A. Chemistry (IUPAC), IUPAC - limit of detection (L03540), https://goldbook.iupac.org/terms/view/L03540, (accessed 8 August 2025).

6 C. Liu, J. Guo, L. Yu, J. Li, M. Zhang, H. Li, Y. Shi and D. Dai, *Light Sci. Appl.*, 2021, **10**, 123.

7 W. Tian, H. Sun, L. Chen, P. Wangyang, X. Chen, J. Xiong and L. Li, *InfoMat*, 2019, **1**, 140–163.

8 I. Kimukin, N. Biyikli, B. Butun, O. Aytur, S. M. Unlu and E. Ozbay, *IEEE Photonics Technol. Lett.*, 2002, **14**, 366–368.

9 X. Li, J. Zhang, C. Yue, X. Tang, Z. Gao, Y. Jiang, C. Du, Z. Deng, H. Jia, W. Wang and H. Chen, *Sci. Rep.*, 2022, **12**, 7681.

10 Y. Ye, H. Ma, J. Wu, B. Sun, J. Jian, M. Wei, R. Tang, Y. Shi, H. Lin and L. Li, *IEEE J. Sel. Top. Quantum Electron.*, 2024, **30**, 1–8.

11 B.-G. An, H.-R. Kim, Y. W. Chang, J.-G. Park and J.-C. Pyun, *J. Korean Ceram. Soc.*, 2021, **58**, 631–644.

12 K. Deng and L. Li, *Adv. Mater.*, 2014, **26**, 2619–2635.

13 A. Rogalski, Z. Bielecki, J. Mikołajczyk and J. Wojtas, *Sensors*, 2023, **23**, 4452.

14 F. Omnes and E. Monroy, in *Nitride Semiconductors*, John Wiley & Sons, Ltd, 2003, pp. 627–660.

15 E. Monroy, E. Muñoz, F. J. Sánchez, F. Calle, E. Calleja, B. Beaumont, P. Gibart, J. A. Muñoz and F. Cussó, *Semicond. Sci. Technol.*, 1998, **13**, 1042.

16 Z. Ma, J. Zhang, H. Lyu, X. Ping, L. Pan and Y. Shi, in *Metal Oxides for Optoelectronics and Optics-Based Medical Applications*, eds S. Sagadevan, J. Podder and F. Mohammad, Elsevier, 2022, pp. 117–150.

17 W. Tian, H. Lu and L. Li, *Nano Res.*, 2015, **8**, 382–405.

18 M. Banari, N. Memarian, P. Kumar, S. You, A. Vomiero and I. Concina, *Ceram. Int.*, 2025, **51**, 9–16.

19 C. Xie, C.-K. Liu, H.-L. Loi and F. Yan, *Adv. Funct. Mater.*, 2020, **30**, 1903907.

20 M. Afroz, R. K. Ratnesh, S. Srivastava and J. Singh, *Sol. Energy*, 2025, **287**, 113205.

21 Y. Yu, B. Luszczynska and M. Z. Szymanski, *Semicond. Sci. Technol.*, 2020, **35**, 104002.

22 S. Sahu and A. J. Pal, in *2007 International Workshop on Physics of Semiconductor Devices*, 2007, pp. 560–562.

23 T. M. H. Nguyen and C. W. Bark, *ACS Appl. Mater. Interfaces*, 2022, **14**, 45573–45581.

24 X. Sheng, C. Yu, V. Malyarchuk, Y.-H. Lee, S. Kim, T. Kim, L. Shen, C. Horng, J. Lutz, N. C. Giebink, J. Park and J. A. Rogers, *Adv. Opt. Mater.*, 2014, **2**, 314–319.

25 S. M. Geyer, J. M. Scherer, N. Moloto, F. B. Jaworski and M. G. Bawendi, *ACS Nano*, 2011, **5**, 5566–5571.

26 Y. Zhu, A. Apostoluk, S. Liu, S. Daniele and B. Masenelli, *J. Semicond.*, 2013, **34**, 053005.

27 M. Portnoi, P. A. Haigh, T. J. Macdonald, F. Ambroz, I. P. Parkin, I. Darwazeh and I. Papakonstantinou, *Light Sci. Appl.*, 2021, **10**, 3.

28 W. Wang and J. C. Ho, *Light Sci. Appl.*, 2022, **11**, 125.

29 N. Ding, Y. Wu, W. Xu, J. Lyu, Y. Wang, L. Zi, L. Shao, R. Sun, N. Wang, S. Liu, D. Zhou, X. Bai, J. Zhou and H. Song, *Light Sci. Appl.*, 2022, **11**, 91.

30 R. Zhang, G. Wang, Q. Zhang, S. Wang, X. Hu, L. Liu, S. Lv, W. Chen, X. Xu and L. Zhang, *J. Mater. Chem. C*, 2025, **13**, 10972–10996.

31 B. Hanna, L. R. Pillai, K. Rajeev, K. P. Surendran and K. N. N. Unni, *Sens. Actuators Phys.*, 2022, **338**, 113495.

32 M. H. Tran, T. M. H. Nguyen and C. W. Bark, *ACS Omega*, 2023, **8**, 35343–35350.

33 F. Xie, Y. Yao, Y. Gu, Z. Hu, B. Yu and G. Yang, *IEEE Trans. Electron Devices*, 2023, **70**, 4685–4688.

34 Y. Xiao, L. Liu, Z.-H. Ma, B. Meng, S.-J. Qin and G.-B. Pan, *Nanomaterials*, 2019, **9**, 1198.

35 D. Shao, W. Zhu, G. Xin, J. Lian and S. Sawyer, *Appl. Phys. Lett.*, 2019, **115**, 121106.

36 S. Jiang, W. Wei, S. Li, Y. Tian, Y. Yun, M. Chen, K. Huang, C. Li and R. Zhang, *ACS Photonics*, 2024, **11**, 3026–3036.

37 S. Guo, X. Zhao, Y. He, Y. Cai, M. Yang, X. Guo, X. Fu and L. Zhang, *IEEE Trans. Electron Devices*, 2021, **68**, 6208–6215.

38 P. Mahala, M. Patel, D.-K. Ban, T. T. Nguyen, J. Yi and J. Kim, *J. Alloys Compd.*, 2020, **827**, 154376.

39 W. Budde, *Appl. Opt.*, 1979, **18**, 1555–1558.

Chapter 6

High performance oligothiophene-based LSCs

In this *Chapter*, a second study on LSCs and their application as photovoltaic devices is presented. The luminophores herein employed are a series of strongly fluorescent thiophene oligomers, designed and synthetized by Dr. Manuela Melucci's research group (CNR-ISOF, Bologna). A state-of-the-art fluorescent organic dye (Lumogen® F Red 305) has been included in the study as benchmark compound. After a pre-screening of the photophysical properties displayed by the molecules in solution, best performing fluorophores have been embedded in 35 μm thick PMMA films, deposited onto glass substrates with active area of 50 × 50 mm^2 via slot die coating. Both LSCs and derived LSC-PV devices have been fully characterized according to the reporting protocols explained in *Chapter 3*. Photodegradation tests have also been carried out to assess the stability of the as prepared devices. Finally, the degree of bifaciality of the LSC-PVs, *i.e.*, the ability of a solar device to generate electricity when illuminated from its back surface rather than the front one, has been determined by testing them in rear-illumination conditions.

6.1 Luminophores

A series of seven oligothiophene derivatives was initially considered for the development of the LSCs. Their molecular structures (**Fig.s 6.1a** to **g**) involve an inner electron deficient fused heterocycle or an oxidized thiophene core, a linear or V shaped geometry and alkyl chain modified rings as end groups.

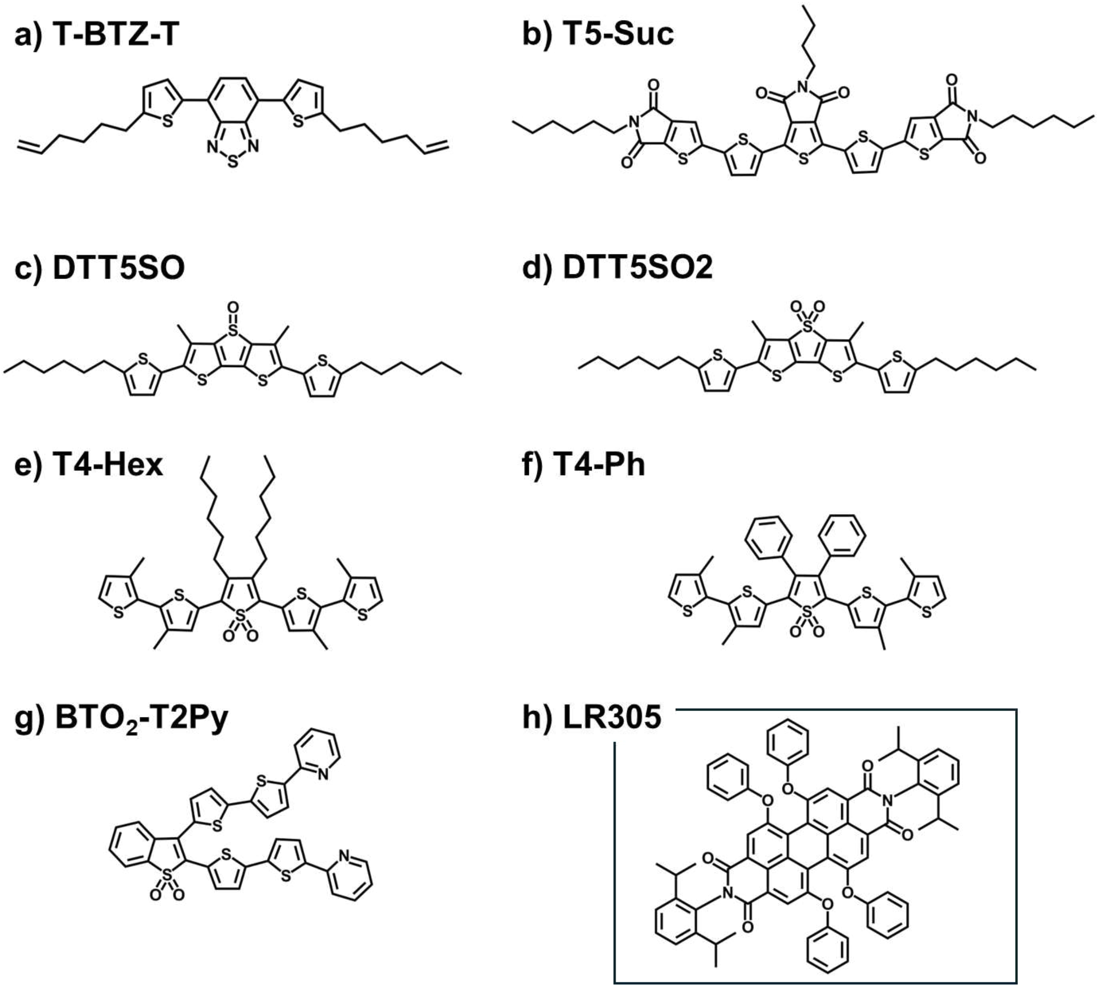

Figure 6.1. Molecular structures of the employed luminophores: **a)** to **g)** oligothiophenes and **h)** reference dye Lumogen® F Red 305.

It is known that the electronic properties of oligothiophenes are heavily influenced by their structure and functionalization.[1,2] By adopting an appropriate molecular design, the emission, charge transfer properties and even aggregation behaviour of these molecules can be tuned to the desired end application. Specifically, previous computational analyses[3–5] carried out on the oligothiophenes used in this study have demonstrated that their unique molecular structures enable absorption and emission in the visible spectrum with large Stokes shift, thereby revealing their potential for LSC development. For LSCs employing organic dyes, the benchmark fluorophore in the field is the perylene-based dye Lumogen® F Red 305 (LR305, **Fig. 6.1h**) developed by BASF, which has been widely employed since earlier LSC studies to theorize their working mechanism[6–8] and to test several polymers as possible embedding mediums.[9] Since LR305 is commercially available and provides benchmark values for LSC optical and electrical performances, it is frequently included in studies proposing novel organic dyes for LSC development.[10,11]

The photophysical properties of the luminophores were first evaluated in a DMSO/THF 3:2 solution, *i.e.*, in the solvent mixture used for the deposition of PMMA films through the slot die coating technique described in *Chapter 2*. The relevant photophysical parameters of each compound are listed in **Table 6.1**, while the absorption and emission spectra are displayed in **Fig. 6.2**.

Table 6.1. Maximum absorption wavelength (λ_{max}), molar extinction coefficient (ε_{max}), maximum emission wavelength (λ_{PL}), photoluminescence quantum yield ($PLQY$), molar brightness ($B = \varepsilon_{max} \times PLQY$) and Stokes shift values collected for $1\cdot10^{-5}$ M solutions of the luminophores in DMSO/THF 3:2.

Luminophore	λ_{max} **/ nm**	ε_{max} **× 10⁴ / M⁻¹ cm⁻¹**	λ_{PL} **/ nm**	$PLQY$	**Brightness / M⁻¹ cm⁻¹**	**Stokes shift / nm**
T-BTZ-T	472	1.49	622	0.75	11 175	150
T5-Suc	470	2.86	581	0.24	6 864	111
DTT5SO	450	2.03	604	0.86	17 458	154
DTT5SO2	447	2.17	589	0.88	19 096	142
T4-Hex	454	2.42	605	–[a]	–[a]	152
T4-Ph	478	2.67	637	–[a]	–[a]	158
BTO$_2$-T2Py	450	2.78	530	–[a]	–[a]	80
LR305	575	3.73	610	1.00	37 300	35

---

[a] $PLQY$ values are not available for these samples because their emission intensities were too low to perform reliable $PLQY$ measurements. Hence, it was not possible to calculate the brightness.

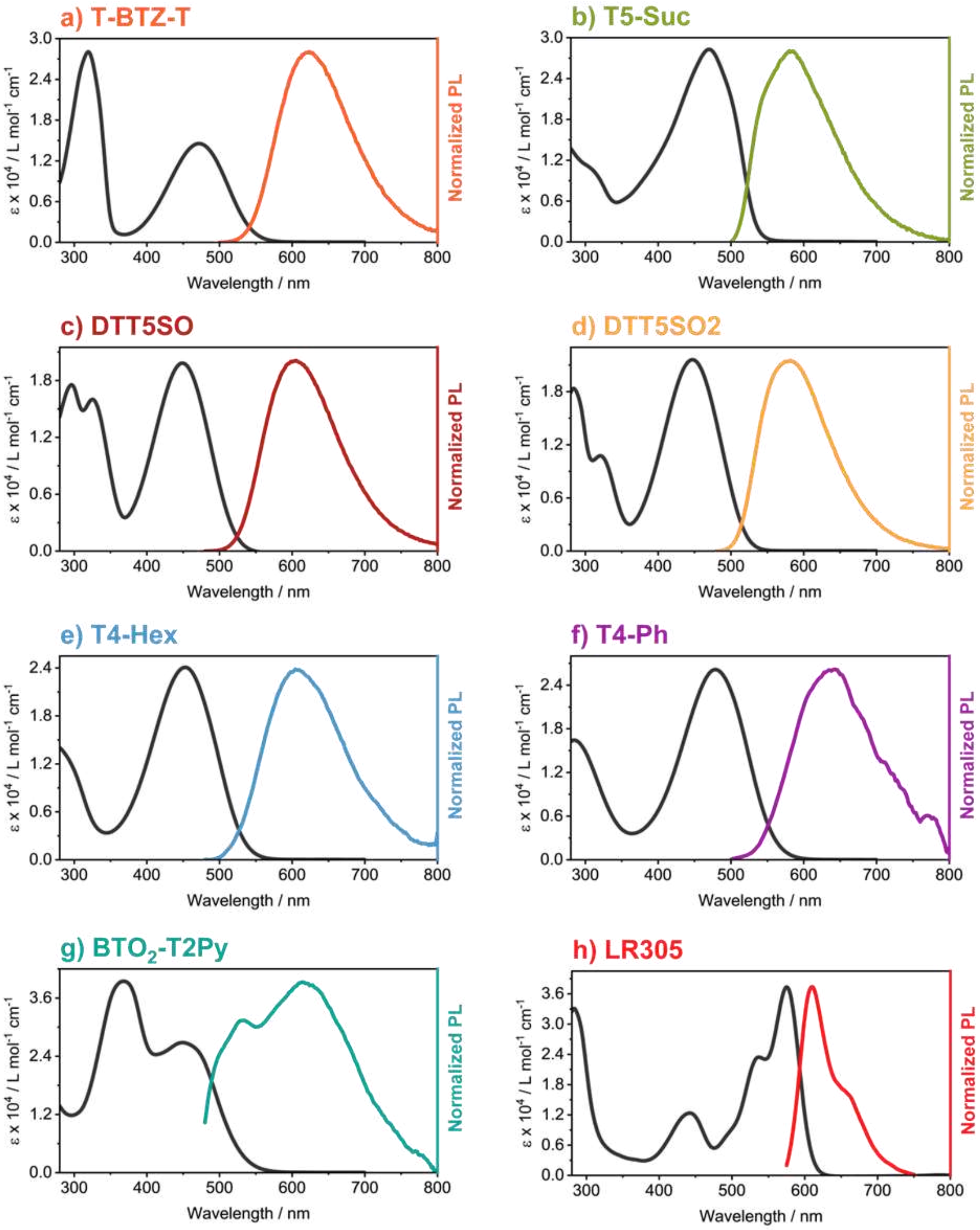

Figure 6.2. Absorption and emission spectra of $1{\cdot}10^{-5}$ M solutions of the luminophores in DMSO/THF 3:2. **a)** to **g)** Oligothiophenes. **h)** Reference dye Lumogen® F Red 305.

All oligothiophenes show two absorption maxima. Starting from the shorter wavelengths, the first peak falls in the UV region, shifting significantly across different molecules: it falls below 300 nm for T4-Hex, T4-Ph and T5-Suc (outside the sampled wavelength window), it is centred at around 300 nm for T-BTZ-T, DTT5SO and DTT5SO2, and finally shifts up to 370 nm in BTO$_2$-T2Py. By contrast, the second peak occurs more regularly, typically between 450 and 470 nm, and exhibits a uniform shape across the absorption spectra. This second absorption maximum has been considered for brightness calculation and has been used as excitation wavelength in collecting the reported emission spectra. LR305 instead exhibits several absorption bands, with the main one centred at 575 nm. LR305 also displays the highest brightness among the investigated luminophores (B = 37300 M^{-1} cm^{-1}), thanks to an increased absorption coefficient and unity $PLQY$. Focusing on the oligothiophenes, DTT5SO and DTT5SO2 are the brightest compounds of the series, with B values around 17400 and 19000 M^{-1} cm^{-1}, respectively. T-BTZ-T (11000 M^{-1} cm^{-1}) and T5-Suc (6800 M^{-1} cm^{-1}) follow, while the remaining BTO_2-T2Py, T4-Hex and T4-Ph are basically non-emitting in solution. All oligothiophenes, except for BTO_2-T2Py, display remarkable Stokes shifts of over 100 nm, with highest values surpassing 150 nm. Conversely, LR305 absorption and emission bands overlap significantly, producing a Stokes shift of just 35 nm.

6.2 Materials

The LSCs have been prepared using a slot die coater, through the optimized deposition procedures described in *Chapter 2*. For all samples, a solution composition of 10% by weight of PMMA in DMSO/THF 3:2 has been employed, introducing the desired amount of luminophore to realize luminescent films. The following discussion concerns the photophysical characterizations of the luminophores embedded in PMMA and the optical characterizations necessary to accurately report LSCs ($T\%$, $R\%$, $A\%$ spectra, AVT, CRI, $CIELAB$ coordinates, $\eta_{s,abs}$). See *Chapter 9: Experimental* for the detailed procedures.

It is known that the emission properties of oligothiophenes are strongly dependent on the solvent and can change based on whether intermolecular aggregates or organized self-assembled structures are present.[12–14] To ascertain if emission enhancing or quenching effects could occur upon embedding into PMMA, the photophysical properties of BTO_2-T2Py, T4-Hex and T4-Ph, which previously showed very weak emission in solution, were further investigated by preparing and characterizing the corresponding supported film LSCs.

Two films were realized for each luminophore, doped at 8 and 25 mM. These concentrations were representative of the accessible luminophore loading range in the PMMA films. Relevant photophysical parameters collected for the films are listed together below in **Table 6.2**, while the absorption and emission spectra are displayed in **Fig. 6.3**, superimposed to solution spectra for direct comparison.

Table 6.2. Maximum absorption (λ_{max}) and emission (λ_{PL}) wavelengths, photoluminescence quantum yield ($PLQY$) and Stokes shift values collected for PMMA films containing the luminophores at the concentration of 8 and 25 mM.

Film concentration / mM	λ_{max} / nm	λ_{PL} / nm	$PLQY$	**Stokes shift / nm**	λ_{max} / nm	λ_{PL} / nm	$PLQY$	**Stokes shift / nm**
	T-BTZ-T				***T5-Suc***			
8	472	602	0.89	130	470	603	0.12	133
25	472	607	0.82	135	470	608	0.10	138
	DTT5SO				***DTT5SO2***			
8	450	584	0.88	134	447	567	0.88	120
25	450	594	0.70	144	447	574	0.83	127
	T4-Hex				***T4-Ph***			
8	453	587	0.24	134	480	620	0.13	140
25	453	595	0.21	142	480	626	0.12	146
	BTO_2-T2Py				***LR305***			
8	450	591	0.05	141	575	652	0.78	77
25	450	605	0.05	155	575	658	0.66	83

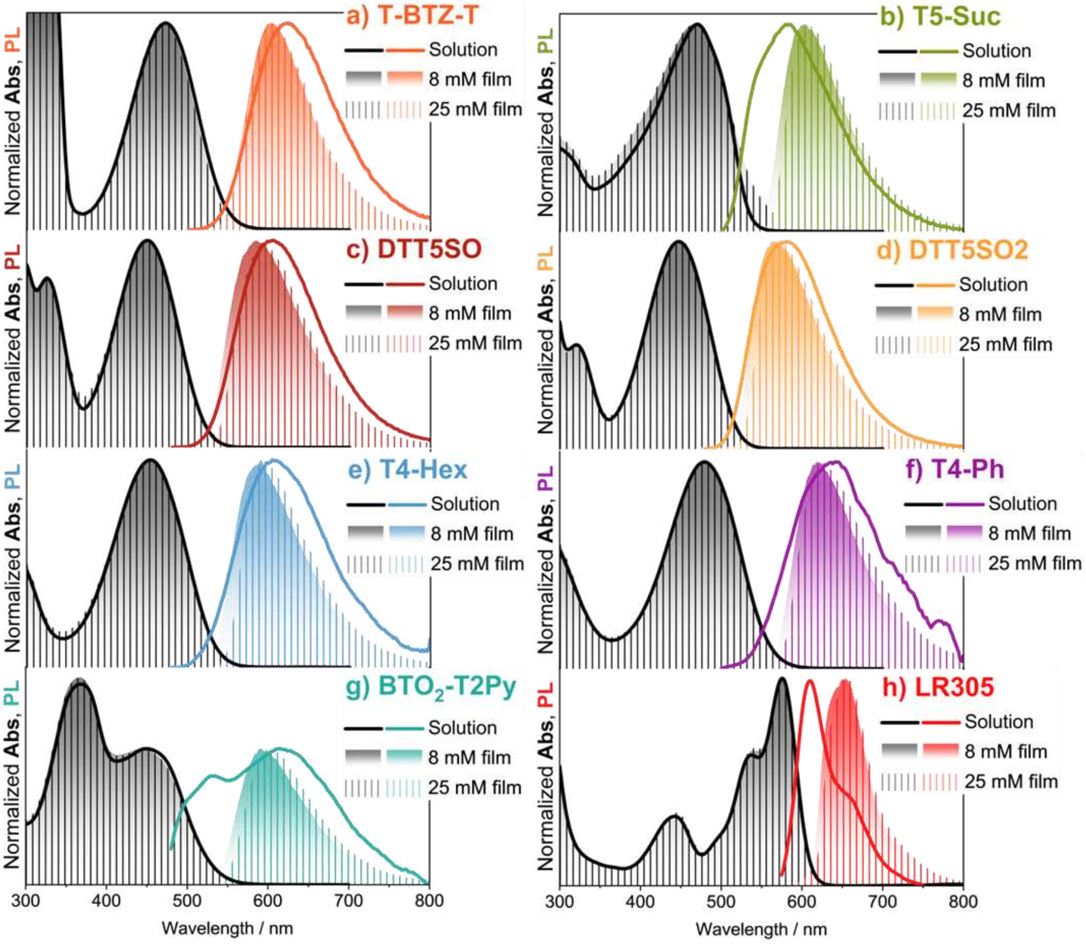

Figure 6.3. Normalized absorption and emission spectra of 25 × 25 mm^2 LSCs containing the different luminophores at 8 mM (colour fill) and 25 mM (stripes fill), superimposed to normalized absorption and emission spectra of the corresponding $1{\cdot}10^{-5}$ DMSO/THF 3:2 solutions (solid lines). **a)** to **g)** Oligothiophenes. **h)** Reference dye Lumogen® F Red 305.

Regarding the absorption of the luminophores embedded in PMMA, the band shape remains essentially unchanged compared to that of the solutions. The PL characterizations instead present a more variegated picture. The spectra of T-BTZ-T, DTT5SO and DTT5SO2 do not show notable alterations in their shape. The $PLQY$ values of DTT5SO 8 mM and both DTT5SO2 samples remain very similar to the ones observed in solution, while DTT5SO 25 mM exhibit roughly a 20% drop with respect to the solution. Conversely, both T-BTZ-T films have their $PLQY$ enhanced, up to a 15% increase for the 8 mM sample. T4-Hex, T4-Ph and BTO$_2$-T2Py, not emitting in solution, displayed instead easily detectable fluorescence in PMMA, with $PLQY$ up to 20% (T4-Hex). For these compounds, a direct comparison between solution and film emission is not straightforward. Finally, T5-Suc and LR305 were the two compounds exhibiting the lowest Stokes shifts among the brightest emitters in solution (B > 6500 M^{-1} cm^{-1}). When embedded in PMMA, self-absorption effects become evident, leading to an apparent red shift of the emission peak and large reduction in $PLQY$: from 24% to 10% for T5-Suc and from unity to 70% for LR305 (25 mM samples).

At this stage, a selection among the different luminophores has been made to identify the best candidates for LSC development. However, it was not possible to accurately determine the film thickness of the samples used for the photophysical characterizations. Assuming that the molar extinction coefficient of the luminophores remains the same in going from the solution to the film, the selection has been based on the $PLQY$ alone. Keeping LR305 as reference dye, the other luminophores chosen for LSC development were T-BTZ-T, DTT5SO and DTT5SO2.

Samples having a standard size of 25 cm^2 active area were then realized for these four luminophores, to later be tested as LSC-PV devices. For each selected compound, four samples were prepared with concentrations progressively increasing from 2.7 up to 28 mM. Precise concentrations and sample labelling are reported in **Fig. 6.4**. The films were 35 μm thick and were deposited onto N-BK7 glass 3 mm thick. All six faces of the glass slides were optically polished. The T% and R% spectra were collected on a spectrophotometer equipped with an integrating sphere, applying the filter correction described in *Section 3.1*.

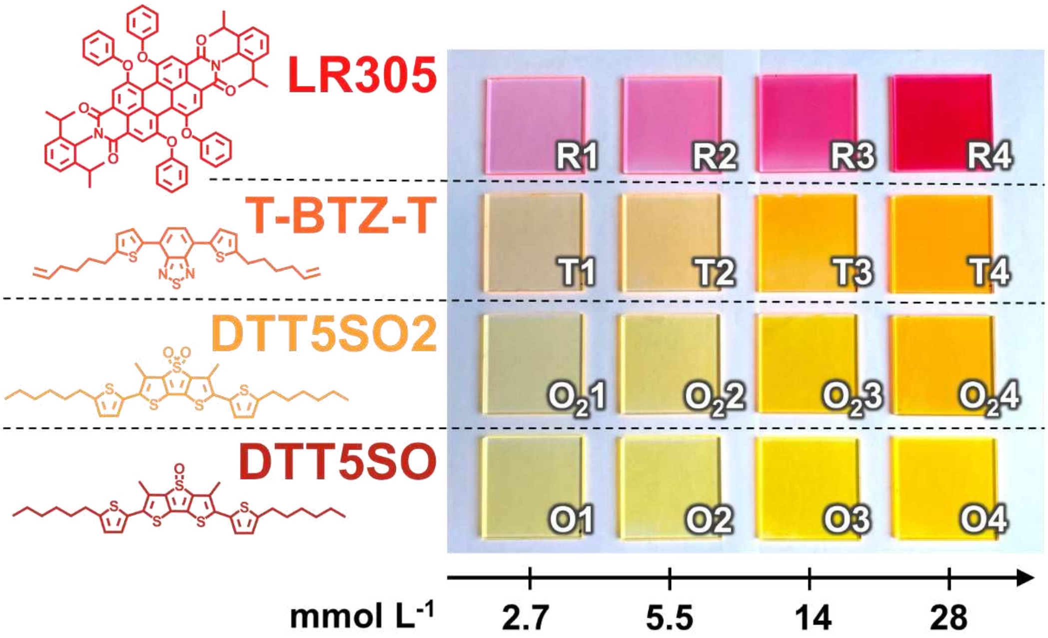

Figure 6.4. Photographs of the 50 × 50 mm^2 LSCs in ambient lighting, with corresponding concentrations and labelling.

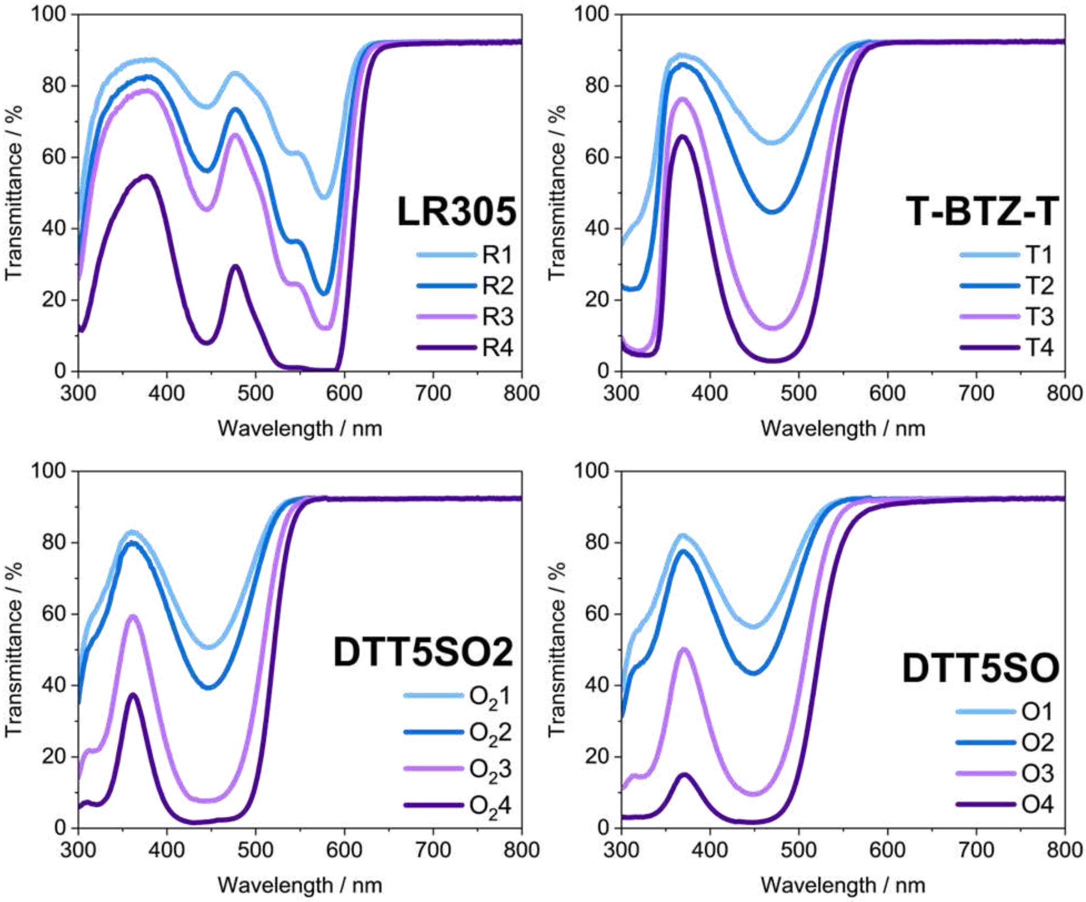

Figure 6.5. Transmittance spectra of the 50 × 50 mm^2 LSCs.

For brevity, only $T\%$ spectra (**Fig. 6.5**) and the derived parameters are reported. $R\%$ characterizations can be found in *Appendix C3.1*. For each series of samples, $T\%$ decreases with increasing luminophore concentration. In the case of the 28 mM samples, $T\%$ is very close to 0% within the absorption maxima, denoting full light absorption. Consequently, AVT values show the same concentration trends, with higher concentrations having lower visible transparency (**Table 6.3**).

LR305, displaying the maximum light absorption in the green region of the visible spectrum, where the human eye's photopic response is the highest, produces the samples with the lowest AVT values at each concentration. **R4** displays the lowest value of the whole LSC set, with AVT = 14%. Among the oligothiophene samples, the DTT5SO and DTT5SO2 series have the highest AVTs, followed by T-BTZ-T (**O$_2$4**: AVT = 77%, **O4**: AVT = 72%, **T4**: AVT = 66%). In particular, **O** and **O$_2$** samples have very similar AVT values at each concentration. Considering the opposite concentration trends between visible transparency and electrical power production, the LSC-PVs based on the 28 mM samples are expected to produce the highest electrical outputs.

Table 6.3. Total absorptance ($\eta_{s,abs}$), average visible transmittance (AVT), color rendering index (CRI) and (a*, b*) $CIELAB$ coordinates calculated for the LSCs. Colour parameters are given for transmittance characterizations.

Sample	$\eta_{s,abs}$ **/ %**	**AVT / %**	**CRI**
LR305			
R1	4.50	66.07	74.90
R2	8.14	46.45	38.82
R3	10.30	35.84	8.36
R4	16.68	13.78	< 0
T-BTZ-T			
T1	2.58	87.58	85.64
T2	4.47	83.46	82.49
T3	8.51	73.27	61.12
T4	10.63	65.98	47.83
DTT5SO2			
O₂1	3.15	89.28	89.45
O₂2	4.09	88.20	85.84
O₂3	8.00	82.37	67.09
O₂4	10.02	76.83	51.03
DTT5SO			
O1	2.73	89.31	90.84
O2	3.89	87.92	86.67
O3	8.00	80.91	68.62
O4	10.61	72.49	49.84

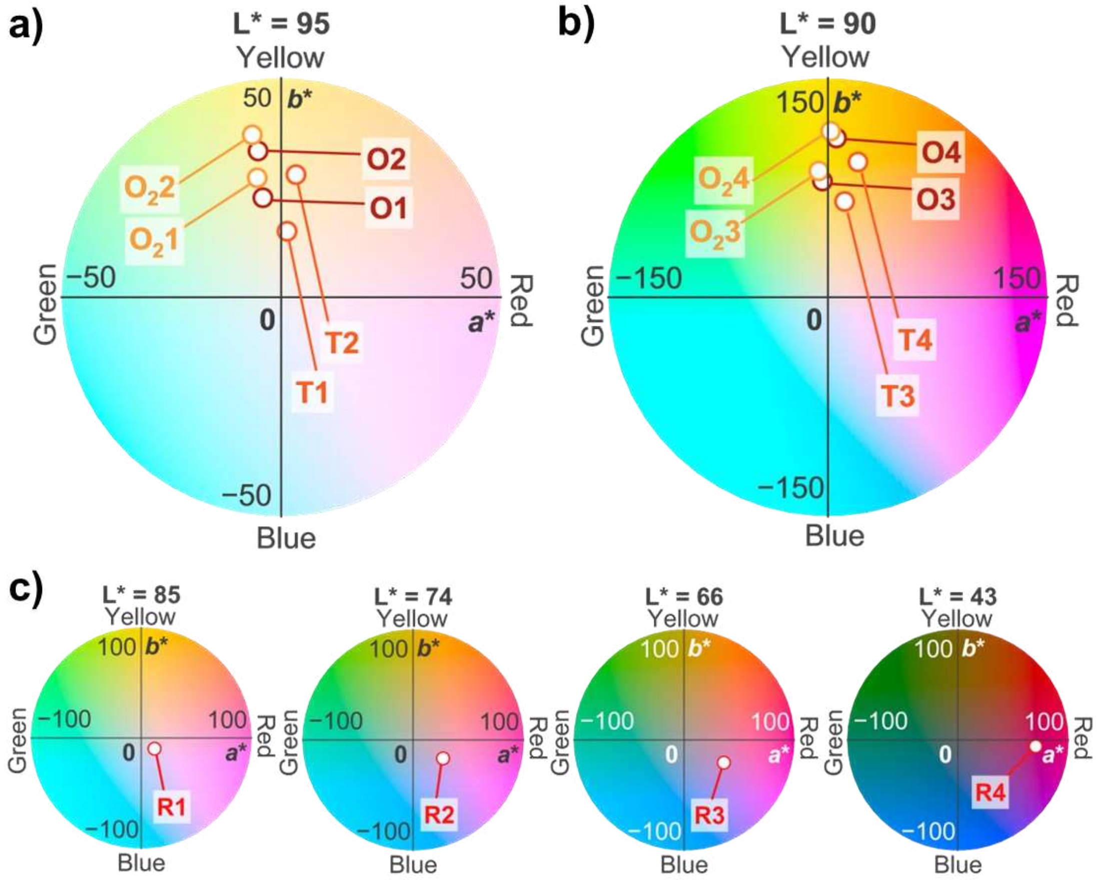

Figure 6.6. $CIELAB$ 2D polar graphs displaying the colour coordinates of the transmitted light for the oligothiophene-based LSCs doped at **a)** 2.7, 5.5 mM and **b)** 14, 28 mM. Samples with similar L^* values have been grouped together. **c)** The same $CIELAB$ graphs for the LR305 series: each sample is displayed in a separate plot due to markedly different L^* values.

Table 6.3 also reports the CRI and the $CIELAB$ coordinates of the LSCs for the transmitted radiation. Heavier colour distortion is observed within each luminophore series with increasing concentration (**Fig. 6.6**), as CRI values decrease and colour coordinates deviate more from the origin (0, 0). The same colour parameters trends are observed also for the reflected radiation (*Appendix C3.1*).

Notably, calculations for **R4** yield a negative CRI value of the transmitted light. Although not contemplated in the standard 0 – 100 scale, the CRI definition allows for negative results, which are often rounded up to zero to indicate that the examined light source provides extremely poor colour fidelity. The occurrence of negative values is one of the known limitations of CRI, for which alternative colour rendering metrics have been proposed.[15,16] In the presented LSC analysis, the relevant conclusion is that **R4**, and in general all LR305 doped samples, distorts the colours of the transmitted light in a significantly larger capacity with respect to the LSCs doped with the oligothiophenes at the same concentrations.

The total absorptance ($\eta_{s,abs}$, **Eq. 3.5**), indicating the fraction of the AM1.5G photon flux that the LSCs effectively absorb, has been calculated for all samples and is reported in **Table 6.3** as well. A clear trend with concentration is found also in this case, with higher loadings determining a larger fraction of absorbed photons. All oligothiophene-doped LSCs display very similar total solar absorptance at each concentration. For example, 28 mM samples all present $\eta_{s,abs}$ around 10%. Conversely, the **R** series holds the highest absorption at all investigated luminophore loadings, reaching a value close to 17% for **R4**.

6.3 Devices

Analogously to the LSC-PV characterizations described in *Chapter 4*, the LSCs were optically coupled to monocrystalline Si solar cells along one edge and their J-V curves and EQE spectra were acquired on the dedicated experimental setups. EQE consistency checks (integrated J_{SC} and device photon balance) were satisfied for all samples and are available in *Appendix C3.2*.

Highest electrical outputs are found for the most concentrated sample in all series (**Fig. 6.7a**), except for DTT5SO, with **O4** (28 mM) showing a J-V even smaller than the one collected for **O2** (5.5 mM). Examining the EQE spectra, the same deviation from the trend is observed, with **O4** showing a markedly different spectral shape with respect to the other DTT5SO samples (**Fig. 6.7b**). Instead, similar EQE shapes at increasing concentration are observed in all other luminophore series.

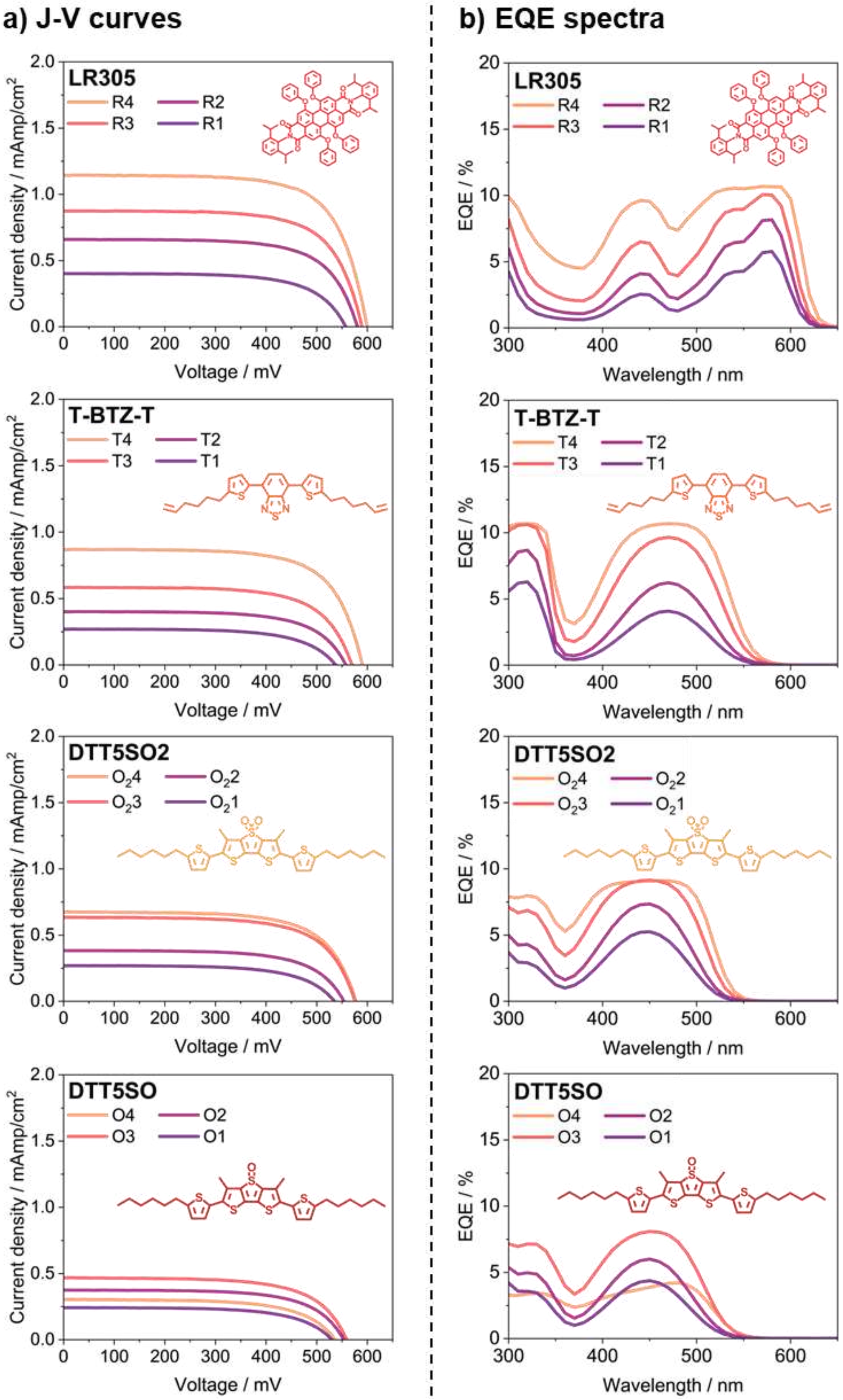

Figure 6.7. a) J-V curves and **b)** EQE spectra of all LSC-PVs. The electrical output generally increases with increasing luminophore concentration. All data has been acquired using the LSC-PV one-edge configuration. For each sample, the displayed EQE spectrum has been derived by averaging equally spaced, position-dependent acquisitions.

The cause of this peculiar behaviour of DTT5SO is not yet ascertained, but the first hypothesis is that fluorescence-quenching aggregation has occurred inside the polymeric matrix for **O4**. As already mentioned, oligothiophenes are known to stack into aggregates, with consequences on their fluorescence properties.[12–14] The molecules developed in this work have been appositely designed to prevent this phenomenon, but it is plausible that beyond a limiting concentration some aggregation occurs anyway. The drop of the $PLQY$ in going from an 8 to a 25 mM concentration observed for the 25 × 25 mm^2 LSCs is another factor pointing in this direction. Further investigation will be needed to determine the existence of such aggregates. Among the oligothiophene-based samples, **T4** (T-BTZ-T) performs best with a PCE of 0.36% (**Table 6.4**), while the reference sample containing LR305 yields a PCE of 0.48%, meaning that the output of **T4** is 75% of that of **R4**.

Table 6.4. Power Conversion Efficiency (PCE) and Light Utilization Efficiency (LUE) of the LSCs, relative to one-edge outputs. J_{SC}, V_{OC} and FF values are reported in *Appendix C3.2*.

Sample	**PCE / %**	**LUE / %**	**Sample**	**PCE / %**	**LUE / %**
LR305			***T-BTZ-T***		
R1	0.15	0.10	**T1**	0.09	0.08
R2	0.26	0.12	**T2**	0.15	0.12
R3	0.36	0.13	**T3**	0.22	0.16
R4	0.48	0.07	**T4**	0.36	0.24
DTT5SO2			***DTT5SO***		
O$_2$1	0.09	0.08	**O1**	0.08	0.07
O$_2$2	0.14	0.12	**O2**	0.14	0.12
O$_2$3	0.25	0.20	**O3**	0.17	0.14
O$_2$4	0.26	0.20	**O4**	0.10	0.07

This is a significant result, considering the marked difference in the absorption capabilities of the two LSCs evidenced by $\eta_{s,abs}$. The drop in $PLQY$ of LR305 due to increased reabsorption at higher luminophore loadings limits its performance, while T-BTZ-T is less affected by such losses and yields good energy production even when increasing the loading. Samples **O₂4** and **O4** follow, with PCEs of 0.27% and 0.18%, respectively.

A comparison with the relevant literature evidences the competitivity of T-BTZ-T among other organic molecular LSC fluorophores. In a study by Bartolini *et al.*, a series of benzodithiophene tetraoxide luminophores with emission maxima tailored beyond 650 nm has been used to develop analogous supported PMMA films for LSCs.[10] Maximum PCE values registered for samples of comparable loadings ranged from 0.2% to 0.7%, although no information on edge and background blackening during J-V acquisitions was specified. The authors included a reference LSC series based on LR305, which produced also in this case the highest electrical outputs, while the best performing novel luminophore reached 90% of the corresponding LR305 sample's PCE. Comparison of the herein reported results with other published LSC organic dyes, as triarylamines,[17] aggregation-induced fluorinated emitters[18] and donor-acceptor combined dye systems[19] revealed comparable if not superior behaviour of **T4** and **O4** samples. However, a detailed reporting of the experimental setup and conditions used for LSC-PV characterizations is lacking also in these cases.

At this point, we have obtained a set of LSC-PVs with different colorations and transparency degrees, two characteristics closely related to their energy production. To account for the global LSC-PV performance yielded by the combination of these two factors, the Light Utilization Efficiency (LUE, %) is the best suited metric. The LUE is defined as the product between PCE and AVT and quantifies the ability of a PV device to simultaneously optimize both visible transparency and power conversion.[20,21] In the present study, while **R4** exhibits the highest PCE, its LUE drops to 30% of that of **T4** due to poorer colour rendering capability. This parameter becomes particularly important if the device is designed for application in BIPVs with strict aesthetic requirements. Otherwise, heavily coloured LSC panels could find better deployment in smart artistic installations or as indoor PVs. Based on such considerations, the bifaciality of the developed LSC-PVs was investigated by collecting their J-V curve when back-illuminated. To evaluate this aspect, a bifaciality coefficient (χ_{bi}) was calculated as the ratio between the power conversion efficiencies of the device when illuminated from the rear side with respect to the front illumination. Both PCEs are relative to standard AM1.5G illumination conditions:[22]

$$\chi_{bi} = \frac{PCE_{rear}}{PCE_{front}} \qquad \textbf{Eq. 6.1}$$

A mean reduction of only 10% in output with respect to the front illumination was observed (**Fig. 6.8**), demonstrating the viability of the prepared LSCs for indoor energy production.

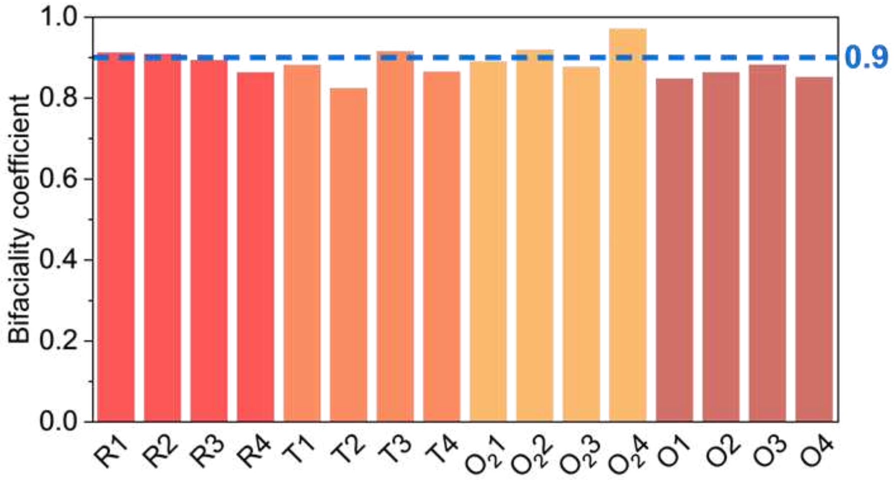

Figure 6.8. Column plot of the bifaciality coefficient calculated for each LSC sample as the ratio between the PCEs extracted in rear and front illumination conditions.

As a recommended reporting metric, the internal photon efficiency (η_{int}, **Eq. 3.15**) was then calculated for all samples and examined as a function of the luminophore concentration (**Fig. 6.9**). A general decrease of η_{int} along all series is observed, which is the result of the simultaneous decrease in $PLQY$ and increase in reabsorption losses with increasing luminophore loading.

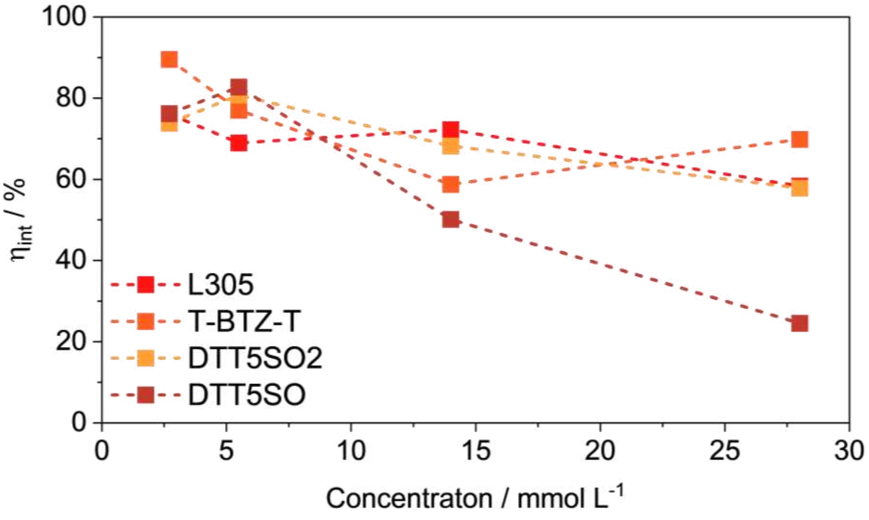

Figure 6.9. Scatter plot of the LSC internal photon efficiency variations with increasing luminophore loading along each sample series.

The most marked effect is observed for **O4** (lowest η_{int} of 25%), which already showed poorer electrical performance with respect to the other 28 mM samples. Interestingly, LR305 and DTT5SO2 show very similar efficiency values, with almost an identical concentration trend. As for T-BTZ-T, both **T1** an **T4** show the highest η_{int} values of the respective concentrations. In particular, **T4** exhibits an internal efficiency of 76%, followed by **R4** and **O$_2$4** with a 20% efficiency decrease.

Finally, the photostability of the most concentrated samples has been ascertained. Although investigation into the photostability of LSC luminophores is scarcely reported, this characterization is extremely important to evaluate the actual deployment feasibility of the device in real-life conditions. Proper photostability tests should be carried out spanning over months of even years, but few to no laboratories are adequately equipped, and there are no certified protocols in this regard. Nonetheless, performing preliminary screenings on a shorter time scale can still offer valuable feedback. A 7-hours photobleaching test was carried out on the 28 mM samples by continuously irradiating them with 1 sun AM1.5G simulated illumination at room temperature. The output short-circuit current density was monitored through an ammeter and referenced to the initial value prior to illumination (**Fig. 6.10**). Edge emission spectra were monitored as well throughout the test.

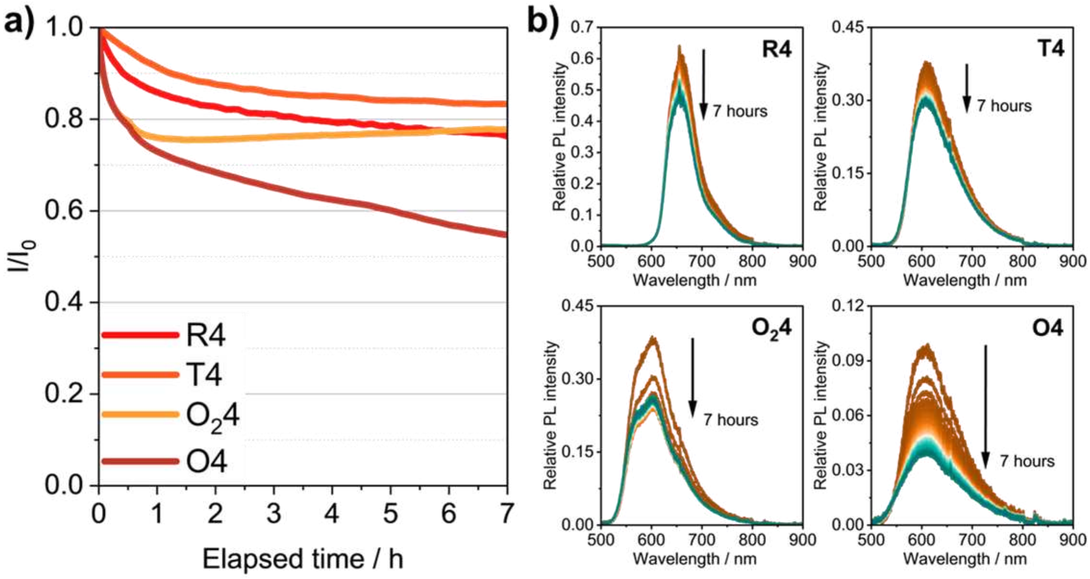

Figure 6.10. a) Short-circuit current and **b)** edge PL spectra trends for the 28 mM LSCs exposed to AM1.5G simulated illumination over a 7 hours long photobleaching test.

Results show that **T4** is the most stable sample, with T-BTZ-T outperforming even a state-of-the-art dye like LR305. **O$_2$4** shows the same output reduction as **R4**, while reaching its plateau value sooner. On the other hand, **O4** exhibits the greatest output drop, and it is also evident that the degradation curve has not yet reached a stationary value.

Considering all factors, as electrical output, LUE and photostability, T-BTZ-T and DTT5SO2 are optimal luminophores for developing high performing LSC-PVs. They provide competitive energy outputs while offering alternative colorations (orange to yellow) with respect to frequently employed red luminophores, contributing to expand the range of available colours and aesthetic characteristics for tinted LSC-PV devices.

6.4 Bibliography

1 Y. Sun, Y. Li, Y. Li and F. Ma, *Comput. Mater. Sci.*, 2007, **39**, 673–677.

2 F. Liu, P. Zuo, L. Meng and S. J. Zheng, *J. Mol. Struct. THEOCHEM*, 2005, **726**, 161–169.

3 C. Santato, L. Favaretto, M. Melucci, A. Zanelli, M. Gazzano, M. Monari, D. Isik, D. Banville, S. Bertolazzi, S. Loranger and F. Cicoira, *J. Mater. Chem.*, 2010, **20**, 669–676.

4 G. Barbarella, L. Favaretto, G. Sotgiu, M. Zambianchi, A. Bongini, C. Arbizzani, M. Mastragostino, M. Anni, G. Gigli and R. Cingolani, *J. Am. Chem. Soc.*, 2000, **122**, 11971–11978.

5 A. Bongini, G. Barbarella, L. Favaretto, G. Sotgiu, M. Zambianchi and D. Casarini, *Tetrahedron*, 2002, **58**, 10151–10158.

6 L. R. Wilson, B. C. Rowan, N. Robertson, O. Moudam, A. C. Jones and B. S. Richards, *Appl. Opt.*, 2010, **49**, 1651–1661.

7 A. A. Earp, J. B. Franklin and G. B. Smith, *Sol. Energy Mater. Sol. Cells*, 2011, **95**, 1157–1162.

8 B. Balaban, S. Doshay, M. Osborn, Y. Rodriguez and S. A. Carter, *J. Lumin.*, 2014, **146**, 256–262.

9 M. Zettl, O. Mayer, E. Klampaftis and B. S. Richards, *Energy Technol.*, 2017, **5**, 1037–1044.

10 M. Bartolini, C. Micheletti, A. Picchi, C. Coppola, A. Sinicropi, M. Di Donato, P. Foggi, A. Mordini, G. Reginato, A. Pucci, L. Zani and M. Calamante, *ACS Appl. Energy Mater.*, 2023, **6**, 4862–4880.

11 A. Picchi, K. Kantarod, M. Ilarioni, M. Carlotti, P. Leowanawat and A. Pucci, *Mater. Today Energy*, 2024, **44**, 101646.

12 Ph. Leclère, M. Surin, P. Viville, R. Lazzaroni, A. F. M. Kilbinger, O. Henze, W. J. Feast, M. Cavallini, F. Biscarini, A. P. H. J. Schenning and E. W. Meijer, *Chem. Mater.*, 2004, **16**, 4452–4466.

13 D. P. Ostrowski, L. A. Lytwak, M. L. Mejia, K. J. Stevenson, B. J. Holliday and D. A. Vanden Bout, *ACS Nano*, 2012, **6**, 5507–5513.

14 S. Ellinger, A. Kreyes, U. Ziener, C. Hoffmann-Richter, K. Landfester and M. Möller, *Eur. J. Org. Chem.*, 2007, **2007**, 5686–5702.

15 F. Zhang, *Optik*, 2020, **219**, 165261.

16 W. Davis and Y. Ohno, *Opt. Eng.*, 2010, **49**, 033602.

17 E. Tatsi, V. Raglione, G. R. Ragno, S. Turri, G. Mattioli, F. Porcelli, D. Caschera, C. Botta, G. Zanotti and G. Griffini, *J. Mater. Chem. C*, 2025, **13**, 14465–14477.

18 F. Corsini, A. Nitti, E. Tatsi, G. Mattioli, C. Botta, D. Pasini and G. Griffini, *Adv. Opt. Mater.*, 2021, **9**, 2100182.

19 E. Tatsi, M. De Marzi, L. Mauri, A. Colombo, C. Botta, S. Turri, C. Dragonetti and G. Griffini, *Macromol. Rapid Commun.*, 2024, **45**, 2300724.

20 C. J. Traverse, R. Pandey, M. C. Barr and R. R. Lunt, *Nat. Energy*, 2017, **2**, 849–860.

21 C. Yang, D. Liu, M. Bates, M. C. Barr and R. R. Lunt, *Joule*, 2019, **3**, 1803–1809.

22 R. Guerrero-Lemus, R. Vega, T. Kim, A. Kimm and L. E. Shephard, *Renew. Sustain. Energy Rev.*, 2016, **60**, 1533–1549.

Chapter 7

A coloured PV modelling study

This final *Chapter* concerns the improvement of a predictive model for the electrical performance and aesthetic quality of coloured PV modules, developed in collaboration with Eurac Research (Bolzano, Italy) and CNR-ICCOM (Firenze, Italy). The study considered a simple prototype device, comprising just a silicon solar cell and a single coloured layer. Three different colouring technologies were investigated for the coloured layer: *i*) non-diffusive coloured glass, *ii*) diffusive white glass and *iii*) luminescent PMMA films doped with organic chromophores synthetized by CNR-ICCOM.

The model provides the simulated spectral response of the coloured PV stack based on discrete input parameters, as the Si cell's spectral response, the transmittance spectrum of the coloured layer and the light source's spectral irradiance. For each colouring technology, the model's results were compared to experimental data to quantify the accuracy of the predictions. The prototype devices obtained by introducing the different colouring layers were characterized using monochromatic light to collect their short-circuit current spectra. The aesthetic impact of the cell coupled with the coloured elements was determined through colorimetric measurements.

The contents of this *Chapter* are based on a recently published research[1] by authors Pelle M., Motta I, Gonnella G., Dessì A., Armelao L., Bottaro G., Calamante M., Mordini A. and Moser D., in Solar RRL (2025, 9, 2400570), reproduced with permission.

7.1 Framework of the study

A significant challenge in the transition towards granular and decentralized photovoltaic installations is integrating PV panels into the built environment. Standard silicon-based PV panels are typically black or dark blue, which can be aesthetically unappealing to architects and building owners. The visual appearance of these panels can clash with architectural design, particularly when installed in already existing structures.[2–4] To address this, two main strategies have emerged:[5,6] *i*) using PV cells as design elements in patterns, and *ii*) incorporating transparent, coloured materials in the PV module to conceal the cell's natural colour. These methods, particularly the use of coloured patterns, have enhanced the aesthetic acceptability of BIPV cells, making them more suitable for architectural applications. The colour modification of PV modules can be achieved using absorptive materials,[7–9] nanostructures that leverage interference effects,[10–12] or optical filters.[13,14]

While modifying the colour of PV modules improves their aesthetic appeal, it negatively impacts their electrical performance. The portion of the electromagnetic spectrum absorbed to create the desired colour is subtracted from the light available for power conversion, reducing the device's overall energy yield.[15–17] This modification also increases the manufacturing costs, with both the addition of coloured layers and the subsequent reduction in energy production impacting the system's economic viability.[18] Hence, it is difficult to accurately assess the overall technical performance of customized coloured PV products, as aesthetic considerations must be balanced with energy yield.

Until now, the development of coloured modules has focused primarily on aesthetics, with less emphasis on simultaneously optimizing both electrical performance and appearance. To improve the understanding of how colour influences power generation, a new modelling framework is herein proposed to predict the electrical performance and colour rendering of coloured PV modules. This tool aims to save time and resources typically spent on prototype development by accurately forecasting the spectral short-circuit current ($I_{SC}(\lambda)$) and integrated I_{SC} value of the device under test (DUT), based on the optical and electrical characteristics of its individual components.

Standard commercial PV modules have a multilayer structure that includes a back sheet, an active PV layer, an encapsulant and a protective front glass cover (**Fig. 7.1a**).

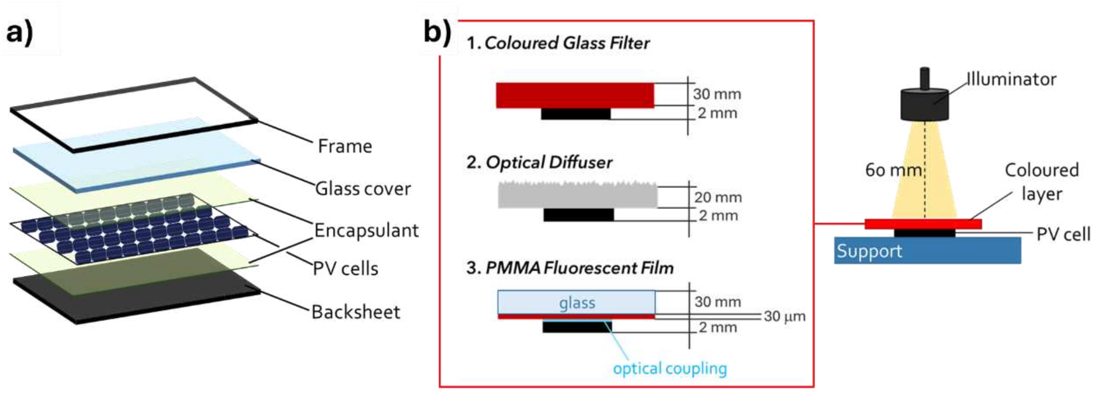

Figure 7.1. a) Simplified schematics of the basic components of a commercial PV module. **b)** List of the DUT configurations used with the different examined coloured layers and placement of the DUT in the experimental setup with respect to the light source.

The colour of the device can be altered by modifying the encapsulant, the front glass, or by introducing coloured interlayers.[6] This complex structure and the proprietary nature of commercial products, which are often protected by patents, make it difficult to replicate them in a laboratory setting or to determine their performance based solely on the optical properties of their individual layers (*i.e.*, transmittance, reflectance, refractive index spectra). To circumvent these challenges, the model was developed based on a simplified DUT, consisting of a monocrystalline silicon PV cell with a single coloured layer placed directly on top of it (**Fig. 7.1b**). This approach allowed for the independent study of both the individual layers and the final DUT. The optical coupling between the PV cell and the coloured layer, when investigated, was introduced using microscopy immersion oil.

Three types of coloured materials were selected, each representing a different colouring technology and increasing in DUT complexity:

- *Schott® coloured glass filters*: scatter-free glass plates that achieve coloration through the selective absorption of light by pigments incorporated in the glass and provide a straightforward example of a coloured layer;
- *Commercial ground glass diffusers*: glass plates with a sandblasted surface which provides a scattering effect and confers a white coloration to the glass through its morphology rather than material composition;
- *Fluorescent polymeric films:* thin interlayer PMMA films doped with a highly fluorescent dye which re-emits a portion of the absorbed photons, effectively acting as a secondary light source that can reach the underlying PV cell. This approach has been previously explored as a method to retrieve part of the

photons lost due to the coloured layer's absorption, consequently enhancing the electrical output of the coloured module, particularly in the high-energy region of the solar spectrum.[19,20]

The following discussion details the acquisition of experimental data on the DUT's electrical performance and colorimetric characteristics and its use in the validation of the model's predictive capabilities.

7.2 Methods

To collect the experimental data needed to validate the model, a dedicated experimental setup was built around a research-grade spectrofluorometer (**Fig. 7.2a**), with analogous operation to the EQE setup described in *Section 3.3* of this work.

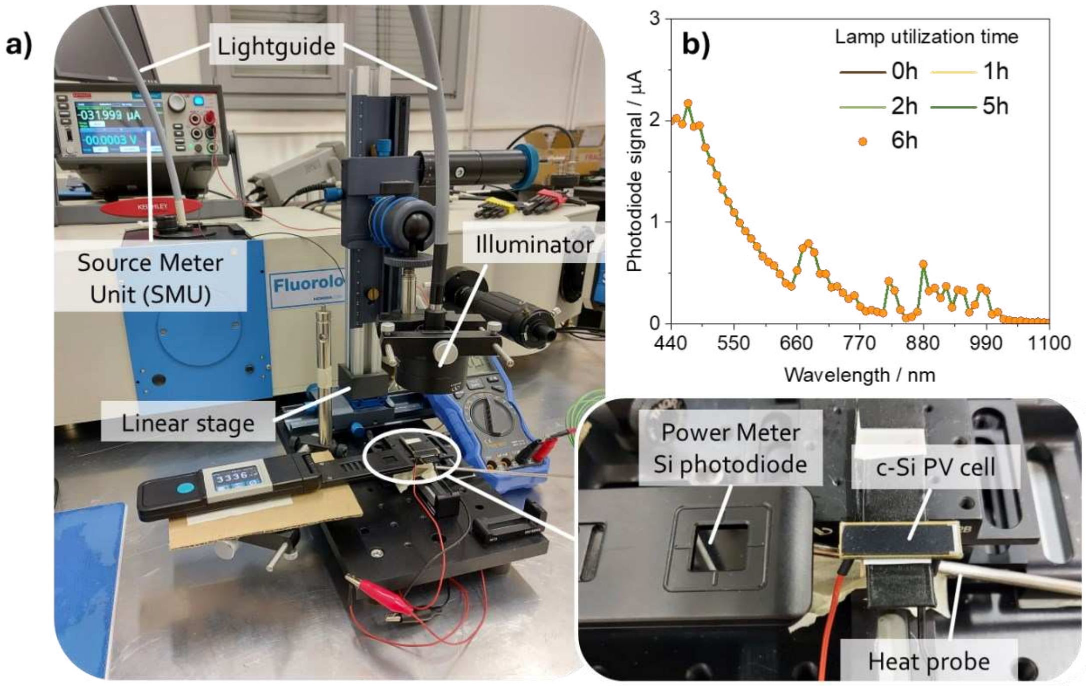

Figure 7.2. a) Experimental setup for the collection of electrical input data. **b)** Lamp intensity monitored with a spectrofluorometer internal photodiode, evidencing the high stability of the illumination system.

The 450 W Xe arc lamp equipped on the spectrofluorometer has been used as a highly versatile light source, providing a light output that could be tailored both spectrally and spatially. A monocrystalline silicon solar cell, with an active area of 22 × 7 mm^2, was used as the PV component of the DUT. Spectral I_{SC} values were collected by illuminating the DUT with monochromatic light and recording the cell's output I_{SC}

with a source meter unit synchronized with the spectrofluorometer. The light from the spectrofluorometer was directed onto the DUT by coupling with a Vis/NIR transmitting optical fibre and collimated in a beam with a circular illumination spot of 50 mm diameter. A photodiode internal to the spectrofluorometer was used to monitor the lamp's stability, which was found to be excellent, with fluctuations below 1% over a 6-hour timeframe (**Fig. 7.2b**). The illuminator was mounted on an XYZ linear stage, allowing for precise alignment of the light spot over the PV cell. Minimum steps along the directions of the stage were 1 mm for X and Y, and 0.25 mm for Z. The optical power of the incident beam was measured using a calibrated silicon photodiode. The reliability of the setup was confirmed through repeated measurements of the bare PV cell's I_{SC} spectrum and of the light source's incident power (P_{in}) spectrum. Both showed negligible variation across the investigated 440 – 1100 nm range (**Fig. 7.3**).

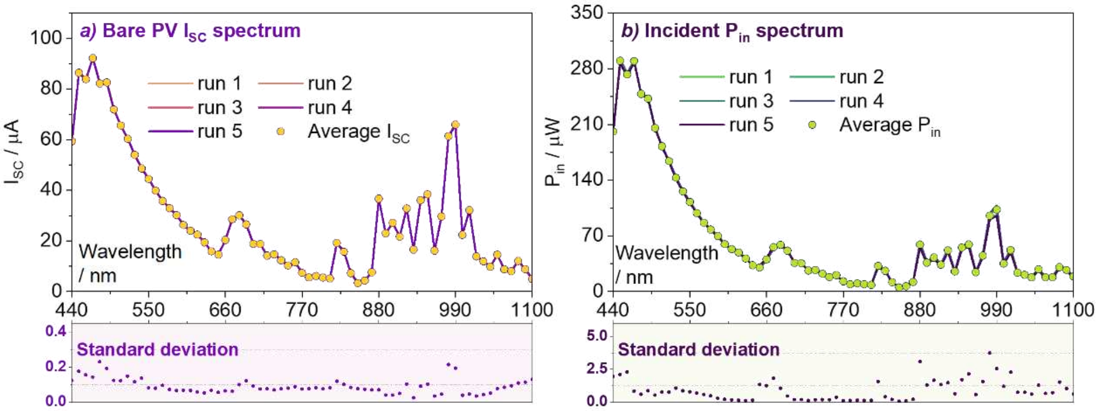

Figure 7.3. Different acquisitions of **a)** the bare PV cell's I_{SC} and **b)** the light source's P_{in} spectra with their average values. Lower panels report the standard deviations of the two sets of measurements.

The core of the predictive model is the ability to forecast how a coloured layer affects the PV cell's electrical output. A brief explanation of the model's workflow follows. For each DUT, the measured spectral transmittance of the coloured layer ($\tau(\lambda)$) is a key input parameter. By multiplying this transmittance by the incident $P_{in}(\lambda)$, an equivalent optical power spectrum ($\Phi(\lambda)$) is obtained, which defines the light spectrum actually reaching the PV cell:

$$\Phi(\lambda) = P_{in}(\lambda) \cdot \tau(\lambda) \qquad \textbf{Eq. 7.1}$$

This way, it is possible to link each spectral transmittance to a colour and to the electrical output of the coloured DUT. The spectral short-circuit current produced by the DUT ($I_{SC}(\lambda)$) is then calculated by weighting the spectral response of the bare cell ($SR_{PV}(\lambda)$) for such equivalent spectrum:

$$I_{SC}(\lambda) = \Phi(\lambda) \cdot SR_{PV}(\lambda) \qquad \textbf{Eq. 7.2}$$

The global short-circuit current of the device ($I_{SC,DUT}$) is finally obtained by integrating the spectral I_{SC} over the investigated wavelength range:

$$I_{SC,DUT} = \int_{400}^{1100} I_{SC}(\lambda)\, d\lambda \qquad \textbf{Eq. 7.3}$$

A critical aspect of commercial PV modules manufacturing is lamination, a thermal and mechanical process that bonds the different layers together, ensuring the safety and reliability of the final product. This process modifies the optical properties of the module by eliminating the air gaps between layers. For instance, the refractive index of the encapsulant (usually polyvinyl butyral, PVB, or ethylene-vinyl acetate, EVA) is very similar to that of the front glass ($n_{\text{EVA}} \approx n_{\text{glass}} \approx 1.5$). Lamination significantly reduces or completely eliminates reflectivity at the glass-EVA interface compared to the glass-air or EVA-air interfaces occurring in the presence of air gaps ($n_{\text{air}} \approx 1$). This reduction in reflectivity increases the total transmittance of the encapsulated components. To accurately account for this behaviour, the proposed model incorporates a correction that simulates the optical coupling of the layers by using Stokes' relations to derive the complex refractive indices of each component from their measured optical properties in air.[21] This approach allows the model to predict the electrical performance of the coloured PV stack more realistically, accounting for the effects of lamination.

Lastly, the aesthetic impact of the coloured DUT was quantitatively assessed through colorimetric tests. A vertical colorimeter was employed to measure the colour coordinates of the samples in the $CIELAB$ colour space. The difference in colour (ΔE_{00}) between the bare PV cell and the coloured DUT was calculated using the CIE 2000 formula, which is an improved version of older colour difference definitions, accounting for the non-uniformity of the human eye's colour perception:[22]

$$\Delta\text{E}_{00} = \sqrt{\left(\frac{\Delta L'}{k_L S_L}\right)^2 + \left(\frac{\Delta C'}{k_C S_C}\right)^2 + \left(\frac{\Delta H'}{k_H S_H}\right)^2 + R_T \left(\frac{\Delta C'}{k_C S_C}\right)^2 \left(\frac{\Delta H'}{k_H S_H}\right)^2} \qquad \textbf{Eq. 7.4}$$

$\Delta L'$, $\Delta C'$ and $\Delta H'$ represent the differences in lightness, chroma and hue, respectively. The weighting functions S_L, S_C, S_H and the rotation term R_T have been introduced to account for the known limitations of the $CIELAB$ colour-space. k_L, k_C and k_H are parametric factors, set to 1 in the present study since the colorimetric characterizations have been performed in reference illumination conditions. The ΔE_{00} value provides a valuable objective metric for assessing the capability of the coloured layer to modify the perceived colour of the underlying PV cell. For reference, a $\Delta E_{00} < 2$ indicates a colour difference that is detectable by the human eye only upon close observation, whereas a $\Delta E_{00} > 2$ identifies a distinct, easily detectable colour difference.

7.3 Results

The first characterized DUT was the bare PV cell, for which the experimental spectral current was measured and used for calculating the spectral response as:

$$SR_{PV}(\lambda) = \frac{I_{SC}(\lambda)}{P_{in}(\lambda)} \qquad \textbf{Eq. 7.5}$$

The external quantum efficiency of the cell was calculated as well (**Eq. 3.11**). Both experimental curves are displayed in **Fig. 7.4**.

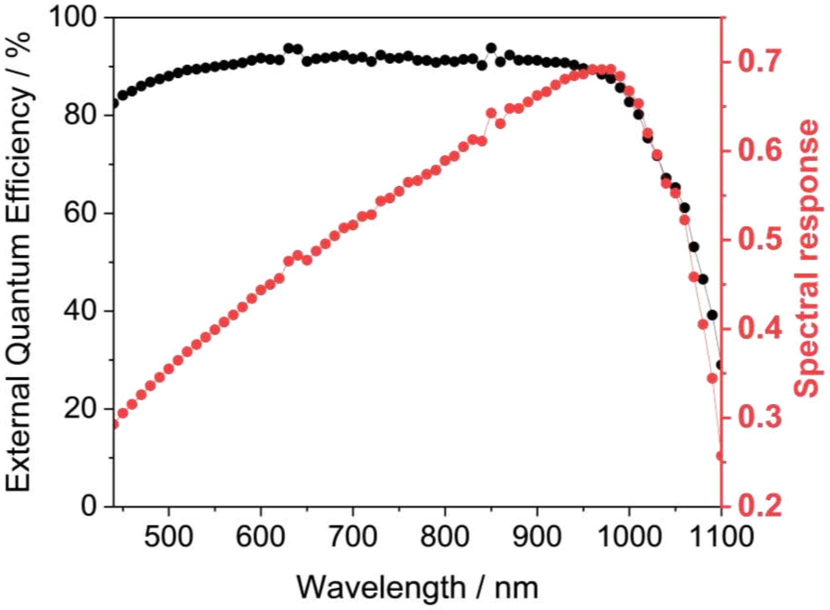

Figure 7.4. EQE (black dotted line) and SR (red dotted line) of the bare PV cell calculated based on experimental data.

The following discussion presents the results of the investigation of each DUT featuring a different colouring layer, providing the coloured layer's transmittance, the experimental I_{SC} spectrum and $I_{SC,DUT}$ value, and the comparison with simulated data. Relevant colorimetric analyses are reported as well. The agreement between experimental (χ_{exp}) and calculated (χ_{calc}) data was evaluated based on the relative percentage square error ($SE\%$), defined as:

$$SE\% = \left(\frac{\chi_{exp} - \chi_{calc}}{\chi_{exp}}\right)^2 \cdot 100 \qquad \textbf{Eq. 7.6}$$

7.3.1 Coloured filters and diffusive glass

The first colouring technology integrated in the DUT was a series of optically clear glass filters, in the form of square 50 × 50 mm^2 slates 3 mm thick (**Fig. 7.5a**). The filters were made from Schott® coloured glass, and were divided between long pass (**OG590**, **RG695**) and bandpass (**BG18**, **KG1**, **VG9**) filters. **Fig.s 7.5b** to **f** illustrate the measured and simulated spectral current for each DUT obtained with the coloured filters, superimposed to their respective transmittance spectrum. Data generated by the model show an excellent agreement with the experimental measurements, with $SE\%$ consistently below 2% for all examined DUTs. The same agreement is found also for the integrated $I_{SC,DUT}$ (**Table 7.1**) with negligible $SE\%$ (< 1%). The experimental value of $I_{SC,DUT}$ has been calculated as the integral of the experimental spectral current.

Table 7.1. Simulated ($I_{SC,DUT}$ calc.) and measured ($I_{SC,DUT}$ exp.) short-circuit currents of the devices under test integrating coloured glass filters, with corresponding error ($SE\%$).

Coloured layer in DUT	$I_{SC,DUT}$ calc. / mA	$I_{SC,DUT}$ exp. / mA	$SE\%$
KG1	10.43	9.54	0.88
RG695	6.64	6.32	0.26
OG590	8.84	8.39	0.28
VG9	1.32	1.29	0.05
BG18	5.65	5.36	0.31

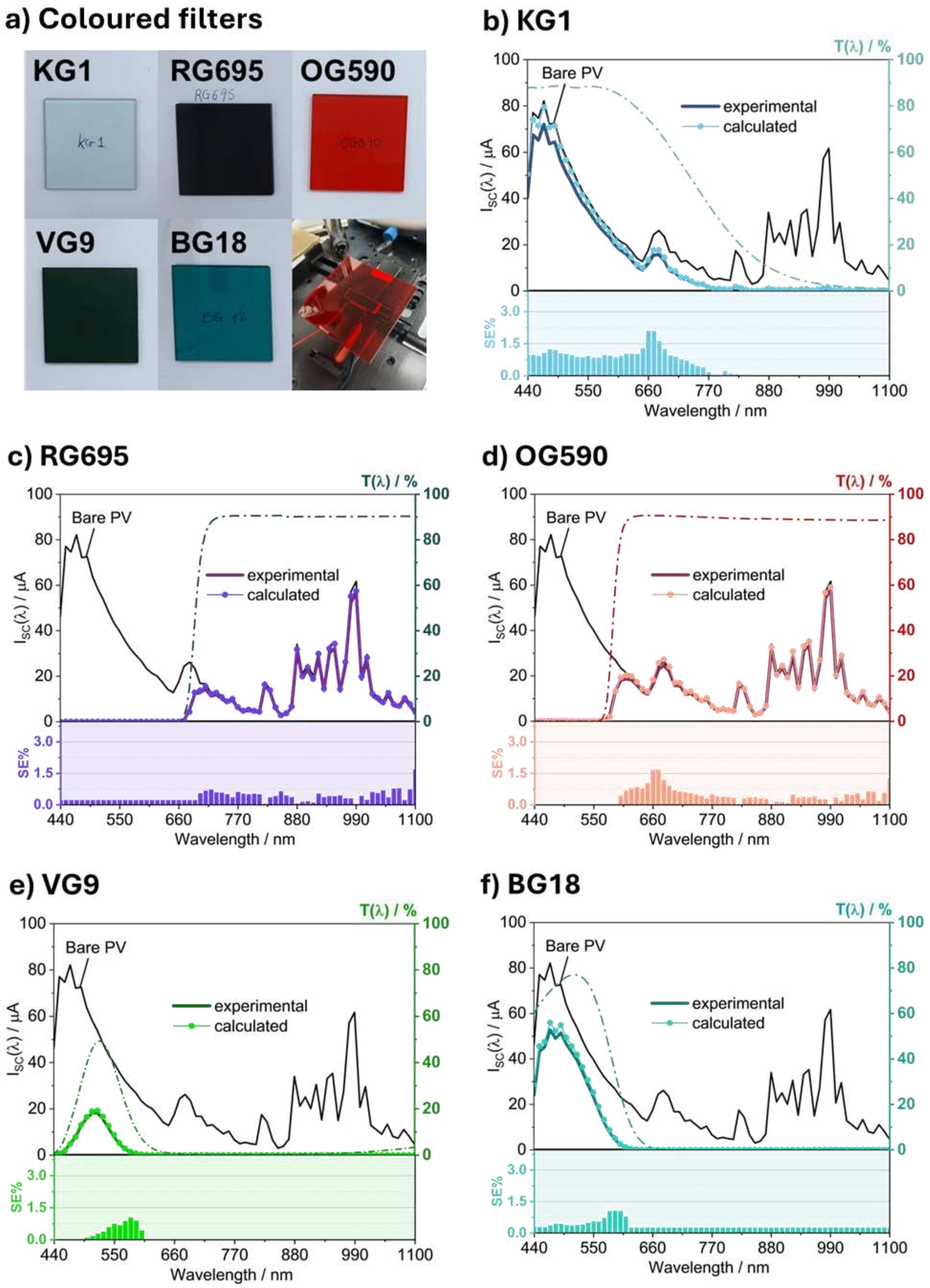

Figure 7.5. a) Photographs of the individual coloured filters with an example of filter placement in the DUT. Comparison between experimental and simulated spectral currents of the DUT incorporating the **b) KG1**, **c) RG695**, **d) OG590**, **e) VG9** and **f) BG18** coloured filter. Each panel also reports the measured transmittance of the filters (upper graph, right Y axis) and the $SE\%$ on the model's prediction (lower graph, column plot).

Colorimetric tests were performed to assess how effectively the coloured filters alter the aesthetic appearance of the bare PV cell. The results are plotted in **Fig. 7.6**, as a function of both the colour difference (ΔE_{00}) and the reduction in the bare cell's short-circuit current. Preliminary results show how the **KG1** filter has the highest colour-altering potential, while reducing the $I_{SC,DUT}$ by 37% with respect to the bare cell. The lowest output reduction is observed when using the **RG695** filter, which also generates the lowest ΔE_{00}.

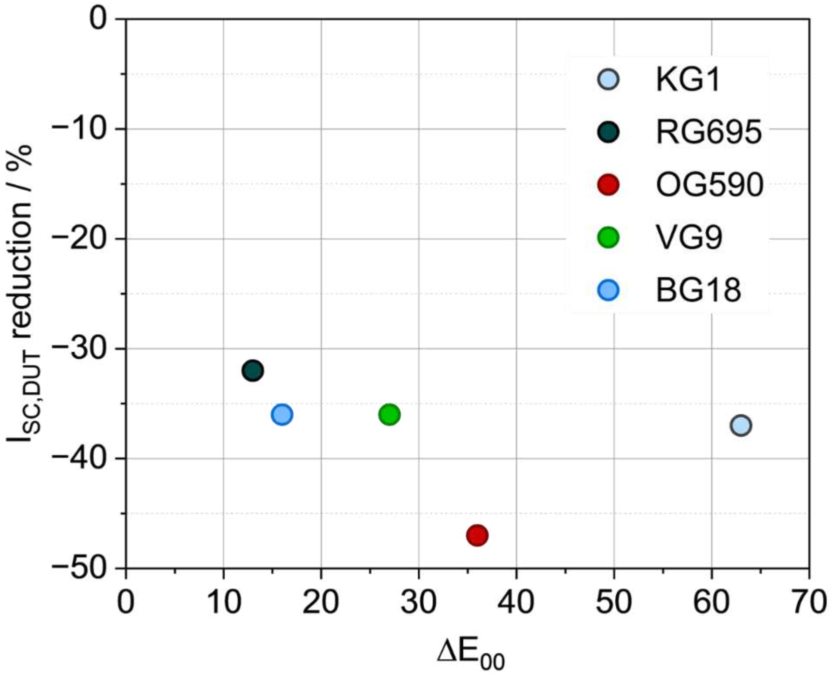

Figure 7.6. Colour difference and reduction in electrical output with respect to the bare cell achieved by the DUT featuring the different coloured filters.

Next, the DUTs were integrated with white ground glass diffusers, having a circular shape with a 50 mm^2 diameter and thickness of 2 mm. Four diffusers, with increasing grit of the sandblasted surface (**120**, **220**, **600**, **1500**), were tested as the coloured layer in the prototype system. Grit refers to the size of the grains of the sandblasted surface, where higher values of grit indicate finer grains. Results of the model validation evidence again an excellent agreement between calculated and experimental data, with negligible $SE\%$ both on the simulated spectral current (**Fig. 7.7**) and integrated $I_{SC,DUT}$ (**Table 7.2**). It is noteworthy that the bare cell's I_{SC} is not significantly altered by the introduction of the glass diffuser.

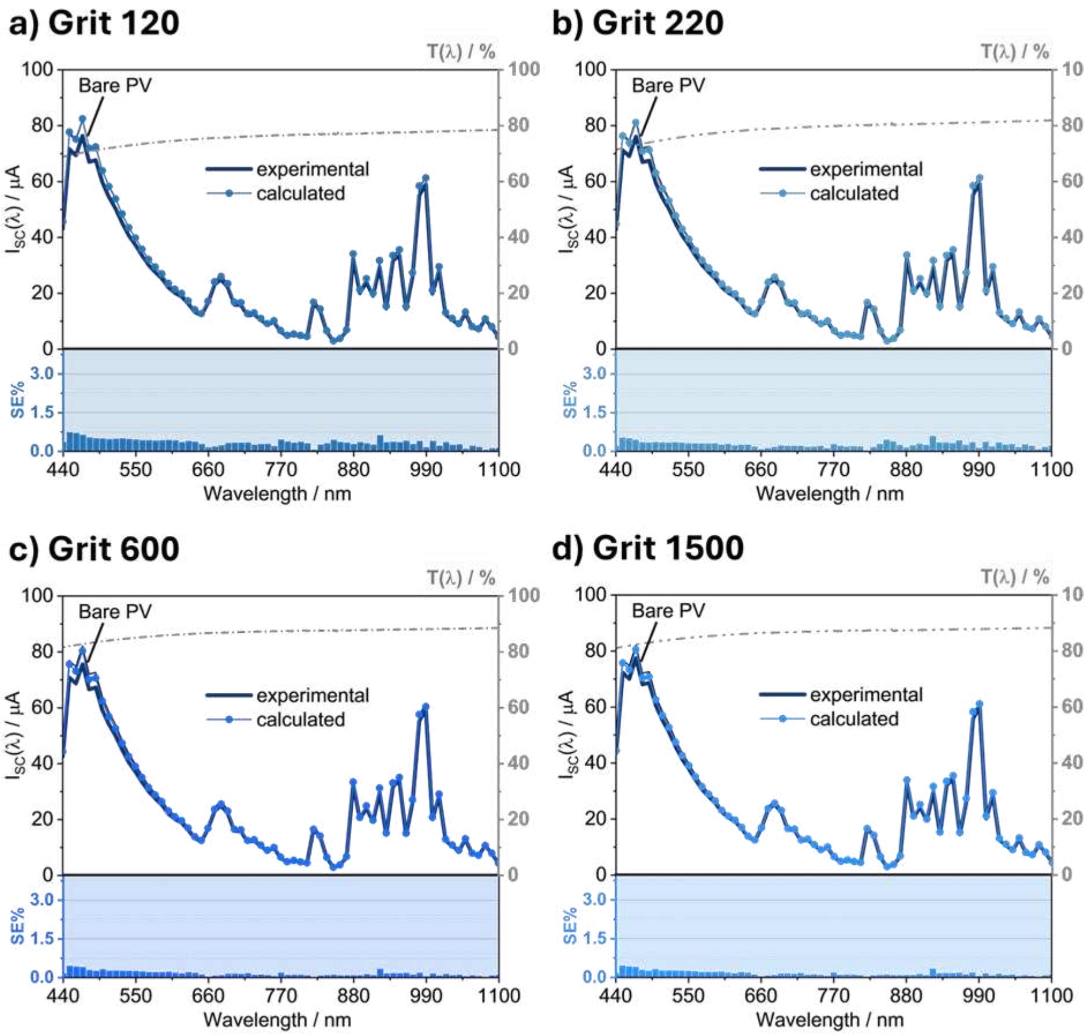

Figure 7.7. Comparison between experimental and simulated spectral currents of the DUT incorporating the diffusers with grit **a) 120**, **b) 220**, **c) 600** and **d) 1500**. Each panel also reports the measured transmittance of the diffuser (upper graph, right Y axis) and the $SE\%$ on the model's prediction (lower graph, column plot).

Table 7.2. Simulated ($I_{SC,DUT}$ calc.) and measured ($I_{SC,DUT}$ exp.) short-circuit currents of the devices under test integrating white ground glass diffusers, with corresponding error ($SE\%$).

Coloured layer in DUT	$I_{SC,DUT}$ **calc. / mA**	$I_{SC,DUT}$ **exp. / mA**	$SE\%$
Grit 120	16.62	16.39	0.020
Grit 220	16.47	16.39	0.003
Grit 600	16.28	16.36	0.002
Grit 1500	16.38	16.61	0.020

7.3.2 Luminescent PMMA films

Fluorescent polymer films were prepared by embedding the organic fluorophores in PMMA, through a drop-casting procedure. Chloroform solutions, containing both the polymer and the fluorophores at varying weight content between 0.4% and 2.0%, were poured onto optically pure glass substrates, having area of 50 × 50 mm^2 and thickness of 3 mm. After solvent evaporation, the dried films were detached from the substrate and ready for use. The average film thickness was 30 μm. The fluorophores consisted in a series of novel quinoxalines with a donor-acceptor-donor molecular structure (**Fig. 7.8**, DQ-Th), designed for use in luminescent solar concentrators.[23]

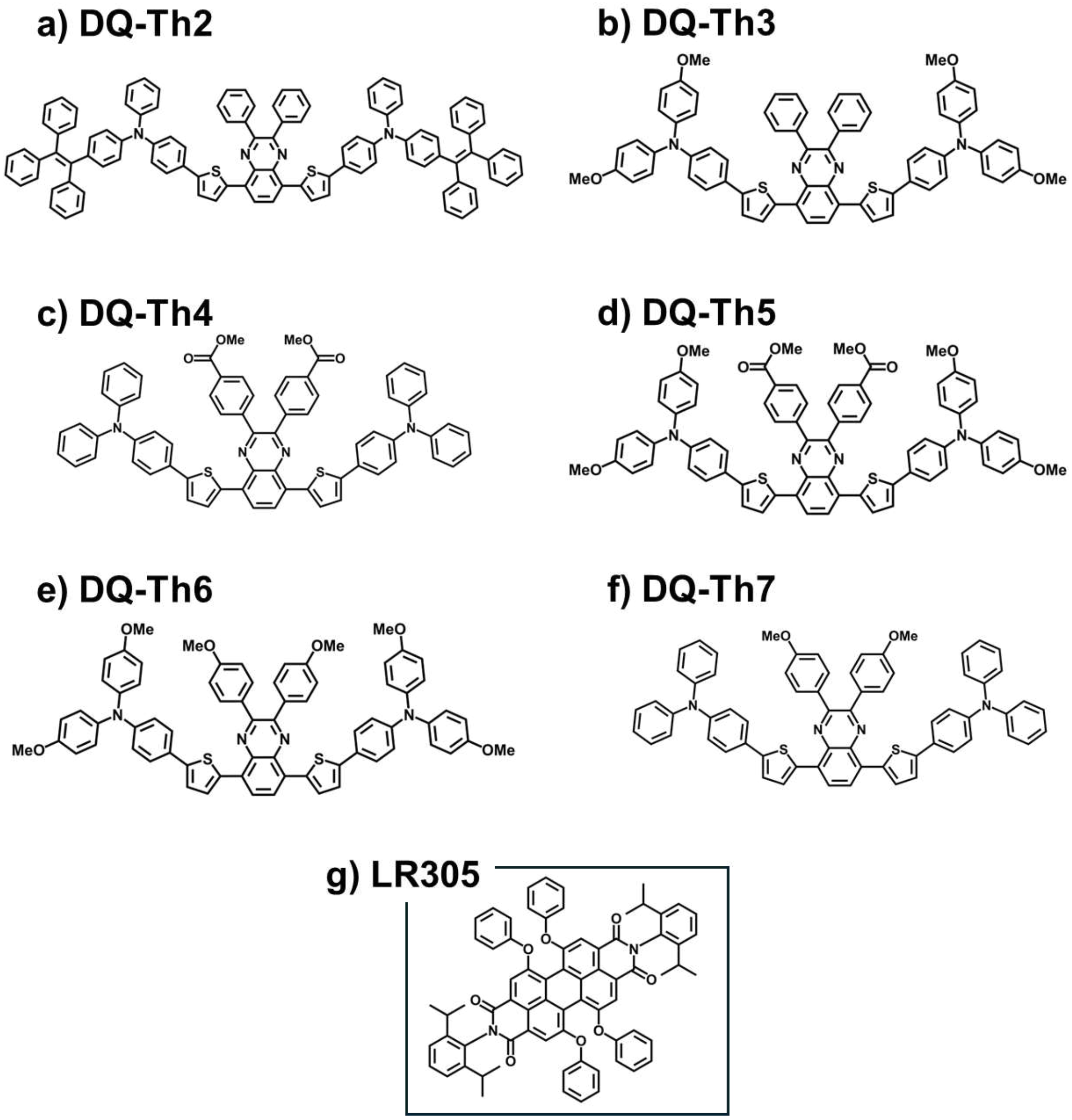

Figure 7.8. Molecular structures of the employed fluorophores: **a)** to **f)** DQ-Th series and **g)** reference dye Lumogen® F Red 305.

Lumogen® F Red 305 (LR305), the commercial perylene diimide dye previously presented in *Chapter 6*, served also in this study as benchmark fluorophore. LR305 is known for its high fluorescence quantum yield, large molar extinction coefficient, and strong absorption of the peak of solar radiation. While presenting similar absorption and emission wavelengths, the DQ-Th fluorophores exhibit lower ε and $PLQY$. However, their generally larger Stokes shift helps to minimize self-absorption effects within PMMA. While the model's validation was performed on all DQ-Th fluorophores, for brevity and thanks to their similar properties, only the data for DQ-Th2 is presented here. Data relative to the other fluorophores of the family are available in *Appendix C4.1*.

The photophysical properties of DQ-Th2 and LR305 are reported in **Table 7.3**, both prior and after embedment into PMMA. It is interesting to note that, while the $PLQY$ of LR305 decreases by 15% in going from the solution to the film, the $PLQY$ of DQ-Th2 sees a slight increase of 8%. Absorption and emission spectra are displayed in **Fig. 7.9.**

Table 7.3. Maximum absorption (λ_{max}) and emission (λ_{PL}) wavelengths, molar extinction coefficient (ε) and $PLQY$ of LR305 and DQ-Th2 measured for $1 \cdot 10^{-5}$ M toluene solutions and PMMA films doped at 0.4% wt.

	λ_{max} / nm	ε / M^{-1} cm^{-1}	λ_{PL} / nm	PLQY
LR305				
Solution	574	48 000	604	1.00
Film 0.4%	575	/	609	0.85
DQ-Th2				
Solution	517	27 400	644	0.57
Film 0.4%	517	/	666	0.65

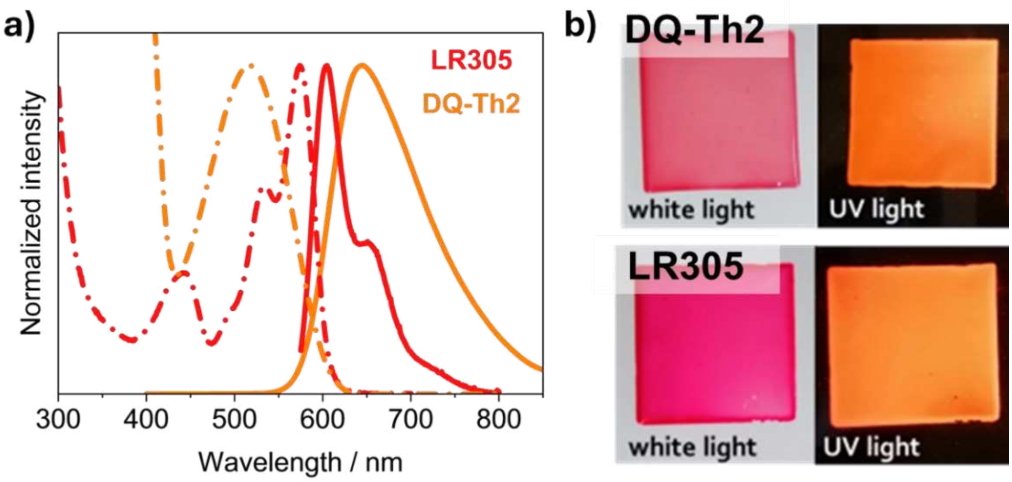

Figure 7.9. a) Normalized absorption (dot-dash line) and emission (solid line) spectra of $1 \cdot 10^{-5}$ M L305 and DQ-Th2 solutions. **b)** Photographs of the 0.4% wt. PMMA films in ambient and UV light illumination conditions.

Similarly to the previous *Section*, the results of the predicted spectral current are shown together with the corresponding experimental data, including the relative square error and the measured transmittance spectra of the films at different concentrations. To keep the PMMA films flat and prevent them from creasing, a 3 mm thick glass slate was added to the top of the coloured PV stack (**Fig. 7.1b**), providing good adhesion to the films. Nonetheless, the focus of the analysis remains on the simple two component system comprised by the cell and the coloured layer. In the following discussion, data relative to the “bare PV” refer to the bare PV cell with just the glass slate placed on top of it. The examined fluorescent films are a good example of how colour can be introduced in a PV module by dyeing the encapsulant material. To simulate lamination between the PV component and the encapsulant, a further degree of complexity was introduced int the prototype system, by optically coupling the PMMA films to the PV cell. Results are then presented first in the simplest configuration, without optical coupling. Later, this aspect is considered by the model as a factor reducing the reflectivity at the Si-PMMA interface. An effective transmittance spectrum of the coloured layer is calculated through Stokes’ relations (*Section 7.1*), which is then used in the model’s workflow to yield the predicted electrical output.

In the absence of optical coupling (**Fig. 7.10**), the simulations well reproduce the trend of the DUT's electrical output with increasing dye concentration. Conversely, a decrease in the predictions’ accuracy is generally observed, particularly within the dye absorption region.

a) LR305

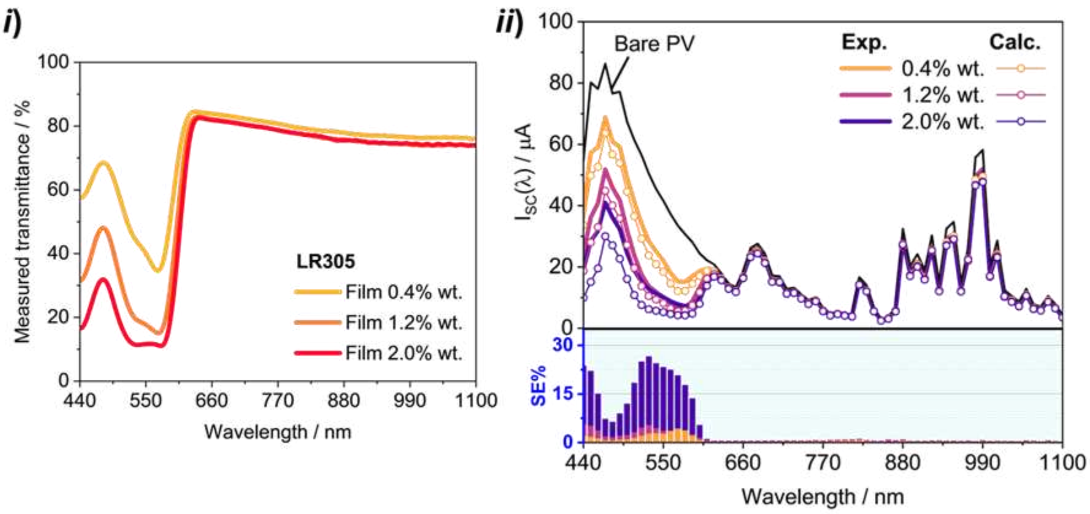

b) DQ-Th2

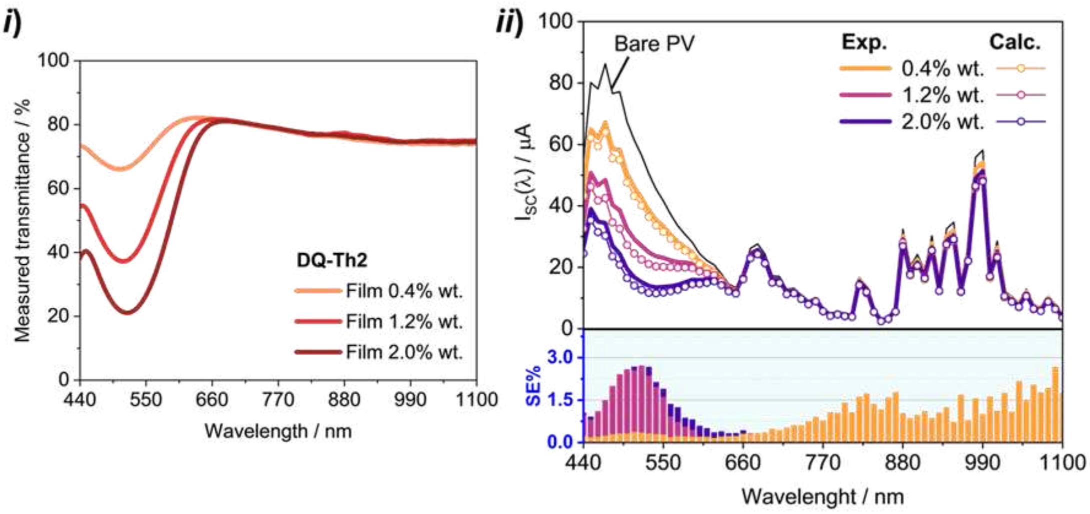

Figure 7.10. Model validation for the DUT incorporating the PMMA films doped with **a) LR305** and **b) DQ-Th2** at increasing weight content, without optical coupling between the PV cell and the film. The ***i*)** panels report the measured transmittance spectra of the films. The ***ii*)** panels display the comparison between experimental and simulated spectral currents of the DUT (upper graph), together with the $SE\%$ on the model's prediction (lower graph, column plot).

The highest discrepancies are found for the highest concentrations and especially for the DUTs integrated with the LR305 films. Being a strongly absorbing and emitting fluorophore, LR305 generates a consistent fraction of fluorescence photons inside the film, which act as a secondary light source for the PV cell. The emitted photons have not yet been accounted for in the model, thus the high spectral $SE\%$ at the wavelengths stimulating fluorophore's emission. The highest $SE\%$ is indeed observed for the LR305 sample doped at 2.0% wt. The reliability of the model is nonetheless confirmed by the acceptable $SE\%$ values (< 10%) on the integrated short-circuit current, as shown in **Table 7.4**.

Table 7.4. Simulated ($I_{SC,DUT}$ calc.) and measured ($I_{SC,DUT}$ exp.) short-circuit currents of the devices under test integrating fluorescent PMMA films with and without optical coupling (OC), with corresponding error ($SE\%$).

Coloured layer in DUT	$I_{SC,DUT}$ **calc. / mA**	$I_{SC,DUT}$ **exp. / mA**	$SE\%$
LR305			
0.4% wt.	11.22	13.93	3.8
1.2% wt.	8.94	11..62	5.3
2.0% wt.	7.78	10.70	7.4
0.4% wt. + OC	14.29	17.52	3.4
1.2% wt. + OC	19.26	16.83	2.1
2.0% wt. + OC	26.10	15.82	42.2
DQ-Th2			
0.4% wt.	11.09	13.98	4.3
1.2% wt.	9.43	12.6	6.3
2.0% wt.	12.38	15.27	3.6
0.4% wt. + OC	13.83	16.82	3.2
1.2% wt. + OC	12.34	15.87	4.9
2.0% wt. + OC	11.99	13.28	1.0

a) LR305

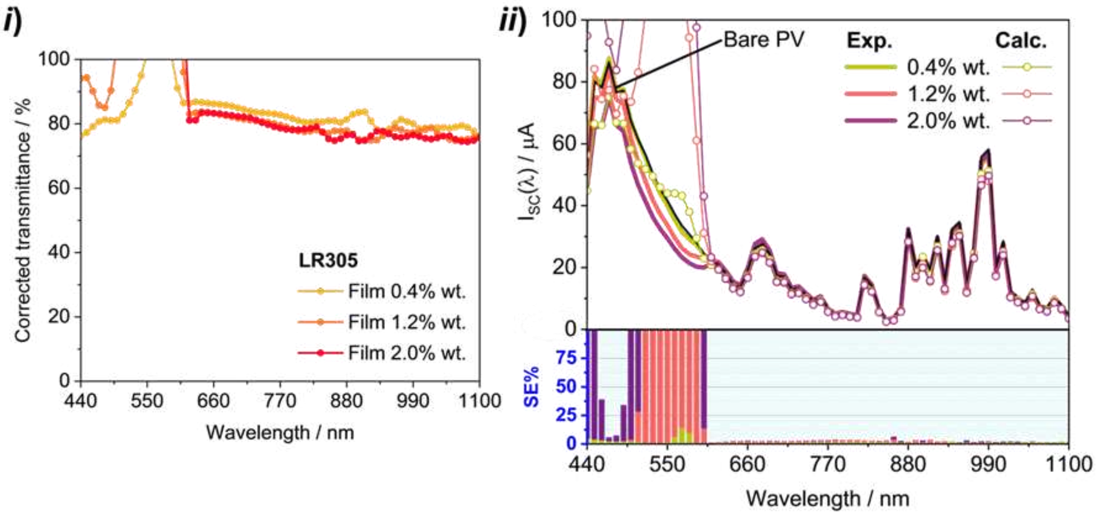

b) DQ-Th2

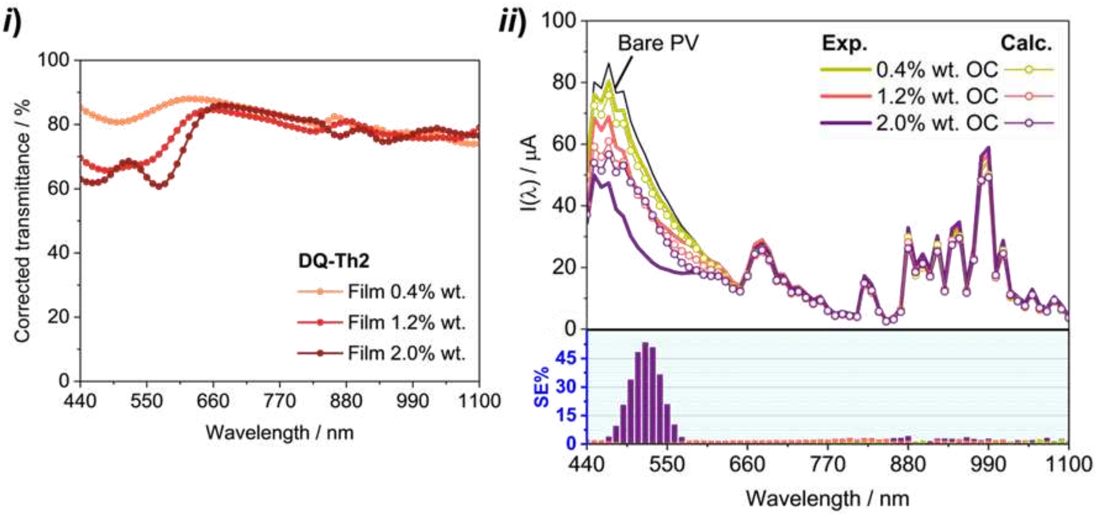

Figure 7.11. Model validation for the DUT incorporating the PMMA films doped with **a) LR305** and **b) DQ-Th2** at increasing weight content, with optical coupling between the PV cell and the film. The ***i)*** panels report the transmittance spectra of the films corrected using Stokes' relations. The ***ii)*** panels display the comparison between experimental and simulated spectral currents of the DUT (upper graph), together with the $SE\%$ on the model's prediction (lower graph, column plot).

Optical coupling was then implemented in the DUT, producing a general increase in its electrical output (**Fig. 7.11**). This improvement suggests that a larger portion of both incident and fluorescent photons successfully reaches the underlying PV cell. This effect is attributed to the removal of the air gap that would otherwise exist between the fluorescent film and the cell. By eliminating the PMMA-air and air-Si interfaces, more incident light is transmitted through the film to the cell. Additionally, some of the light that is emitted and then trapped within the film can now travel through the optical coupling medium, which has a refractive index similar to that of PMMA, and reach the cell's surface. Again, the simulations accurately reproduce the trend of the spectral current with increasing dye concentration. However, the effect of the optical coupling on the fluorescence photons exacerbates the discrepancies between calculated and experimental data already observed for the DUT without optical coupling. The effect becomes more evident for higher fluorophore loadings and for the samples containing a strongly absorbing and emitting dye such as LR305. The amplified spectral $SE\%$ at the excitation wavelengths underscores the importance of a further refinement of the model by quantifying the emitted photons, which constitute a non-negligible light source. On the other hand, such analysis successfully demonstrated how a fluorescent layer can effectively enhance the performance of a coloured PV module, by returning to the cell part of the incident photons it absorbs. As for the integrated I_{SC} (**Table 7.4**), the $SE\%$ values are generally lower with respect to the configuration without optical coupling, except for the sample doped with LR305 at 2.0% wt., which prediction deviates significantly from the observed data.

Finally, colorimetric tests were conducted to evaluate how effectively the films change the aesthetic appearance of the bare photovoltaic cell. The colour difference between the bare PV and the various DUTs was calculated both with and without optical coupling and is reported in **Fig. 7.12** together with the $I_{SC,DUT}$ relative reduction.

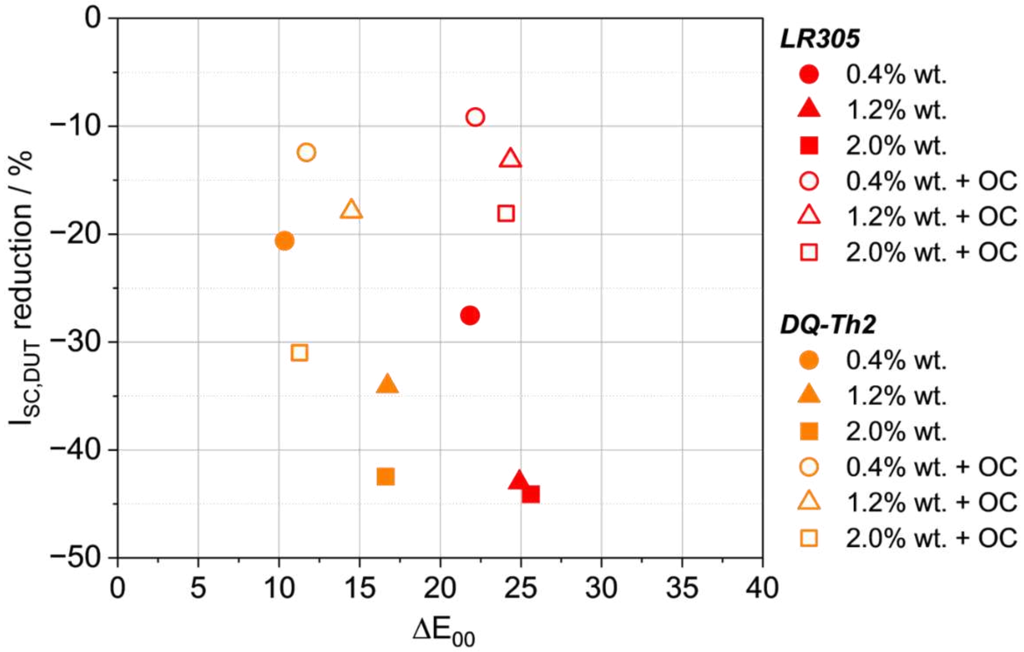

Figure 7.12. Colour difference and reduction in electrical output with respect to the bare cell achieved by the DUT featuring the different fluorescent PMMA films, with and without optical coupling.

Preliminary results indicate that the optically coupled LR305 samples produced a more significant change in the perceived colour and a smaller reduction in the short-circuit current of the final laminate, compared to the optically coupled DQ-Th2 series. Specifically, devices integrating the DQ-Th2 films exhibited a smaller colour difference relative to the bare PV cell. The primary changes were a slight shift in hue toward the red spectrum, a minor alteration in chroma, and a reduction in lightness. In contrast, the LR305 films showed a more pronounced shift in hue toward the red region, accompanied by a substantial increase in chroma. For both the DQ-Th2 and LR305 series, the lightness of the devices decreased when optical coupling was included, likely due to a reduction in the total reflectance. The colour representation of these devices within the $CIELAB$ colour space is shown in **Fig. 7.13**.

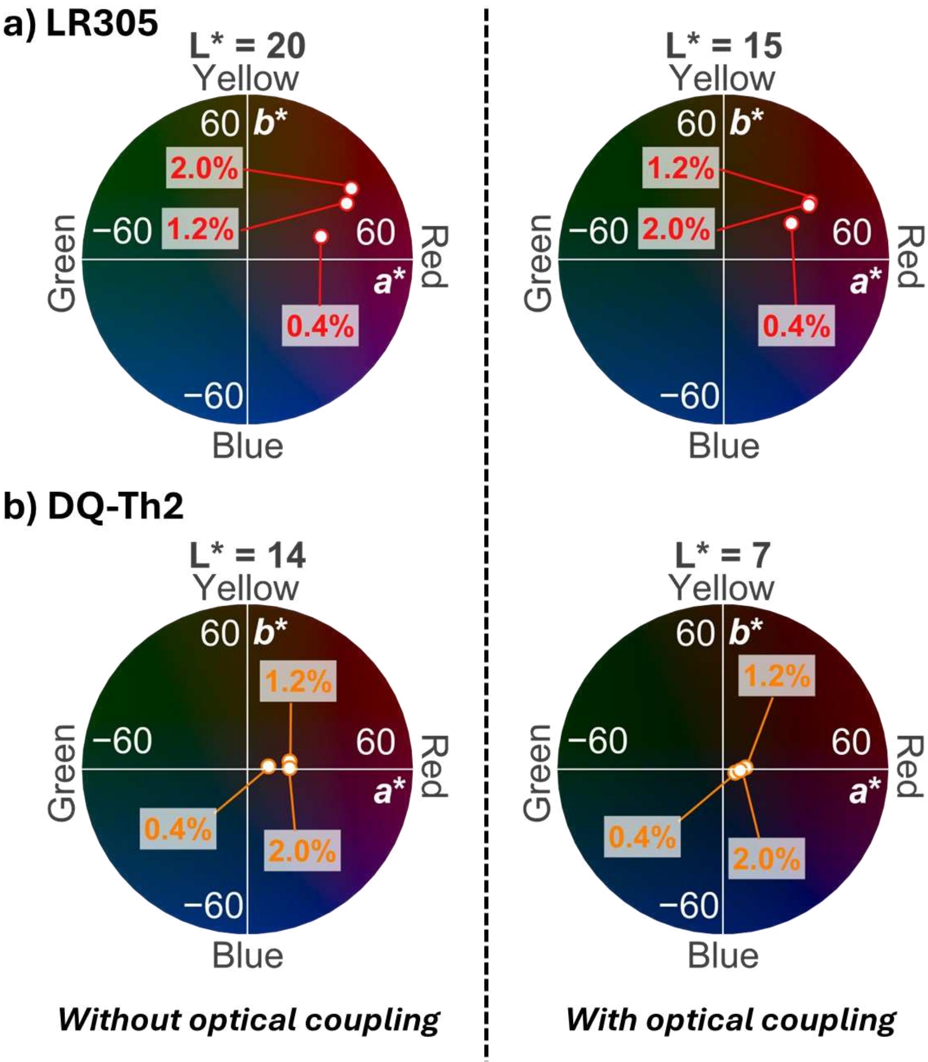

Figure 7.13. $CIELAB$ 2D polar graphs displaying the colour coordinates of the DUT integrated with the PMMA films containing **a)** LR305 and **b)** DQ-Th2. Samples with similar L^* values have been grouped together.

7.4 Bibliography

1 M. Pelle, I. Motta, G. Gonnella, A. Dessì, L. Armelao, G. Bottaro, M. Calamante, A. Mordini and D. Moser, *Sol. RRL*, 2025, **9**, 2400570.

2 M. Pelle, E. Lucchi, L. Maturi, A. Astigarraga and F. Causone, *Energies*, 2020, **13**, 4506.

3 J. Escarré, H.-Y. Li, L. Sansonnens, F. Galliano, G. Cattaneo, P. Heinstein, S. Nicolay, J. Bailat, S. Eberhard, C. Ballif and L.-E. Perret-Aebi, in *2015 IEEE 42nd Photovoltaic Specialist Conference (PVSC)*, 2015, pp. 1–2.

4 I. Del Hierro López and L. Olivieri, *J. Build. Eng.*, 2025, **108**, 112883.

5 L. O. Grobe, M. Terwilliger and S. Wittkopf, presented in part at the ATI 2020: Smart Buildings, Smart Cities, August, 2020.

6 T. E. Kuhn, C. Erban, M. Heinrich, J. Eisenlohr, F. Ensslen and D. H. Neuhaus, *Energy Build.*, 2021, **231**, 110381.

7 T. Masuda, Y. Kudo and D. Banerjee, *Coatings*, 2018, **8**, 282.

8 A. Morlier, B. Lim, S. Blankemeyer, H. Schulte-Huxel, R. Witteck, T. Daschinger, S. Bräunig, M. Köntges and R. Brendel, *Sol. RRL*, 2022, **6**, 2100356.

9 A. Borja Block, J. Escarre Palou, M. Courtant, A. Virtuani, G. Cattaneo, M. Roten, H.-Y. Li, M. Despeisse, A. Hessler-Wyser, U. Desai, A. Faes and C. Ballif, *Energy Build.*, 2024, **314**, 114253.

10 G. Peharz, K. Berger, B. Kubicek, M. Aichinger, M. Grobbauer, W. Nemitz, J. Gratzer, B. Großschädl, C. Prietl, W. Waldhauser, G. C. Eder and C. Auer, *Renew. Energy*, 2017, 542–550.

11 B. Bläsi, T. Kroyer, T. E. Kuhn and O. Höhn, *IEEE J. Photovolt.*, 2021, **11**, 1305–1311.

12 P. Shen, G. Wang, B. Kang, W. Guo and L. Shen, *ACS Appl. Mater. Interfaces*, 2018, **10**, 6513–6520.

13 J. C. Ortiz Lizcano, S. Villa, Y. Zhou, G. Frantzi, K. Vattis, A. Calcabrini, G. Yang, M. Zeman and O. Isabella, *Sol. RRL*, 2023, **7**, 2300256.

14 J. C. Ortiz Lizcano, P. Procel, A. Calcabrini, G. Yang, A. Ingenito, R. Santbergen, M. Zeman and O. Isabella, *Prog. Photovolt. Res. Appl.*, 2022, **30**, 401–435.

15 A. Røyset, T. Kolås and B. P. Jelle, *Energy Build.*, 2020, **208**, 109623.

16 G. Peharz and A. Ulm, *Renew. Energy*, 2018, **129**, 299–308.

17 T. Gewohn, C. Schinke, B. Lim and R. Brendel, *AIP Adv.*, 2021, **11**, 095104.

18 M. Pelle, F. Causone, L. Maturi and D. Moser, *Energies*, 2023, **16**, 1991.

19 E. Klampaftis, D. Ross, K. R. McIntosh and B. S. Richards, *Sol. Energy Mater. Sol. Cells*, 2009, **93**, 1182–1194.

20 N. K. Kalluvettukuzhy, M. R. Maciejczyk, I. Underwood and N. Robertson, *J. Mater. Chem. A*, 2023, **11**, 13195–13200.

21 Hecht, Eugene, *Optics*, Boston: Pearson Education, Inc, 5 edition. Global edition., 2017.

22 CIE TC 1-85, .

23 C. Papucci, R. Charaf, C. Coppola, A. Sinicropi, M. Di Donato, M. Taddei, P. Foggi, A. Battisti, B. De Jong, L. Zani, A. Mordini, A. Pucci, M. Calamante and G. Reginato, *J. Mater. Chem. C*, 2021, **9**, 15608–15621.

Chapter 8

Conclusions and perspectives

This thesis explored some of the most promising emerging technologies in the current solar energy landscape, focusing on devices for distributed applications, such as Building-Integrated Photovoltaics (BIPVs). In particular, it delved into the field of Luminescent Solar Concentrators (LSCs), highlighting their potential for realizing BIPV windows and their inherent versatility for applications across a wider range of sectors. The presented research encompassed the development, characterization and evaluation of new luminescent materials and device architectures, with an emphasis on understanding the interaction between the optical properties, the electrical performance and the aesthetic impact of the final product.

At first instance, the methodological approach and characterization fundamentals for accurately researching and reporting on LSC devices have been discussed. The development and optimization of laboratory protocols for preparing LSCs, both in the bulk and in the glass-supported film configurations, have been detailed. For bulk-doped PMMA tiles, these were achieved by polymerizing MMA in an appropriate mould to obtain $50 \times 50 \times 2.7$ mm^3 planar LSCs. The challenges related to the volumetric shrinkage occurring during the free radical bulk polymerization were addressed by modifying the casting procedure and equipment to improve the repeatability of the technique in obtaining samples with high optical quality. It was also shown how a post-curing step is essential to ensure the homogeneity and long-term durability of the PMMA tiles, preventing delayed polymerization of residual monomer which would otherwise cause visible defects inside the materials. For the films obtained via the slot die coating process, an optimal feedstock formulation and coating program were developed to attain highly homogeneous and defect-free PMMA luminescent films, with target active area of 50 × 50 mm^2 and thickness of 35 μm. Notably, excellent repeatability of the deposition process was achieved, where the use of sacrificial substrates and the pre-treatment of the target glass substrate with an O_2 cold plasma were key factors.

Due to the historical lack of standardized directives for LSC characterization and reporting, a rigorous framework of terminology and experimental protocols, based on recently published guidelines, has been used to accurately relay the scientific results of the thesis. Optical metrics (total solar absorptance, internal photon efficiency), aesthetic parameters (average visible transmission, colour rendering index, $CIELAB$ colour coordinates) and electrical characterizations (current-voltage curves, external quantum efficiency spectra) have all been defined for a standard LSC system and their measuring extensively detailed. Additionally, a MATLAB Live Script was developed to facilitate data processing and the extraction of all key figures of merit from experimental data.

Having laid the groundwork for an accurate characterization and reporting of LSC materials and devices, two case studies were investigated: i) Eu^{3+}-based LSCs with aesthetically compliant visual impact and UV-blocking features, and ii) highly performant LSCs based on visible absorbing oligothiophenes.

The first case study examined devices incorporating bright Eu^{3+} bis-β-diketonates with general formula $[Eu_2L_4]^{2-}$ as luminophores, which conferred to the final material high transparency and complete absence of tinting, thanks to a selective absorption of UV photons. The $[Eu_2L_4]^{2-}$ cages showed promising photophysical properties when dissolved in MMA, with molar brightness values as high as $9.6 \cdot 10^4$ M^{-1} cm^{-1}, an order of magnitude higher when compared to the reference compound $Eu(tta)_3phen$. Furthermore, the pseudo-Stokes shift of 200 nm ensured that no reabsorption losses affected the LSC systems. The LSCs were realized as bulk-doped PMMA tiles, where compatibility between luminophore and embedding medium proved to be the discriminant factor among the different available luminophores. The best performing devices were developed based on the $[Eu_2L^F{}_4]^{2-}$ cage and on $Eu(tta)_3phen$, both exhibiting excellent aesthetic quality, with appearance and colour parameters comparable to standard window glass (AVT = 92%, $CRI > 98$, $-7 < a^* < 0$ and $-3 < b^* < 7$). Concerning the energy production, the two devices obtained by edge-coupling the LSCs to silicon solar cells reached overall PCE values of 0.1%. Noticeably, the device based on the $[Eu_2L^F{}_4]^{2-}$ cage produced such results while employing an eight times smaller europium weight content with respect to the sample containing $Eu(tta)_3phen$. The developed LSCs also demonstrated excellent UV-blocking capabilities, with absorptance values close to 92% within their absorption region. Such interesting feature prompted a further investigation into the multifunctionality of these Eu^{3+}-based LSCs, exploring their potential as large area, visible-blind UV photodetectors. A series of devices based on $[Eu_2L^F{}_4]^{2-}$ and $Eu(tta)_3phen$, featuring progressively larger collecting area, was realized and characterized according to key evaluation criteria for photodetector performance. A minimal setup, consisting only of the waveguide and an edge-coupled PV cell, was deliberately employed to demonstrate the markedly simpler device architecture provided by LSCs compared to conventional multijunction photodetectors. The samples with largest active area proved to be the most efficient in distinguishing the signal from background noise, with specific detectivity values as high as 10^{12} Jones for the $[Eu_2L^F{}_4]^{2-}$ derived devices. The cage-based LSCs also exhibited the highest selectivity toward UV radiation, showing no response under white light exposure. The linear dynamic range was around 40 dB, with a limit of detection down to a few tenths of nW cm^{-2}. Finally, with response times on the order of milliseconds, the LSC-based photodetectors achieved performances matching those of state-of-the-art, wide bandgap visible-blind UV photodetectors, while relying on a far simpler device architecture.

The second LSC case study focused on developing supported film devices incorporating a series of strongly fluorescent oligothiophenes as luminophores. The study aimed at coloured BIPV solutions, as the compounds exhibited absorption in the visible region of the solar spectrum. The state-of-the-art commercial dye Lumogen® F Red 305 was included as benchmark luminophore. When dealing with organic dyes, the issue of reabsorption losses is a critical factor affecting the efficiency of the device. The proposed oligothiophenes demonstrated exceptionally large Stokes shifts (100 – 150 nm), significantly higher than the one exhibited by LR305 (35 nm). The dyes were incorporated into PMMA films using the slot die coating technique. After embedment in the matrix, a general decrease in $PLQY$ was observed with increasing luminophore loading, due to larger reabsorption losses. However, the oligothiophenes exhibited a smaller reduction in $PLQY$ compared to LR305. In terms of electrical performance, the LSCs with the highest luminophore content were the most efficient. The highest PCE value was observed for the device containing LR305, followed by the one based on the T-BTZ-T oligothiophene, which produced 75% of LR305 electrical output. Furthermore, when considering the light utilization efficiency, a better suited metric for evaluating the overall performance of transparent PVs, T-BTZ-T and DTT5SO2 showed superior performance compared to LR305. These findings highlight the advantage of the oligothiophenes-based devices in meeting BIPV aesthetic requirements. The bifaciality of these LSC-PVs was also studied, with an average reduction of only 10% in output power under back-illumination conditions, confirming their suitability even for indoor energy generation. Photostability was another key point, with T-BTZ-T outperforming even LR305 in a 7-hour photobleaching test under AM1.5G illumination. Overall, T-BTZ-T and DTT5SO2 emerged as optimal luminophores, offering excellent energy production and chromatic alternatives (from orange to yellow) to typical red luminophores.

Finally, the thesis offered insights on other topics concerning BIPV technologies, such as coloured PV modules. A predictive model for evaluating the electrical performance and aesthetic quality of coloured PV panels has been presented and validated through collection of experimental data on coloured PV prototypes. The model was developed using a simplified DUT, composed of a Si cell and a single coloured layer, for which different colouring technologies were investigated. Schott® coloured non-diffusive glass filters and white ground glass diffusers were first examined as straightforward means of introducing colour in a PV stack, either by altering the glass cover's chemical composition or morphology, respectively. For both solutions, the model predicted the DUT's electrical output with great accuracy ($SE\% < 2\%$). Next, fluorescent PMMA films incorporating quinoxaline dyes were introduced in the DUT to test the beneficial effect of the emission process in enhancing the performance of the PV cell. In absence of optical coupling between Si and PMMA, the model well reproduced the trend of the DUT's outputs at varying dye loading, maintaining acceptable errors ($SE\% < 10\%$). When introducing optical coupling to simulate lamination of a real PV module, evident discrepancies were observed between simulated and experimental data in correspondence of the dyes' absorption spectral regions, *i.e.*, the wavelengths stimulating photon emission. Future model refinement will be required to account for the PL photons generated inside the film, considering them as an effective secondary light source incident on the PV cell. Nonetheless, a general increase in the electrical output of the DUT occurred, suggesting that a larger portion of incident and fluorescent photons reached the photovoltaic cell thanks to optical coupling.

The results of this thesis open several promising directions for future research and technological development of LSCs. Future breakthroughs in the LSC field will surely stem from progress in luminophore design, as maximising both the emission of the molecule and its Stokes shift is a crucial goal to reach higher efficiencies. Tandem devices, incorporating both UV and NIR absorbers, will be necessary to provide aesthetically pleasing BIPV solutions while reaching the electrical performance thresholds required for commercialization. In this perspective, the development of luminophores with improved photothermal and photochemical stability, guaranteeing a prolonged device lifetime, is equally important to reach commercialization. Progress into device light management (increased waveguide trapping efficiency through surface nano-structuring) and embedding medium properties (hybrid waveguide materials offering a balance between environmental stability and optical quality) will be another cornerstone of the future technological development in the LSC field. Introducing multifunctionality in such devices will also favour their deployment in different contexts, as in sensing and optical communications.

In conclusion, the research presented in this thesis has contributed significantly to the understanding and development of LSCs as a versatile and multifunctional photovoltaic and optical technology. The results obtained from the LSC case studies, but also from the investigation of the coloured PV systems, provide valuable insights and perspectives on the future development of such technologies, for a smart and aesthetically compliant building integration of distributed photovoltaics.

Chapter 9

Experimental section

9.1 Synthesis of Eu^{3+} complexes

All reagents were purchased from Merck and used as received. The bis-β-diketone ligands L^A, L^B and L^M, as well as the corresponding $\{[Eu_2L_4](NEt_4)_2\}$ cages, were prepared according to previous reports.[1,2]

9.1.1 $Eu(tta)_3phen$

The synthesis was carried out according to a literature protocol.[3] 2-thenoyltrifluoroacetone (1.72 g, 7.7 mmol) and 1,10-phenathroline (0.46 g, 2.6 mmol) have been introduced in a 250 mL 3 necks round bottom flask and dissolved in 40 mL of ethanol at 60 °C. An ethanol solution of NaOH (50 mL) has been added to the above solution. $EuCl_3 \cdot 6H_2O$ (0.96 g, 2.6 mmol) in ethanol (70 mL) has been added dropwise to the deprotonated ligand solution, observing immediate formation of a white precipitate. After reacting at reflux for 4 hours, the mixture has been removed from heating and left to cool at ambient temperature, then left at 0 °C overnight. The precipitate has been filtered on paper (porosity: 6 μm), washed with cold ethanol and dried over $CaCl_2$ under vacuum. The reaction crude has been purified by hot filtration from 60 mL of THF at 50 °C, using a gooch filter (porosity: 3). The solvent has been removed under reduced pressure and the solid left drying under vacuum. The final product has been obtained as a yellowish white powder (1.96 g). Yield: 75%.

9.1.2 L^F ligand precursor

p-bromoacetophenone (7.20 g, 36.2 mmol), *tert*-butylcarbamate (1.45 g, 12.4 mmol), K_3PO_4 (15.73 g, 74,0 mmol), and CuI (0,70 g, 3.7 mmol) have been introduced in a 250 mL 3 necks round bottom flask and dissolved in 60 mL of anhydrous toluene under Ar atmosphere. N,N-dimethylethylenediamine (1.2 mL, 11.1 mmol) has been added to the solution, which immediately turned blue. The formation of a white precipitate has been observed, and the reaction mixture has been stirred at 110 °C for 48 hours. After 24 hours, the mixture appeared red and presented dark yellow precipitate, and after 48 hours the solution had turned to brown. The reaction has been quenched by the addition of water (150 mL) and ethyl acetate (160 mL). After transferring the mixture in a separating funnel, the blue aqueous phase has been washed with ethyl acetate (2 × 50 mL) and then removed. The brown organic phase has been washed with water (3 × 100 mL) and dried over $MgSO_4$. The solvent has been removed under reduced pressure, obtaining a dark orange dense oil. The product has been purified by SiO_2 column flash chromatography (n-hexane/ethyl acetate 6:4) to give 4.09 g of a yellow dense oil. ^{1}H-NMR (25 °C, 300 MHz, $CDCl_3$): δ [ppm] = 7,92 (4H, m), 7,26 (4H, m), 2,59 (6H, s), 1,46 (9H, s).

9.1.3 L^F ligand

Metallic Na (0.94 g, 40.9 mmol) has been introduced in a 250 mL 3 necks round bottom flask and dissolved in ethanol (40 mL) under Ar atmosphere, keeping the flask in an ice and water bath. After complete dissolution of Na (≈ 1 hour), ethyl pentafluoropropionate (4.2 mL, 30.6 mmol) and the L^F precursor (4.09 g, 11.6 mmol), pre-dissolved in 10 mL of ethanol, have been added under magnetic stirring, giving a yellow solution that turned dark red over time. The reaction mixture has been stirred at room temperature overnight. Next, the solvent has been removed under reduced pressure, obtaining a dark orange oil. After addition of water (100 mL) and HCl 10% aqueous solution (15 mL), the formation of a yellow precipitate occurred. The solution has been transferred in a separatory funnel and the product extracted (100 mL) and washed (2 × 40 mL) with CH_2Cl_2. The organic phase has been dried over $MgSO_4$ and the solvent has been removed under reduced pressure, obtaining a dark orange oil. The product has been purified by recrystallization from acetonitrile/water (1:4), isolated through filtration on paper (porosity: 6 μm) and dried on $CaCl_2$ under vacuum. The final product has been obtained as 5.75 g of yellow coarse solid. Yield: 72%. ^{1}H-NMR (25 °C, 300 MHz, $CDCl_3$): δ [ppm] = 7,93 (4H, m), 7,32 (4H, m), 6,56 (2H, s), 1,48 (9H, s).

9.1.4 {[$Eu_2L^F{}_4$](NEt_4)$_2$} cage

In a 4 mL screw cap vial, the L^F ligand (80.1 mg, 0.12 mmol) has been dissolved in 2 mL of ethanol at 50 °C. A ≈ 1.5 M methanol solution of tetraethylammonium hydroxide (167 µL, 0.25 mmol) has been added to the ligand solution, followed by addition of $EuCl_3 \cdot 6H_2O$ (18.4 mg, 0.05 mmol), previously dissolved in 1 mL of ethanol. The ratio Eu^{3+}:ligand:base used was 1:2.5:5. The formation of a suspension of fine white solid has been immediately observed, and the reaction mixture has been stirred at 50 °C for 4 hours. Next, the precipitate has been isolated from the mixture through centrifugation cycles of 3 minutes at 6000 rpm with cold ethanol and dried on $CaCl_2$ under vacuum. The final product has been obtained as 46.3 mg of white powder. Yield: 30%.

9.2 Single crystal X-ray diffraction

Single crystals for the {[$Eu_2L^F{}_4$](NEt_4)$_2$} cage were obtained from mother liquors (ethanol) after two weeks. Ligand L^F single crystal were obtained by slow evaporation of an acetonitrile/water (1:4) solution.

Data for ligand L^F were collected using an Oxford Diffraction Gemini E diffractometer, equipped with a 2K × 2K EOS CCD area detector and sealed–tube Enhance (Mo) and (Cu) X–ray sources. A suitable single crystal of L^F was fastened on a nylon loop and measured at room temperature. Empirical multi-scan absorption corrections using equivalent reflections have been performed with the scaling algorithm SCALE3 ABSPACK. Data reduction, finalization and cell refinement were carried out through the CrysAlisPro software. Accurate unit cell parameters were obtained by least squares refinement of the angular settings of strongest reflections, chosen from the whole experiment.

A suitable crystal for the Eu cage was mounted at room temperature in NVH oil and measured at 150K. Data were collected on a Bruker D8 Venture diffractometer equipped with Incoatec IµS3.0 (EF) microfocus sealed-tube (Cu-Kα, $\lambda = 1.54178$ Å), a

Montel layer optics monochromator, and a Photon III C14 CPAD area detector. Data integration was done with SAINT, data scaling and absorption correction were performed with SADABS, in the APEX3 software.

The structures were solved with Olex2[4] by using ShelXT[5] structure solution program by Intrinsic Phasing and refined with the ShelXL[6] refinement package using least-squares minimization. In the last cycles of refinement, non-hydrogen atoms were refined anisotropically. Hydrogen atoms were included in calculated positions, and a riding model was used for their refinement.

Cambridge Crystallographic Data Centre (CCDC) numbers 2349361 and 2349362 contain the crystallographic data of L^F and $\{[Eu_2L^F{}_4])(NEt_4)_2\}$, respectively. These data are provided free of charge by the joint CCDC and Fachinformationszentrum Karlsruhe Access Structures service www.ccdc.ca-m.ac.uk/structures.

9.3 Electrospray ionization mass spectrometry (ESI-MS)

Electrospray ionization mass spectrometric measurements (ESI-MS) were performed using a LCQ Fleet ion trap instrument (ThermoFisher), equipped with a HESI source, operating in negative ion mode. The mass spectra were acquired using the following experimental parameters: T_{HESI} = 35 °C; $T_{transfer\ capillary}$= 275 °C; Voltage HESI= 4 kV; nebulizer gas flow rate (N_2): 10 a.u.; auxiliary gas flow rate (N_2): 5 a.u. Sample solutions (10^{-6} M in acetonitrile) were introduced by direct infusion using a syringe pump at a flow rate of 8 $\mu L \cdot min^{-1}$.

9.4 Materials preparation

All glass substrates used either for the casting of polymer blends or for slot die coating of PMMA films were cleaned with soap and rinsed with deionized water, acetone, and 2-propanol, in this sequence. An acid pre-treatment was then carried out by keeping the glass slides in a HCl 6 M bath ≈ 15 hours. The substrates were then removed and rinsed with de-ionized water and 2-propanol, in this sequence.

9.4.1 Bulk-doped PMMA tiles

Bulk-doped PMMA tiles have been prepared through bulk radical polymerization of methyl methacrylate solutions containing the desired amount of luminophore, 20% wt. of commercial polymethylmethacrylate powder (AMW = 350 000 g mol^{-1}) and 0.1% wt. of azobisisobutyronitrile. For a standard $50 \times 50 \times 2.7$ mm^3 sample, the polymerization solution has been prepared by dissolving the luminophore and 2.8 g of PMMA powder in 15 mL of MMA, heating the mixture at 60 °C. After complete PMMA incorporation, the syrup has been left to cool at ambient temperature, before adding 15 mg of AIBN. After initiator dissolution, the mixture has been transferred to the casting mould, filling it from the upper open side using a plastic funnel. The mould was comprised of two glass plates held in parallel by metal clamps and separated by a PVC gasket 3 mm thick. Any air bubbles incorporated in the syrup during mould filling have been removed by waiting for them to reach the solution surface and popping them with a needle. The mould has been closed and placed in a vacuum-sealed plastic bag, before putting it in a pre-heated 60 °C water bath. After conducting the polymerization for 5 – 8 hours, the bath has been removed from heating and left to cool at room temperature. The mould has then been placed in a hot-air oven and the PMMA tile post-cured using a temperature ramp. Finally, the polymerised tile has then been extracted from the mould by removing the glass plates and cutting off the plastic gasket. The tile's edges have been polished with increasing grit sandpaper and with CeO_2 on cloth to yield the finished product.

9.4.2 Glass-supported PMMA films

Glass-supported PMMA films been prepared through slot die coating of PMMA/luminophore solutions. The employed instrument was the Ossila Ltd. slot die coater, first version. Square N-BK7 glass (Edmund Optics) slates having dimensions of $50 \times 50 \times 3$ mm^3 and all six faces optically polished have been used as substrates. For a standard 35 μm thick film with 50×50 mm^2 area, 0.5 g of commercial PMMA powder (AMW = 350 000 g mol^{-1}) have been dissolved in 5 mL of DMSO/THF 3:2 solvent mixture, heating at 40 °C. The desired amount of luminophore has been introduced before the polymer. The cooled solution has then been filtered using a Luer lock syringe clogged with cotton wool. The filtered solution has been loaded in a new syringe and fastened in the dedicate lodging on the coater. The syringe has been connected to the head's inlet with a Luer lock PTFE tube having inner diameter of 1.5 mm. The dispensing outlet of the coating head featured a 50 mm width and a 200 μm lateral aperture, achieved by using two intermediate shims each 100 μm thick. Before carrying out the deposition procedure, both the stage and the head of the coater were levelled using the two-point gauge system equipped on the instrument. The substrate-head gap was set at 800 μm. The film deposition has been carried out with the optimized program described in *Chapter 2*. The target glass substrate was pre-treated in low-pressure vacuum plasma reactor (Tucano, Gambetti Kenologia Srl) with O_2 gas. The plasma treatment has an overall duration of 3 minutes, employed a RF source power of 100 W and a gas flow of 40 sccm. Film depositions were carried out with the stage heated at 60 °C, while a first film drying step was performed by heating the stage at 90 °C for ≈ 1 hour. Full drying was performed at 90 °C hot-air oven overnight.

9.5 Photophysical characterizations

9.5.1 UV/Vis absorption spectroscopy

All absorption spectra were recorded on a CARY5000 double-beam spectrophotometer in the $300 - 800$ nm range, with a spectral bandwidth of 2 nm. In the case of liquid solution samples, the contribution of the solvent and of the cuvette was subtracted by using an equal quantity of pure solvent as blank sample. For bulk-doped LSCs, an equivalent undoped PMMA tile was used as blank sample. Finally, for luminescent PMMA films, the blank sample consisted in an analogous undoped PMMA film. The absorbance of LSC samples was measured by placing the tile/slate perpendicularly to the incident beam. For glass-supported film, the film-coated face faced away from the incident light beam.

Transmittance ($\tau(\lambda)$) and reflectance ($\rho(\lambda)$) spectra of LSCs have been recorded on the same instrument, equipped with a poly(tetrafluoroethylene)-coated integration sphere, and with the same parameters. Absorptance ($\alpha(\lambda)$) spectra have been calculated as $\alpha(\lambda) = 1 - \tau(\lambda) - \rho(\lambda)$. When necessary, shortpass filters (Asahi spectra, models ZHS0350 and ZVS0590) were placed between the sample and the integrating sphere to remove the contribution of escaped PL photons.

9.5.2 Emission spectroscopy

Photoluminescence spectra have been collected on a Horiba JobinYvon *Fluorolog-3* spectrofluorometer equipped with double-grating monochromators in excitation and iHR320 spectrograph in the emission side. A *R928P* Hamamatsu photomultiplier or a Horiba Sincerity CCD detector where employed. A 450 W Xe arc lamp was used as excitation source.

The measurements were performed using the usual 90° geometry both for the solutions and LSCs, with the latter facing the direction of the incident beam. Emission spectra were corrected for detection and optical spectral response of the spectrofluorometer supplied by the manufacturer. Absolute $PLQY$ measurements have been performed on the same instrument equipped with a poly(tetrafluoroethylene)-coated integration sphere accessory (4”, F-3018, Horiba Jobin Yvon), using a 90° excitation-collection geometry.

The luminescence lifetimes in the microsecond – millisecond scales and the relative luminescence decay curves were measured using a pulsed Xe lamp with variable repetition rate and elaborated with standard DAS6 software fitting procedures.

9.6 LSC electrical characterizations

9.6.1 Current-voltage curves

Current-voltage curves of the LSC-PVs have been collected under simulated solar irradiation (100 mW cm^{-2}, AM1.5G) with a Keithley 2450 Graphical Source Measure Unit. Monocrystalline Si cells coupled to the LSCs were purchased from IXYS Corporation (series IXOLAR^{TM} SolarBIT, model KXOB22-12X1F). Optical coupling was performed using Dow Corning^{TM} High-Vacuum grease.

9.6.2 External Quantum Efficiency

External quantum efficiency measurements have been performed on a custom-assembled setup, comprised of a UV/Vis transmitting optical fibre (Ocean Insight QP1000-2-UV/Vis, 300–1100 nm) coupled to the Horiba JobinYvon *Fluorolog-3* spectrofluorometer, and an appropriate sample and PV cell holder. The incident light has been focused on the LSC surface (spot diameter 1 mm) through a lens doublet. The focusing optics have been mounted on a XYZ linear stage allowing alignment of the light spot and scanning over the whole sample surface (25 mm^2). Incident power readings were acquired using a Thorlabs Power and Energy Meter (PM103A) equipping a compatible UV extended Si photodiode head (Thorlabs, S130VC). Current readings were collected with a Keithley 2450 Graphical Source Meter Unit. Optical coupling was performed using Dow Corning^{TM} High-Vacuum grease.

9.7 Photodetector characterizations

9.7.1 Current response

The LSC-PV photodetectors were mounted on analogous sample and PV cell holders used for previous LSC-PV characterizations. A series of Thorlabs UV LEDs (M275D2, M310D1, M325D3, M340D4, M375D4 and M395D4) was employed as light source, mounting them on a XYZ linear stage that allowed easy alignment of the light source over the DUT. The LED were powered using a driver (Thorlabs DC2200) able to provide both continuous and pulsed illumination. Current readings were acquired through a Keithley 2450 Graphical Source Measure Unit, while LED incident power readings were acquired using a Thorlabs Power and Energy Meter (PM103A) equipping a compatible UV extended Si photodiode head (Thorlabs, S130VC). Data used for calculating responsivity and specific detectivity were acquired in continuous illumination conditions. Limit of detection and selectivity tests employed pulsed illumination, using a square form and a 50% duty cycle. In the latter, a white LED array was used to provide a white light bias. Spectrum in **Fig. C5** of *Appendix C2.1*.

9.7.2 Time response

Rise and fall times were measured by connecting the DUT to an Agilent DSO5054A 5000 Series Oscilloscope (500 MHz, 4 Channels). The LED driver output was monitored through the oscilloscope as well and served as digital trigger for synchronization to the DUT signal. Pulsed illumination was set with a square waveform and duty cycle of 50%. The oscilloscope allowed for a real time averaging of the readings, which was set at 32. Rise and fall times were calculated using the oscilloscope's dedicated functions.

9.8 Coloured PV

9.8.1 Materials

The optical filters used as absorptive coloured layers are a series of squared 50 × 50 × 3 mm^3 long pass and bandpass filters (Melles Griot) made from different colours of Schott® glass (long pass: OG590, RG695; bandpass: BG18, KG1, VG9).

The optical diffusers used as scattering white layers are a series of round (diameter 50 mm, thickness 2 mm) ground glass diffusers made of N-BK7 glass. They possess one polished side and one sandblasted side, available with four different grits: Thorlabs DG20-120, DG20-220, DG20-600, DG20-1500.

Fluorescent polymer films were prepared by dispersing organic fluorophores into PMMA. Specifically, they were prepared using the drop-casting procedure starting from chloroform solutions of the fluorophore and PMMA in different weight ratios, according to a previously published procedure.[7] A solution containing 60 mg of PMMA and the appropriate amount of fluorophore to reach concentrations ranging from 0.4% to 2.0% was poured onto a 50 × 50 × 3 mm^3 optically pure glass substrate (Edmund Optics Ltd. BOROFLOAT window 50 × 50 TS). The product was obtained after evaporation at room temperature in a closed environment.

A low autofluorescence microscopy immersion oil with refractive index of 1.518 (Thorlabs OILCL30) was employed for the optical coupling between the PV cell and the coloured layer.

9.8.2 Optical characterizations

The transmittance of the coloured filters and diffusers were collected on a CARY5000 double-beam spectrophotometer, equipped with a poly(tetrafluoroethylene)-coated integration sphere, and with a spectral bandwidth of 2 nm. The transmittance of PMMA fluorescent films were collected on a Shimadzu UV-2600 spectrometer, equipped with an integration sphere and with a spectral bandwidth of 1 nm. The colorimetric measures were performed by using a vertical spectrophotometer 3color SV-300 (wavelength range 400 – 700 nm, D65 illuminant and CIE 10° standard observer).

9.8.2 Electrical characterizations

A Horiba JobinYvon *Fluorolog-3* spectrofluorometer equipped with double-grating monochromators on the excitation side and iHR320 spectrograph on the emission side was used a light source. The excitation monochromator is equipped with two 1200 lines/mm gratings blazed at 330 nm (2nm/mm dispersion). A spectral bandwidth of 6 nm was used for the experiments. A Vis/NIR transmitting optical fibre (Thorlabs liquid lightguide LLG3-4Z, 5 mm diameter, 420 – 2000 nm) was used to direct the light from the *Fluorolog-3* onto the PV cell. An uncoated UV fused silica plano-convex lens (Melles Griot 01LUP049, diameter 50 mm, 185 – 2100 nm) was used to collimate the beam. The optical power of the incident beam was measured through a Gentec-EO PowerMeter, model PRONTO-Si. A monocrystalline, single module Si photovoltaic cell (IXYS Corporation, series IXOLAR^{TM} SolarBIT, model KXOB22-12X1F) with active area of 22 × 7 mm^2 has been chosen as test PV cell. Spectral short-circuit current was measured with a Keithley 2450 Graphical Source Measure Unit synchronized with the *Fluorolog-3*. Current spectra were acquired between 440 and 1100 nm with a step of 10 nm.

9.9 Bibliography

1 M. Rancan, M. Rando, L. Bosi, A. Carlotto, R. Seraglia, J. Tessarolo, S. Carlotto, G. H. Clever and L. Armelao, *Inorg. Chem. Front.*, 2022, **9**, 4495–4505.

2 M. Rancan, J. Tessarolo, A. Carlotto, S. Carlotto, M. Rando, L. Barchi, E. Bolognesi, R. Seraglia, G. Bottaro, M. Casarin, G. H. Clever and L. Armelao, *Cell Rep. Phys. Sci.*, 2022, **3**, 100692.

3 L. R. Melby, N. J. Rose, E. Abramson and J. C. Caris, *J. Am. Chem. Soc.*, 1964, **86**, 5117–5125.

4 O. V. Dolomanov, L. J. Bourhis, R. J. Gildea, J. a. K. Howard and H. Puschmann, *J. Appl. Crystallogr.*, 2009, **42**, 339–341.

5 G. M. Sheldrick, *Acta Crystallogr. Sect. Found. Adv.*, 2015, **71**, 3–8.

6 G. M. Sheldrick, *Acta Crystallogr. Sect. C Struct. Chem.*, 2015, **71**, 3–8.

7 C. Papucci, R. Charaf, C. Coppola, A. Sinicropi, M. Di Donato, M. Taddei, P. Foggi, A. Battisti, B. De Jong, L. Zani, A. Mordini, A. Pucci, M. Calamante and G. Reginato, *J. Mater. Chem. C*, 2021, **9**, 15608–15621.

Appendix A

Film thickness measurements

Thin film reflectometry is a non-invasive technique for determining several properties of a material deposited in the form of a film, among which its thickness. The Swanepoel method for film thickness extrapolation allows to determine thicknesses from a few nanometres up to a few hundreds of micrometres.[1]

This method relies upon the interaction between light and two partially reflecting, closely paced interfaces, like the upper and lower surfaces of the film. The light reflected by the two interfaces can add in a constructive or destructive manner, giving rise to interference fringes in the reflectance spectrum of the film (**Fig. A1**). The spacing between fringes depends on the distance between the two interfaces, namely the film thickness.

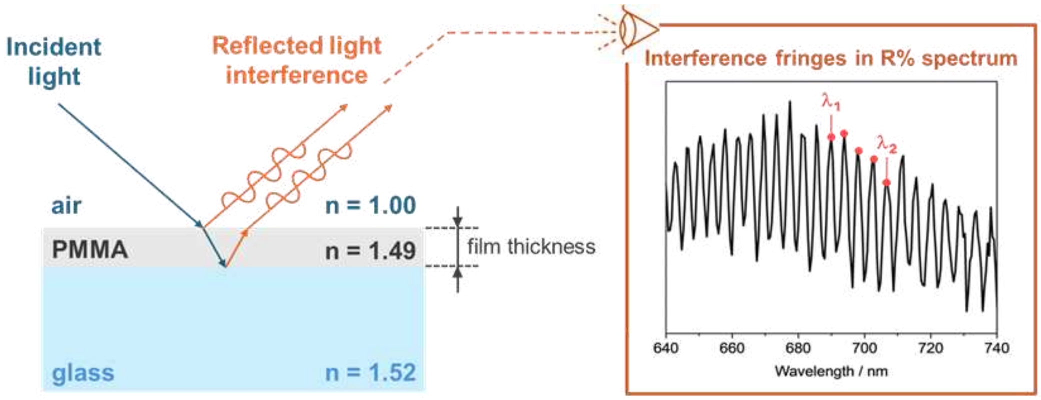

Figure A1. Depiction of interference fringes generation in a glass-supported PMMA film upon interaction with light.

---

[1] R Swanepoel *J. Phys. E: Sci. Instrum.*, 1983, **16**, 1214.

When using a normal incidence geometry, thickness is derived from the spectrum as:

$$thickness\ (nm) = \frac{1}{2V} \quad ; \quad V = \frac{n\left(\frac{1}{\lambda_1} - \frac{1}{\lambda_2}\right)}{N - 1} \qquad \textbf{Eq. A1}$$

where n is the refractive index of the film, λ_1 and λ_2 are the wavelengths of two fringes maxima (or minima) and N is the number of maxima (or minima) comprised between λ_1 and λ_2, ends included. Reflectance spectra acquisitions for thickness determination can be carried out with a basic experimental setup. The one used in this work is schematized in **Fig. A2**. A white LED is employed as light source, while the detector is a CCD spectrometer. The two branches of a bifurcated quartz optical fibre are connected to light source and detector, while the bundle end is placed perpendicular to the film top surface. The film can be moved manually to probe different spots across its area. Interference fringes were already observed in the raw spectra, which were used for calculating the thickness without further elaboration.

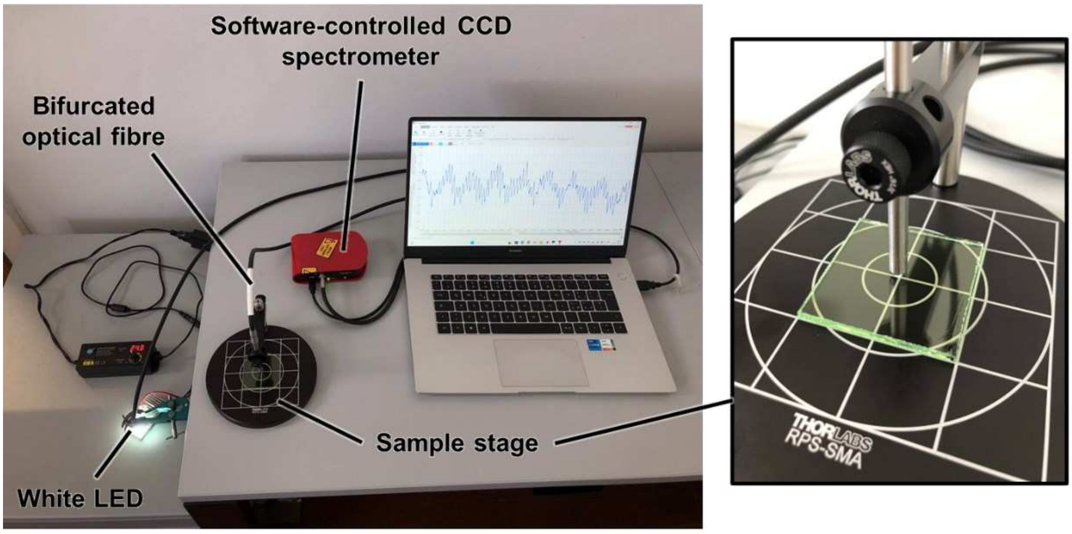

Figure A2. Experimental reflectance setup used for film thickness measurements.

Appendix B

Plasma cleaning

Plasma is often referred to as the fourth state of matter. It is generated when an energy trigger, such as an electric discharge, is applied to a gas to ionize it. The ionized state of the gas is a collection of free-moving ions, electrons and neutral atoms or molecules, overall electrically neutral.[1] Plasma can be used in surface cleaning processes to remove contaminants from a substrate or alter its surface properties. Plasma cleaning has become increasingly popular in several industries (semiconductors, biomedical, precision mechanics, ophthalmic) thanks to the process not depending on hazardous or aggressive chemical agents and to the high control over plasma properties that make it suitable for targeted applications. Depending on the nature of the gas, physical or chemical plasma cleaning can be achieved.[2] Physical cleaning is obtained by using non-reactive gases such as argon or nitrogen, which effect on the substrate is purely ballistic. The ionized atoms interact with the surface by inelastic collisions, physically dislodging particles from the surface. This treatment is useful to deep-clean the substrate from organic and inorganic residues, remove thin films, oxide layers and unwanted substances in general. Chemical cleaning instead uses reactive species such as oxygen or hydrogen. These gases react with the substrate by breaking existing surface molecular bonds or forming new ones, ultimately altering the surface energy of the material. Chemical cleaning activates the surface by enhancing its wettability and improving its bonding capabilities.

---

[1] Alfred Grill, *Cold Plasma Materials Fabrication: From Fundamentals to Applications*, Wiley, 1994

[2] S. Sammut, *Appl. Sci.*, 2025, **15**, 7361.

In this work, O_2 plasma cleaning was used to activate the glass substrates needed for PMMA film depositions with slot die coating. In the case of glass, the O_2 treatment maximises the concentration of surface hydroxyl groups, thus greatly enhancing the substrate's wettability.[3,4] The cleaning was carried out with a low-pressure vacuum plasma reactor (Tucano, Gambetti Kenologia Srl), which generates the plasma by applying an alternating radiofrequency (RF) signal between two electrodes.[2] User editable parameters are the gas flow volume (in sccm, *i.e.*, standard cubic centimetre per minute), the RF signal power and the treatment time. A recipe using O_2 at 40 sccm and RF at 100 W for 3 minutes was employed to clean the substrates, with optimal improvement of the glass wettability (**Fig. B1**). This plasma pre-treatment resulted in a higher thickness uniformity of the coatings over the whole substrate area and in reduced edge defects.

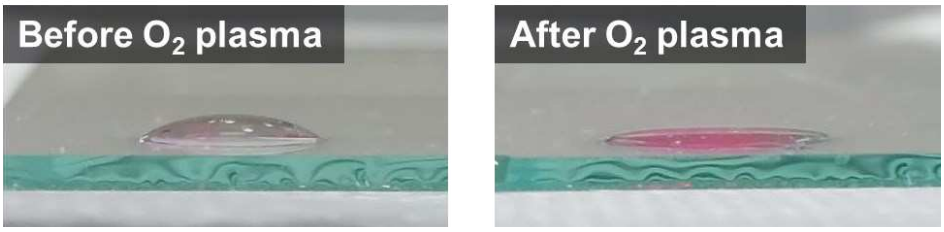

Figure B1. Visual comparison of the wettability of a glass surface before and after treatment with O_2 plasma. The liquid droplets have been deposited from a Rhodamine B aqueous solution.

---

[3] D. Li, M. Xiong, S. Wang, X. Chen, S. Wang and Q. Zeng, *Appl. Surf. Sci.*, 2020, **503**, 144257.

[4] A. U. Alam, M. M. R. Howlader and M. J. Deen, *J. Micromechanics Microengineering*, 2014, **24**, 035010.

Appendix C

Additional figures and data

C1.1 Chapter 4: XRD analysis

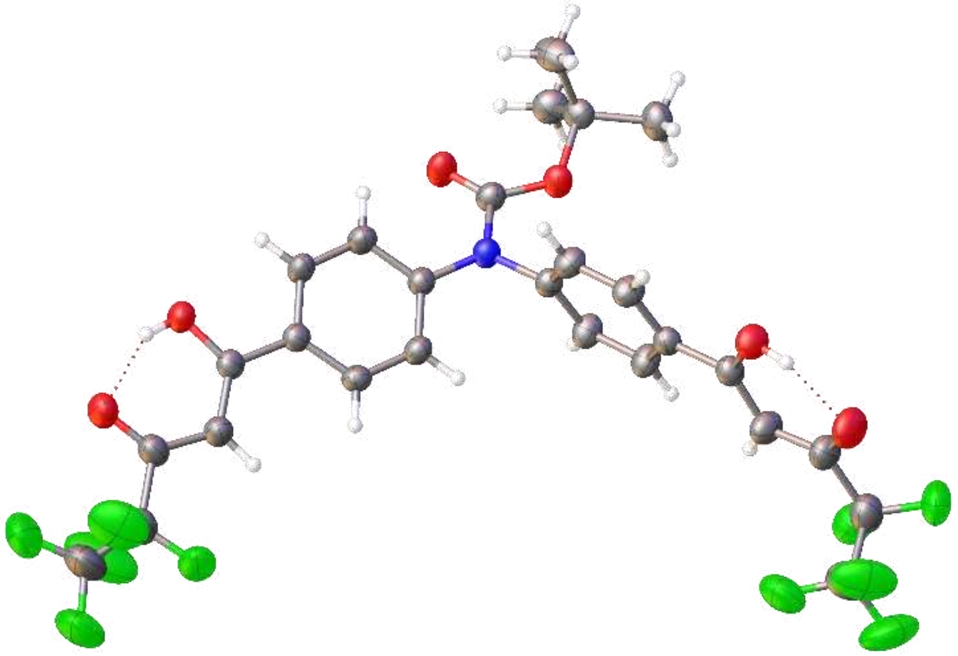

Figure D1. The asymmetric unit of L^F, thermal ellipsoid drawn at 30% probability level. Color code: C, grey; O, red; N, blue; F, green; H, white.

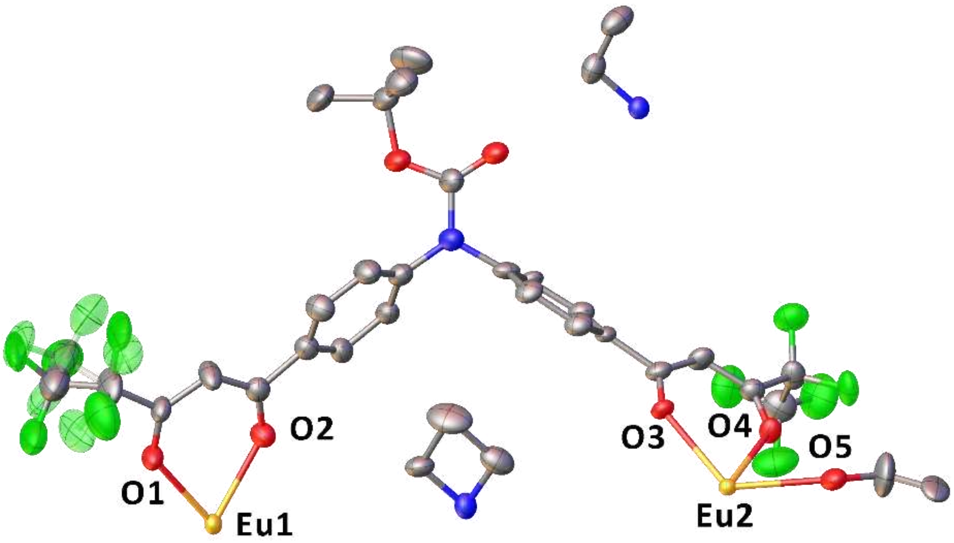

Figure D2. The asymmetric unit for the {$[Eu_2L^F{}_4]$)$(NEt_4)_2$} cage, thermal ellipsoid drawn at 50% probability level. Color code: C, grey; O, red; N, blue; F, green; Eu, orange. Disordered parts translucent. H atoms omitted for clarity.

Refinement details for Eu cage

The compound crystallizes in the *P*4/*ncc* space group. In the asymmetric unit, a quarter of the cage is present. One of the two terminal fluorinated groups has been split in two parts the occupancies of which were constrained to sum to 1.0. Ligand and ethanol molecule were modelled with the help of the FragmentDB plugin[1] in the framework of OLEX2. RIGU restraints were applied. The final Fourier map revealed the presence of non-negligible residual peaks located in a large array of voids. A total accessible void volume per unit cell of 1772 Å^2 was calculated (SQUEEZE,[3] probe radius 1.2 Å) corresponding to the 11.9 % of the total unit cell volume divided in four voids of 443 Å^2 each. A single void contains 103 electrons. This value closely close fits the presence of 4 ethanol molecules accounting for 96 electrons.

---

[1] D. Kratzert and I. Krossing, *J Appl Crystallogr*, 2018, **51**, 928–934.

[2] L. R. Melby, N. J. Rose, E. Abramson and J. C. Caris, *J. Am. Chem. Soc.*, 1964, **86**, 5117–5125.

[3] A. L. Spek, *Acta Cryst C*, 2015, **71**, 9–18.

Table D1. Crystal data and structure refinement for the L^F ligand and the $\{[Eu_2L^F{}_4])(NEt_4)_2\}$ cage.

	L^F	**$\{[Eu_2L^{F}{}_4])(NEt_4)_2\}$**
Empirical formula	$C_{27}H_{21}F_{10}NO_6$	$C_{126}H_{122}Eu_2F_{40}N_6O_{25}$
Formula weight/ g mol^{-1}	645.45	3184.21
Temperature/K	297.1(3)	150.00
Crystal system	triclinic	tetragonal
Space group	P-1	P4/ncc
a/Å	5.66571(15)	18.6338(5)
b/Å	14.1061(4)	18.6338(5)
c/Å	18.5822(6)	42.6165(19)
α/°	72.299(3)	90
β/°	85.374(2)	90
γ/°	88.917(2)	90
Volume/Å^3	1410.17(7)	14797.2(10)
Z	2	4
ρ_{calc} / g cm^3	1.520	1.429
μ/mm^{-1}	1.336	7.027
F(000)	656.0	6424.0
Crystal size/mm^3	0.15 × 0.21 × 0.22	0.089 × 0.082 × 0.041
Radiation	Cu Kα (λ = 1.54184)	CuKα (λ = 1.54178)
2Θ range for data collection/°	6.954 to 140.924	4.146 to 148.972
Index ranges	$-5 \leq h \leq 6$, $-17 \leq k \leq 17$, $-22 \leq l \leq 20$	$-22 \leq h \leq 23$, $-23 \leq k \leq 21$, $-53 \leq l \leq 53$
Reflections collected	14833	166245
Independent reflections	5259 [Rint = 0.0319, Rsigma = 0.0303]	7570 [Rint = 0.1300, Rsigma = 0.0394]
Data/restraints/parameters	5259/0/402	7570/710/531
Goodness-of-fit on F^2	1.048	1.024
Final R indexes [I>=2σ (I)]	R1 = 0.0710, wR2 = 0.2043	R1 = 0.0896, wR2 = 0.2404
Final R indexes [all data]	R1 = 0.0976, wR2 = 0.2345	R1 = 0.1120, wR2 = 0.2609
Largest diff. peak/hole / e Å^{-3}	0.41/−0.29	1.71/−1.82
CCDC number	2349361	2349362

Continuous shape measures analysis

A continuous shape measures analysis of Eu ions coordination polyhedra has been performed with the SHAPE 2.1 software considering an eight-coordination for Eu1 and a nine-coordination for Eu2. The closer the value to zero, the better it fits to the ideal geometry.

Table D2. Coordination geometries evaluated for the eight-coordination of Eu1 and output of the SHAPE 2.1 software for Eu1.

Abbreviation	**Ideal geometry**	**Symmetry**	**Output**
OP-8	Octagon	D_{8h}	27.195
HPY-8	Heptagonal pyramid	C_{7v}	24.486
HBPY-8	Hexagonal bipyramid	D_{6h}	15.677
CU-8	Cube	O_h	7.954
SAPR-8	**Square antiprism**	$\boldsymbol{D_{4d}}$	**0.334**
TDD-8	Triangular dodecahedron	D_{2d}	2.275
JGBF-8	Johnson gyrobifastigium J26	D_{2d}	16.227
JETBPY-8	Johnson elongated triangular bipyramid J14	D_{3h}	28.892
JBTPR-8	Biaugmented trigonal prism J50	C_{2v}	2.992
BTPR-8	Biaugmented trigonal prism	C_{2v}	2.188
JSD-8	Snub disphenoid	D_{2d}	5.412
TT-8	Triakis tetrahedron	T_d	8.831
ETBPY-8	Elongated trigonal bipyramid	D_{3h}	23.763

Table D3. Coordination geometries evaluated for the eight-coordination of Eu2 and output of the SHAPE 2.1 software for Eu2.

Abbreviation	Ideal geometry	Symmetry	Output
EP-9	Enneagon	D_{9h}	38.385
OPY-9	Octagonal pyramid	C_{8v}	20.890
HBPY-9	Heptagonal bipyramid	D_{7h}	21.309
JTC-9	Triangular cupola (J3) = trivacant cuboctahedron	C_{3v}	17.511
JCCU-9	Capped cube (Elongated square pyramid, J8)	C_{4v}	10.960
CCU-9	Capped cube	C_{4v}	9.774
JCSAPR-9	Capped sq. antiprism (Gyrœlongated square pyramid J 10)	C_{4v}	1.025
CSAPR-9	**Capped square antiprism**	$\boldsymbol{C_{4v}}$	**0.029**
JTCTPR-9	Tricapped trigonal prism (J51)	D_{3h}	2.849
TCTPR-9	Tricapped trigonal prism	D_{3h}	1.116
JTDIC-9	Tridiminished icosahedron (J63)	C_{3v}	13.660
HH-9	Hula-hoop	C_{2v}	13.549
MFF-9	Muffin	C_S	0.897

C1.2 Chapter 4: ESI-MS analysis

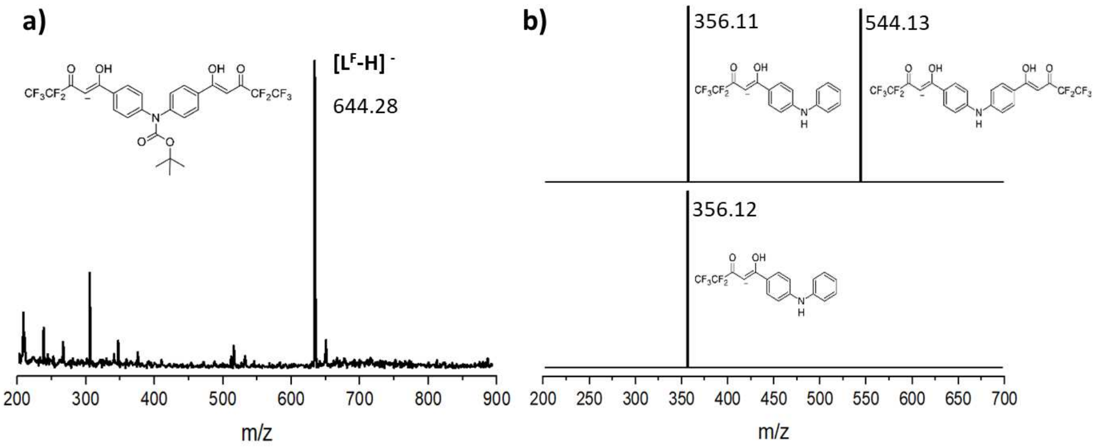

Figure D3. a) ESI-MS spectrum of the L^F ligand. **b)** MS/MS fragmentations relative to 644.28 m/z (top) and 544.13 m/z signals (bottom).

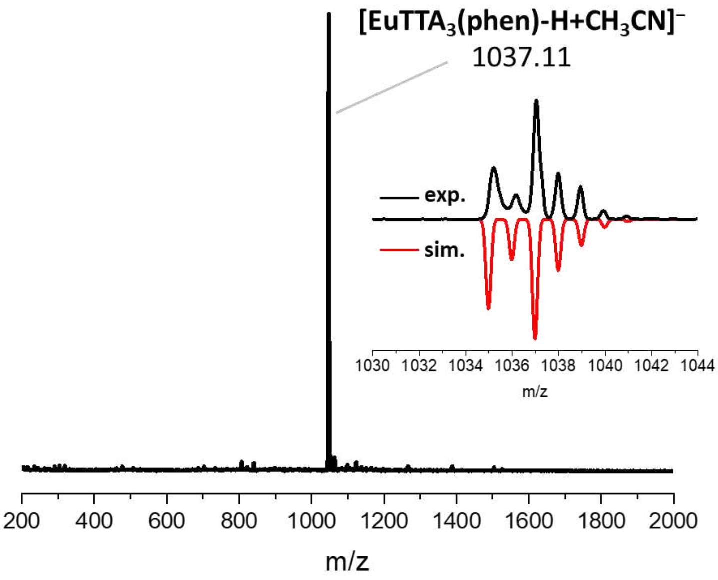

Figure D4. ESI-MS spectra of [Eu(tta)$_3$phen]. Inset: experimental (black line) and simulated (red line) isotopic pattern.

C2.1 Chapter 5: White LED spectrum

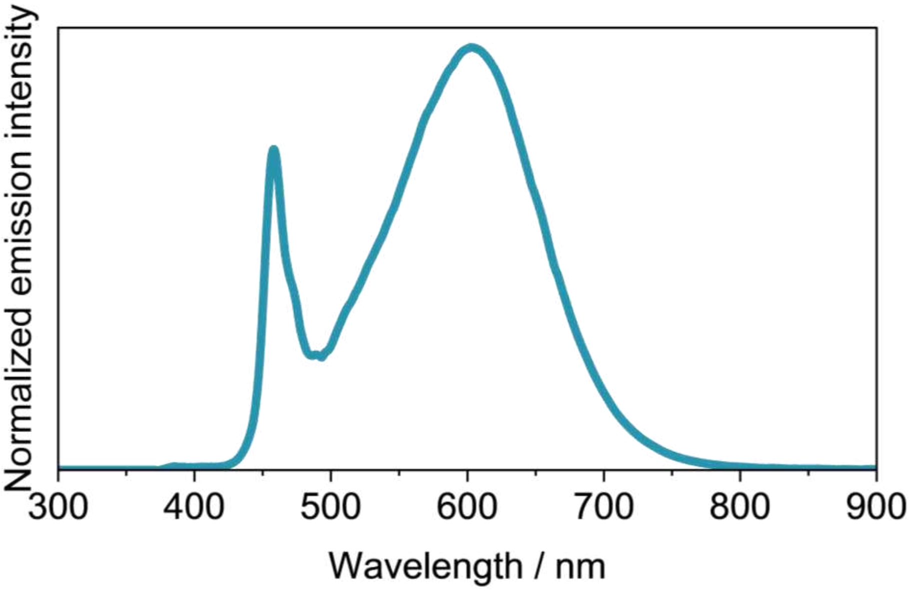

Figure D5. Emission profile of the white LED used for selectivity tests.

C3.1 Chapter 6: Reflectance characterizations

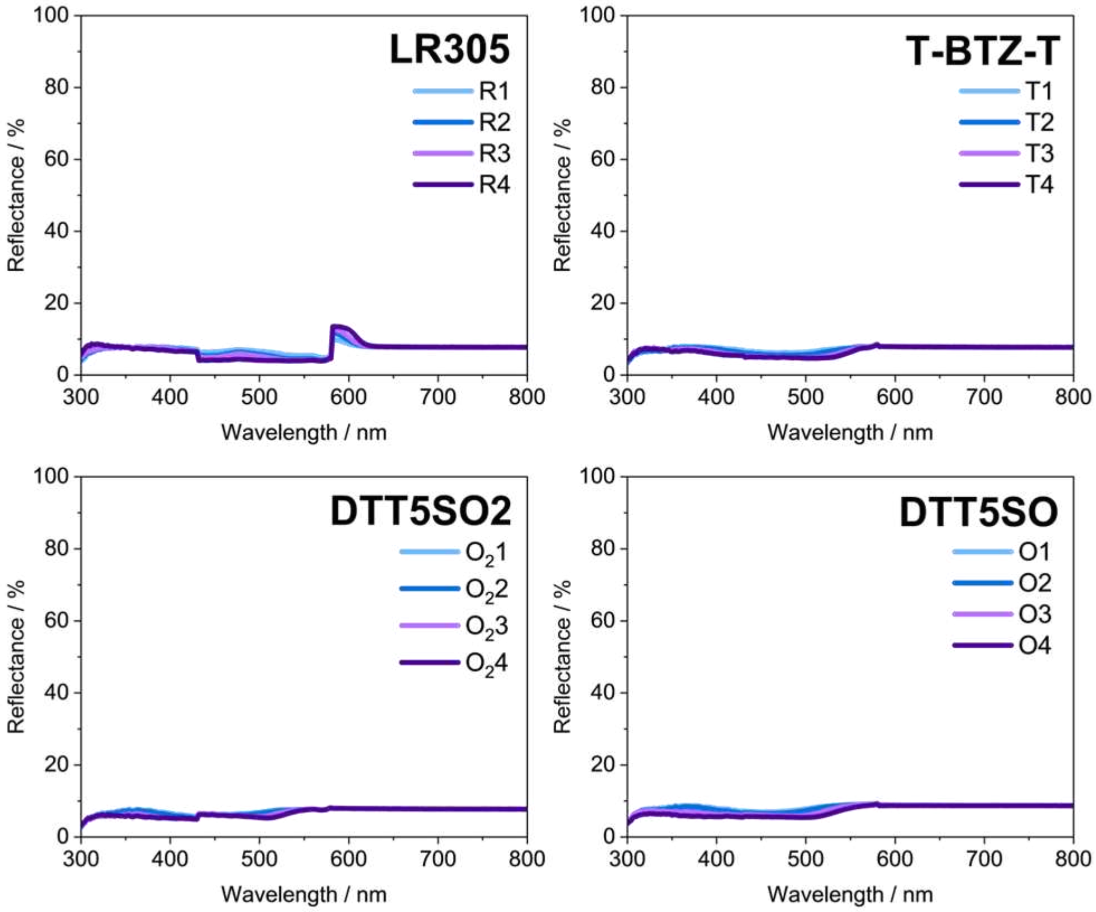

Figure D6. Reflectance spectra of the 50 × 50 mm^2 LSCs.

Table D4. Complete $T\%$ and $R\%$ data relative to the colour rendering index (CRI) and ($a*$, $b*$) $CIELAB$ coordinates calculated for the LSCs.

Sample	**T%**			**R%**		
	CRI	***a****	***b****	**CRI**	***a****	***b****
R1	74.90	12.18	-9.81	81.26	7.36	-0.90
R2	38.82	27.22	-16.82	73.71	11.44	0.84
R3	8.36	36.22	-20.67	71.50	13.40	2.45
R4	< 0	70.43	-5.87	67.69	16.12	7.26
T1	85.64	1.43	14.98	91.41	0.98	4.23
T2	82.49	3.46	27.92	87.20	1.92	6.08
T3	61.12	11.65	65.39	85.08	4.39	7.41
T4	47.83	20.72	92.53	83.32	5.96	7.14
$O_2$1	89.45	-5.38	27.21	94.48	-0.16	4.82
$O_2$2	85.84	-6.51	37.00	87.27	0.01	5.51
$O_2$3	67.09	-5.99	86.34	88.12	1.60	5.47
$O_2$4	51.03	2.10	113.60	88.99	3.10	5.33
O1	90.84	-4.08	22.65	94.45	-0.94	5.66
O2	86.67	-5.18	33.34	92.78	-0.83	7.01
O3	68.62	-3.52	79.43	82.81	1.10	8.48
O4	49.84	6.05	108.91	7.82	3.31	8.68

C3.2 Chapter 6: J-V parameters and EQE consistency checks

Table D5. Short-circuit current density (J_{SC}), open-circuit voltage (V_{OC}), fill factor (FF), maximum power (P_{max}) and power conversion efficiency (PCE) values of tested LSC-PVs. The "Exp." and "Int." labels indicate the experimental J_{SC} extracted from the J-V curves and the J_{SC} integrated from the EQE spectra, respectively.

Sample	**J_{SC} / mA cm^{-2}**		**V_{OC} / mV**	**FF**	**P_{max} / mW**	**PCE / % 1 edge (4 edges)**
	Exp.	**Int.**				
R1	0.402	0.407	558	0.66	3.71	0.148 (0.592)
R2	0.659	0.629	581	0.68	6.55	0.262 (1.048)
R3	0.874	0.925	590	0.69	8.93	0.357 (1.428)
R4	1.144	1.299	600	0.70	12.06	0.483 (1.932)
T1	0.269	0.242	538	0.66	2.34	0.093 (0.372)
T2	0.401	0.381	558	0.66	3.71	0.148 (0.592)
T3	0.584	0.667	570	0.67	5.61	0.224 (0.896)
T4	0.868	0.837	590	0.69	8.87	0.355 (1.420)

O$_2$1	0.269	0.263	535	0.64	2.31	0.092 (0.368)
O$_2$2	0.383	0.384	554	0.66	3.49	0.139 (0.556)
O$_2$3	0.634	0.571	576	0.67	6.16	0.246 (0.984)
O$_2$4	0.675	0.656	578	0.67	6.56	0.263 (1.052)
O1	0.242	0.225	530	0.64	2.04	0.082 (0.328)
O2	0.375	0.320	554	0.66	3.41	0.136 (0.544)
O3	0.467	0.506	560	0.65	4.27	0.171 (0.684)
O4	0.304	0.291	537	0.63	2.58	0.103 (0.412)

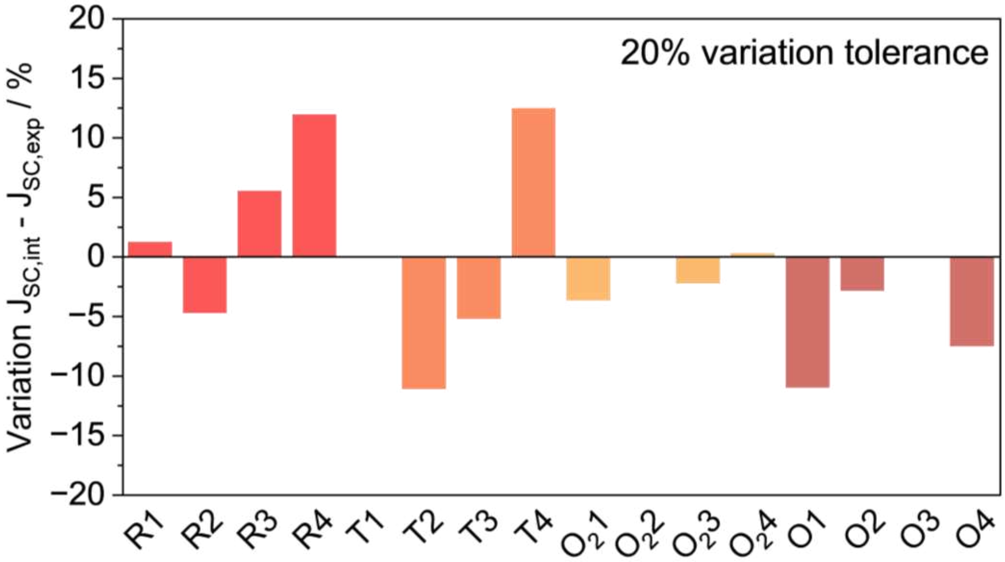

Figure D7. Consistency check on the EQE-integrated J_{SC} for all samples. The variation between the experimental ($J_{SC,exp}$) and the integrated ($J_{SC,int}$) J$_{SC}$ values has been calculated as: $[(J_{SC,int} - J_{SC,exp})/J_{SC,int}] \cdot 100$.

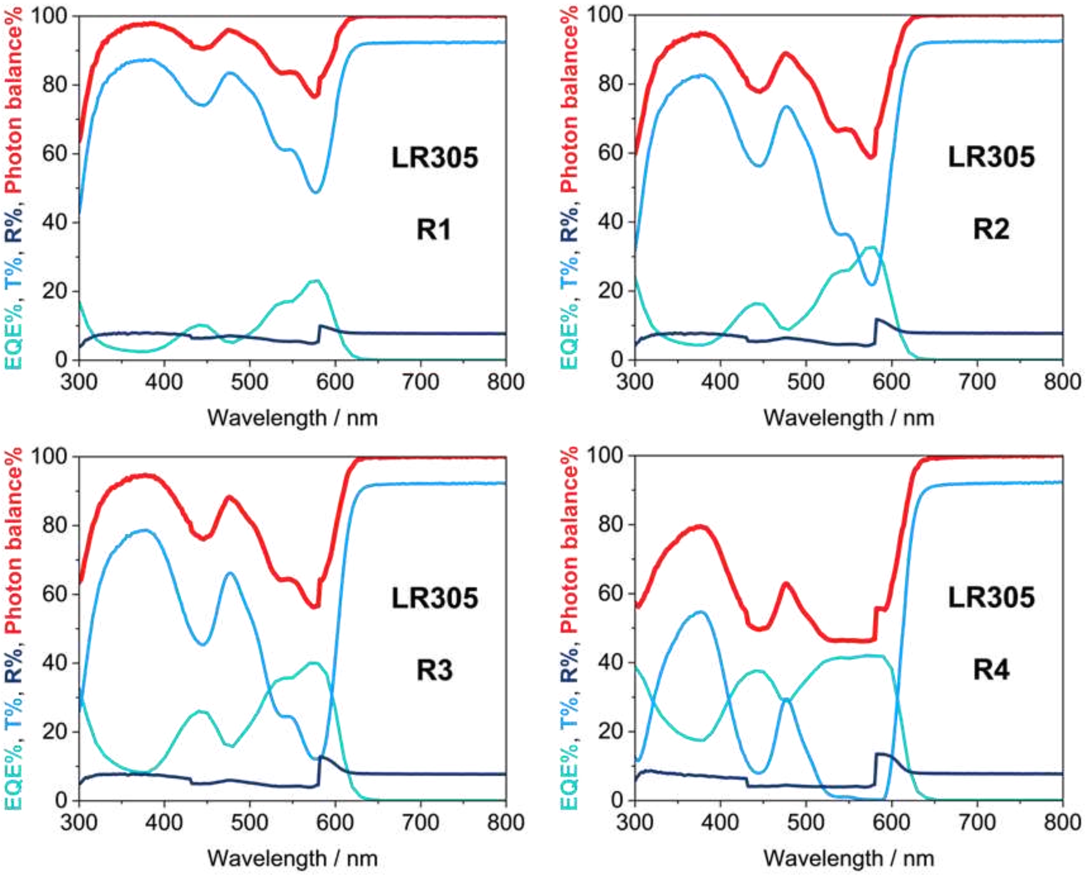

Figure D8. Consistency checks on the photon balance for the **R** sample series. Displayed EQE spectra are relative to a four-edge LSC-PV configuration and have been derived by correcting one-edge measurements for the geometric factor and averaging the corrected spectra. Colour code: red, photon balance; light blue, transmittance spectrum; aqua green, EQE spectrum; blue: reflectance spectrum.

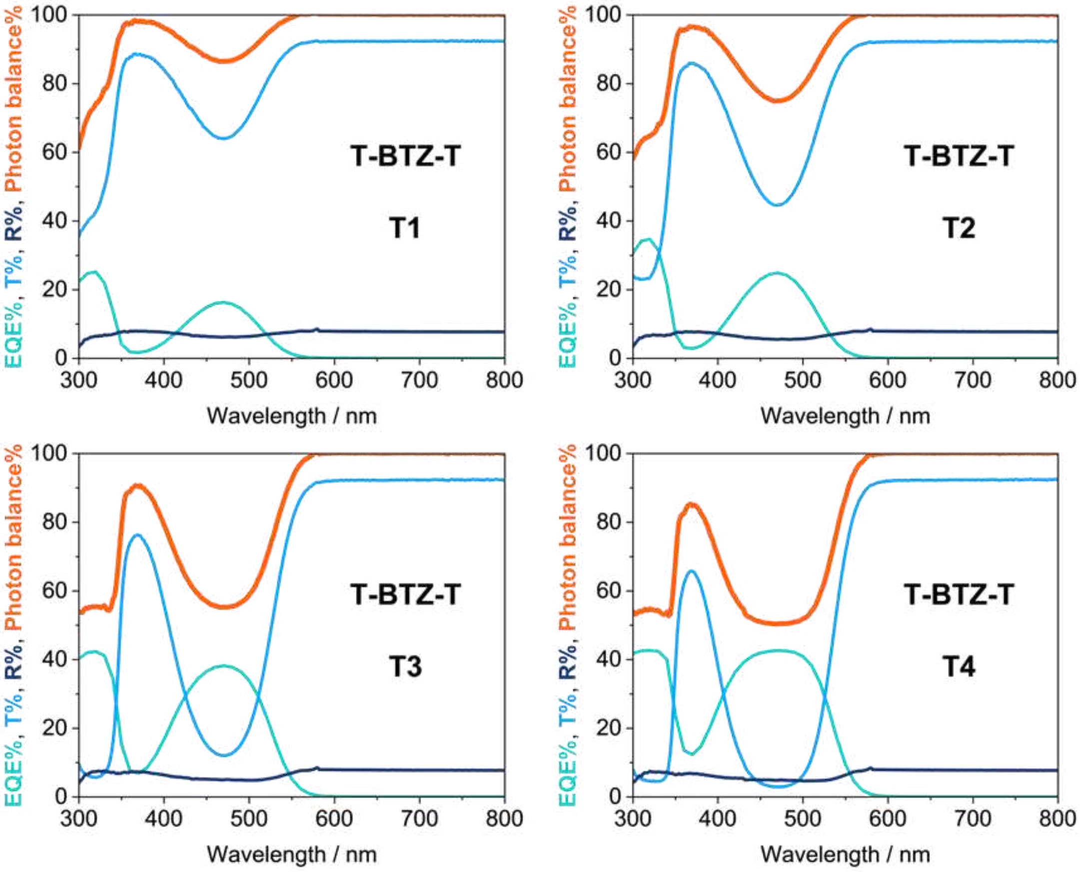

Figure D9. Consistency checks on the photon balance for the **T** sample series. Displayed EQE spectra are relative to a four-edge LSC-PV configuration and have been derived by correcting one-edge measurements for the geometric factor and averaging the corrected spectra. Colour code: orange, photon balance; light blue, transmittance spectrum; aqua green, EQE spectrum; blue: reflectance spectrum.

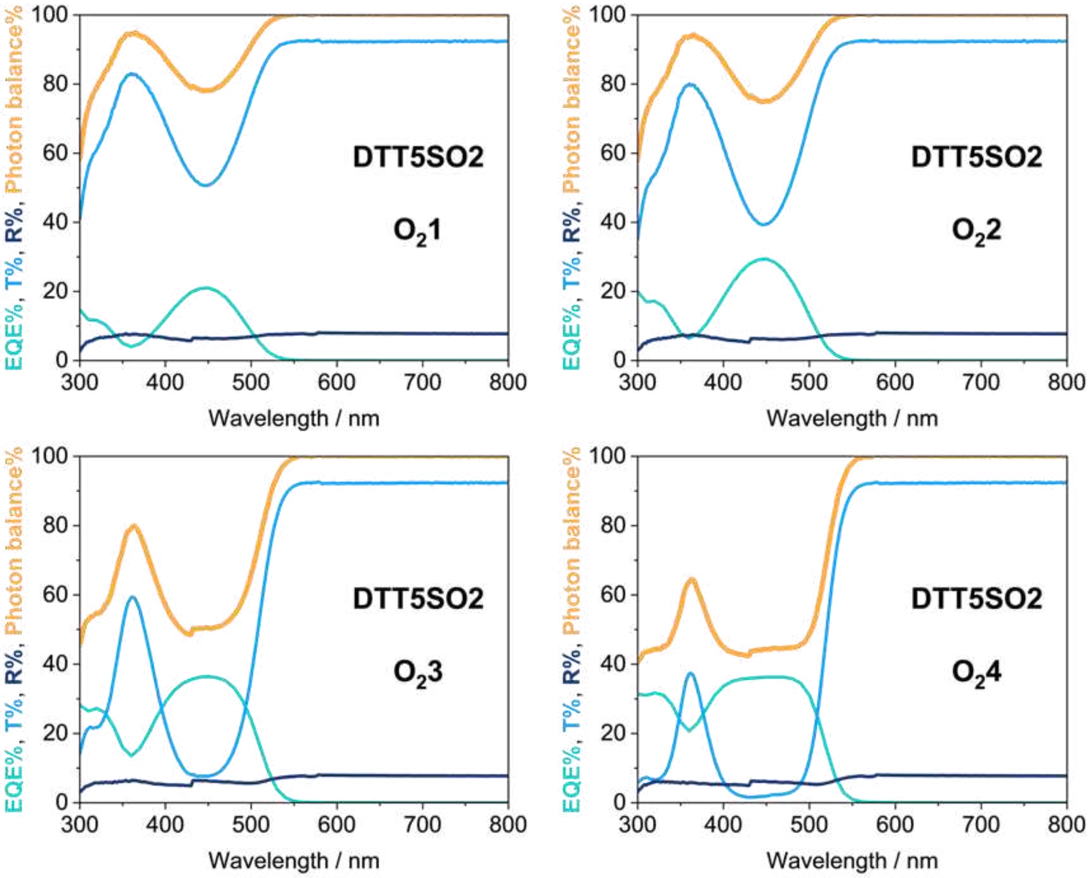

Figure D10. Consistency checks on the photon balance for the **O$_2$** sample series. Displayed EQE spectra are relative to a four-edge LSC-PV configuration and have been derived by correcting one-edge measurements for the geometric factor and averaging the corrected spectra. Colour code: yellow, photon balance; light blue, transmittance spectrum; aqua green, EQE spectrum; blue: reflectance spectrum.

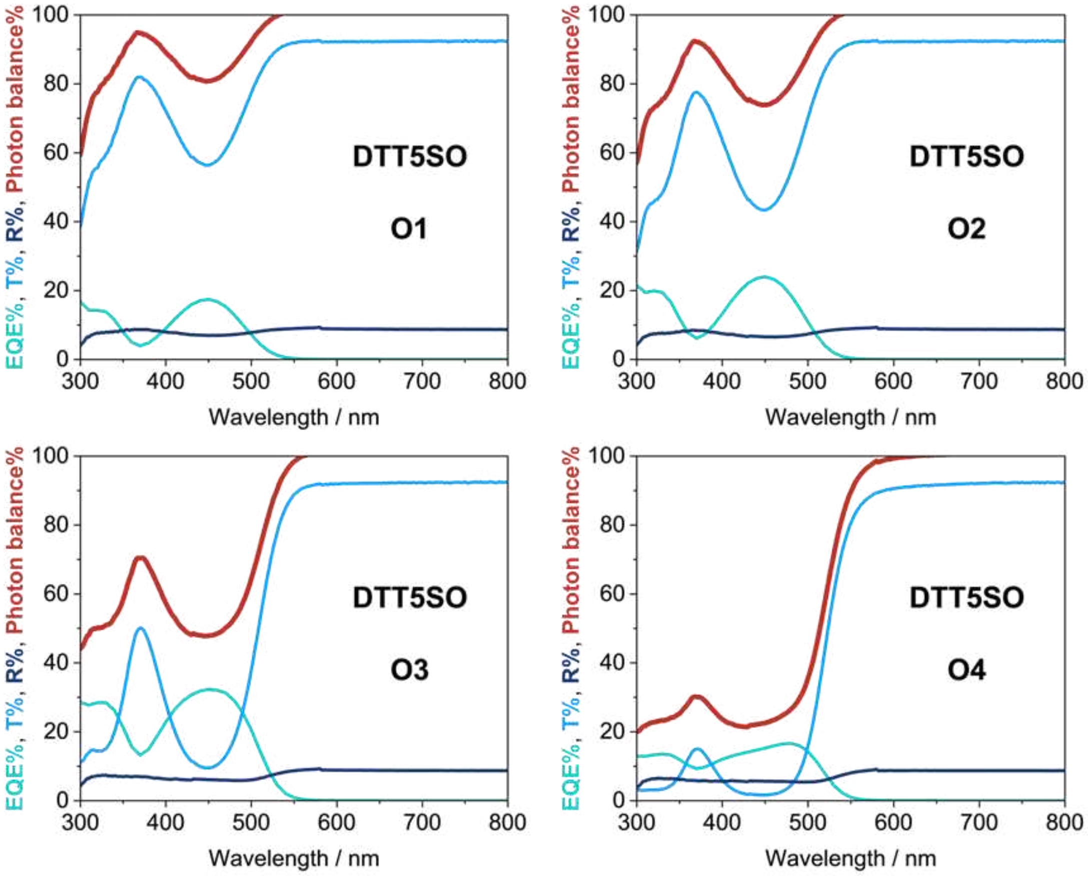

Figure D11. Consistency checks on the photon balance for the **O** sample series. Displayed EQE spectra are relative to a four-edge LSC-PV configuration and have been derived by correcting one-edge measurements for the geometric factor and averaging the corrected spectra. Colour code: brown, photon balance; light blue, transmittance spectrum; aqua green, EQE spectrum; blue: reflectance spectrum.

C4.1 Chapter 7: DQ-Th fluorophores, DUT analysis

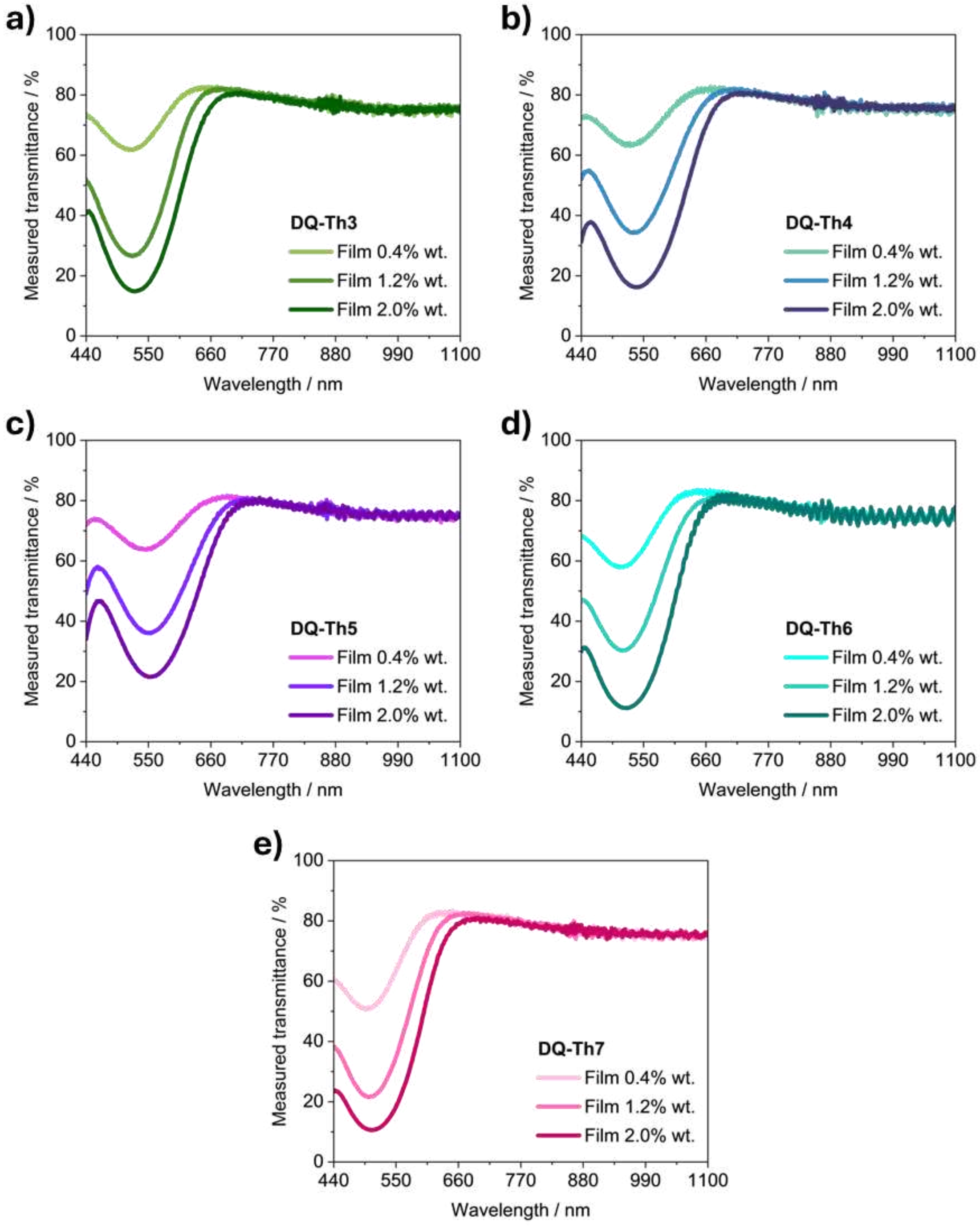

Figure D12. Measured transmittance spectra of the fluorescent PMMA films doped at 0.4%, 1.2% and 2.0% wt. with **a) DQ-Th3**, **b) DQ-Th4**, **c) DQ-Th5**, **d) DQ-Th6** and **e) DQ-Th7**.

a) DQ-Th3

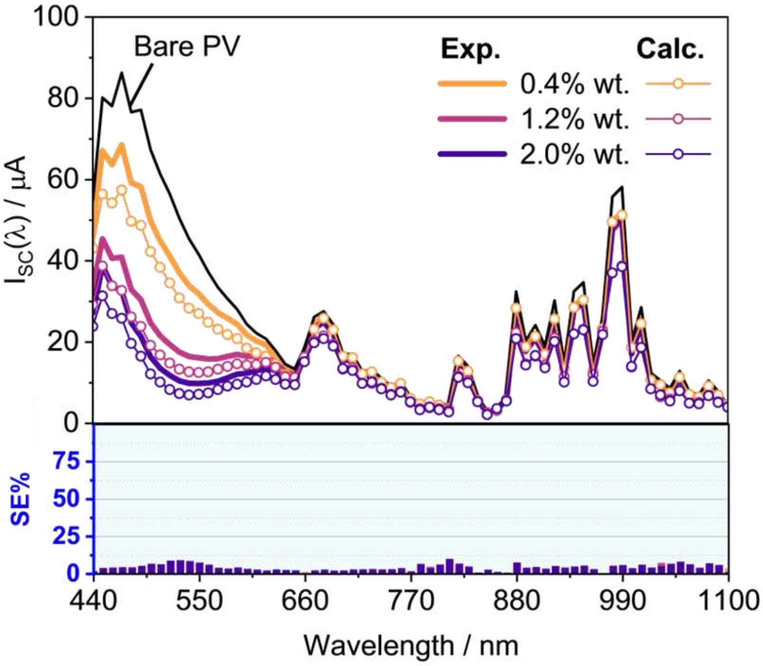

b) DQ-Th3 + OC

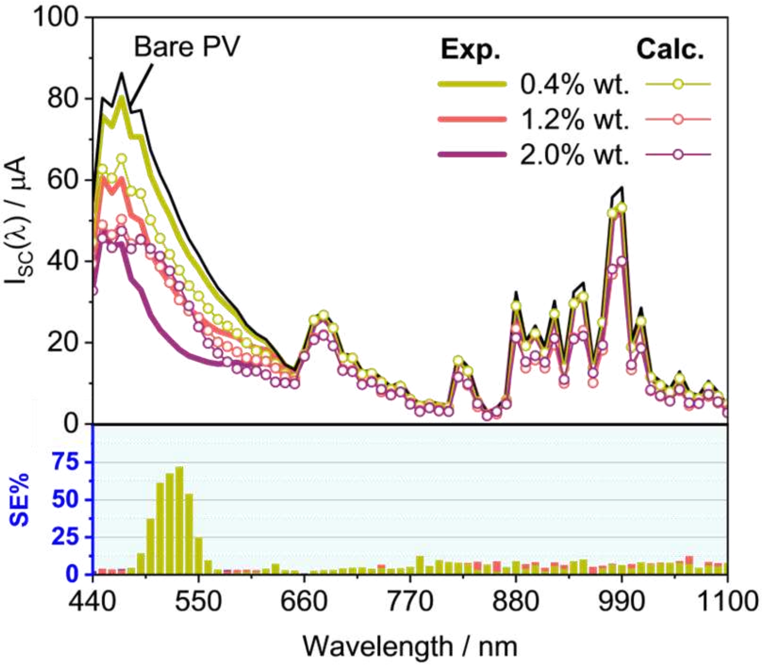

Figure D13. Model validation for the DUT incorporating the PMMA films doped with **DQ-Th3** at increasing weight content, **a)** prior and **b)** after introducing optical coupling (OC) between the PV cell and the film. The lower panels display the $SE\%$ on the model's prediction as column plots.

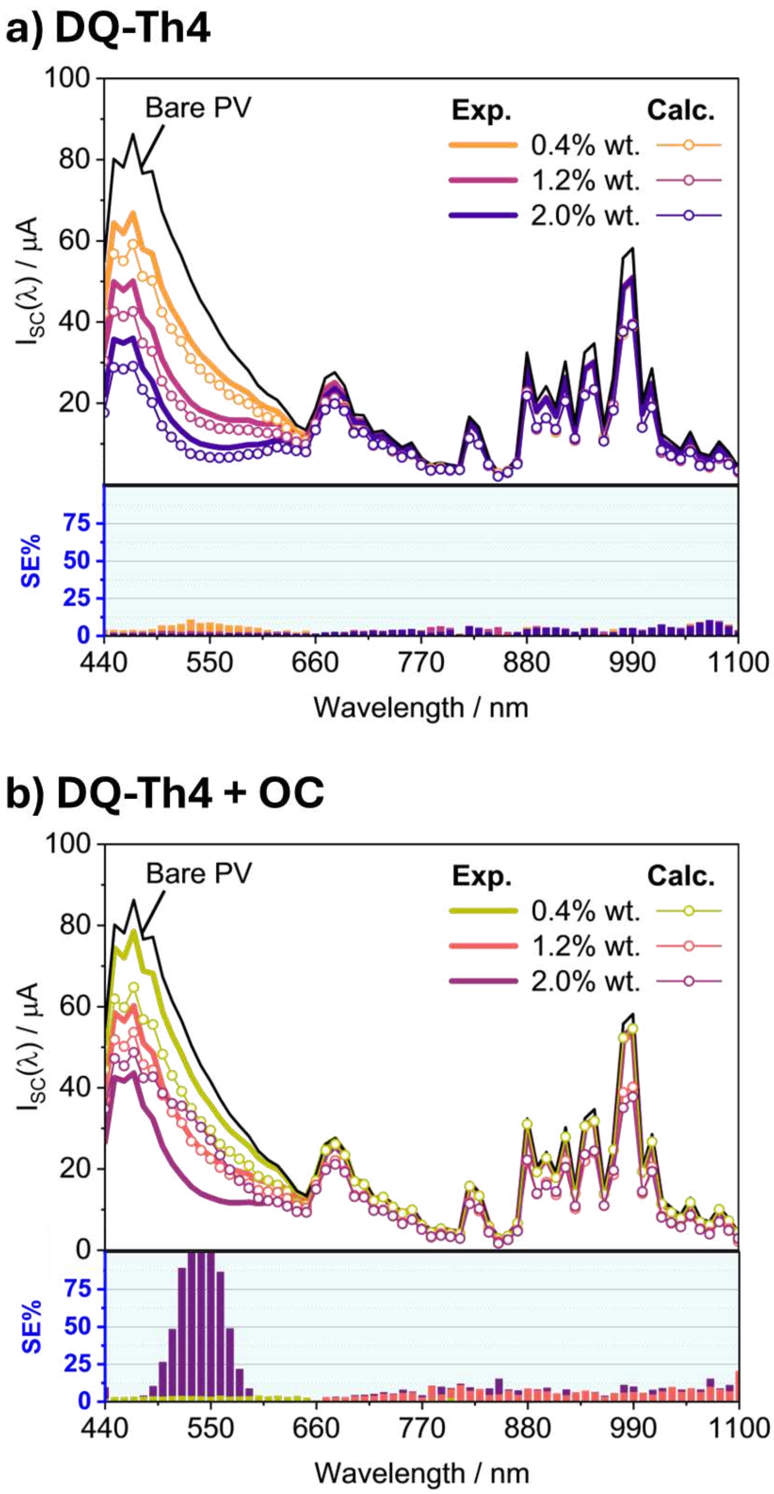

Figure D14. Model validation for the DUT incorporating the PMMA films doped with **DQ-Th4** at increasing weight content, **a)** prior and **b)** after introducing optical coupling (OC) between the PV cell and the film. The lower panels display the $SE\%$ on the model's prediction as column plots.

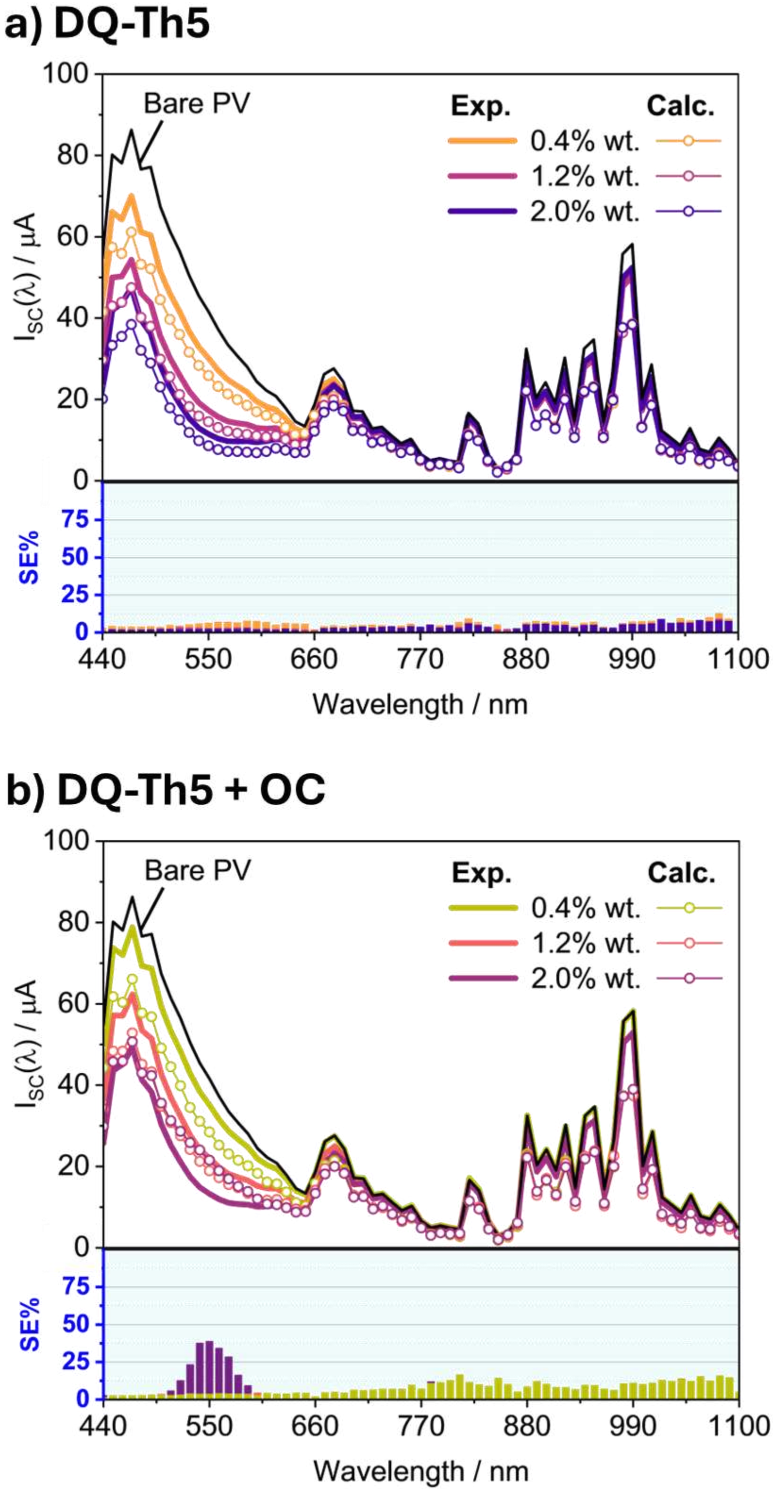

Figure D15. Model validation for the DUT incorporating the PMMA films doped with **DQ-Th5** at increasing weight content, **a)** prior and **b)** after introducing optical coupling (OC) between the PV cell and the film. The lower panels display the $SE\%$ on the model's prediction as column plots.

a) DQ-Th6

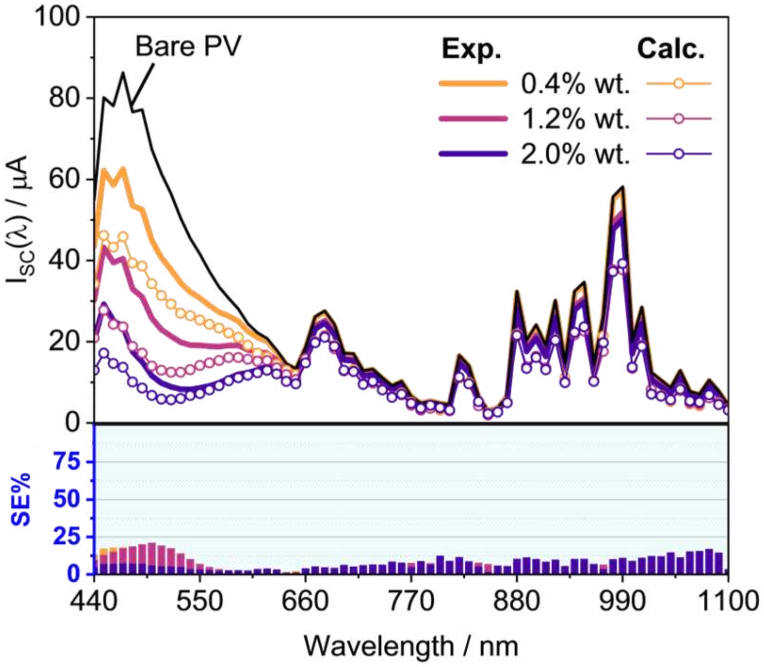

b) DQ-Th6 + OC

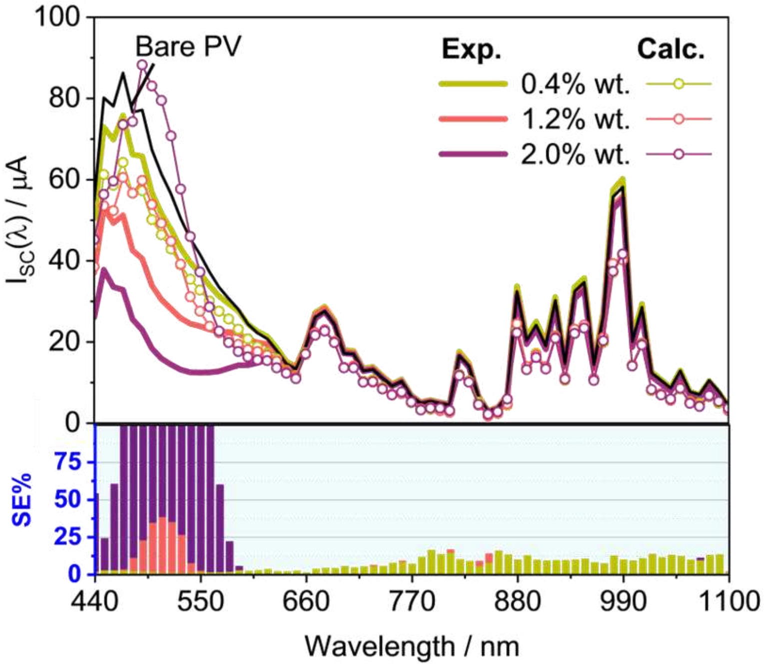

Figure D16. Model validation for the DUT incorporating the PMMA films doped with **DQ-Th6** at increasing weight content, **a)** prior and **b)** after introducing optical coupling (OC) between the PV cell and the film. The lower panels display the $SE\%$ on the model's prediction as column plots.

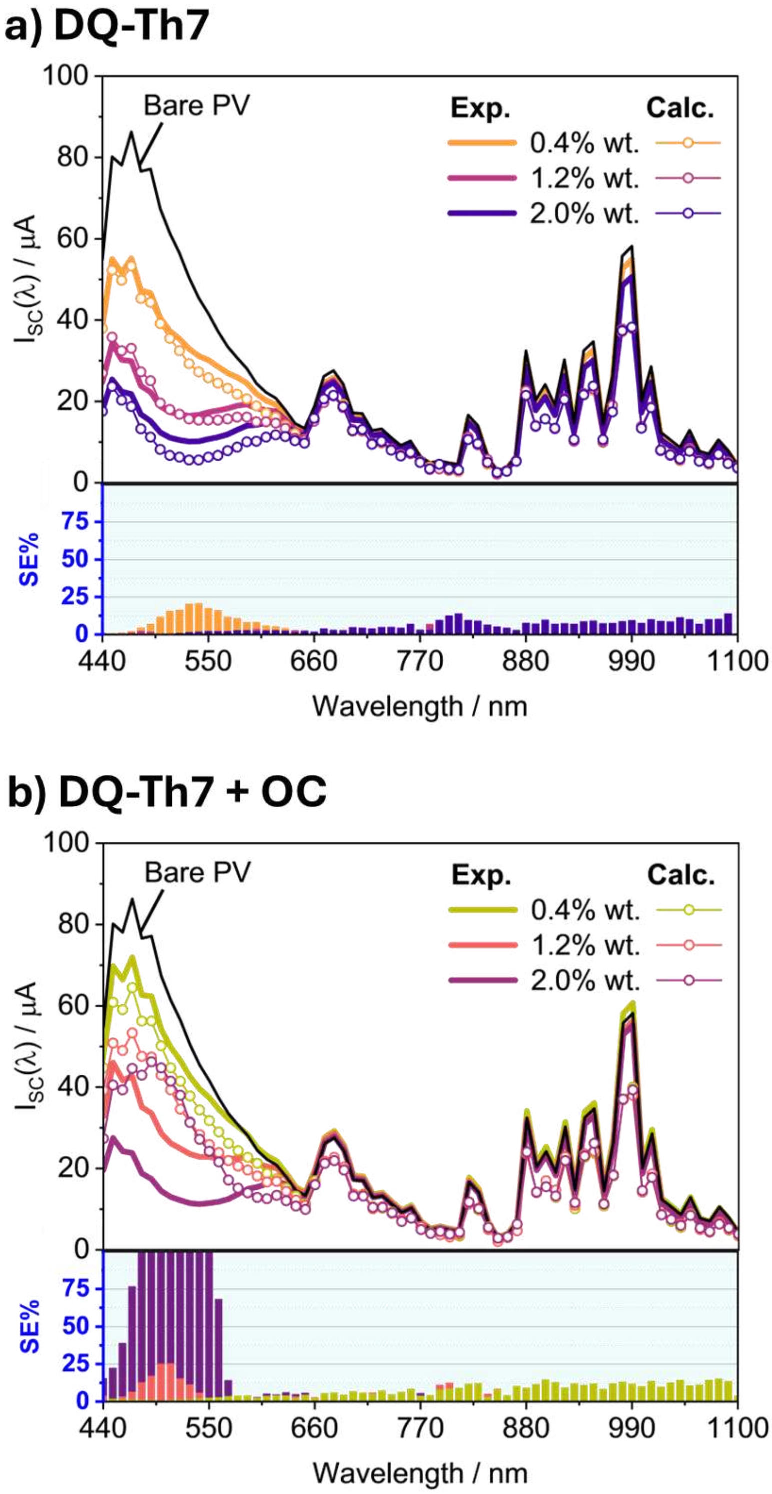

Figure D17. Model validation for the DUT incorporating the PMMA films doped with **DQ-Th7** at increasing weight content, **a)** prior and **b)** after introducing optical coupling (OC) between the PV cell and the film. The lower panels display the $SE\%$ on the model's prediction as column plots.